ISBN 978-82-326-5058-3 (printed ver.)
ISBN 978-82-326-5059-0 (electronic ver.)
ISSN 1503-8181

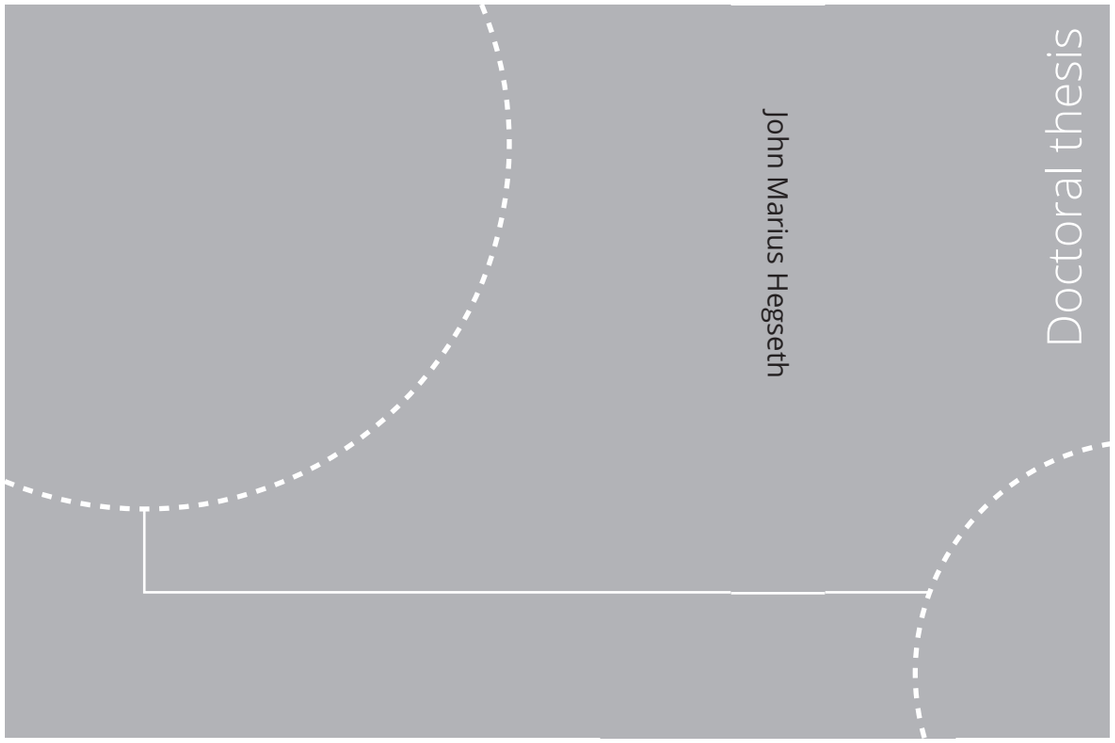

Doctoral theses at NTNU, 2020:356

John Marius Hegseth

Efficient Modelling and Design Optimization of Large Floating Wind Turbines

NTNU
Norwegian University of Science and Technology

Doctoral theses at NTNU, 2020:356

NTNU

NTNU
Norwegian University of Science and Technology
Thesis for the degree of Philosophiae Doctor
Faculty of Engineering
Department of Marine Technology

NTNU
Norwegian University of Science and Technology

John Marius Hegseth

Efficient Modelling and Design Optimization of Large Floating Wind Turbines

Thesis for the degree of Philosophiae Doctor

Trondheim, November 2020

Norwegian University of Science and Technology
Faculty of Engineering
Department of Marine Technology

NTNU
Norwegian University of
Science and Technology

NTNU
Norwegian University of Science and Technology

Thesis for the degree of Philosophiae Doctor

Faculty of Engineering
Department of Marine Technology

ISBN 978-82-326-5058-3 (printed ver.)
ISBN 978-82-326-5059-0 (electronic ver.)
ISSN 1503-8181

Doctoral theses at NTNU, 2020:356

PRINTED IN NORWAY
NO - 1598

NORDIC SWAN ECOLABEL
Printed matter
2041 0731

Printed by Skipnes Kommunikasjon AS

Abstract

Floating wind turbines (FWTs) are considered a promising solution for wind energy harvesting in deep water, but are currently too expensive to compete with other energy sources. Being a relatively new and immature technology means that there still is a large potential for cost reductions through optimization of the FWT structure. Optimized designs will bring the construction costs of FWTs down and increase profitability, which is currently the major challenge for the industry. Optimized designs can also result in increased reliability, which is an important issue.

A FWT may encounter a large number of different loading situations during its lifetime, including operational, parked, fault, start up, and shutdown events. In each of these situations, various combinations of environmental loads from wind and waves must be considered. Combined with computationally expensive response analyses, this results in a comprehensive design process.

FWTs are also highly multidisciplinary systems, primarily combining the areas of aerodynamics, hydrodynamics, structural dynamics, and control theory. The interactions between the disciplines, and between different components in the system, calls for integrated analysis and design. Due to the complex dynamics, strong couplings, and potentially large number of design variables, identifying optimal design solutions become a difficult task.

The main purpose of this work was to improve the design process for FWTs and thus contribute to reducing the cost of energy. This is addressed through two overall research objectives, which consider i) increased computational efficiency of global design analyses for FWTs, and ii) methods for numerical

design optimization which can help identify cost-effective and reliable design solutions. The main focus was on the support structure and controller for 10 MW spar-type turbines, considering fatigue and ultimate loads.

A linearized aero-hydro-servo-elastic model was shown to yield good results for the fatigue loads in the support structure, where agreement within ± 30 % was achieved for the long-term fatigue damage compared to nonlinear time-domain simulations. Acceptable agreement was also observed for short-term extreme response, especially for the support structure bending moments, which were quite Gaussian also in harsh environmental conditions. The resonant platform pitch response was overestimated by the linear model, especially in near-rated conditions.

A gradient-based optimization approach with analytic derivatives was developed to perform integrated design optimization of the support structure, blade-pitch controller, and mooring system for an elastic 10 MW spar FWT, including the scantling design of the hull, where the goal was to minimize a combination of design costs and rotor speed variation. Different control strategies were compared through integrated design of the controller and support structure, which allowed for identification of optimal control parameters in a lifetime perspective, and fair comparisons between different strategies.

The impact of environmental modelling on the long-term fatigue reliability, and associated design costs, of the support structure was assessed through re-design of the tower and platform. Considering stochastic turbulence intensity, wind-wave misalignment and the wind directional distribution reduced the long-term fatigue damage by approximately two-thirds along the support structure, compared to the base model. Implications of the chosen fatigue safety factor on the trade-offs between CAPEX and OPEX were also assessed.

The methodologies for global response analyses and integrated design optimization developed in the present work have been shown to be suitable for preliminary design of spar FWTs, where they can provide a starting design for later and more detailed design phases. Different modelling and design aspects for cost-effective and reliable solutions have been identified and assessed. The methodologies can be further extended to account for different FWT concepts, additional design parameters, and other load cases, and may help identify novel design solutions.

Acknowledgements

This thesis is submitted in partial fulfilment of the requirements for the degree of philisophiae doctor (PhD) at the Norwegian University of Science and Technology (NTNU). The research has been carried out at the Department of Marine Technology, in affiliation with the Centre for Autonomous Marine Operations and Systems (AMOS). Support has been provided by the Research Council of Norway (NFR) through project number 274827 - 'Green Energy at Sea'.

Firstly, I would like to express my gratitude to my supervisor, Professor Erin E. Bachynski. Her commitment and genuine interest in my research have been invaluable throughout this PhD, and despite a busy schedule, her door has always been open for discussions or advice. I am hugely grateful for the patience she has shown with me and my problems along the way, and for the thorough and prompt feedback she has provided on my work. Her incredible knowledge and passion for offshore wind energy research have truly been inspiring.

During my PhD I was invited to spend three months with the MDO Lab at the University of Michigan. I would like to thank my co-supervisor, Professor Joaquim R. R. A. Martins, for welcoming me into his lab, for sharing some of his vast knowledge about multidisciplinary design optimization, and for taking me running on the beautiful trails of Pinckney Recreation Area. The enthusiastic help of Dr. John Jasa was crucial for the work concerning OpenMDAO. A word of thanks goes also to the rest of the lab for making my stay so enjoyable.

At NTNU, my co-supervisor Professor Michael Muskulus is acknowledged for his ideas and feedback. I am also grateful to Professor Bernt J. Leira

for discussions and guidance on the work concerning structural reliability. Furthermore, Bjørn Tore Bach deserves thanks for the hours spent setting up the computers that was used to perform many of the numerical calculations.

I have enjoyed many interesting conversations with my office mate for three years, Øyvind Rabliås, spanning everything from potential flow theory to cross-country skiing. Carlos Eduardo Silva de Souza has been a frequent discussion partner, especially on the topic of wind turbine control, which resulted in a co-authored paper (and some sightseeing in Boston). I also appreciate the friendship and discussions I have shared with my fellow PhD students and other colleagues at the Department of Marine Technology.

Finally, I would like to thank my family - my parents and my sisters - who have provided lifelong support and encouragement, and my friends, who made sure I spent most of my weekends running or skiing rather than at the office.

Publications

The thesis consists of an introductory part and a collection of papers. The papers that form the basis of the thesis, as well as additional papers and a declaration of authorship, is presented in the following.

List of publications

The following five papers are considered part of this thesis:

P1 John Marius Hegseth and Erin E. Bachynski (2019). A semi-analytical frequency domain model for efficient design evaluation of spar floating wind turbines. *Marine Structures, 64, 186-210.*

P2 Carlos Eduardo S. Souza, John Marius Hegseth and Erin E. Bachynski (2020). Frequency-dependent aerodynamic damping and inertia in linearized dynamic analysis of floating wind turbines. *Journal of Physics: Conference Series, 1452, 012040.*

P3 John Marius Hegseth, Erin E. Bachynski and Joaquim R. R. A. Martins (2020). Integrated design optimization of spar floating wind turbines. *Marine Structures, 72, 102771.*

P4 John Marius Hegseth, Erin E. Bachynski and Joaquim R. R. A. Martins (2020). Design optimization of spar floating wind turbines considering different control strategies. *Journal of Physics: Conference Series. Accepted for publication.*

P5 John Marius Hegseth, Erin E. Bachynski and Bernt J. Leira (2020). Effect of environmental modelling and inspection strategy on the op-

timal design of floating wind turbines. *Submitted to Reliability Engineering and System Safety.*

The following paper is not regarded as part of the thesis due to scope:

P6 John Marius Hegseth, Erin E. Bachynski and Madjid Karimirad (2018). Comparison and validation of hydrodynamic load models for a semi-submersible floating wind turbine. *Proceedings of the ASME 2018 37th International Conference on Ocean, Offshore and Arctic Engineering (OMAE2018), Madrid, Spain.*

Declaration of authorship

In **P1**, **P3**, **P4**, and **P5**, J. M. Hegseth had the main ideas for the papers, developed the numerical models, performed all calculations, and wrote the manuscripts. Profs. E. E. Bachynski, J. R. R. A. Martins and B. J. Leira contributed with valuable suggestions and feedback during the processes. **P2** was initiated by C. E. Souza, who also developed the forced oscillation method and wrote the manuscript. J. M. Hegseth derived the analytic expressions for the aerodynamic damping and inertia coefficients, developed the linearized model, and participated in discussions. Prof. E. E. Bachynski provided guidance and feedback.

Contents

Chapter 1

Introduction

This chapter gives an overview of the background and motivation for this work, and states the objectives of the research. A summary of the main contributions to the scientific community, as well as their relations to the research objectives and appended papers, are also presented.

1.1 Motivation and background

The high global demand for energy has led to a large consumption of fossil fuels, with several negative consequences, most notably climate change. The last decades have seen a large increase in the use of wind energy, which more recently has moved offshore. Offshore wind is an attractive energy source due to higher wind speeds with less turbulence, larger areas less susceptible to conflicts with other interests, and with smaller environmental impact than its land-based counterpart.

The majority of energy producing offshore wind turbines installed to date are bottom-fixed, and located in shallow waters. Because suitable sites for such wind parks are limited, it is desirable to develop offshore wind farms in deeper waters. In water depths above 50-60 m, bottom-fixed structures are not economically feasible, and FWTs are expected to be the most cost-effective option (Musial et al. 2006). As 80 % of the offshore wind resources in Europe are located at water depths above 60 m (The Carbon Trust 2015), there is a vast potential market for floating wind power, which could become a crucial part of the energy mixture of the future.

The technical potential floating wind capacity across Europe, USA, and Japan is estimated to about 7000 GW, where 4000 GW is located in Europe

Table 1.1: Floating wind farms in Europe with expected commissioning date within 2022 (WindEurope 2019).

Country	Wind farm	Floater type	Capacity (MW)	No. of turbines	Water depth (m)
Portugal	Windfloat Atlantic Phase 1	Semi-sub	25.0	3	100
France	EolMed	Barge	24.0	4	55
France	Provence Grand Large	TLP	28.5	3	100
France	EFGL Eoliennes	Semi-sub	30.0	3	65-80
France	Flottantes de Groix	TLP	28.5	3	60
UK	Kincardine	Semi-sub	50.0	5	60-80
Norway	Hywind Tampen	Spar buoy	88.0	11	260-300

(The Carbon Trust 2015). However, moving the energy production to deeper water and larger distances from shore increases the complexity and requires innovative technology. To date, the world's only floating wind farm is the Hywind Scotland pilot park, which consists of five turbines with an installed capacity of 30 MW. However, more than 30 different FWT concepts have been proposed (Leimeister et al. 2018), and several floating wind farms are planned to start operation in the near future. Seven European farms, listed in Table 1.1, are expected to be commissioned within the next three years, with a total capacity of 274 MW.

The cost of floating wind is currently higher than for bottom-fixed turbines, and large reductions are needed to reach a competitive level. Floating wind turbines have larger construction costs than the bottom-fixed alternative; however, installation costs are expected to be smaller, because the turbines can be assembled at port using onshore cranes instead of expensive jack-up vessels at site (Katsouris and Marina 2016). The current levelized cost of energy (LCOE) is estimated to €180-200/MWh for pre-commercial projects, but large reductions are expected as the technology matures and reaches commercial-scale deployment, and may attain values of €40-60/MWh in 2030 (WindEurope 2018).

Lower LCOE can be achieved in several ways, such as reduction of capital

costs (CAPEX) or operation and maintenance costs (OPEX), increase in the capacity factor, or through lifetime extension. As floating wind is a relatively new and immature technology, there is still a large potential for cost reductions through optimization of the FWT structure. A breakdown of typical CAPEX for floating wind farms is shown in Fig. 1.1, where the turbine and platform are seen to comprise more than 60 % of the total costs, suggesting that significant cost reductions in these components may be necessary to reach a sustainable and competitive LCOE. This is also supported by feedback from concept designers, who identify platform size as the most critical technical barrier with respect to cost savings for floating wind farms (The Carbon Trust 2015).

As the technology matures, turbines grow larger, and during the last decade, the average capacity of newly installed offshore wind turbines in Europe has more than doubled, from 3 MW in 2009 to 7.8 MW in 2019 (WindEurope 2019). The turbines are expected to grow further as the technology improves, and could reach 15-20 MW by 2030 (IEA 2019). The increase in turbine size is expected to be the largest driver of cost reduction, because it allows the same amount of energy to be captured with fewer machines, and thus reduces the balance-of-system costs (Smith et al. 2015). In addition, it results in lower relative costs of the substructure, tower and mooring costs, compared to a larger number of turbines with smaller rating (Müller et al. 2019). The increase in size also introduces new challenges and opportunities for design, with innovative turbine and substructure technologies having a large impact on the achieved cost reductions (Chaviaropoulos et al. 2014). It may also help new materials, such as concrete, become more attractive solutions (Müller et al. 2016).

A FWT is subjected to a large number of different loading conditions during its lifetime, involving a highly stochastic environment with irregular loads from wind and waves. According to DNV GL (2018a), the structure shall be designed to sustain all loads during temporary, operating, and damaged conditions, ensure safe operation of the wind turbine, maintain acceptable safety for personnel and environment, and have sufficient durability against deterioration. Because FWT structures are unmanned, the consequences of failure are normally limited to economic losses. Failures may, however, also affect the environment or nearby structures, and FWTs should be designed for an annual target probability of failure of 10^{-4} (DNV GL 2018a).

Four different limit states are considered in design (DNV GL 2016):

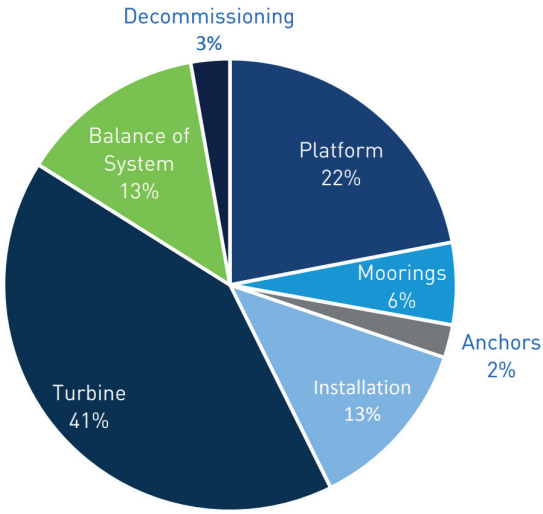

Figure 1.1: Estimated breakdown of capital costs for commercial scale floating wind farms (The Carbon Trust 2015).

Ultimate limit state	*(ULS):*	Exceedance of maximum load carrying resistance.
Fatigue limit state	*(FLS):*	Failure due to cyclic loading.
Accidental limit state	*(ALS):*	Failure due to accidental or abnormal loads.
Serviceability limit state	*(SLS):*	Exceedance of criteria for normal use or durability.

Offshore wind turbines are highly dynamic systems subjected to static, periodic, stochastic, and transient loads. Combined with compliant structures and a relatively long design lifetime, this often leads to FLS being design driving for several components (Vorpahl et al. 2013). Contrary to the design of conventional offshore structures, which tends to be driven by ultimate loads, this is also the case for the floating platform (Strach-Sonsalla and Muskulus 2016). To give a realistic estimate of the fatigue life of the structure, all relevant environmental conditions throughout the lifetime of the system must be considered, which leads to a comprehensive set of design calculations. This is especially the case if directionality of wind and waves is considered, which is of particular importance for fatigue design (DNV GL 2018a).

In addition to fatigue, the survival of the platform and turbine in extreme

conditions must be ensured. Typical ULS criteria consider overturning, capsizing, yielding, and buckling (DNV GL 2018a). Further constraints may be applied to prevent water on deck, negative air gap, and sloshing inside ballast tanks during storm events (Strach-Sonsalla and Muskulus 2016). Failure caused by accidental loads, or exceedance of ultimate resistance of damaged structures, is covered by ALS criteria (DNV GL 2018a), and is not considered in this thesis.

Lastly, SLS deals with criteria to ensure normal operation of the turbine. It involves limitations on inclinations, accelerations and motions due to sensitive equipment and the power cable (Strach-Sonsalla and Muskulus 2016), in addition to ensurement of sufficient hydrostatic stability for efficient power production.

In general, the design criteria can be written

$$S_d \leq R_d, \tag{1.1}$$

where S_d is the design load effect, and R_d is the design resistance. These are usually found using the partial safety factor method, where the different characteristic load effects and resistances are multiplied by individual load and material factors to obtain their design values. The safety factors reflect the uncertainty in the respective design parameters, as well as the required reliability level.

Probability-based design is an alternative to the partial safety factor method, where the load and resistance variables are described by their probability distributions. The design of the system is then performed to meet a safety level which is expressed by the failure probability:

$$P_F = P[S > R], \tag{1.2}$$

which should be equal to the annual target failure probability (DNV GL 2018a). In practical applications, the partial safety factor method is by far the most popular, and probability-based design is mainly used to calibrate safety factors, or in design of systems where limited experience is available (DNV GL 2018b).

To evaluate the structure's margin of safety against the different limit states, an extensive number of design load cases (DLCs) must be assessed. Relevant DLCs for FWTs are defined by DNV GL (2016), and consider eight distinct design situations:

- Power production

- Power production plus fault
- Start up
- Normal shutdown
- Emergency shutdown
- Parked turbine
- Parked turbine plus fault
- Transport, installation and repair

Within each of these design situations, a subset of load cases are specified. The subsets consider different wind and wave conditions, fault types, and limit states, and the total number of load cases in a design process may therefore add up to several thousands.

The goal of the design optimization process is to find the design that minimizes or maximizes a given performance measure, such as costs or power production, and at the same time meets the appropriate design criteria. In traditional design optimization, the performance of an initial design is evaluated through analyses or experiments. Based on the results, the designer makes changes to the design, and the process is repeated until a satisfactory design is achieved. This process is typically limited to a few iterations, where changes to the design to a large extent depend on the experience of the designer (Muskulus and Schafhirt 2014).

In contrast, numerical optimization techniques can efficiently explore large parts of the design space to identify improved and possibly non-intuitive solutions, as illustrated in Fig. 1.2. Such techniques have been widely utilized in the automotive and aerospace industries, but have seen limited use in design of wind turbine structures (Muskulus and Schafhirt 2014). Similarly to a conventional design process, the performance of an initial design is evaluated based on results from analyses, and iterations are performed until a satisfactory solution has been achieved. The key differences are that the design changes are made automatically by an optimization algorithm, and that the design process does not end until certain optimality criteria are satisfied. These criteria ensure that the final design not only complies with the relevant constraints, but that it indeed is the solution that minimizes or maximizes the chosen performance measure, at least in that particular neighbourhood of the design space (Martins and Ning 2020).

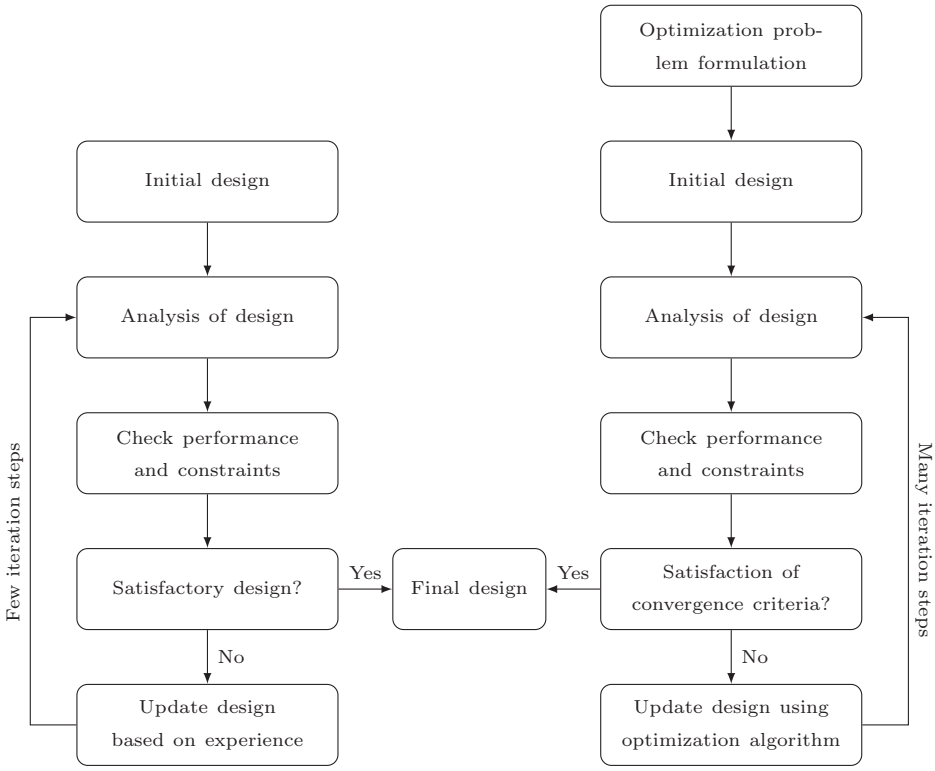

Figure 1.2: Comparison of main steps in a manual and numerical design optimization process. Adapted from Muskulus and Schafhirt (2014).

Although these techniques enable automation of the design process, they do not remove the need for field-specific expertise from the designer. The outcome of a numerical optimization procedure relies heavily on the formulation of the optimization problem. An appropriate objective function must be chosen, whose value is the only measure of the performance for a given design. Further, relevant constraints should be identified, and proper enforcement strategies must be defined. Finally, a parametrization of the design space is needed, which determines the possibilities for the optimization algorithm to modify the design. The successful application of such methods thus requires profound knowledge about the nature of the system that is considered, and possibly more so than in a traditional design process (Martins and Ning 2020).

As a FWT system experiences important interactions between several different subsystems and disciplines, integrated design is needed to find optimal solutions on the overall system level (Muskulus and Schafhirt 2014). In an

integrated design process, all relevant disciplines are coupled, and the subsystems are designed simultaneously. An integrated optimization approach involves a large number of design variables and load cases, and requires sophisticated and multidisciplinary numerical tools. Although the overall system in terms of total cost and energy production is the whole wind farm, the studies are limited to a single turbine in the present work, and farm-level effects are not considered.

1.2 Research objectives

The overall aim of the thesis is to improve the efficiency and reliability of the design process for FWTs, especially catenary-moored spar-type turbines, and develop methodologies to identify novel and optimized design solutions. This is addressed by defining two separate research objectives.

During the design process, a numerical model of the FWT system is created and analysed. The global dynamic response is evaluated using fully coupled aero-hydro-servo-elastic analyses, considering combined wind-wave loading. The computational costs associated with such analyses are high, and due to the variety of design situations and environmental conditions that a FWT may encounter during its lifetime, a large number of load simulations must be carried out. There is therefore a need for more efficient analysis tools, especially during the conceptual and preliminary design phases. While simplified simulation models may not be able to provide accurate response predictions for all relevant design situations, they should capture important interactions and response characteristics in the system, and provide consistent design load estimates in comparisons with high-fidelity simulations for applicable loading conditions.

The first research objective of this thesis is related to reduction of the computational burden associated with global design analyses of FWTs, and is formulated as:

O1 Suggest and verify methods to increase the computational efficiency of global design analyses for floating wind turbines.

Due to the complex and multidisciplinary dynamic system, with a large number of parameters and load cases, the design space cannot be efficiently explored through traditional design procedures. The important couplings in the system call for integrated optimization, which further complicates the design problem. Numerical optimization techniques may help develop

improved and possibly novel solutions, but have seen limited use for FWT structures. Consequently, there is currently no software or framework available for efficient FWT optimization, and there are uncertainties related to the formulation of the optimization problem. Design methodologies with improved accuracy and efficiency, which can help identify innovative and optimized solutions, are expected to result in cost reductions and increased reliability, and can help floating wind technology become commercially feasible.

The second research objective addresses the potential for design improvements through numerical optimization, and is formulated as:

O2 Develop methodologies for numerical design optimization of floating wind turbine systems, considering ultimate strength and fatigue, and identify possible cost-effective and reliable design solutions.

The two research objectives are connected because contributions related to **O1** can be implemented in, and thus improve the feasibility of, models developed in relation to **O2**. The objectives are achieved using numerical simulations, which are performed for a 10 MW wind turbine rotor mounted on a floating support structure[1]. Because a limited amount of available and relevant measurement data from full- or model-scale FWTs exists, results from state-of-the-art numerical simulations are used as benchmark for the models and methods developed over the course of the thesis.

1.3 Main contributions

Based on the research objectives defined in Section 1.2, several contributions to the scientific community have been made. The main contributions are further discussed in Chapter 4, and briefly summarized in the following. The relations between research objectives, papers, and contributions are illustrated in Fig. 1.3.

C1 A linearized aero-hydro-servo-elastic model for efficient global response analyses of FWTs, extensively verified against state-of-the-art simulations with regards to both fatigue damage and extreme response.

C2 Derivation of closed-form expressions for frequency-dependent aerodynamic damping and inertia, and an assessment of their impact on frequency-domain calculations.

[1]The term *support structure* corresponds to the combined tower and platform structure.

C3 A methodology for integrated design optimization of spar FWTs, considering simultaneous design of platform, tower, controller, and mooring system, using gradient-based optimization with analytic derivatives.

C4 Evaluation and comparison of different control strategies for FWTs, based on integrated optimization of support structure and blade-pitch controller with realistic design limits.

C5 Quantification of the impact of environmental modelling on the long-term fatigue reliability and costs of FWT support structures.

C6 Assessment of trade-off effects between CAPEX and OPEX, and derivation of cost-optimal fatigue safety factors, considering reliability-based inspection planning.

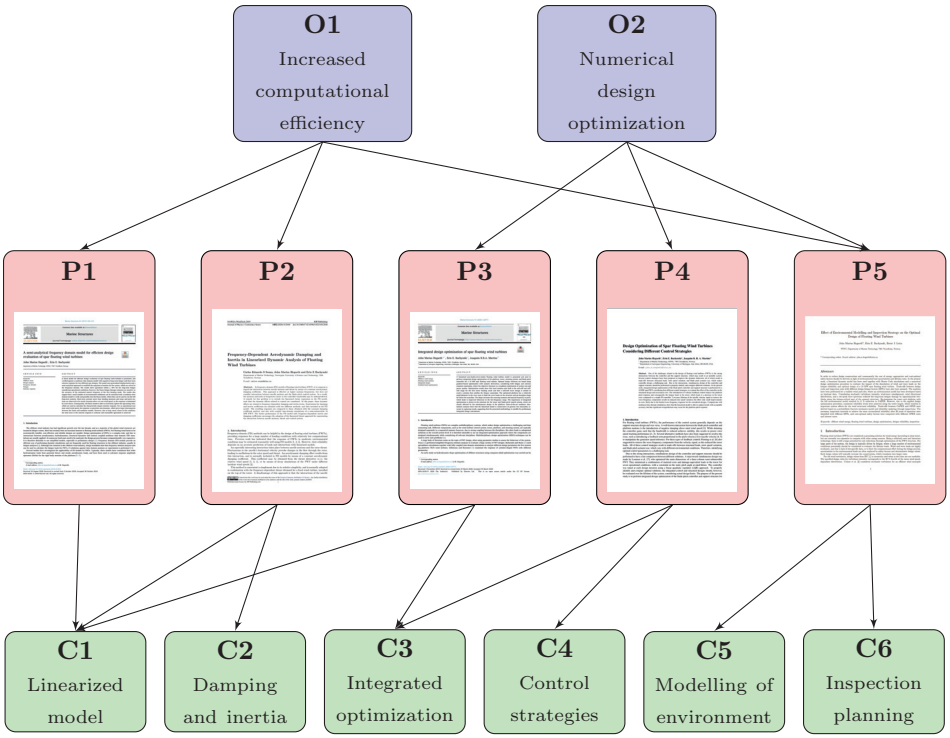

Figure 1.3: Relations between research objectives, papers, and contributions.

Chapter 2

Literature Survey

This chapter summarizes previous work relevant for global response analyses and numerical design optimization of FWT structures. Methods used in state-of-the-art and simplified dynamic simulations are described, some basic optimization theory is given, and specific aspects and challenges related to design optimization of FWTs are discussed.

2.1 Global response analyses

2.1.1 Environmental modelling

FWTs are subjected to stochastic environmental loading, which require a proper statistical description for evaluation of lifetime loads in design. Temporal environmental variations occur at many different time scales, which in engineering applications are separated into short-term and long-term variability. In short-term conditions, the wind and wave processes are considered stationary Gaussian stochastic processes, and are generally assumed to be uncorrelated (DNV GL 2016). Short-term variations in wind speed and wave elevation are commonly given in terms of their power spectral densities, which describe the distribution of energy at different frequencies. For wind, a description of the spatial coherence is also needed. The long-term statistics consider the variation of the statistical properties describing the short-term process, and describe the correlation between wind and waves through a joint probability distribution.

The joint distribution of wind and waves is ideally fitted to measured data from the actual site over a long period of time, and is used to establish scatter diagrams for fatigue calculations, or identify environmental conditions

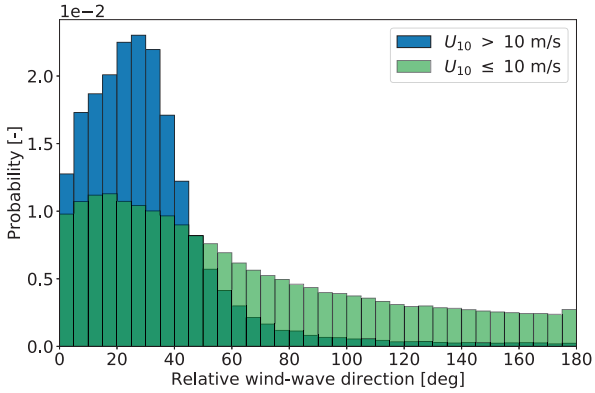

Figure 2.1: Relative wind-wave direction distributions for two wind speed bins at a North Sea location 25 km west of Norway.

with a certain return period. As a minimum, the environmental model should include distributions for the mean wind speed (U) at a reference height, the significant wave height (H_s), and the spectral peak period (T_p). A joint distribution based on measurements from the Northern North Sea was presented by Johannessen et al. (2002), using the marginal distribution of the 1-h mean wind speed at 10 m (U_{10}), and conditional distributions of H_s and T_p:

$$f_{U_{10},H_s,T_p}(u,h,t) = f_{U_{10}}(u) f_{H_s|U_{10}}(h|u) f_{T_p|U_{10},H_s}(t|u,h). \tag{2.1}$$

It is also of interest to include directional data in the environmental model. Waves are typically short-crested, which requires a spreading function in addition to the main propagation direction. Also, the wind and waves are in general misaligned, and larger misalignment angles typically occur at smaller wind speeds (Fischer et al. 2011). This is illustrated in Fig. 2.1, where the wind-wave misalignment distribution, based on 60 years of hindcast data from a location in the North Sea, is shown for two wind speed bins. While relative wind-wave directions of more than 90° are quite rare for $U_{10} > 10$ m/s, larger misalignment angles occur more than 25 % of the time for the lower wind speed bin. The relative wind-wave direction may have a large effect on the response of the structure, and is of particular importance for fatigue design (DNV GL 2018a). While misaligned wind and waves tend to increase the tower fatigue damage for bottom-fixed turbines, the opposite has been observed for FWTs (Barj et al. 2014, Bachynski et al. 2014).

The wind speed in a given point in space consists of longitudinal, lateral,

and vertical components, where the longitudinal component varies around the mean wind speed, and the other two components typically are assumed to have zero mean. Short-term variations in the wind speed are known as turbulence, which are described by so-called turbulence spectra. A measure of the overall level of turbulence is given by the turbulence intensity, which is defined as the ratio between the standard deviation of the wind speed and its mean. In general, the turbulence intensity takes values between 0.1 and 0.4, where higher values occur for lower wind speeds (Manwell et al. 2009). If site-specific data is unavailable, values for the turbulence intensity can be taken from design standards. The IEC Class B normal turbulence model (NTM) (IEC 2005), which is applicable for moderate turbulence levels, is used in the present work.

In addition to temporal variations, the turbulence also varies spatially, which is described by the cross-correlations between fluctuations at points separated laterally and vertically (Burton et al. 2011). The resulting turbulent wind field is assumed to follow Taylor's frozen turbulence hypothesis (Taylor 1938), where the turbulence is considered as time-invariant eddies moving forward with the mean wind speed. To generate the three-dimensional turbulence box in time domain, several methods are available. A one-dimensional fast Fourier Transform (FFT) can be applied, based on spectra, to each of the three turbulence components independently, together with a coherence function for the spatial cross-correlations. Alternatively, the Mann model can be applied, where correlated components are generated using a three-dimensional FFT (Burton et al. 2011). In the present thesis, the Kaimal spectrum and an exponential coherence function are used to describe the turbulent wind field (IEC 2005).

The mean wind speed also increases with the height above ground. This variation is known as shear, and is commonly modelled using either a logarithmic or power law. The present work uses a power law with exponent 0.14, which is recommended for offshore locations (IEC 2009).

The physics of ocean waves are highly complex; however, for engineering applications, several simplifications can be made while still maintaining reasonable estimates of the wave dynamics. The waves are typically described using linear (Airy) wave theory, which assumes potential (irrotational, inviscid, and incompressible) flow (Faltinsen 1990). The irregular wave elevation process can then be generated from linear superposition of a large number of independent wave components with different frequencies, where the amplitude of each component is found from the wave spectrum.

The wave conditions in a sea state can be separated into two categories: wind seas, which are generated by local wind, and swell, which are waves that have travelled out of the areas where they were generated (DNV GL 2019a). For wind seas, the Pierson–Moskowitz (PM) and JONSWAP spectra are frequently applied (DNV GL 2019a). The JONSWAP spectrum, which was developed for North Sea conditions, is used in the present work.

If the sea state is expected to contain swell components in addition to wind-generated waves, these must also be properly represented (DNV GL 2018a). This can be done through two-peaked spectra, such as the Torsethaugen model (Torsethaugen 1996, Torsethaugen and Haver 2004), which take into account both wind and swell sea. Alternatively, the wind and swell components can be separated and described using two JONSWAP spectra, possibly with different directions, which are superimposed to represent the total wave elevation process (DNV GL 2018a).

2.1.2 State-of-the art simulations

Due to important interactions between aerodynamics, hydrodynamics, structural dynamics, and control dynamics, fully coupled aero-hydro-servo-elastic models are needed to properly simulate the global response of FWTs. Different aspects and interactions considered in such analyses are illustrated in Fig. 2.2. Over the last decade, several fully coupled simulation tools for global analysis of FWTs have been developed, often based on existing codes for either conventional offshore structures or land-based wind turbines. The present thesis uses the SIMA workbench developed by SINTEF Ocean, which couples the RIFLEX and SIMO programs (SINTEF Ocean 2016a;b). A brief summary of common structural, aerodynamic, hydrodynamic, and control capabilities in state-of-the-art analysis tools is given in the following.

The structural dynamics of FWTs are usually modelled using multibody dynamics, modal analysis, finite elements, or a combination of these (Robertson et al. 2014). While modal analysis is computationally efficient, finite elements offer the possibility of geometric and material nonlinearities, and do not require pre-calculation of the system modes. Most finite element models for FWTs are limited to beam elements, which are applicable for long, slender structures such as the tower and blades, whereas the large volume platform typically is considered rigid. The drivetrain is usually modelled using a multibody dynamics approach, where the shaft flexibility often is included through a torsional spring-damper to capture the first torsional mode of the drivetrain (Smilden 2019). The mooring lines are either

represented using nonlinear force-displacement relationships found from a quasi-static analysis, or modelled explicitly using finite elements or lumped masses. While the latter approach is computationally more expensive, it captures the mooring line dynamics, and the effects of mooring line inertia and damping on the platform response. The importance of mooring line dynamics is highly dependent on the considered platform concept and response parameters, but should be included for designs with natural frequencies inside the wave-frequency range and fairleads far away from the platform's center of mass (Hall et al. 2014b), or if extreme mooring line tension is considered (Azcona et al. 2017).

Various methods exists for calculation of aerodynamic loads on wind turbines. For global response analyses of FWTs, the aerodynamic loads on an operational turbine are commonly computed using blade element momentum (BEM) theory, due to its computational efficiency. Here, the aerodynamic lift and drag forces on the blades are balanced by the change in axial and angular momentum of the air passing through the swept annulus (Burton et al. 2011). However, BEM requires several engineering corrections to give satisfactory results, where the most commonly applied are the Glauert correction for high induction factors, and the Prandtl corrections for tip and hub loss factors. Further, additional corrections are often imposed to account for skewed inflow conditions, dynamic wake, and dynamic stall effects. The generalized dynamic wake (GDW) method is an alternative to BEM, which is based on the potential flow solution of the Laplace equation. GDW inherently includes skewed wake, tip losses, and dynamic wake effects, but is only valid for lightly loaded rotors (high wind speeds), and does not account for wake rotation (Moriarty and Hansen 2005).

Hydrodynamic loads on large volume floating structures are commonly computed from potential flow theory, where the diffraction and radiation loads are found numerically using a panel method. For many structures, the first order solution, which assumes small wave amplitudes and small motions around the equilibrium position, is sufficient to capture the dominant wave loads (Faltinsen 1990). The outputs from the hydrodynamic analysis are frequency-dependent wave excitation, added mass, and wave radiation damping, which are transformed to the time domain before they are applied in the simulations. For structures with natural frequencies outside the wave-frequency range, higher-order wave loads may also be of importance. Second-order loads from potential flow theory, which consist of sum- and difference-frequency terms, can then also be included through so-called quadratic transfer functions (QTFs). To capture important viscous effects,

the quadratic drag term in Morison's equation is often superimposed to the potential flow solution in the aero-hydro-servo-elastic simulations.

The majority of modern horizontal axis wind turbines are regulated using variable-speed variable-pitch control. Below the rated wind speed, the generator torque, and consequently the rotational speed of the turbine, is varied to maximize the power output. Above the rated wind speed, the blades are pitched to reduce the structural loads and maintain a constant rotational speed, while the generator torque is kept constant or varied to maintain a constant (rated) power output. While the controllers in below- and above-rated conditions operate independently, they are typically combined in near-rated conditions to limit the tip speed at rated power (Jonkman et al. 2009). For wind turbine analysis tools, control system models should contain, as a minimum, routines for the blade-pitch and generator torque control, in addition to start-up and shut-down procedures (Smilden 2019).

Despite their extensive use in analysis and design, the accuracy of aero-hydro-servo-elastic simulation codes is still somewhat uncertain. As identification of limitations and sources of error in the theoretical models is crucial to reduce safety factors and achieve safe and efficient design solutions, verification and validation of numerical design tools are important. Extensive code-to-code verification studies have been conducted through the OC3, OC4, and OC5 projects (Jonkman and Musial 2010, Popko et al. 2012, Robertson et al. 2014; 2017, Popko et al. 2018; 2019), which have contributed to an understanding of the applicability of different modelling approaches, helped resolve errors in the codes, and identified future improvement needs (Robertson et al. 2014). The recent OC5 project has also considered validation against experiments (Robertson et al. 2017) and full-scale data (Popko et al. 2019).

Limited full-scale measurements from FWTs exist, with very few results being publicly available, and validation studies must therefore to a large degree rely on model-scale experiments. Model tests which consider combined wind-wave response are challenging due to scaling issues. Recently, hybrid testing, where parts of the load picture are calculated numerically and applied on the experimental model using actuators, has shown promise. A real-time hybrid testing method for FWTs has been developed by SINTEF Ocean (Sauder et al. 2016, Bachynski et al. 2016, Berthelsen et al. 2016), where wave basin tests are conducted with aerodynamic loads from simultaneous numerical simulations. A complimentary approach using wind tunnel tests with numerically computed hydrodynamic loads has also been

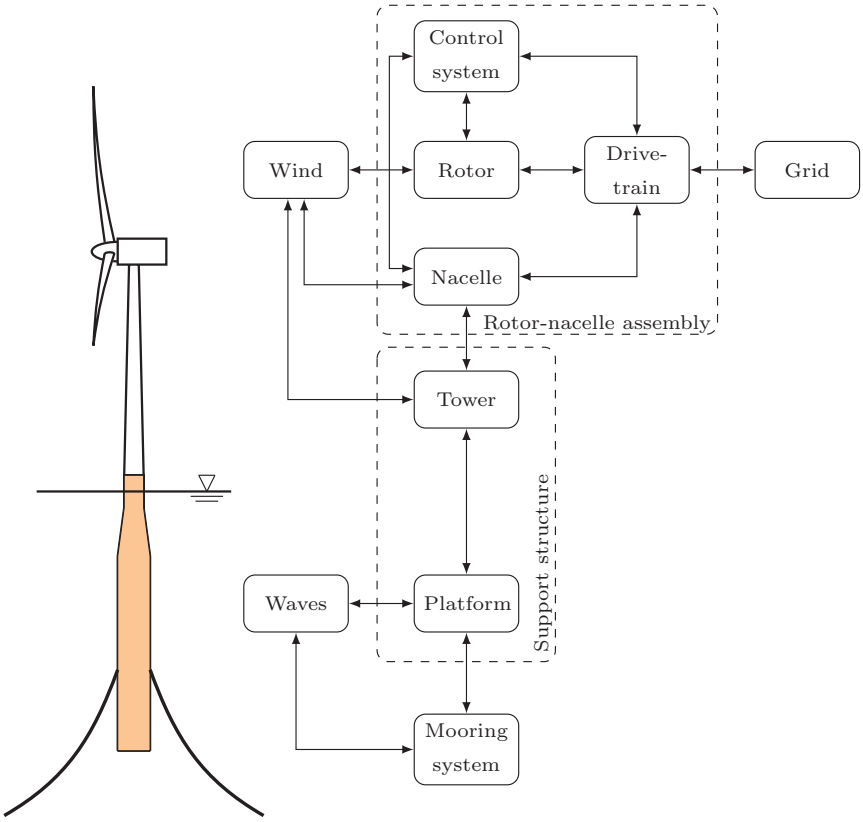

Figure 2.2: Aspects of global aero-hydro-servo-elastic analyses for floating wind turbines. Based on a figure presented by Vorpahl et al. (2013).

developed at the Politecnico di Milano (Bayati et al. 2017; 2018).

2.1.3 Linear models

Although FWTs are nonlinear systems, linearized formulations are desirable for several reasons. In addition to the computational efficiency, methods based on linear models are extensively used for analysis of eigenvalues, stability, and control systems, and may provide increased insight in the properties of the underlying system. Because linearity often is an accurate assumption for small displacements, even for nonlinear structures, such models are regarded as suitable for fatigue. Assuming harmonic response, the linear model can be solved very efficiently in the frequency domain. This is also preferable for gradient-based optimization, since the stochastic nature of time-domain results, which depend on the random realization of the environment, complicates the computation of accurate gradients (Zahle

et al. 2015).

Frequency-domain models have a long history for offshore structures, which is reflected in the early efforts on frequency-domain modelling of FWTs (Wayman et al. 2006, Tracy 2007, Sclavounos et al. 2008, Philippe et al. 2011), where response amplitude operators (RAOs) were established based on diffraction and radiation loads from an external potential flow solver. As hydrodynamic loads from numerical panel codes are computed in the frequency domain, they can be readily applied in such global response models without modification. A drawback with this approach in a design process is that it requires an additional hydrodynamic analysis each time changes are made to the design, which must be run prior to the response analysis, and prevents quick examination of different design solutions. More computationally efficient options include Morison's equation and MacCamy–Fuchs theory; however, the validity of these methods is limited to simple geometries.

While early studies on frequency-domain methods for FWTs considered only rigid-body modes, Bachynski and Moan (2012) compared a frequency-domain model for a tension-leg platform (TLP) wind turbine with nonlinear time domain simulations, and found that the linear model was insufficient for design calculations, partly due to the rigid modelling of the tower. The effect of tower flexibility on the global response was confirmed by full-scale measurements from the Hywind Demo FWT, where the tower bending moment spectra clearly showed peaks around the first bending mode (Skaare et al. 2015). Kvittem and Moan (2014) used a frequency-domain model, which included the first tower bending mode, to evaluate the fatigue loads for a semi-submersible FWT in stochastic wind-wave conditions, where the shape of the bending mode was found from decay tests in calm air with a coupled time-domain model. A stochastic linearization procedure, considering the two first tower modes, was presented by Kluger et al. (2016), who computed the modes from the eigenvalue problem with an isolated tower. Although more recent efforts on frequency-domain modelling have included tower modes, platform flexibility has been little explored. As turbines grow larger, support structure flexibility is expected to become more important, and may need to also include the platform to properly capture the correct global behaviour.

Due to the relatively complex aerodynamic calculations, and because the design of the rotor usually is separated from the support structure design, frequency-domain methods have typically focused on decoupling of the rotor dynamics. Early work on FWTs considered only stochastic response due to

waves, while the aerodynamic excitation forces typically were treated as a constant thrust force on the tower top. However, to properly capture the combined wind-wave response, turbulent wind excitation loads are needed, which can be estimated in several ways (Muskulus 2015). A method based on turbulent wind simulations in the time domain, with a fixed rotor and an active controller, was presented by Bachynski (2014), who compared results from linear and nonlinear analyses on a TLP wind turbine. The approach gave reasonably accurate estimates for the low-frequency wind response in certain environmental conditions, but the agreement was highly dependent on the damping in the model.

Calculation of frequency-dependent aerodynamic loads based on time series has some drawbacks. Firstly, the turbulent wind loads are stochastic, meaning that a large number of time-domain simulations may be needed. Secondly, the low-frequency response is sensitive to how the thrust force spectrum is estimated from the time series (Kvittem and Moan 2014). In addition, using pre-calculated aerodynamic loads means that the controller cannot be modified without re-running the time domain simulations. Another approach, which allowed for simultaneous design of the controller, was taken by Sandner et al. (2014), who computed linearized aerodynamic loads on the tower top as a function of wind speed, rotor speed, and blade pitch angle. The formulations were based on a Taylor expansion, using pre-computed look-up tables for the thrust and power coefficients, and a rotor effective wind speed. More sophisticated linear models, involving blade elasticity, unsteady aerodynamics, and hundreds of degrees-of-freedom (DOFs), have previously been developed for wind turbine analysis (Merz 2015, Tibaldi et al. 2016), and more recently, full-system linearization of FWT models based on the OpenFAST software has been presented by Jonkman et al. (2018). The implementation has later been verified against nonlinear simulations from OpenFAST by Johnson et al. (2019).

For support structure models with decoupled rotor dynamics, the change in aerodynamic forces due to the motions of the turbine should also be included. The most important component is the aerodynamic damping, which typically has been represented using a linear dashpot at the tower top, and a number of methods has been applied to calculate an appropriate damping coefficient. Early studies on frequency-domain methods for offshore wind turbines used a value of 4 % of critical based on engineering estimate (van der Tempel 2006). Bachynski (2014) derived a mean wind speed-dependent value from the change in thrust for a small change in wind speed, assuming that the rotor speed and blade pitch angle were

kept unchanged. However, due to interaction with the controller and rotor dynamics, the damping is frequency-dependent, and neglecting these interaction effects leads to non-conservative damping estimates (Jonkman 2008). As damping is most important for the response around resonance, individual values for each mode can be found from decay tests with steady wind and an active controller (Jurado et al. 2018). Model tests have shown that there also is a frequency-dependent inertia (or stiffness) effect from the controller, which results in changes in the pitch natural frequency for the system (Bachynski et al. 2016, Goupee et al. 2017). Souza and Bachynski (2019) computed frequency-dependent inertia and damping coefficients for the NREL 5MW turbine numerically, based on forced harmonic oscillations of the nacelle, and were able to accurately predict pitch decay periods for three different FWTs, using a simplified 2-DOF model with modified inertia and damping matrices.

As linearized models assume small displacements, they are seen as unsuitable for extreme response. However, results from previous studies have shown that both the tower base bending moment (Karimirad and Moan 2011) and global motions (Aggarwal et al. 2017) for spar FWTs can be quite Gaussian in harsh environmental conditions, which suggests that a linear model also may be used to assess the extreme response in early stages of design, or reduce the computational burden by quickly identifying critical load cases. The degree of nonlinearity depends on the considered response parameter, and also varies with location, floater geometry, environmental conditions, and design situations. Therefore, the results obtained with a linear model cannot be generalized to any FWT structure, and such models must be continuously verified against more sophisticated tools during a design process.

2.1.4 Structural reliability

In the design of FWTs, stochastic variables such as turbulence intensity, wind-wave directionality, and fatigue strength are typically replaced by design values, which are obtained from their characteristic values combined with a given safety factor. In order to reduce conservatism and thus the design costs caused by these safety factors, probabilistic analyses can be performed to assess the safety level of the structure through the probability of failure. Such analyses can also be used to evaluate the importance of different model uncertainties on the resulting structural reliability, and possibly calibrate appropriate safety factors, which has been the focus of several studies for bottom-fixed wind turbines. Márquez-Domínguez and Sørensen (2012) calibrated design fatigue factors (DFFs) for a 2.3 MW off-

shore wind turbine, and investigated the effect of inspections on the required DFF values. Horn et al. (2019) quantified the effect of environmental load uncertainties on the fatigue reliability of a 10 MW monopile, and derived corresponding differences in DFFs resulting from the increased model fidelity. Velarde et al. (2020) designed a 10 MW monopile with different DFFs by varying the wall thickness, and used reliability analyses to identify the necessary safety factor to achieve the target probability of failure during a service life of 25 years without inspections.

Structural reliability problems consider the probability of failure for the system, which can be expressed as

$$P_F = P\left[g(\mathbf{x}) \leq 0\right] = \int\limits_{g(\mathbf{x})\leq 0} f_{\mathbf{X}}(\mathbf{x})\,\mathrm{d}\mathbf{x}, \tag{2.2}$$

where $\mathbf{X} \in \mathbb{R}^n$ is a random vector with joint probability density function (PDF) $f_{\mathbf{X}}(\mathbf{x})$, which represents the uncertainties in the system. $g(\mathbf{x})$ is commonly known as the limit state function, where $g(\mathbf{x}) \leq 0$ denotes the failure domain.

The evaluation of this integral must typically be done numerically, commonly through Monte Carlo simulations or the first- or second-order reliability methods (FORM, SORM) (Madsen et al. 1986). In the widely used and computationally efficient FORM, $\mathbf{X}$ is transformed into a vector of independent standard normal variables ($\mathbf{U}$), and the limit state function is linearized about the most probable point, which is the point on $g(\mathbf{u}) = 0$ closest to the origin. The reliability index, β, which is the distance from the origin to the most probable point, can be used to calculate the failure probability through the following relation:

$$P_F = \Phi(-\beta), \tag{2.3}$$

where Φ is the standard normal cumulative distribution function (CDF).

2.2 Design optimization

2.2.1 Basic optimization theory

An optimization problem can be formally written as (Nocedal and Wright 2006):

$$\begin{aligned} \text{minimize} \quad & f(x) \\ \text{with respect to} \quad & x \in \mathbb{R}^n \\ \text{subject to} \quad & \hat{c}_j(x) = 0, \quad j = 1, 2, ..., \hat{m} \\ & c_k(x) \geq 0, \quad k = 1, 2, ..., m \end{aligned} \tag{2.4}$$

where f is the *objective function*, x is a vector of *design variables*, $\hat{c}$ is a vector of *equality constraints*, and c is a vector of *inequality constraints*.

In general, two approaches can be used to solve the optimization problem, namely *gradient-free* and *gradient-based* methods (Martins and Ning 2020). Gradient-free methods are relatively easy to combine with existing analysis tools, and do not require differentiability of the simulation outputs. However, as illustrated in Fig. 2.3, these methods scale poorly with the number of design variables, and become infeasible for large-scale optimization problems. The scaling properties are particularly important when expensive analyses are needed to evaluate the objective function or constraints.

Gradient-based methods require derivatives to determine the search direction, which can be acquired in different ways. Numerical gradients are commonly found using either finite-differences or the complex-step method. While finite difference formulas are easier to implement and do not require access to the source code, the complex step approximation is more accurate, as it is not susceptible to subtractive errors (Martins and Ning 2020). Both methods, however, scale linearly with the number of design variables, and thus become prohibitively costly as the problem size increases.

The most preferable way of obtaining gradients is to compute the derivatives analytically. This method requires significant implementation effort, as modification of the specific components of the source code is needed, but offers large improvements in efficiency. Analytic gradients can be computed using either the direct method or the adjoint method, where the preferred approach depends on the problem. The adjoint method, whose cost is independent of the number of design variables, tends to be the most commonly used approach in practice (Gray et al. 2019). This method is further described in Section 3.8.

A function can be either unimodal, meaning that it only has a single minimum, or multimodal, which implies that several minima exist. Unless an optimization problem is known to be convex, it is usually difficult to prove that a global minimum has been found (Nocedal and Wright 2006). However, to prove multimodality, it is sufficient to find two separate local minima. Therefore, Martins (2020) argues that 'an optimum should be assumed to be the global one until proven otherwise'. This requires that an effort to search for additional minima has been made by performing the optimization with a number of different initial designs.

For certain problems, it may be desirable to minimize several performance

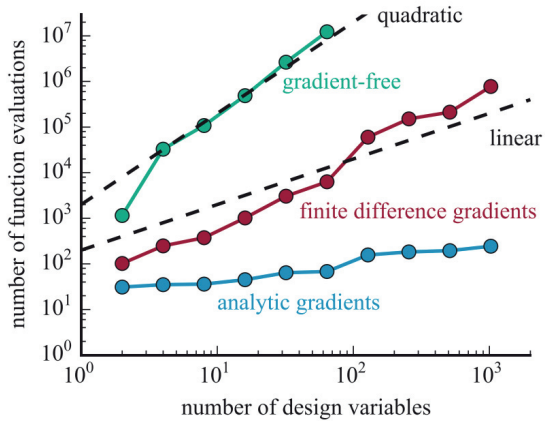

Figure 2.3: Comparison of required function evaluations until convergence to the optimum using a gradient-free algorithm, finite differences, and analytic derivatives for a multidimensional generalization of the Rosenbrock function (Ning and Petch 2016).

measures. This is known as a multi-objective problem, and may be useful to quantify trade-offs between different parameters, or to produce a number of possible designs when a final decision must be made during a later design stage (Martins and Ning 2020). For these problems, there will no longer be a single optimal solution, but an infinite number of solutions which forms a surface in the objective function space. Multi-objective optimization therefore uses the term *Pareto optimality*, where a design is considered Pareto optimal if it is impossible to improve the performance in one objective, without worsening the performance in another (Boyd and Vandenberghe 2004).

2.2.2 Offshore wind substructures

Most of the work on numerical design optimization of offshore wind substructures has considered bottom-fixed turbines. The focus has mainly been on jacket structures, because of the complex geometry and large number of potential design variables, which complicates a manual design process, and increases the potential for cost savings by automation. Hydrodynamic shape optimization of floating structures has a long history in the offshore community, using RAOs to identify designs with favourable response to wave loads. An early study on numerical hydrodynamic shape optimization was performed by Clauss and Birk (1996), where various offshore structures were designed to minimize forces or motions, based on a panel

code and a gradient-free optimizer, and in recent years, similar techniques have also been applied on FWT structures (Hall et al. 2013, Steinert et al. 2016, Karimi et al. 2017). Most of the work has considered linear frequency-domain models to limit the computational effort, with an exception of Myhr and Nygaard (2012), who optimized a floating substructure for two extreme load cases using nonlinear time-domain simulations. Due to the computational effort, such optimization studies have rarely included more than two or three design load cases, and the resulting optimized designs may therefore be highly dependent on the chosen environmental conditions. In addition, the applied numerical models may also impact the results. Hall et al. (2013) performed single- and multi-objective hull shape and mooring line optimization for different platform concepts spanning all stability classes, and found that the Pareto front was dominated by relatively complex platforms with several legs and taut mooring lines. The work was later extended by Karimi et al. (2017), using an updated dynamic FWT model and a new optimization algorithm, which significantly affected the derived optimal solutions.

One of the challenges related to design optimization of substructures for floating wind is the parametrization of the geometry. Several platform concepts, with significantly different properties, have been suggested, and there is currently no consensus on the optimal platform type. An illustration of three main classes of FWTs is shown in Fig. 2.4. The derivation of a general formulation that accurately can describe all platform types, including different stability classes, various mooring system configurations, and both single- and multi-hull platforms, possibly connected by braces or pontoons, is a highly involved and difficult task. Consequently, the main properties of the system, including the general shape of the platform, are typically chosen before the optimization problem is formulated, which limits the design space and reduces the chance of obtaining truly novel design solutions. Hall et al. (2014a) tried to overcome this issue by introducing a basis function approach, where the platform design was expressed as a combination of basic geometries with pre-calculated hydrodynamic coefficients. The design space had numerous local minima, and the resulting optimized design was thus highly dependent on the initial starting point. Also, some issues arose when physical geometries was created based on optimal combinations of basis designs, as the resulting hydrodynamic behaviour tended to differ from the superimposed case, due to nonlinearities and interaction effects. While such generalizations can remove the potential bias towards certain concepts and allow for a more direct comparison between different solutions, it remains uncertain whether they are able to fully represent the relevant physics for

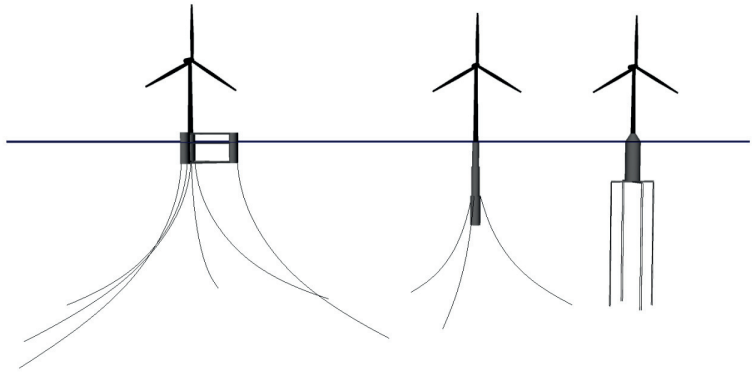

Figure 2.4: Semi-submersible, catenary moored spar, and tension-leg platform wind turbine concepts (Bachynski 2014).

all platform types, or if more concept-specific formulations are needed.

Several studies have considered shape optimization of FWT platforms, but little exists in the literature concerning structural optimization. The hydrodynamic loads on the hull are typically found from a separate hydrodynamic analysis and given as resultant point loads, and complicates a structural optimization procedure based on global response analyses, which requires distributed hydrodynamic loads combined with a formulation for the scantling design criteria. While comprehensive finite element models may be necessary for the detailed structural design of the hull, design criteria based on global forces and moments, such as the formulas provided by DNV GL (2019b), may be used for structural sizing in early phases of design.

2.2.3 Integrated design

Common to previous studies on FWT design optimization is that they consider the design of the platform, mooring system, or both, whereas the tower, rotor, and control system are considered fixed during the optimization. A possible reason is that design of wind turbines and offshore structures, which traditionally have been two completely separated fields, is performed by designers with specific engineering backgrounds. In addition, different companies are responsible for the design of different components. This may lead to partly integrated procedures where loads are exchanged between the support structure designer and the wind turbine manufacturer at a pre-defined interface (Vorpahl et al. 2013). A fully integrated design approach, on the other hand, may be practically impossible in reality, due

to confidentiality issues between the companies. However, because FWTs are multidisciplinary systems, with important interactions between the different subsystems and disciplines, optimizing components separately will in general lead to suboptimal, and in many cases infeasible, solutions on the overall system level (Muskulus and Schafhirt 2014). To find the true optimum, an integrated optimization approach should be applied, where all relevant components are considered simultaneously.

Despite gradient-based optimization being desirable due to its efficiency, a large majority of the work on FWT design optimization has been performed using gradient-free methods. Typical analysis tools for FWTs have not been developed for optimization purposes, which require differentiability, and in the case of analytic gradients, substantial modifications to the source code. One exception is Fylling and Berthelsen (2011), who optimized the hull shape, mooring lines and power cable for a spar FWT using a gradient-based approach with numerical gradients obtained from finite differences. While these methods may be feasible for optimization of smaller parts of the FWT system with a limited amount of design variables and load cases, integrated design optimization considering lifetime loads would result in a large number of input variables and expensive function evaluations, which requires analytic derivatives.

As there are important interactions between the control dynamics and the support structure response, the control system should preferably be integrated in the design optimization procedure. Numerical optimization of a land-based wind turbine controller has earlier been performed by Tibaldi et al. (2014), but has rarely been considered simultaneously to support structure optimization, which typically decouple the rotor dynamics. Sandner et al. (2014) manually derived optimal blade-pitch controller gains for three different spar FWT designs, where the goal was to minimize a weighted combination of rotor speed variation and tower bending. The gains that minimized the cost function was shown to be highly dependent on the platform design. A more automated approach was presented by Lemmer et al. (2017), who optimized four parameters for a FWT substructure to minimize a combination of material cost and damage-equivalent loads, where the blade-pitch controller was tuned in each design iteration using a linear quadratic regulator (LQR). However, the effect of including control system tuning in the substructure optimization loop was not quantified.

Perhaps the most important interaction between the controller and support structure response is the potential introduction of negative damping for the platform motions above rated wind speed (Larsen and Hanson 2007). Sev-

eral methods have been suggested to resolve the issue, such as detuning the controller gains (Larsen and Hanson 2007, Jonkman 2008), or to introduce a feedback term proportional to the pitch velocity (Lackner 2009) or nacelle velocity (van der Veen et al. 2012, Fleming et al. 2014) to manipulate the rotor speed reference. For the latter approach, Fleming et al. (2019) suggested that such controllers should not include the wave-frequency range within their bandwidth, as doing so yielded an increase in the loads around these frequencies. All methods lead to trade-offs between structural loads, rotor speed tracking, and blade-pitch actuator use, and an integrated control and structural design optimization approach is therefore needed to properly evaluate and compare different solutions.

The shapes and natural frequencies of the tower modes, and thus the tower response, are dependent on the platform design. In addition, as turbines grow larger, the flexibility of the platform may become important, which also can affect the response of the tower. In Fig. 2.5, the first bending mode for a 10 MW spar is shown for both a rigid and flexible platform. In addition to the modal shape being clearly affected by the platform flexibility, a 17 % decrease in the natural frequency is observed. A similar effect was seen for the OO-Star 10 MW semi-submersible, where the natural frequency of the first tower mode was reduced by 25 % when the flexibility of the floater was included (Müller et al. 2018). As the first bending mode of FWT towers typically is located close to the 3P range, an accurate estimation of the natural frequency is important to capture the correct modal excitation forces. Souza and Bachynski (2020) studied the effect of flexible pontoons for a 5 MW TLP wind turbine, and found that the flexible platform resulted in a 12.7 % reduction in the weighted 1-h fatigue damage at the tower base, due to the reduced natural frequency of the tower mode, which resulted in less 3P excitation.

Commonly, wind turbine towers are designed with linearly tapered diameter and wall thickness (Jonkman et al. 2009, Bak et al. 2013, Müller et al. 2018), and are thus fully described by the values at the base and top. However, the load picture for a FWT tower alters significantly from a land-based or bottom-fixed offshore tower, with inertial and gravitational loads arising from large platform motions, as well as possible restrictions at the tower base due to compliance with the platform. An integrated design process which considers the actual loads on the FWT system, and consistent reliability levels, may therefore result in cost reductions.

Some effort has been made to perform integrated design optimization of the blades and tower for onshore (Ning and Petch 2016) and bottom-fixed off-

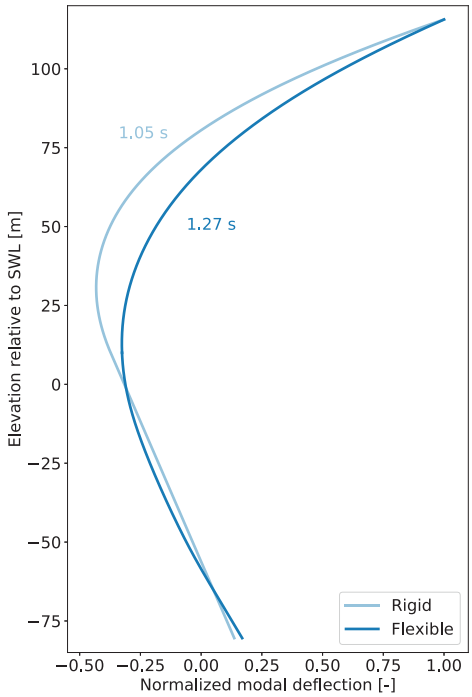

Figure 2.5: First support structure bending mode for a 10 MW spar with flexible and rigid platform, and associated natural periods.

shore (Ashuri et al. 2014) wind turbines, which experience interaction effects due to coupled eigenmodes, increased blade loads from tower shadow effects, and the possibility of tower strike by the blade tips. It is expected that the inclusion of blade design in an integrated optimization process will affect the results also for FWTs. However, design optimization of wind turbine blades is a separate body of literature, which requires high-fidelity aerodynamic and structural formulations to properly capture the blade response, and is therefore considered outside the scope of this thesis.

2.2.4 Formulation of objective and constraints

The success of a numerical optimization process depends heavily on the formulation of objective function and constraints for the design problem. Because the goodness of a design is measured purely through the value of a scalar objective function, it is essential that the applied function reflects a relevant performance measure. The constraints should ideally cover all important limit states, in addition to any restrictions that may be necessary to avoid non-physical or impractical solutions. However, the goal of an optimization process is not necessarily to provide a ready-to-build design, but may also be used to study the sensitivity of different input parameters, or identify design trends that are non-intuitive for a human designer.

A common objective function in design optimization of offshore wind substructures is the structural weight (Pasamontes et al. 2014, Chew et al. 2016, Oest et al. 2017), which is assumed to be closely related to the cost of the design. The weight is a convenient cost parameter in an engineering optimization problem, because it is easily calculated with small uncertainty. However, the weight, or associated material costs, may not be a good measure of the actual cost optimality, and even in the case where only capital costs are considered, manufacturing costs due to e.g. welding of joints should be included (Muskulus and Schafhirt 2014). The manufacturing costs are more uncertain, and are typically expressed as empirically fitted functions of the structural dimensions. Cost models for manufacturing of general steel structures are presented e.g. by Farkas and Jármai (2013); however, their accuracy with respect to FWT structures have not been verified.

Operational costs are rarely considered in design optimization of offshore wind turbines. For conventional offshore structures, the focus has been on inspection planning, where a cost optimal schedule for crack inspection and repair is sought. Madsen et al. (1989) presented an early formulation of an optimization problem which minimized expected costs related to construction, inspection, repair, and failure, where a set of structural design para-

meters, as well as inspection times and qualities, were included as design variables, and a constraint was placed on the reliability index. A small example was solved using gradient-based optimization for the outer problem, combined with FORM for the inner reliability problem. Such approaches may lead to more cost-effective solutions in a lifetime perspective, but increase the complexity of the design problem considerably. In addition, little information exists in the literature regarding costs related to inspection and repair of offshore structural elements, which vary with the inspection technique, location of potential cracks, and extent of the repairs.

An important difference in design optimization of FWTs, compared to conventional offshore structures, is that it is not the cost of the system which should be minimized, but rather the cost of energy. The energy production should therefore be taken into account in the optimization process. Studies, e.g. by Roddier et al. (2017), have suggested that the movement of the platform has a small effect on the total energy production, which is mostly related to the wind farm site. However, the energy quality, which is a measure of how much the energy output fluctuates, is also a relevant parameter. High-quality power, which has low variability in the output, is desirable, and its value is closely related to the rotor speed tracking performance of the system. The power quality may be regarded as an SLS criterion, and thus be constrained based on system specifications, or treated as a performance measure that should be maximized. Because the monetary cost of reduced power quality is difficult to quantify, multi-objective optimization may be needed to take this parameter into account. Ideally, an optimization process should also consider the power quality for the complete wind farm, which may result in different solutions compared to a single turbine.

A commonly constrained response parameter in FWT design optimization is the platform tilt angle, which should be limited due to stability requirements and SLS criteria for the rotor and nacelle assembly (RNA). Such criteria are project-specific, and there is currently no consensus on how the tilt angle should be constrained; both the static and dynamic angle have been considered in the literature, and different values have been applied. The dynamic tilt angle constraint has commonly been expressed using the standard deviation, which is easily obtained from the response spectrum for a frequency-domain analysis. Typical values for the total angle have been 10° (Hall et al. 2013, Karimi et al. 2017, Leimeister et al. 2020) or 15° (Steinert et al. 2016), with possibly different values in operational and survival conditions (Ramachandran et al. 2017).

The constraint on the maximum static tilt angle is mostly related to the

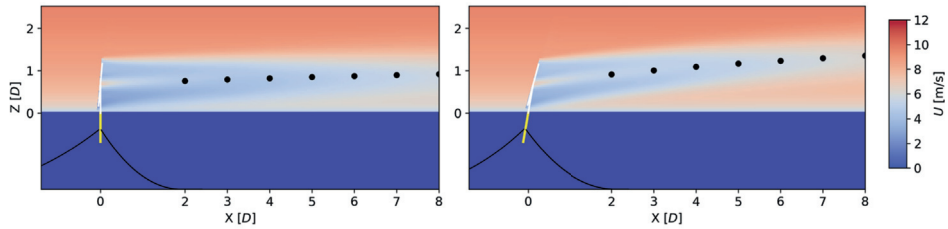

Figure 2.6: Side view of the wind speed for a spar FWT without tilt (left) and with a tilt angle of 10° (right). The black dots represent the vertical wake center position (Wise and Bachynski 2020).

reduction in projected rotor area and consequently the resulting power production. The use of a static tilt angle has computational benefits, because it can be computed without the need of simulations, using the platform restoring stiffness and the specified rated thrust for the turbine. Common constraint values in the literature are 5° (Matha et al. 2015, Steinert et al. 2016) or 10° (Wayman et al. 2006, Tracy 2007, Hall et al. 2013, Karimi et al. 2017), which, given that the produced energy is proportional to the cosine of the tilt angle to the power three (Matha et al. 2015), result in energy losses of about 1 % and 4.5 %, respectively. Increased stability is likely to translate into larger design costs, and the static tilt angle varies with the mean wind speed. Additionally, Wise and Bachynski (2020) showed that larger tilt reduced the wake loss for a downstream turbine due to vertical wake deflection, as illustrated in Fig. 2.6. Concept-specific assessments of the trade-off with energy loss, also considering farm level effects, are therefore needed to find cost-optimal values for this constraint.

An important consideration in design is to maintain the structural integrity of the power cable, which is designed for relatively small curvatures. The maximum offset of the platform is often constrained in lieu of an explicit dynamic model and design criterion for the power cable. As the relation between offset and power cable loads is somewhat dependent on the design of the specific system, no general offset criterion exists in design guidelines, but limitations are typically expressed as a fraction of the water depth. The maximum offset is also of interest in relation to the tendon connectors for TLP wind turbines, where a maximum offset limitation of 10 % of the water depth has been common industry practice for conventional TLPs (Bachynski 2014).

The offset is to a large degree a function of the mooring system design, which in addition must possess sufficient breaking strength to withstand the design

tension in the ULS and ALS (DNV GL 2018a). A minimum tension should also be maintained at all times, as slack line events may result in high snap loads when the line regains its tension. For drag anchors, which are not designed to take vertical loads, a constraint may also be needed to prevent uplift at the anchors for extreme offsets (Brommundt et al. 2012).

Mooring lines should be designed against fatigue failure; however, as the design life of a mooring line often is shorter than that of the platform and wind turbine, replacement of mooring lines during the design life of the platform is an implicit design assumption (DNV GL 2018a). Consequently, fatigue is not considered a key criterion in mooring system optimization (Benassai et al. 2014). The effect of including a fatigue life constraint for the mooring lines was demonstrated by Fylling and Berthelsen (2011), who found that it resulted in a 20 % more expensive mooring system and about 5 % increase in spar buoy costs for the optimized system.

A challenge related to constraint formulations for FWTs is to derive expressions based on actual design criteria for fatigue and ultimate loads. Often, constraints are expressed in terms of response parameters which can indicate the level of response, but are only applicable for relative comparison of solutions. However, to achieve cost-effective structures with a consistent reliability level, the constraints should reflect the actual limit state criteria. This requires a large number of simulations, and often, no closed-form solution is available for the design loads. Steinert et al. (2016) attempted to properly express ULS constraints, where the 50-year extreme response in a single parked condition was considered. The constraints were based on the assumption of Gaussian response, which simplifies the estimation of the extreme value distribution considerably. Fatigue damage in the tower and possibly the platform is of concern, but has rarely been assessed directly in design optimization studies, where proxy variables such as tower top displacement due to bending (Sandner et al. 2014, Lemmer et al. 2017) or nacelle acceleration (Hall et al. 2013, Karimi et al. 2017) have been used to assess the support structure loads. Although the large number of required load cases makes optimization for fatigue challenging, it is typically the design-driving limit state for large parts of the support structure, and accurate and consistent fatigue design will thus lead to more effective use of material.

Another reason for constraining the nacelle acceleration has been the assumption of strong correlation with loads on the drivetrain; however, Nejad et al. (2019) showed that the accelerations at the tower top were not a good indicator for either maximum or fatigue loads on the main bearings of the

gearbox. As the drivetrain is associated with relatively frequent failures (Nejad et al. 2014), and has been shown to be sensitive to control strategies (Lee et al. 2020) and platform concept (Nejad et al. 2015), it is desirable to have a measure of the drivetrain response in the design optimization process. Global analyses are not appropriate for detailed drivetrain analysis, which typically is performed using de-coupled multibody simulations, but simplified formulations based on global response parameters can be used for qualitative analysis of the gear, shaft, and pitch actuator response with different control system designs (Smilden et al. 2018). Although these methods may be inappropriate to assess the actual fatigue damage in the components, they are applicable for relative comparison between different solutions.

In addition to general requirements, concept-specific constraints may also be needed. For instance, spar platforms are susceptible to Mathieu instability (Haslum and Faltinsen 1999), and TLPs may show ringing responses (Bachynski and Moan 2014). The critical load cases also depend on the system components that are considered. While the largest values for the tower base bending moment, mooring line tension, and global motions of FWTs may occur in operational conditions, the drivetrain and blades are more affected by fault conditions (Bachynski et al. 2013). Insight about the behaviour of the considered system, as well as the specific components that are to be designed, is therefore needed to ensure that feasible solutions are achieved.

Chapter 3

Numerical Models

The results presented in Chapter 4 and the appended papers are based on a linearized numerical model for global response analyses of floating wind turbines, which was developed over the course of the thesis. The main features of the model are summarized in the following. A brief description of the evolution of the model, and the associated publications, is also given.

3.1 Linearized formulation

The coupled dynamics of FWTs are typically analysed using nonlinear time-domain analyses, which capture the complex interactions between aerodynamics, hydrodynamics, structural dynamics and control. For a design procedure which requires several iterations, each involving a large number of load cases, the process becomes computationally prohibitive, and simplified models are therefore desirable.

Using Newton's second law, the nonlinear equations of motion for the displacement vector $\mathbf{q}$ is expressed as

$$\mathbf{M}\ddot{\mathbf{q}} = \tilde{\mathbf{f}}(\dot{\mathbf{q}}, \mathbf{q}, \mathbf{u}), \tag{3.1}$$

where $\mathbf{M}$ is the mass matrix, and $\tilde{\mathbf{f}}$ contains position- and velocity-dependent terms, in addition to forces due to external inputs ($\mathbf{u}$). By defining a state vector, $\mathbf{x} = \begin{bmatrix}\mathbf{q}^\top & \dot{\mathbf{q}}^\top\end{bmatrix}^\top$, Eq. (3.1) can be written as a set of first order differential equations (Balchen et al. 2003):

$$\dot{\mathbf{x}} = \mathbf{f}(\mathbf{x}, \mathbf{u}). \tag{3.2}$$

Considering small perturbations, Δ, about an operational point defined by

$(\mathbf{x_0}, \mathbf{u_0})$, the state and input vectors are written

$$\mathbf{x} = \mathbf{x_0} + \Delta\mathbf{x}, \quad \mathbf{u} = \mathbf{u_0} + \Delta\mathbf{u}, \tag{3.3}$$

while the system in Eq. (3.2) can be linearized by a Taylor series expansion:

$$\dot{\mathbf{x}} \approx \mathbf{f}(\mathbf{x_0}, \mathbf{u_0}) + \frac{\partial \mathbf{f}}{\partial \mathbf{x}}\Delta\mathbf{x} + \frac{\partial \mathbf{f}}{\partial \mathbf{u}}\Delta\mathbf{u}. \tag{3.4}$$

If the operational point is chosen such that $\dot{\mathbf{x}}_\mathbf{0} = \mathbf{f}(\mathbf{x_0}, \mathbf{u_0}) = 0$, the linearized dynamic system for the differential state and input variables can be written in state-space form as (Chen 2013):

$$\Delta\dot{\mathbf{x}} = \mathbf{A}\Delta\mathbf{x} + \mathbf{E}\Delta\mathbf{u}, \tag{3.5}$$

where $\mathbf{A}$ is the state matrix, and $\mathbf{E}$ is the input matrix. Given a set of system outputs, $\mathbf{y}$, which are described by $\mathbf{y} = \mathbf{g}(\mathbf{x}, \mathbf{u})$, a similar linearization can be applied:

$$\Delta\mathbf{y} = \mathbf{C}\Delta\mathbf{x} + \mathbf{D}\Delta\mathbf{u}. \tag{3.6}$$

Here, $\mathbf{C}$ and $\mathbf{D}$ are commonly known as the output matrix and feedthrough matrix, respectively. If the system is time-invariant, the matrices in Eq. (3.5) and Eq. (3.6) are constant (Balchen et al. 2003).

3.2 System overview

An overview of the considered FWT system is shown in Fig. 3.1. The model is valid for single-hull spar platforms with circular cross sections, supporting an arbitrary three-bladed horizontal-axis wind turbine, where the hull is partially filled with solid ballast from the bottom to achieve stability. A catenary mooring system consisting of three lines spread symmetrically about the vertical axis is used for station-keeping, where the so-called crowfeet are neglected, and the lines are assumed to have constant cross-sectional properties and no discrete line components such as buoys or clump weights. Only 2D response is detailed in the following; however, out-of-plane motions have also been included in the present work using the same methodology.

The support structure is modelled as a slender flexible beam with varying cross sectional properties. The model is regarded unsuitable for local blade response, and rotor design is considered outside the scope of the current work. The dynamic response of the blades is assumed to have a small effect on the support structure response, and are therefore considered rigid. Consequently, the RNA is replaced by a point mass and inertia, with resultant aerodynamic loads acting on the tower top. The considered resultant

loads are the thrust force (F_T), the tilting moment (M_T), and the aerodynamic torque (Q_A). In addition, distributed wave excitation forces ($\mathrm{d}F_W$) are applied on the hull.

For each wind-wave condition, the linearization point is found from equilibrium when the system is subjected to the mean environmental loads. As the model neglects current and mean wave loads, the wind forces on the rotor and tower are the only load components with non-zero mean. The operational point for a given system design is thus solely a function of the mean wind speed, which determines the references for the rotor speed, collective blade pitch angle, and generator torque, as well as the equilibrium position of the support structure and mooring system.

The model presented here considers three support structure degrees-of-freedom (DOFs), namely surge, pitch, and the first bending mode. For deep-draught spar platforms, the first order wave excitation in heave is small. As a consequence, the heave response is not considered to have a large effect on the structural loads on the system, and is thus not included in the model. However, the natural period can be estimated, and subsequently used in the design process to avoid heave resonance in the wave-frequency range. Another issue relevant for spar platforms is the phenomenon known as Mathieu instability, which can occur when the pitch restoring moment varies harmonically due to large heave motions (Koo et al. 2004). Haslum and Faltinsen (1999) reported that unstable solutions occur for certain ratios between the frequency of the heave motion and the pitch natural frequency, and can thus be prevented assuming that the heave response is dominated by resonant motions.

In addition to the support structure DOFs described above, a rotor speed DOF is included. The inputs to the structural system consist of both control system outputs and disturbances due to wind and wave loads. The control outputs, i.e. the generator torque and the collective blade pitch angle, are described by a separate control system model, which can be combined with the structural model to create a single closed-loop system.

The model considers coupled response of four disciplines: structural dynamics, hydrodynamics, aerodynamics, and control dynamics. The applied formulations for each of the disciplines are detailed in the following subsections.

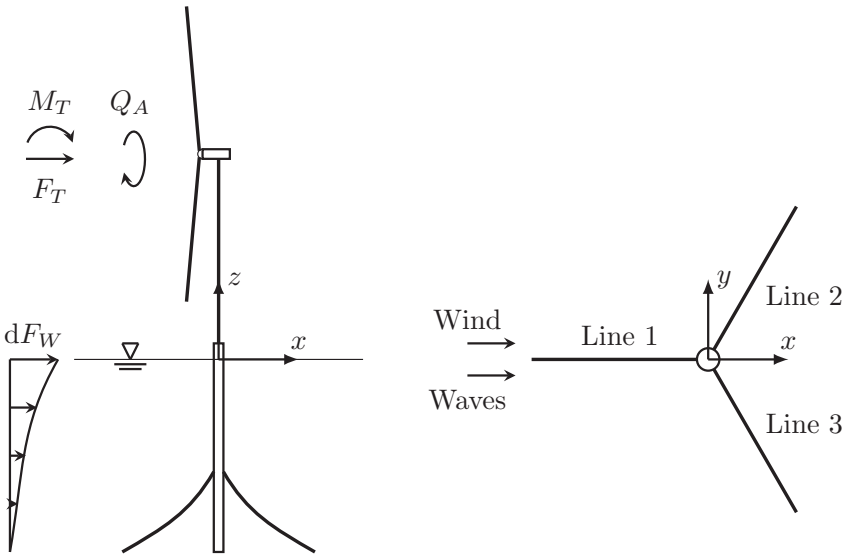

Figure 3.1: Overview of modelled FWT system.

3.3 Structural dynamics

The linear dynamic response of the support structure is found using generalized coordinates. The total displacements are written as a weighted sum of a set of pre-defined spatial shape functions, ψ, and the accuracy of the formulation thus depends on how well the actual displacement field is captured by the shape functions. If the eigenmodes of the system are chosen as shape functions, the method corresponds to *modal superposition*. An illustration of the applied shape functions for the present support structure modes is shown in Fig. 3.2.

The total displacement of the support structure at time t is found by multiplying the shape functions by time-dependent weight functions, χ, i.e., (Naess and Moan 2013)

$$w(z,t) = \sum_{k=0}^{n} \psi_k(z)\chi_k(t) = \boldsymbol{\psi}(z)^\top \boldsymbol{\chi}(t). \tag{3.7}$$

The weight functions are assumed harmonic, i.e. $\chi(t) = \chi_0 \mathrm{e}^{i\omega t}$, and are found by solving the generalized equations of motion. Using the principle of virtual work, the generalized system matrices can be established as a combination of continuous and discrete terms. The support structure is modelled as a slender beam undergoing pure bending deformations, and

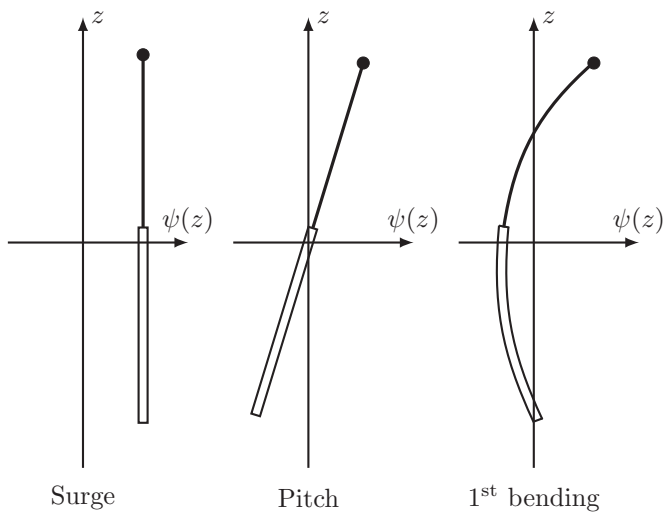

Figure 3.2: Generalized DOFs for the support structure response.

is assumed to follow Euler–Bernoulli beam theory. Including only terms relevant for the considered FWT support structure, the generalized mass, damping, and stiffness matrices can be expressed as

$$\begin{aligned}\mathbf{M}_\chi = &\int_{-d}^{l} m(z)\boldsymbol{\psi}(z)\boldsymbol{\psi}^\top(z)\mathrm{d}z + \sum_p M_p\boldsymbol{\psi}(z_p)\boldsymbol{\psi}^\top(z_p)\\ &+ \sum_p I_p\boldsymbol{\psi}_{,z}(z_p)\boldsymbol{\psi}_{,z}^\top(z_p),\end{aligned} \tag{3.8}$$

$$\mathbf{B}_\chi = \int_{-d}^{l} b(z)\boldsymbol{\psi}(z)\boldsymbol{\psi}^\top(z)\mathrm{d}z + \sum_p B_p\boldsymbol{\psi}(z_p)\boldsymbol{\psi}^\top(z_p), \tag{3.9}$$

and

$$\begin{aligned}\mathbf{K}_\chi = &\sum_p K_p\boldsymbol{\psi}(z_p)\boldsymbol{\psi}^\top(z_p) + \int_{-d}^{l} EI(z)\boldsymbol{\psi}_{,zz}(z)\boldsymbol{\psi}_{,zz}^\top(z)\mathrm{d}z\\ &+ \int_{-d}^{l} N(z)\boldsymbol{\psi}_{,z}(z)\boldsymbol{\psi}_{,z}^\top(z)\mathrm{d}z,\end{aligned} \tag{3.10}$$

respectively, where m and b are distributed masses and dampers, M_p, I_p, B_p, and K_p represent discrete masses, inertias, dampers, and springs, EI is the bending stiffness, N is the axial force, d is the platform draft, and l is the height of the tower top above the still water line (SWL). Here, the mass matrix includes both structural and hydrodynamic mass. In addition to

hydro- and aerodynamic damping, the damping matrix contains structural damping terms, which are described using stiffness-proportional Rayleigh damping.

The generalized force vector is written:

$$\mathbf{F}(t) = \int_{-d}^{l} \mathrm{d}F(z,t)\boldsymbol{\psi}(z)\mathrm{d}z + \sum_{p} F_p(t)\boldsymbol{\psi}(z_p) + \sum_{p} Q_p(t)\boldsymbol{\psi}_{,z}(z_p), \quad (3.11)$$

where $\mathrm{d}F$ are distributed forces, and F_p and Q_p are discrete forces and moments, respectively. The linear system of equations for the weight functions then becomes

$$\mathbf{M}_\chi \ddot{\boldsymbol{\chi}}(t) + \mathbf{B}_\chi \dot{\boldsymbol{\chi}}(t) + \mathbf{K}_\chi \boldsymbol{\chi}(t) = \mathbf{F}(t). \quad (3.12)$$

To include the controller and power production in the design process, a model for the rotor and drivetrain is needed. Here, a rigid drivetrain is assumed, and a single-DOF model is thus applied for the angular rotation of the shaft. The differential equation is written:

$$I_D\, \ddot{\varphi} = Q_A - N_{\mathrm{gear}} Q_G, \quad (3.13)$$

where I_D is the drivetrain inertia, N_{gear} is the gear ratio, Q_G is the high-speed shaft (HSS) generator torque, and $\dot{\varphi}$ is the low-speed shaft (LSS) rotational speed.

With the structural DOFs described above, the state vector is defined as

$$\mathbf{x} = \begin{bmatrix} \boldsymbol{\chi}^\top & \dot{\boldsymbol{\chi}}^\top & \dot{\varphi} \end{bmatrix}^\top. \quad (3.14)$$

The state matrix in Eq. (3.5) can now be derived from the total mass, damping, and stiffness matrices for the system (Chen 2013):

$$\mathbf{A} = \begin{bmatrix} \mathbf{0} & \mathbf{I} \\ -\mathbf{M}^{-1}\mathbf{K} & -\mathbf{M}^{-1}\mathbf{B} \end{bmatrix}, \quad (3.15)$$

while the input matrix $\mathbf{E}$ relates the system inputs to the external forces acting on the states.

The mean configuration of the mooring system, as well as the linearized mooring stiffness, for a given mean thrust is found using the elastic catenary equations. For the dynamic response of the mooring lines, the simplified dynamic model proposed by Larsen and Sandvik (1990), and later extended by Lie and Sødahl (1993), is utilized. Here, each line is modelled as a single-DOF spring/damper system, that consider inertia and drag forces due to

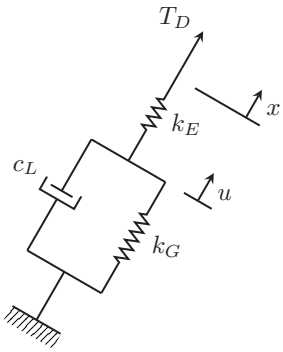

Figure 3.3: Simplified dynamic mooring line model as illustrated by Lie and Sødahl (1993).

the line motion in addition to elastic and geometric stiffness. Given the displacement of the upper end of the line in the tangential direction, $x(t)$, the dynamic tension in the line can then be calculated from

$$T_D = k_E\left[x(t) - u(t)\right] = c^*|\dot{u}(t)|\dot{u}(t) + k_G u(t) + \omega^2 m^* x(t) \tag{3.16}$$

where $u(t)$ is the generalized displacement of the line, found from a quasi-static analysis where the upper end is displaced two times the standard deviation of the platform motion from the equilibrium position (significant motion). The geometric stiffness, k_G, is found as the secant stiffness when the line is moved from equilibrium to the position of significant motion. m^* and c^* are the generalized inertia and damping coefficients due to Morison-type hydrodynamic forces, respectively, which are found using the quasi-static line configuration as the shape function. k_E is the elastic line stiffness. The model is illustrated in Fig. 3.3.

3.4 Hydrodynamics

Assuming a circular cross section for the hull, the first order wave excitation forces can be calculated using the analytic expression developed by MacCamy and Fuchs (1954). The force per unit length, $\mathrm{d}F_W$, for a regular wave with unit amplitude is then given by

$$\mathrm{d}F_W(z,\omega) = \frac{4\rho g}{k}\frac{\cosh k(z+h)}{\cosh kh}\, G\, e^{i(\omega t-\alpha)}, \tag{3.17}$$

where ρ is the water density, g is the gravitational acceleration, k is the wave number, h is the water depth, and

$$G = \frac{1}{\sqrt{\left(J_1'(ka)\right)^2 + \left(Y_1'(ka)\right)^2}}, \quad \tan\alpha = \frac{J_1'(ka)}{Y_1'(ka)}. \tag{3.18}$$

Here, J_n' and Y_n' are the derivatives of the Bessel function of the first and second kind, respectively, of order n, and a is the hull radius. The assumption of a circular cross section also allows for simplification of the radiation forces. The transverse added mass per unit length can be approximated using the analytical 2D coefficient for a circular cylinder in infinite fluid (Newman 1977):

$$a_{11}(z) = \rho\pi D^2(z)/4, \tag{3.19}$$

where D is the hull diameter. For a relatively slender structure, radiation damping will be small and can be neglected, especially at the relevant natural frequencies.

The calculation of the natural period in heave requires an estimate of the added mass in the vertical direction. Here, the vertical added mass is approximated as the value for a 3D circular disc (DNV GL 2017), with the same diameter as the bottom of the platform (D_b), which was found to yield good agreement with numerical linear potential flow solutions for several considered spar designs:

$$A_{33} = \rho D_b^3/3. \tag{3.20}$$

The viscous drag forces on the hull are nonlinear, and must therefore be linearized. While viscous wave excitation is small compared to the wind excitation forces and thus not included in the model, viscous damping is important for the low-frequency surge motions. Neglecting the wave particle velocities, the viscous damping due to the velocity of the structure ($\dot{x}$) can be added based on stochastic linearization of the quadratic drag term in Morison's equation (Borgman 1969):

$$B_{\text{visc}}|\dot{x}|\dot{x} \approx B_{\text{visc}}\sqrt{\frac{8}{\pi}}\sigma_{\dot{x}}\dot{x} = B_{\text{visc,lin}}\,\dot{x}, \tag{3.21}$$

where B_{visc} is the dimensional quadratic damping coefficient, and $B_{\text{visc,lin}}$ is the stochastically linearized coefficient. The standard deviation of the velocity, $\sigma_{\dot{x}}$, depends on the damping forces and vice versa, and must therefore be found using an iteration scheme.

Second order potential flow forces may be important if eigenfrequencies in the system are located close to the excitation frequencies of the sum- or difference-frequency loads. However, as studies have shown that these loads have limited effect on the response for spar-type FWTs (Roald et al. 2013, Duarte et al. 2014), they are not considered in the model.

3.5 Aerodynamics

Aerodynamic loads in global response analyses of FWTs are typically computed using BEM theory, where induction factors, and subsequently blade element forces, are found iteratively (Burton et al. 2011). Assuming that the rotor design does not change during the course of the design process, induction factors can be pre-calculated and stored in look-up tables, before they are used in the response analyses. For each blade element, the induction factors are functions of the blade pitch angle (θ) and tip-speed ratio (λ), where the latter is defined as

$$\lambda = \frac{\dot{\varphi} R}{v}. \tag{3.22}$$

Here, R is the rotor radius, and v is the wind speed. In the present model, the induction factors are computed from the BEM equations following the procedure presented by Ning (2013), which includes Prandtl hub and tip loss factors, and a modified Glauert correction as described by Buhl (2005) for high induction factors. A quasi-static approach is used, meaning that dynamic wake and dynamic stall effects are neglected. The calculated induction factors at midspan for the DTU 10 MW blade design are shown in Fig. 3.4.

Following quasi-steady BEM theory, the aerodynamic forces on a blade element are nonlinear functions of (relative) wind speed, rotor speed, and blade pitch angle, which can be found once the induction factors are known. Linearizing the equations, the normal and tangential blade element forces relative to the rotor plane can be expressed as:

$$F_n(v, \dot{\varphi}, \theta) \approx F_{n0} + \frac{\partial F_n}{\partial v}\Delta v + \frac{\partial F_n}{\partial \dot{\varphi}}\Delta\dot{\varphi} + \frac{\partial F_n}{\partial \theta}\Delta\theta, \tag{3.23a}$$

$$F_t(v, \dot{\varphi}, \theta) \approx F_{t0} + \frac{\partial F_t}{\partial v}\Delta v + \frac{\partial F_t}{\partial \dot{\varphi}}\Delta\dot{\varphi} + \frac{\partial F_t}{\partial \theta}\Delta\theta. \tag{3.23b}$$

The blade root loads of interest, i.e. the flapwise shear force F_y, the flapwise bending moment M_z, and the edgewise bending moment M_y, are found by

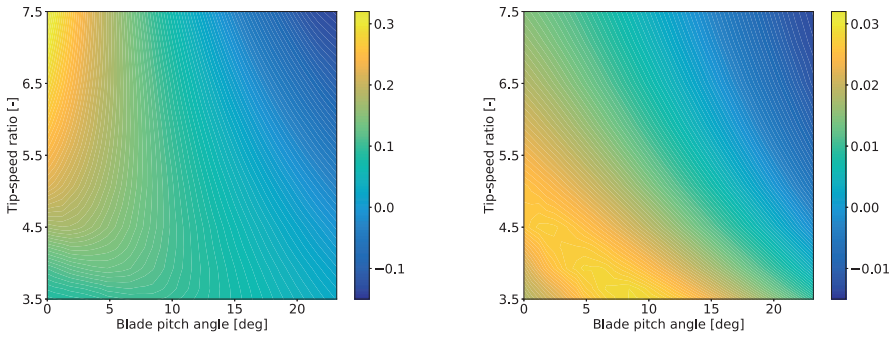

(a) Axial induction factor. **(b)** Tangential induction factor.

Figure 3.4: Calculated induction factors at midspan for the DTU 10 MW blade.

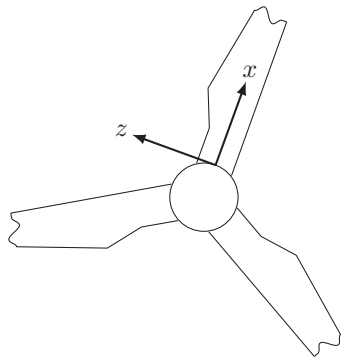

Figure 3.5: Blade coordinate system.

integrating the loads over the length of the blade

$$F_y = \int_0^R F_n \, \mathrm{d}r, \tag{3.24a}$$

$$M_z = \int_0^R r \, F_n \, \mathrm{d}r, \tag{3.24b}$$

$$M_y = \int_0^R r \, F_t \, \mathrm{d}r. \tag{3.24c}$$

Here, the subscripts point to the blade coordinate system, which is defined as in Fig. 3.5. The resultant rotor loads can then be calculated as:

$$F_T = \sum_{i=1}^{3} F_{y,i}, \tag{3.25a}$$

$$M_T = \sum_{i=1}^{3} M_{z,i} \cos \varphi_i, \tag{3.25b}$$

$$Q_A = \sum_{i=1}^{3} M_{y,i}. \tag{3.25c}$$

As only the resultant loads on the rotor are of interest in the global response model, it is desirable to simplify the wind field and express it using a single scalar variable. This is achieved by expressing a rotor effective wind speed for each of the resultant rotor loads in Eq. (3.25). The rotor effective wind speed is a spatially constant wind speed which yields identical resultant loads as the full wind field, and can be established from the incoming wind spectrum, the spatial coherence function, and the transfer functions between wind speed and blade element loads from Eq. (3.23). A detailed derivation of the rotor effective wind speed, based on the thesis by Halfpenny (1998), is provided in Appendix B.

In addition to the rotor loads, the aerodynamic drag forces on the tower are taken into account, using a Morison drag formulation. The tower loads are expressed as a combination of a mean force, which is added directly, and a frequency-dependent force, which is found using stochastic linearization. Here, only the excitation forces are considered, meaning that the tower drag forces arising from the movement of the turbine are neglected.

3.6 Control system description

The baseline control system determines the changes in collective blade pitch and generator torque based on the rotor speed error, and follows the generic approach for variable-speed variable-pitch wind turbines described by e.g. Jonkman et al. (2009). It consists of two separate and independent regions, namely below and above rated wind speed. Typically, wind turbine controllers also include transition strategies to ensure smooth switchovers between regions, however, for simplicity, this is not included in the model.

In both regions, the rotor speed is low-pass filtered to avoid high-frequency actuation, using a first-order filter:

$$\ddot{\overline{\varphi}} + \omega_c \dot{\overline{\varphi}} = \omega_c \dot{\varphi}, \tag{3.26}$$

where ω_c is the corner frequency, and $\dot{\overline{\varphi}}$ is the filtered rotor speed. Below rated wind, the blade pitch angle is kept at fine pitch, while the generator

torque is set proportional to the squared rotor speed, to track the optimal tip-speed ratio and thus optimize the power output:

$$Q_G = K_g \dot{\overline{\varphi}}^2, \tag{3.27}$$

where K_g is the generator torque constant. The change in generator torque for a rotor speed error $\Delta\dot{\overline{\varphi}}$ then becomes

$$\Delta Q_G = \frac{\partial Q_G}{\partial \dot{\overline{\varphi}}} \Delta\dot{\overline{\varphi}} = 2K_g \dot{\varphi}_0 \Delta\dot{\overline{\varphi}}, \tag{3.28}$$

where $\dot{\varphi}_0$ is the rotor speed reference. Alternatively, the generator torque can be regulated using a proportional-integral (PI) controller:

$$\Delta Q_G = k_{p,Q} \Delta\dot{\overline{\varphi}} + k_{i,Q} \int_0^t \Delta\dot{\overline{\varphi}} \, \mathrm{d}\tau, \tag{3.29}$$

where $k_{p,Q}$ and $k_{i,Q}$ i are the proportional and integral gains for the rotor speed error feedback, respectively. Above rated wind speed, the blade pitch angle is found using a gain-scheduled PI controller:

$$\Delta\theta = \eta_k k_{p,\theta} \Delta\dot{\overline{\varphi}} + \eta_k k_{i,\theta} \int_0^t \Delta\dot{\overline{\varphi}} \, \mathrm{d}\tau, \tag{3.30}$$

where $k_{p,\theta}$ and $k_{i,\theta}$ are the proportional and integral gains, respectively, and η_k is the gain-scheduling parameter. For the torque controller, two common strategies exist for the above-rated regime: (1) constant power or (2) constant torque. The variation in generator torque then becomes

$$\Delta Q_G = \begin{cases} -\frac{P_r}{N_{\mathrm{gear}} \dot{\varphi}_r^2} \Delta\dot{\overline{\varphi}}, & \text{constant power,} \\ 0, & \text{constant torque,} \end{cases} \tag{3.31}$$

where P_r and $\dot{\varphi}_r$ are the rated power and rotor speed, respectively.

To avoid the potential problem of negative damping for the platform motions above rated wind speed, a feedback term proportional to the platform pitch velocity or nacelle velocity may also be included, to manipulate the rotor speed reference. Here, a modified rotor speed reference, $\dot{\varphi}_0'$, as defined by Lackner (2009) is used:

$$\dot{\varphi}_0' = \dot{\varphi}_0 (1 + k_f \dot{x}_f), \tag{3.32}$$

where k_f is the velocity feedback gain, and $\dot{x}_f$ is the nacelle or pitch velocity. An updated expression for the rotor speed error can then be established as

$$\Delta\dot{\overline{\varphi}}' = \dot{\overline{\varphi}} - \dot{\varphi}_0' = \Delta\dot{\overline{\varphi}} - \dot{\varphi}_0 k_f \dot{x}_f. \tag{3.33}$$

Here, $\dot{x}_f$ may also be passed through a low-pass filter before it is fed back to the blade-pitch controller.

3.7 Response to stochastic input

After establishing the linearized model, the transfer matrix between system inputs ($\mathbf{u}$) and outputs ($\mathbf{y}$) is defined using the system matrices in Eq. (3.5) and Eq. (3.6) (Chen 2013):

$$\mathbf{H}(\omega) = \mathbf{C}\left(i\omega\mathbf{I} - \mathbf{A}\right)^{-1}\mathbf{E} + \mathbf{D}. \tag{3.34}$$

The cross spectral density matrix of the response vector $\mathbf{y}$ can be calculated from

$$\mathbf{S}_{\mathbf{y}}(\omega) = \mathbf{H}(\omega)\mathbf{S}_{\mathbf{u}}(\omega)\mathbf{H}(\omega)^{H}, \tag{3.35}$$

where $(\cdot)^{H}$ denotes the conjugate transpose (Naess and Moan 2013). The response spectra of $\mathbf{y}$ are then found along the diagonal of $\mathbf{S}_{\mathbf{y}}(\omega)$.

The input vector is expressed as

$$\mathbf{u} = \begin{bmatrix} v_{F_T} & v_{M_T} & v_{Q_A} & \mathbf{F}_W^{\top} \end{bmatrix}^{\top}, \tag{3.36}$$

where v_{F_T}, v_{M_T} and v_{Q_A} are rotor effective wind speeds for thrust, tilting moment and aerodynamic torque, respectively. The wave load vector, $\mathbf{F}_W$, contains the generalized wave excitation force for each support structure DOF. $\mathbf{S}_{\mathbf{u}}(\omega)$ is the cross spectral density matrix for the load process, which has the following structure:

$$\mathbf{S}_{\mathbf{u}}(\omega) = \begin{bmatrix} \mathbf{S}_{\text{wind}}(\omega) & \mathbf{0} \\ \mathbf{0} & \mathbf{S}_{\text{wave}}(\omega) \end{bmatrix}, \tag{3.37}$$

as the wind and wave processes are assumed to be uncorrelated (DNV GL 2016). Both the wind speed and the wave elevation are assumed to be stationary Gaussian processes, and the response will thus also be a stationary Gaussian process. The n^{th} spectral moment of an arbitrary response parameter y, given the variance spectrum $S_y(\omega)$, is defined as

$$m_n = \int_0^{\infty} \omega^n S_y(\omega)\mathrm{d}\omega. \tag{3.38}$$

The standard deviation of y can then be found from

$$\sigma_y = \sqrt{m_0}. \tag{3.39}$$

3.7.1 Fatigue damage

To calculate the fatigue damage, formulations for the fatigue resistance and fatigue loading are needed. The fatigue resistance is commonly described

by SN curves, where the relation between the stress range (S) and number of cycles to failure (N) is given as (DNV GL 2019c):

$$N = KS^{-m}, \tag{3.40}$$

where K and m are material parameters dependent on the type of fatigue detail. Using the Palmgren-Miner hypothesis of linear accumulation of damage, the fatigue damage in time T can be expressed as (Naess and Moan 2013):

$$D = \int_0^\infty \frac{\nu T}{K} s^m f_S(s) \mathrm{d}s. \tag{3.41}$$

Here, the fatigue loading is described by the cycle rate, ν, and the PDF of the stress ranges, $f_S(s)$. If the response process is narrow-banded and Gaussian, the stress ranges can be described by a Rayleigh distribution; however, because the response of FWTs in general is wide-banded, the narrow-band formulation may result in overly conservative damage estimates. For a general wide-banded response, cycle counting methods based on the stress time series are typically applied, with rainflow counting being considered the most accurate for estimation of fatigue damage (Naess and Moan 2013). This method has no closed-form solution in the frequency domain for wide-banded Gaussian response, and given a stress response spectrum, the stress range distribution must thus be estimated either by transformation of the response spectra to the time domain, or directly in the frequency domain using empirical formulae. For the latter approach, various methods have been proposed, where the formulae presented by Dirlik (1985) and Benasciutti and Tovo (2005) have been shown to yield accurate approximations of the rainflow counting method for a variety of spectral shapes and bandwidths (Gao and Moan 2008).

The Dirlik method, which is implemented in the current model, uses the stress response spectrum and empirical factors to fit the PDF of the stress cycles to a combination of an exponential and two Rayleigh distributions, and the accuracy of the method is therefore dependent on how well the rainflow-count can be represented by these distributions. The resulting stress range distribution is given as:

$$f_S(s) = \frac{\frac{G_1}{Q} \exp\left\{-\frac{Z}{Q}\right\} + \frac{G_2 Z}{R^2} \exp\left\{-\frac{Z^2}{2R^2}\right\} + G_3 Z \exp\left\{-\frac{Z^2}{2}\right\}}{2\sqrt{m_0}}, \tag{3.42}$$

where G_1, G_2, G_3, R, and Q are empirical weight factors found from the spectral moments, and Z is the normalized stress range:

$$Z = \frac{S}{2\sqrt{m_0}}. \tag{3.43}$$

3.7.2 Extreme response

Estimation of extreme values for a stochastic process can be performed using upcrossing analysis, which is based on the assumption that upcrossings of high levels are statistically independent (Naess 1984). Consequently, the number of upcrossings in time T will be Poisson distributed, which, for the response process y, gives the following CDF for the extreme value Ξ:

$$F_{\Xi}(\xi) = \exp\left\{-\nu_{\xi}^{+}\, T\right\}, \tag{3.44}$$

where ν_{ξ}^{+} is the mean upcrossing rate of the level ξ. Assuming a stationary Gaussian process with zero mean, the CDF can be written (Naess and Moan 2013)

$$F_{\Xi}(\xi) = \exp\left\{-\nu_{0}^{+}\, T \exp\left(-\frac{\xi^2}{2\sigma_y^2}\right)\right\}, \tag{3.45}$$

where ν_0^+ is the mean zero-upcrossing rate, which can be found from the zeroth and second order spectral moments:

$$\nu_0^+ = \frac{1}{2\pi}\sqrt{\frac{m_2}{m_0}}. \tag{3.46}$$

The p-fractile of the distribution, i.e. the value which is exceeded with probability (1 - p) during the time T, becomes (Naess and Moan 2013):

$$\xi_p = \sigma\sqrt{2\ln\left(\frac{\nu_0^+ T}{\ln(1/p)}\right)}, \tag{3.47}$$

while the most probable maximum value, ξ_c, also known as the characteristic largest extreme, can be found approximately from the relation $F_{\Xi}(\xi_c) = \mathrm{e}^{-1}$:

$$\xi_c = \sigma\sqrt{2\ln\left(\nu_0^+ T\right)}. \tag{3.48}$$

3.8 Optimization framework

To enable efficient gradient-based optimization, the FWT model is implemented in the OpenMDAO framework (Gray et al. 2019). OpenMDAO is an open-source framework for multidisciplinary design, analysis and optimization, which contains a large number of solvers and other features making it suitable for large-scale optimization of complex systems. The model is constructed in a modular fashion, where the complex multidisciplinary model

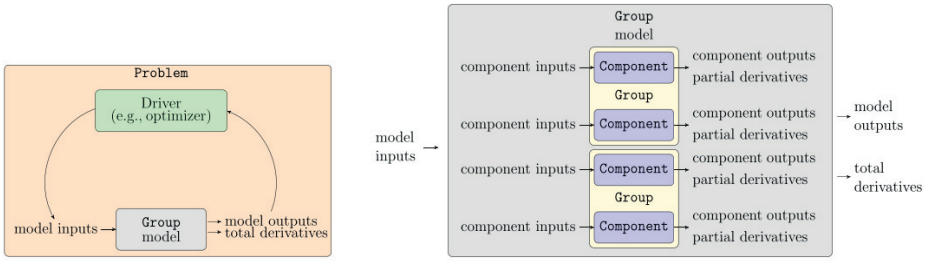

Figure 3.6: OpenMDAO problem structure (Gray et al. 2019).

is broken down into smaller units of code (components). The components are gathered in groups that again can be part of other groups, and thus forms a hierarchical structure which can be used to organize the model or define different solver strategies. An overview of the OpenMDAO problem structure is shown in Fig. 3.6.

The partial derivatives of the component outputs with respect to the component inputs can either be calculated numerically using e.g. finite differences, or be provided as analytic functions by the user. Analytic derivatives are desirable due to their computational efficiency and accuracy; however, they require significant implementation effort. In the present work, analytic derivatives are computed for the complete coupled model, which ensures a feasible optimization process even as the number of design variables and load cases become large.

One of the main purposes of the optimization framework is to compute overall model-level derivatives given the component-level derivatives. For a model where all relations are given by explicit functions, the total derivatives can be calculated using the chain rule. However, if implicit relationships between variables exist, more elaborate methods are needed. Given an output of interest, $\mathbf{f}$, which is described by the function $\mathbf{f} = \mathbf{F}(\mathbf{x}, \mathbf{y}(\mathbf{x}))$, where $\mathbf{x}$ is the vector of input variables, and $\mathbf{y}$ is a vector of implicit variables dependent on $\mathbf{x}$, the total derivative can be found from (Martins and Ning 2020):

$$\frac{\mathrm{d}\mathbf{f}}{\mathrm{d}\mathbf{x}} = \frac{\partial \mathbf{F}}{\partial \mathbf{x}} + \frac{\partial \mathbf{F}}{\partial \mathbf{y}} \frac{\mathrm{d}\mathbf{y}}{\mathrm{d}\mathbf{x}}. \tag{3.49}$$

The relationship between $\mathbf{y}$ and $\mathbf{x}$ is defined by the solution of the residual equations $\mathbf{r} = \mathbf{R}(\mathbf{x}, \mathbf{y}(\mathbf{x})) = 0$. The total derivative of $\mathbf{r}$ with respect to $\mathbf{x}$ can be expressed as:

$$\frac{\mathrm{d}\mathbf{r}}{\mathrm{d}\mathbf{x}} = \frac{\partial \mathbf{R}}{\partial \mathbf{x}} + \frac{\partial \mathbf{R}}{\partial \mathbf{y}} \frac{\mathrm{d}\mathbf{y}}{\mathrm{d}\mathbf{x}} = 0. \tag{3.50}$$

It is desirable to calculate $\mathrm{d}\mathbf{f}/\mathrm{d}\mathbf{x}$ using only partial derivatives, as they do not require solving the residual equations and thus have a lower computational cost. The only term in Eq. (3.49) that is not a partial derivative is $\mathrm{d}\mathbf{y}/\mathrm{d}\mathbf{x}$, which from Eq. (3.50) can be expressed as

$$\frac{\partial \mathbf{R}}{\partial \mathbf{y}} \frac{\mathrm{d}\mathbf{y}}{\mathrm{d}\mathbf{x}} = -\frac{\partial \mathbf{R}}{\partial \mathbf{x}}. \tag{3.51}$$

Given the partial derivatives of $\mathbf{R}$ with respect to $\mathbf{x}$ and $\mathbf{y}$, $\mathrm{d}\mathbf{y}/\mathrm{d}\mathbf{x}$ can then be found by solving the linear system in Eq. (3.51). This is known as the direct (forward) method, where the linear system must be solved once for each model input (Martins and Ning 2020).

Alternatively, $\mathrm{d}\mathbf{y}/\mathrm{d}\mathbf{x}$ in Eq. (3.49) can be replaced by the expression in Eq. (3.51):

$$\frac{\mathrm{d}\mathbf{f}}{\mathrm{d}\mathbf{x}} = \frac{\partial \mathbf{F}}{\partial \mathbf{x}} - \underbrace{\frac{\partial \mathbf{F}}{\partial \mathbf{y}} \left[\frac{\partial \mathbf{R}}{\partial \mathbf{y}}\right]^{-1}}_{\boldsymbol{\psi}^\top} \frac{\partial \mathbf{R}}{\partial \mathbf{x}}. \tag{3.52}$$

Here, $\boldsymbol{\psi}$ is known as the *adjoint vector*, which can be described through the following relation (Martins and Ning 2020):

$$\left[\frac{\partial \mathbf{R}}{\partial \mathbf{y}}\right]^\top \boldsymbol{\psi} = \left[\frac{\partial \mathbf{F}}{\partial \mathbf{y}}\right]^\top. \tag{3.53}$$

Now, $\boldsymbol{\psi}$ can be found by solving the linear system in Eq. (3.53), and used together with Eq. (3.52) to calculate the total derivative. This is known as the adjoint (reverse) method. The linear system in Eq. (3.53) must, contrary to the forward method, be solved once for each model output, and this method therefore offers increased computational efficiency when the number of model inputs is larger than the number of model outputs. OpenMDAO supports both direct and adjoint gradient computations, and the method is chosen based on the specific problem structure.

To illustrate the extent of the analytic gradient implementation, the required calculations are shown for a single model component. The component which calculates the uncoupled heave natural period (T_{n3}), given the structural mass of the system (M), the added mass in heave (A_{33}), and the heave restoring stiffness (C_{33}), uses the following relation:

$$T_{n3} = 2\pi \sqrt{\frac{M + A_{33}}{C_{33}}}. \tag{3.54}$$

The required partial derivatives for the component become:

$$\frac{\partial T_{n3}}{\partial M} = \frac{\pi}{C_{33}\sqrt{\frac{M+A_{33}}{C_{33}}}}, \tag{3.55a}$$

$$\frac{\partial T_{n3}}{\partial A_{33}} = \frac{\pi}{C_{33}\sqrt{\frac{M+A_{33}}{C_{33}}}}, \tag{3.55b}$$

$$\frac{\partial T_{n3}}{\partial C_{33}} = -\frac{\pi\sqrt{\frac{M+A_{33}}{C_{33}}}}{C_{33}}. \tag{3.55c}$$

As both M, A_{33}, and C_{33} are dependent on the design variables for the optimization problem, the chain rule in Eq. (3.49) is then needed to compute the total derivative of T_{n3} with respect to an arbitrary design variable p:

$$\frac{\mathrm{d}T_{n3}}{\mathrm{d}p} = \frac{\partial T_{n3}}{\partial p} + \frac{\partial T_{n3}}{\partial M}\frac{\mathrm{d}M}{\mathrm{d}p} + \frac{\partial T_{n3}}{\partial A_{33}}\frac{\mathrm{d}A_{33}}{\mathrm{d}p} + \frac{\partial T_{n3}}{\partial C_{33}}\frac{\mathrm{d}C_{33}}{\mathrm{d}p}. \tag{3.56}$$

If there is an implicit relationship between M, A_{33}, or C_{33}, and p, obtaining the total derivative also requires solving the linear system in Eq. (3.51) or Eq. (3.53).

The component-level derivatives must be provided for all parts of model, and may result in rather involved computations, especially for more advanced components. The complexity and required effort related to the gradient implementation are thus comparable to the development of the analysis model itself, and makes up about 70 % of the total code volume in the present work.

The model layout and data dependencies are illustrated using an extended design structure matrix (XDSM) (Lambe and Martins 2012) in Fig. 3.7. Here, the rounded blue box is the optimizer, green boxes are analysis models, gray parallelograms are data, white parallelograms are fixed input parameters, and grey lines represent data dependencies. The data moves from top to bottom and left to right in the upper triangular part, and from bottom to top and right to left in the lower triangular part.

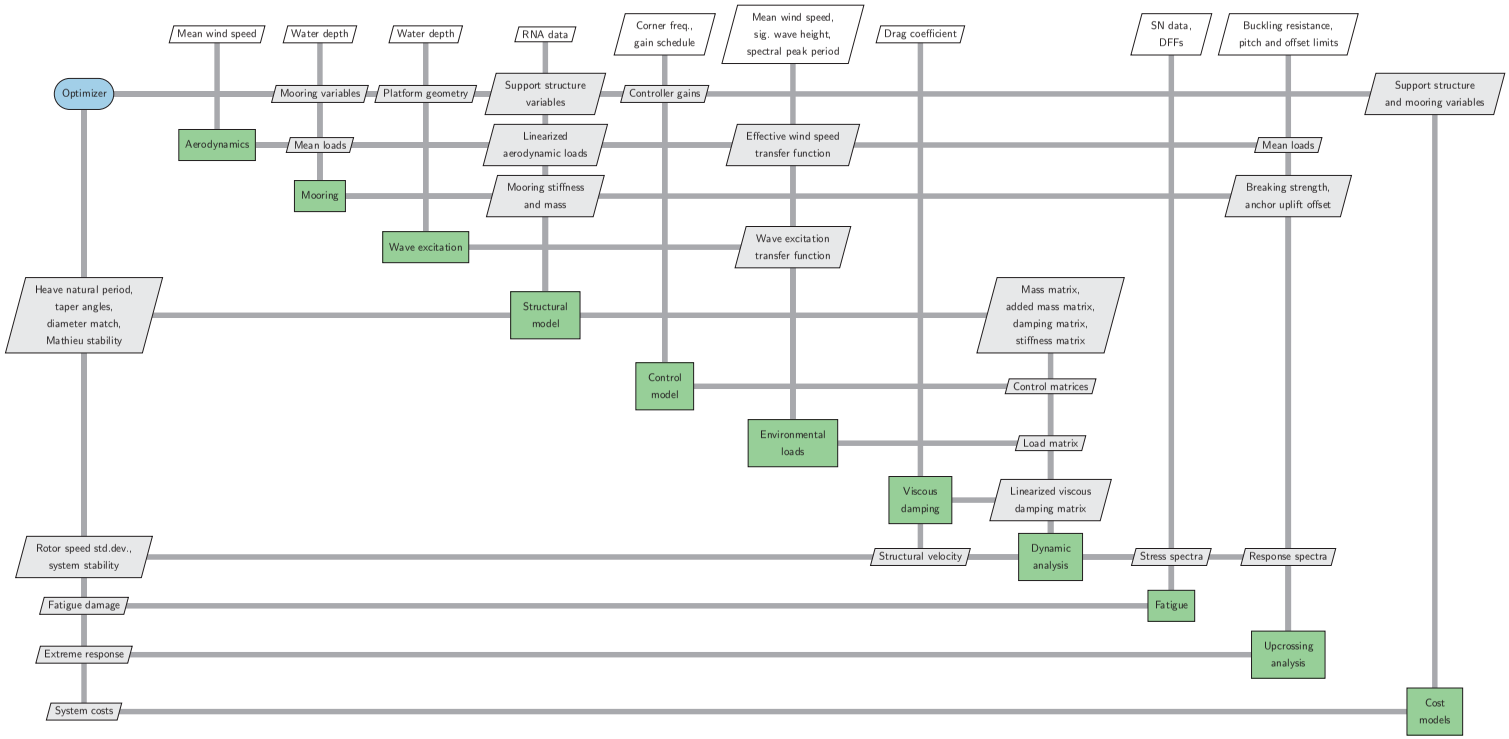

Figure 3.7: XDSM diagram showing the model layout and data dependencies.

3.9 Model development

The linearized FWT model has been developed over the course of the thesis, and the versions applied in the different papers have therefore not been the same. The evolution of the model is briefly summarized in the following.

V1, applied in **P1**: The structural model for the support structure using generalized coordinates is established, but assumes a rigid platform, while the elasticity of the tower is considered. The hydrodynamic formulations presented in Section 3.4 are implemented, and the quasi-static mooring system response is found from the elastic catenary equations. The rotor DOF is not included, and aerodynamic excitation (thrust and tilting moment) is computed from time-domain simulations with turbulent wind and an active controller. The aerodynamic damping is found as the change in thrust due to a small change in wind speed, assuming no reaction from the rotor or controller. The Dirlik method for fatigue damage in the support structure and extreme response based on upcrossing analysis are implemented.

V2, applied in **P3**: Building off of *V1*, A single-DOF model for the rotation of the shaft is implemented, and a flexible platform is included. Linearized aerodynamic loads are derived as functions of wind speed, rotor speed, and blade-pitch angle, using quasi-steady BEM theory and a rotor effective wind speed. Generator-torque and blade-pitch controllers are added to the model. Dynamic mooring line tension is found based on a single-DOF model which consider drag and inertia forces due to the motion of the line. Analytic gradients are calculated for the model, which is implemented in the OpenMDAO framework.

V3, applied in **P4**: More advanced control strategies for the blade-pitch controller are implemented. The new controllers consider velocity feedback using either the nacelle or the platform pitch velocity, with an optional low-pass filter on the velocity signal.

V4, applied in **P5**: The model is extended to account for out-of-plane response, and thus allow for wind-wave misalignment.

Chapter 4

Research Findings

This chapter presents the main research findings from the papers included in the thesis, and discusses their relation to the contributions stated in Section 1.3.

4.1 Linearized dynamic analyses

Findings related to the use of linearized dynamic analyses to predict global design loads for FWT structures are presented in the following. First, closed-form expressions for frequency-dependent aerodynamic damping and inertia are derived. Then, verification of the linear model against nonlinear simulations for fatigue and extreme response is presented, and some important aspects and limitations to the model are discussed.

4.1.1 Aerodynamic damping and inertia

The motions of the FWT give rise to changes in the aerodynamic forces on the turbine, which depend on the mean wind speed, motion amplitude, and oscillation frequency. Commonly, frequency-domain analyses of offshore wind turbines have considered aerodynamic damping coefficients which are either constant, or vary only with the mean wind speed. These methods neglect the impact of the controller and rotor dynamics, and consequently overestimate the damping at low oscillation frequencies.

In addition, the forces which arise from the platform motions that are out of phase with the velocity, and thus result in an inertia (or stiffness) effect, are neglected. For FWTs, which typically experience low-frequency resonant motions, frequency-dependent forces should be considered in response

calculations. In the present work, closed-form expressions for frequency-dependent aerodynamic damping and inertia were derived. The key results are presented in the following, while a detailed derivation can be found in **P2**.

Using linearized aerodynamic forces and a 2-DOF wind turbine model, with the horizontal nacelle displacement (x) and the rotation of the shaft (φ), the following expressions were obtained for the aerodynamic inertia (a_{aero}) and damping (b_{aero}) coefficients:

$$a_{\text{aero}}(\omega) = -\frac{1}{\omega^2}\,\text{Re}\left\{i\omega\frac{\partial F_T}{\partial v} - \left[i\omega\left(\frac{\partial F_T}{\partial \dot{\varphi}} + k_P\frac{\partial F_T}{\partial \theta}\right) + k_I\frac{\partial F_T}{\partial \theta}\right]\tilde{C}_\varphi(\omega)\right\}, \tag{4.1a}$$

$$b_{\text{aero}}(\omega) = \frac{1}{\omega}\,\text{Im}\left\{i\omega\frac{\partial F_T}{\partial v} - \left[i\omega\left(\frac{\partial F_T}{\partial \dot{\varphi}} + k_P\frac{\partial F_T}{\partial \theta}\right) + k_I\frac{\partial F_T}{\partial \theta}\right]\tilde{C}_\varphi(\omega)\right\}. \tag{4.1b}$$

Here, F_T is the thrust force, v is the wind speed, k_P and k_I are the proportional and integral gains of the blade-pitch controller, and θ is the blade-pitch angle. $\tilde{C}_\varphi$ is the complex transfer function between x and φ, i.e.,

$$\varphi(\omega) = \tilde{C}_\varphi(\omega)x(\omega). \tag{4.2}$$

The derived coefficients in Eq. (4.1) were compared to results from numerical simulations using forced oscillations with AeroDyn as described by Souza and Bachynski (2019), as well as constant damping coefficients, which neglect the controller and rotor dynamics. In Fig. 4.1, the coefficients are shown for the low-frequency range, for a mean wind speed of 25 m/s. The overall agreement between the analytical and numerical solutions was good, while the constant damping coefficient was found to significantly overestimate the aerodynamic damping at low frequencies. The magnitude of the aerodynamic inertia is low compared to the total mass of typical FWTs, resulting in negligible consequences for the surge response. Due to the height of the nacelle, however, the contribution to the moment of inertia in pitch is considerable.

To assess the importance of frequency-dependent coefficients, a frequency-domain model of the OO-Star 10 MW semi-submersible, which was part of the the LIFES50+ project (Müller et al. 2018), was created. Results from the frequency-domain model, using different formulations for the aerodynamic damping and inertia, are compared to nonlinear time-domain simulations using SIMA. The response spectra for platform pitch and tower base

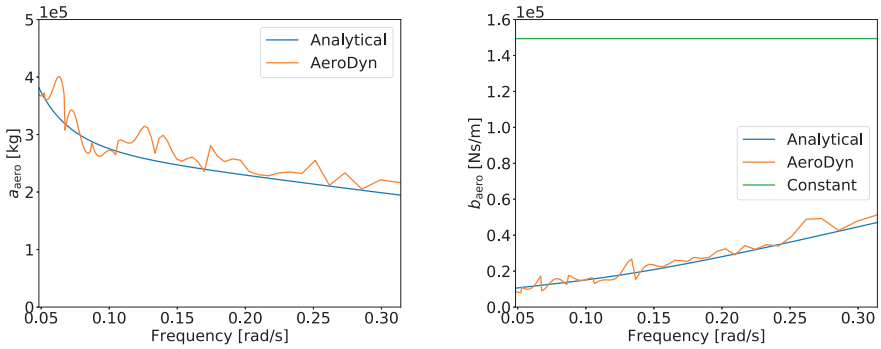

(a) Inertia. **(b)** Damping.

Figure 4.1: Aerodynamic inertia and damping coefficients, 25 m/s mean wind speed.

Table 4.1: Error in standard deviations compared to time domain simulations.

Response parameter	Constant (%)	Analytical (%)	AeroDyn (%)
Platform pitch	-29.6	+55.0	+30.6
Tower base moment	-33.0	+19.2	+5.3

bending moment are shown in Fig. 4.2, and relative errors in the standard deviations are presented in Table 4.1.

While the constant damping coefficient underestimated the responses, the opposite was observed for the frequency-dependent coefficients. There were also notable differences between the analytical and AeroDyn models, despite the good agreement for the damping coefficient, which suggested that the response was sensitive to resonant motions and consequently the damping level in the model. Although the actual numbers also depend on the considered wind-wave conditions, platform concept, and additional damping in the model, the results demonstrated that the use of constant damping coefficients is non-conservative, and that this can be avoided in a simple manner through the frequency-dependent coefficients in Eq. (4.1).

The deviations in response between the frequency-domain models in Fig. 4.2 can be attributed to differences in aerodynamic damping coefficients. The effect of aerodynamic inertia was much less prominent, but can be seen in the calculated platform pitch natural period. Calculated natural periods in pitch, with and without aerodynamic inertia, are shown in Fig. 4.3.

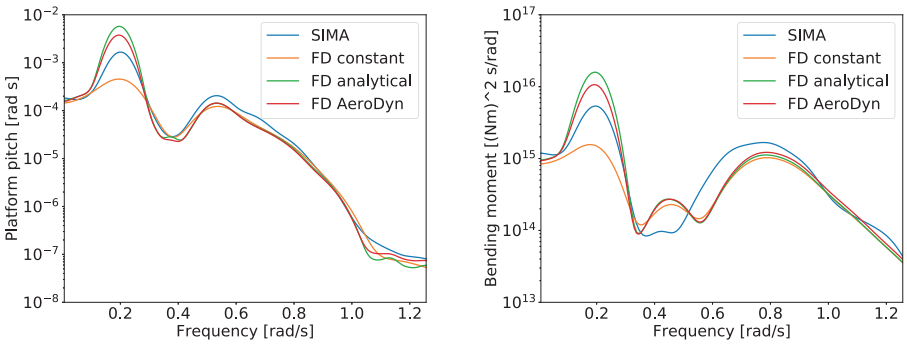

(a) Platform pitch. **(b)** Tower base bending moment.

Figure 4.2: Response comparison between SIMA and frequency-domain analyses, 25 m/s mean wind speed.

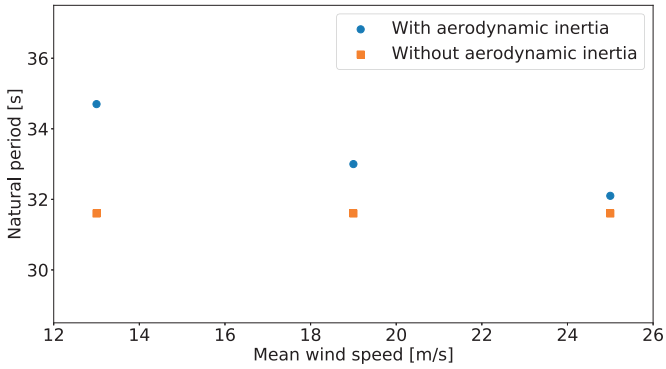

Figure 4.3: Pitch natural period with and without aerodynamic inertia effect.

An alternative method of achieving frequency-dependent damping and inertia effects in the support structure analysis is to include a description of the rotor and controller dynamics in the support structure model, as described in **P3**. These effects will then be implicitly included.

4.1.2 Long-term fatigue damage

To assess the applicability of the linearized model in design, the degree of nonlinearity in the global response of the support structures is evaluated. Because both the wind speed and the wave elevation in the short term are assumed stationary Gaussian processes, the linear response of the FWT is also stationary and Gaussian. One way to evaluate the nonlinearity of the response is therefore to look at the skewness and (Pearson's) kurtosis values, which are 0 and 3 for a Gaussian process, respectively. The skewness and kurtosis for the tower bending moment, based on nonlinear time-domain simulations in SIMA, are shown in Fig. 4.4. The results are based on one wind-wave condition for each mean wind speed from 1 to 30 m/s, using a bin size of 1 m/s and six random realizations. The most probable values for H_s and T_p were applied for each mean wind speed, and represent typical fatigue conditions.

For most wind speeds, the response is quite linear, especially above the rated wind speed of 11.4 m/s. Here, the wave loads become increasingly more important relative to the wind loads, which exhibit a larger degree of nonlinearity. Close to the tower top, the response is dominated by aerodynamic loads, and overall more non-Gaussian behaviour is observed. In the rest of the tower, the pattern is more or less identical to the tower base, suggesting that the same load effects are dominating along most of the tower length.

A comparison of weighted 1-h fatigue damage at the tower base, based on both linear and nonlinear analyses, is shown as a function of the mean wind speed in Fig. 4.5, taken from **P1**. Here, 546 environmental conditions were considered, which corresponded to all conditions within the operational range with probability of occurrence greater than 10^{-4} at the considered site. The linear model was, for most wind speeds, able to accurately capture the fatigue response, and the damage estimates based on response spectra using the Dirlik method were found to agree well with inverse Fourier transform combined with rainflow counting. Large errors in the damage estimates were observed at 9 m/s mean wind speed, where the first tower bending mode coincided with the 3P frequency. In such resonance conditions, nonlinear effects become important, and the linear model significantly overestimated

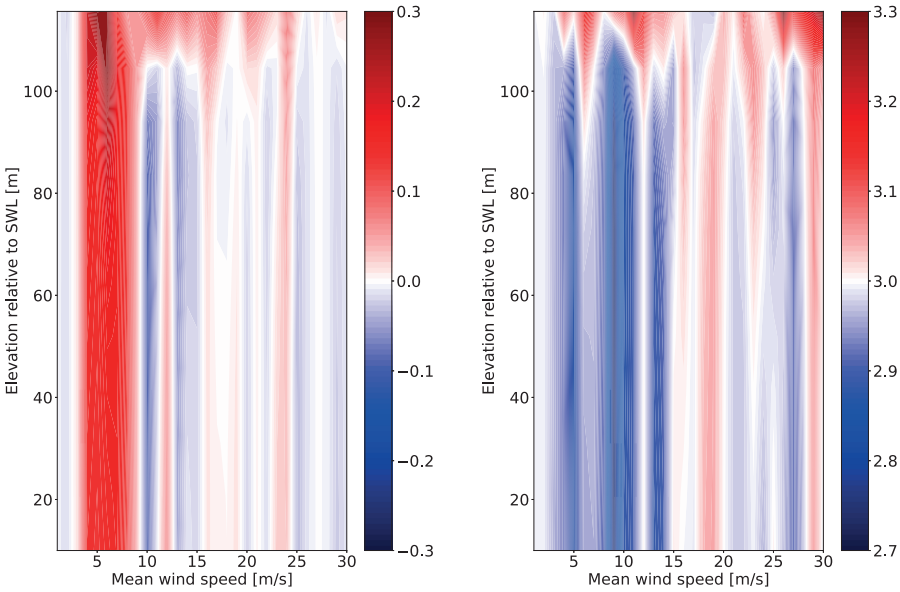

(a) Skewness. **(b)** Kurtosis.

Figure 4.4: Skewness and kurtosis values for tower fore-aft bending moment.

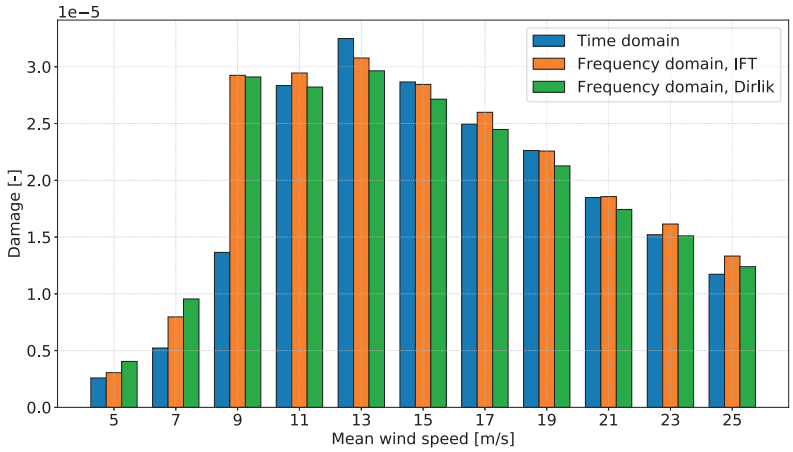

Figure 4.5: 1-h weighted tower base fatigue damage arranged by wind speed.

the bending mode response.

These results suggest that the linearized model should be used with care if the first bending mode is close to the blade-passing frequency, which is often the case for FWTs. It also highlights the importance of accurate estimation of the tower bending mode and associated natural period, as the modal excitation forces may change rapidly with frequency. This is illustrated for the tower base bending moment response spectrum in Fig. 4.6, based in the linearized model, where the natural frequency of the first bending mode is artificially increased in steps of 0.06 rad/s by modifying the modal stiffness. As the natural frequency approaches the 3P frequency, the resonant response, and consequently the fatigue damage, is significantly increased.

This effect may also be important in the context of the numerical modelling of the platform in the global response analyses. For large turbines, the flexibility of the platform can have a large impact on the tower modes, and should therefore be included to ensure that the correct dynamic behaviour is captured.

4.1.3 Short-term extreme response

Similarly to the skewness and kurtosis values for the fatigue conditions, upcrossing rates were used to assess the linearity of the extreme response in 50-year conditions. For a Gaussian process, the upcrossing rate of level y can be calculated from the process' standard deviation (σ) and mean

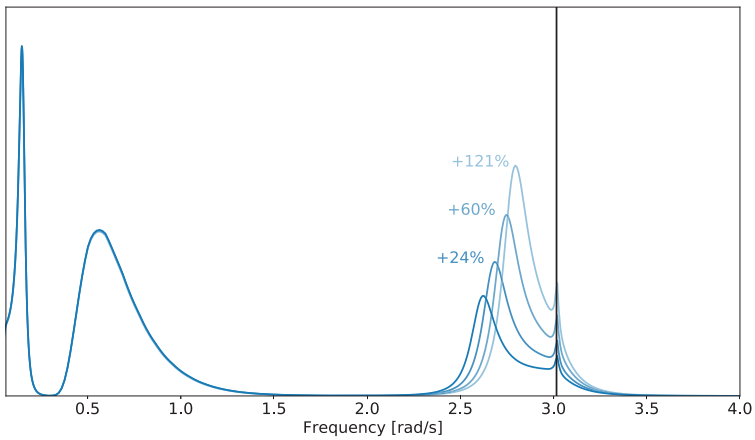

Figure 4.6: Linearized tower base bending moment response spectrum for $U = 15$ m/s, $H_s = 3$ m, and $T_p = 12$ s, where the natural frequency of the first bending mode is artificially increased in steps of 0.06 rad/s (≈ 0.01 Hz) by modifying the modal stiffness. The corresponding increase in calculated 1-h fatigue damage is shown, together with the 3P frequency at rated speed (black line).

zero-upcrossing rate ($\nu^+(0)$):

$$\nu^+(y) = \nu^+(0) \exp\left(-\frac{y^2}{2\sigma^2}\right) \tag{4.3}$$

For the nonlinear time-domain simulations, a function for the tail of the mean upcrossing rates can be established empirically, as described in **P1**. The nonlinear and linear average upcrossing rates (AUR) for surge, pitch, and tower base bending moment are shown for two 50-year conditions in 4.7. The plots show the multiplication factor κ, which is related to the extreme response, y, through the relation

$$y = \mu + \kappa\sigma, \tag{4.4}$$

where μ and σ are the mean and standard deviation of the process.

Very good agreement was obtained with an extreme wind speed in the parked condition, where the response was governed by wave loads. Larger nonlinearities are observed near the rated wind speed, due to the large thrust forces in this condition. This was especially the case for the pitch response. The tower base bending moment, on the other hand, was also quite Gaussian in the operational condition, due to the large influence of inertial forces arising from wave-frequency motions.

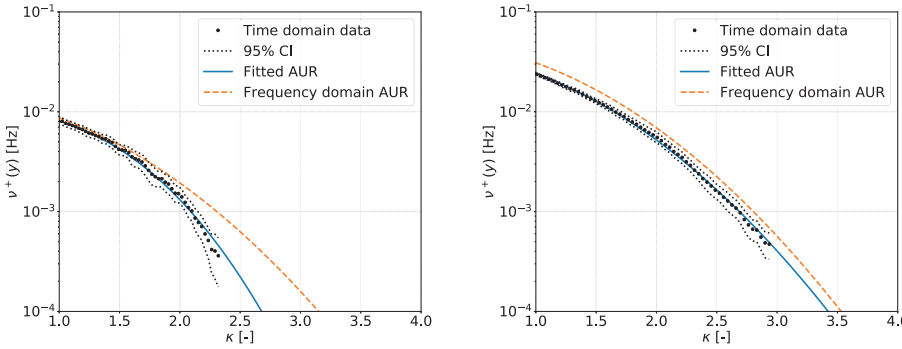

(a) Surge.

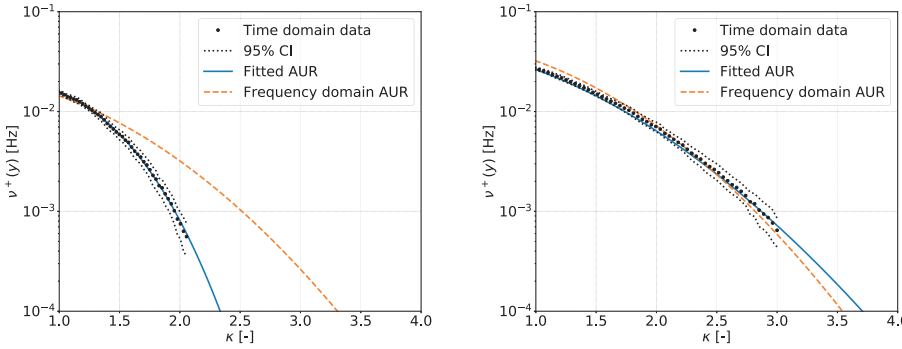

(b) Pitch.

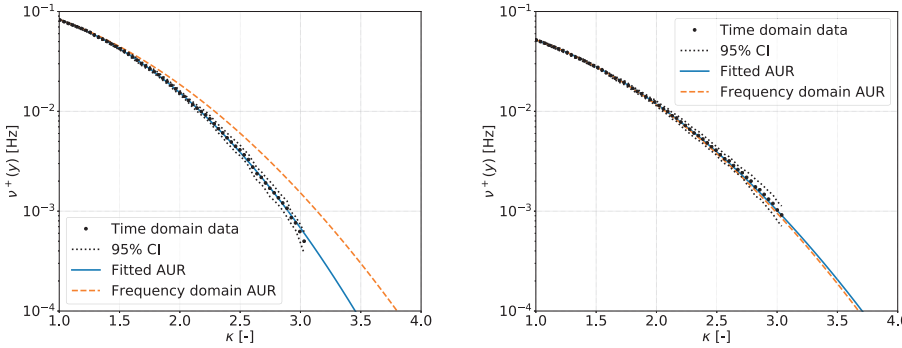

(c) Tower base bending moment.

Figure 4.7: Upcrossing rates for 11 m/s (left) and 50 m/s (right) mean wind speed.

While these results suggest that a linear model also can be used to evaluate extreme response in early phases of design, especially for the bending moments in the support structure, such a conclusion cannot be drawn in the general case. The accuracy of the linear model depends on the importance of nonlinearities in the system, which will vary with location, floater geometry, and different operational conditions. The agreement with nonlinear analyses also depends on how the system is represented in the time-domain model, and care should be taken to make sure that relevant nonlinearities are included.

4.2 Integrated design optimization

The following subsections present key results and discussion regarding integrated numerical design optimization of FWT systems. The findings are based on the methodology presented in **P3**, where the tower, spar platform, blade-pitch controller, and mooring system were optimized simultaneously, including the scantling design of the hull, using gradient-based optimization with analytic gradients. The optimization considered buckling and long-term fatigue damage along the hull and tower, maximum offset and pitch angle of the platform during selected extreme conditions, and extreme mooring line tension and anchor uplift.

4.2.1 Multimodality

During the optimization runs performed in the present work, local minima were identified for the tower design. The fatigue damage in the support structure increases significantly if the natural frequency of the first tower bending mode coincides with the blade passing frequency, and the optimizer will therefore try to move the tower mode away from the 3P range. The direction that the mode is moved during the optimization depends on the initial design, as illustrated in Fig. 4.8. Due to the 'barrier' created by the blade passing frequency, the optimizer will not be able to move over to the stiff-stiff range if the initial design has a soft-stiff tower, and vice versa. Early studies with the optimization model suggested that no feasible solution existed in the soft-stiff range for the applied design problem, and all subsequent studies were therefore performed with a stiff-stiff initial design. However, this should not be treated as proof that a soft-stiff solution does not exist, as the design analyses were based on a simplified model and a reduced set of environmental conditions. In addition, more advanced control strategies, such as a speed exclusion zone to prevent tower resonance in the below-rated regime, could improve the fatigue behaviour. More detailed studies of potential designs are therefore needed to conclude whether

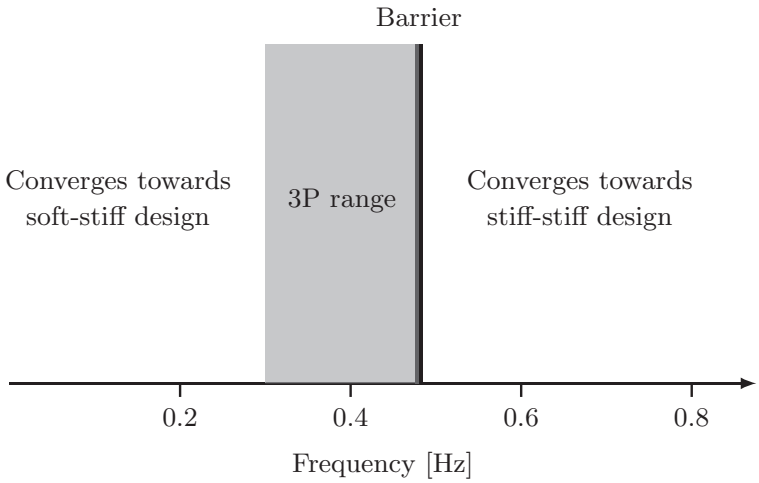

Figure 4.8: Impact of initial tower bending natural frequency on optimization results.

a feasible soft-stiff tower design exists.

4.2.2 Cost and power quality

The goal of the design optimization was to minimize a combination of system costs and rotor speed variation, where the latter was considered a measure of the (inverse) power quality. The monetary cost of reduced power quality is difficult to quantify, and the terms could therefore not be combined in a straightforward manner. The optimization was therefore performed with different weights on the two sub-objectives, to assess the trade-off effects for the system.

The relative importance of costs and power quality in the objective function primarily affected the blade pitch control system parameters, as shown in Fig. 4.9, where the optimized PI gains for different weight factors are plotted against the resulting normalized rotor speed variation. Increasing the gains results in a faster controller, leading to lower variation in the rotor speed, but increased loads in the support structure.

Within the range of the objective function weights considered in **P3**, the power quality was found to be much more sensitive to the applied weighting than the system costs, as shown in Fig. 4.10. While a 15 % decrease in rotor speed variation was observed from lowest to highest power quality weighting, the corresponding increase in design costs was only 0.7 %.

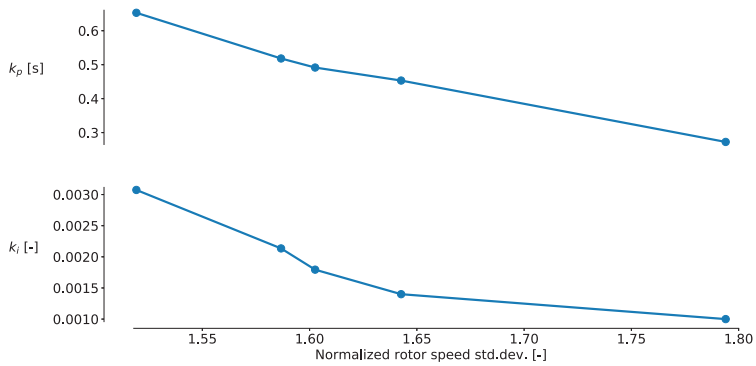

Figure 4.9: Optimized blade-pitch controller gains plotted against resulting rotor speed variation.

As the applied design optimization process considered only stationary conditions, relatively slow controllers were obtained. To ensure proper control action during transient events such as wind gusts, extensions to the presented methodology are needed, which may result in faster controllers with larger negative effects on the support structure costs.

4.2.3 Support structure design

The optimized tower and platform design for a selected combination of objective function weights, based on the integrated approach applied in **P3**, is shown in Fig. 4.11, together with fatigue and buckling utilization factors. The platform took an hour-glass shape below the wave-zone, which increased the restoring stiffness in pitch and thus improved the low-frequency behaviour. The sharp edges and constant taper angles along the platform were caused by a constraint on the maximum taper angle, which was included to ensure a platform shape that was captured correctly by the numerical model. The fact that this constraint was active for most of the platform length, suggests that reductions in costs could be achieved if the constraint is relaxed. More comprehensive numerical models, and possibly more information about the sensitivity of the platform shape on the manufacturing costs, would be needed in order to relax this constraint.

The tower base diameter was forced to match the top diameter of the platform, which gave rise to conflicting influences. The platform diameter should be low to limit the wave loads, whereas the tower diameter should be large, as this is the most cost-effective way to achieve the required fatigue resistance. The resulting compromise led to an unconventional tower design,

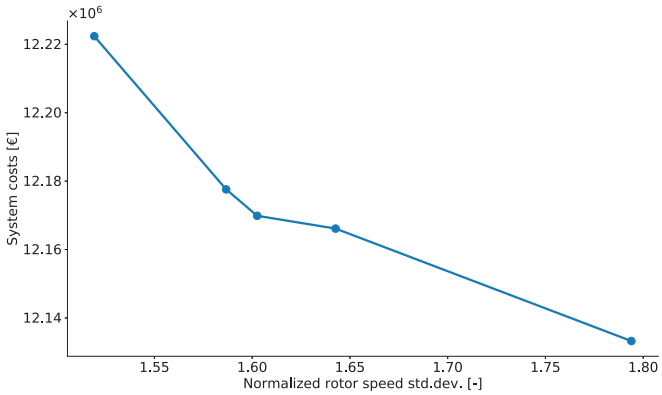

Figure 4.10: Trade-offs between rotor speed variation and system costs in the multiobjective optimization.

where the diameter increased from the base. The importance of integrated design optimization was demonstrated here, as simultaneous design of the platform and tower is needed to identify the optimal solution near the interface.

Tower shape

While typical wind turbine towers are linearly tapered, the integrated optimization procedure employed in the present work suggested a different and somewhat unconventional tower design. The reduction in costs achieved by adopting such a design was quantified by optimizing the tower using three different strategies. In all strategies, 20 years fatigue life and global buckling in selected 50-year conditions were considered, while a 15° pitch angle constraint was applied on the platform.

In T1, the tower and platform were optimized in an integrated fashion, as described in previous sections. The same procedure was used in T2, but here, the tower was constrained to a linearly tapered shape. Finally, T3 considered a procedure where only the tower was optimized with a linearly tapered shape using a fixed platform design, taken as the optimal design from T1. The main consequence is then that the tower base diameter is fixed in the optimization, such that it matches the platform. The resulting optimized tower designs are shown in Fig. 4.12.

The resulting normalized tower and platform costs are shown in Table 4.2. The consequence of constraining the tower shape depends on the optimiz-

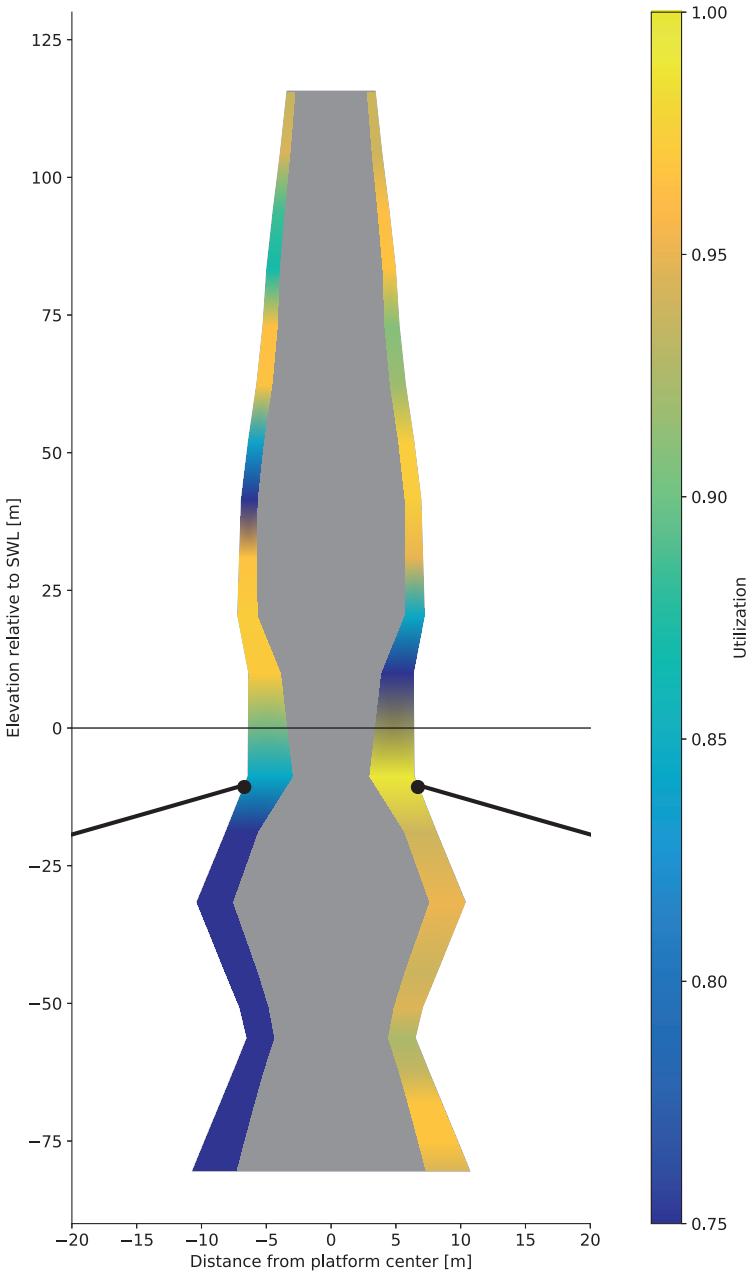

Figure 4.11: Optimized tower and platform design with fatigue utilization (left) and buckling utilization (right). The wall thickness is scaled by a factor of 40 relative to the diameter for illustration purposes.

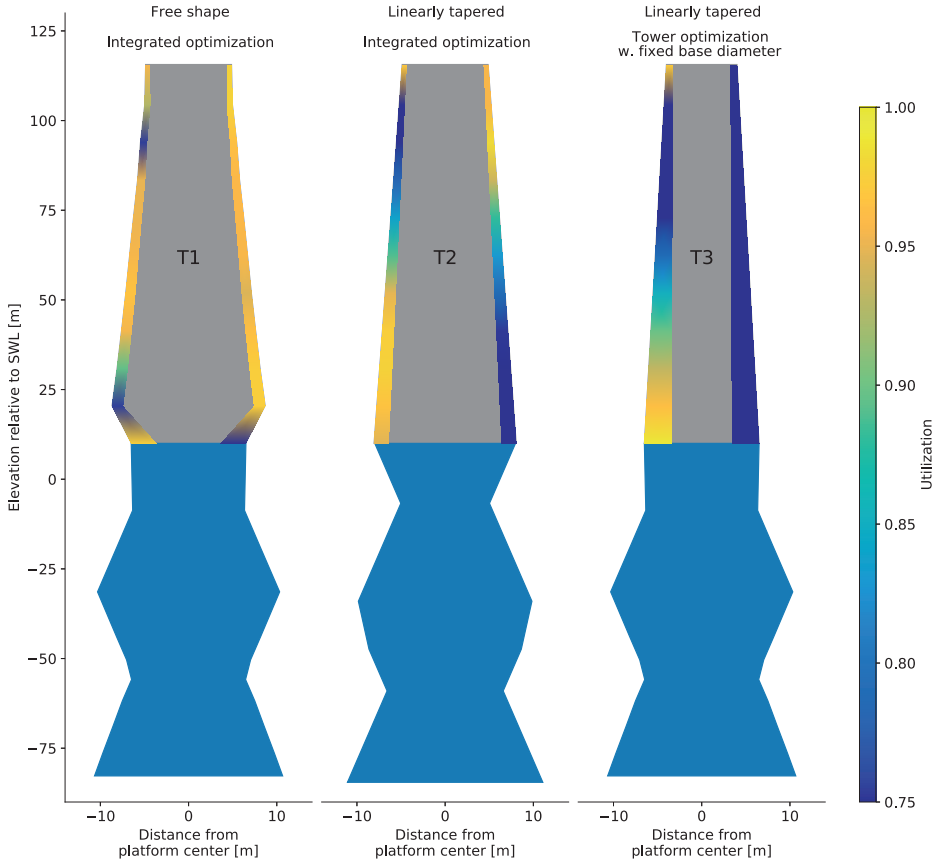

Figure 4.12: Optimized tower designs using three different design strategies, with fatigue utilization (left) and buckling utilization (right). The wall thickness is scaled by a factor of 40 relative to the diameter for illustration purposes.

Table 4.2: Normalized platform and tower costs using different design strategies.

Design	Tower cost	Platform cost	Total cost
T1	1.00	1.00	1.00
T2	1.00	1.03	1.02
T3	1.29	1.00	1.11

ation strategy. In the event of an integrated optimization (T2), the tower base diameter is significantly increased to maintain a cost-effective fatigue design, which actually results in a tower with equal costs as the T1 design. However, a consequence of the increased base diameter is an increase in wave loads, which requires a more expensive platform design to satisfy the 15° pitch criterion. For the tower optimized with a fixed platform design (T3), a large wall thickness is needed to satisfy the fatigue criterion at the base, which results in an inefficient tower design with almost 30 % increase in costs.

From the results in Figs. 4.11 and 4.12, the presented optimization methodology is seen to result in support structure designs which are close to fully utilized with respect to fatigue over a large part of the length, which minimizes the design costs within the applied constraints. However, this affects the fatigue reliability of the total support structure, as discussed in **P5**. The reliability index after 20 years of operation for support structures optimized with different design fatigue factors (DFFs) is shown in Fig. 4.13(a). Here, the names of the designs indicate the DFF used for the tower, while values twice as high were applied for the platform due to more difficult inspection access. As expected, relatively constant reliability levels are observed along the tower length.

For structures where a single component (i.e. potential fatigue crack location) dominates the failure probability, system effects for the reliability can be neglected. However, the almost constant fatigue reliability along the length of the optimized FWT structures means that system reliability must be considered. The support structure of a spar FWT can be modelled as a series system, where failure in one of the components results in failure of the whole structure.

The importance of system effects on the resulting reliability is illustrated in Fig. 4.13(b), where the system reliability index after 20 years of operation is shown with different number of components included in the system reliability calculations. For systems with less than 12 components, the most

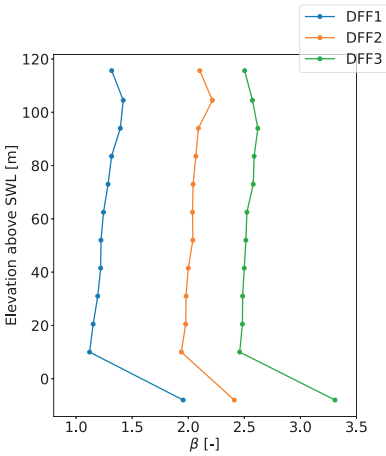

(a) Reliability as a function of support structure location.

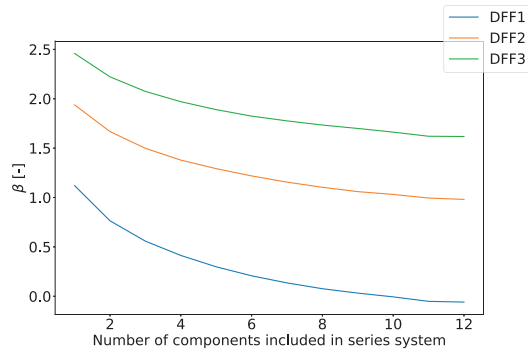

(b) System reliability as a function of components included in the series system.

Figure 4.13: Reliability index after 20 years service life.

critical ones, based on the results in Fig. 4.13(a), were included.

The importance of system effects depended on the correlation between the components. A common assumption is to use independent fatigue strength in different components, while the loads are taken as fully correlated. This assumption, using typical values from the literature, resulted in relatively low correlation values between the components.

A large reduction in reliability is observed in Fig. 4.13(b) as the number of components increases, due to the consistent failure probabilities and low correlation between the components. Based on the results presented here, the fatigue safety factor needs to be doubled for a system with eight fatigue-critical components to achieve the same reliability after 20 years as a support structure with a single critical component.

These effects must be appropriately considered in design, which can be done in a simple manner by increasing the required DFF along the entire support structure, and optimizing the structural design with consistent probabilities of failure in a large number of components. However, the system effects observed here suggest that more cost-effective designs might be achieved if less steel-intensive components are designed with longer fatigue life (or larger DFF), in order to reduce the system effects. To derive truly optimized fatigue designs for a given safety level, inclusion of system reliability con-

siderations within the design optimization problem is required, which has not been considered in the present work.

4.2.4 Control strategies

Control of FWTs is a complex subject, and several strategies for the blade-pitch controller have been suggested in the literature. All of these control strategies result in trade-offs between structural loads, rotor speed variation, and blade pitch actuator use, which vary with different environmental conditions, and identifying optimal control parameters is a challenging task. Also, due to the strong interactions, simultaneous design of the controller and support structure should be performed to have a fair comparison between different strategies. To properly identify and compare optimal solutions, the integrated control and structural designs should be evaluated over the lifetime of the system, considering actual design limits.

To illustrate the trade-offs between rotor speed variation, blade-pitch actuator use, and structural loads in the tower, the effect of the blade-pitch controller PI gains on the linearized system response is shown in Fig. 4.14 for a given support structure design. To evaluate blade-pitch actuator use, the actuator duty cycle (ADC), defined as the total number of degrees pitched divided by the total simulation time, is used. Here, the ADC values are also normalized by the maximum allowable blade pitch rate for the turbine, which for the DTU 10 MW is equal to 10 deg/s. The contours are shown for the area where the closed-loop system is stable (i.e. no negative damping in any modes). As shown, the optimal solution for an integrated design optimization process depends heavily on the relative importance of the response parameters.

Integrated optimization of the blade-pitch controller and support structure design, considering different control strategies, were investigated in **P4**. A baseline strategy, using a gain-scheduled PI controller, was considered in addition to three different velocity feedback controllers, as described in Table 4.3. In CS4, the nacelle velocity signal was passed through a first order low-pass filter to remove the wave-frequency components before it was fed back to the blade-pitch controller. On the control side, the considered design variables were the PI gains (CS1-4), the velocity feedback gain from Eq. (3.32) (CS2-4), and the corner frequency of the low-pass filter for the velocity signal (CS4).

In addition to the controller parameters, the design optimization considered the diameter and wall thickness distribution of the tower, with constraints

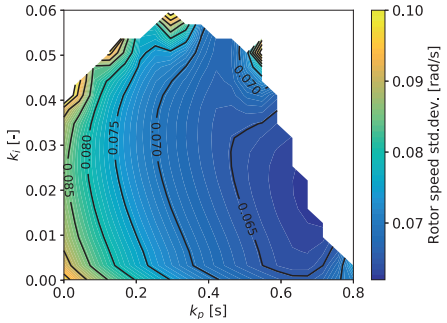

(a) Weighted average rotor speed variation.

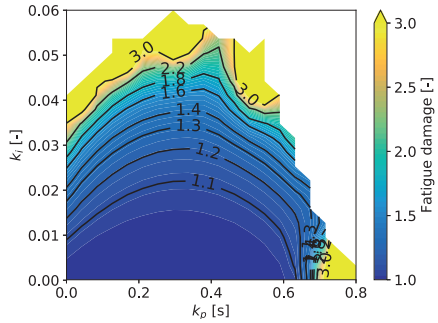

(b) Long-term tower base fatigue damage.

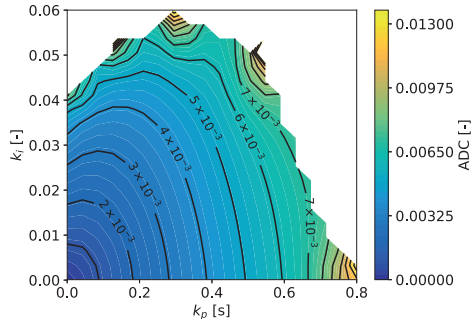

(c) Weighted average ADC.

Figure 4.14: Response parameters as functions of PI controller gains.

Table 4.3: Considered strategies for blade-pitch controller.

Strategy	Description
CS1	PI controller
CS2	PI controller + platform pitch velocity feedback
CS3	PI controller + nacelle velocity feedback
CS4	PI controller + nacelle velocity feedback + low-pass filter

on long-term fatigue and global buckling. Because the structural design of the platform was found to mostly be driven by hydrostatic buckling loads unaffected by the controller, the study considered only the geometry of the platform through the draft and diameter distribution, while the wall thickness was assumed fixed. This procedure thus neglected the potential cost savings from reduced wall thickness in the uppermost part of the hull, where fatigue loads were more critical.

The optimization aimed to minimize the costs of the support structure, while constraints on the rotor speed standard deviation and actuator duty cycle (ADC) were included to ensure a certain rotor speed tracking and pitch actuator fatigue performance. As appropriate values for these constraints are difficult to quantify, values based on simulations with an onshore DTU 10 MW turbine were used.

The velocity feedback controllers increased the aerodynamic damping and thus reduced the response around the pitch natural frequency. This led to a decrease in fatigue loads, which were the design-driving constraint for the tower. For all four design strategies, a 50-year storm condition with parked turbine was found to be the critical load case for the extreme responses, and the ULS design was therefore not affected by the controller.

The optimized costs of the tower, platform, and tower plus platform for CS2-4 are shown in Fig. 4.15(a), compared to the costs for the optimized CS1. The majority of the cost reductions came from the tower, due to the improved fatigue behaviour, whereas the platform was less affected due to the fixed costs related to the 15° pitch angle constraint. However, because a lighter tower resulted in a lower overall center of gravity, the platform pitch response was somewhat improved, and a small reduction in platform costs of about 2 % was also achieved. Because the platform accounted for 70-75 % of the total costs for the considered designs, the resulting total cost reduction was approximately 6 %.

The rotor speed standard deviations and ADCs, normalized by their maximum allowable values, are shown in Fig. 4.15(b). For each control strategy, there exists a limit where no further reduction in cost can be achieved by increasing the actuator use, as seen from Fig. 4.14. This limit is higher for the velocity feedback controllers than for a controller using only the rotor speed error as input, which caused the ADC constraint to be inactive at the optimum for CS1. For the rotor speed variation, better performance was achieved with CS4 than with the other control strategies. Since there is a trade-off between rotor speed variation and structural loads (and thus costs)

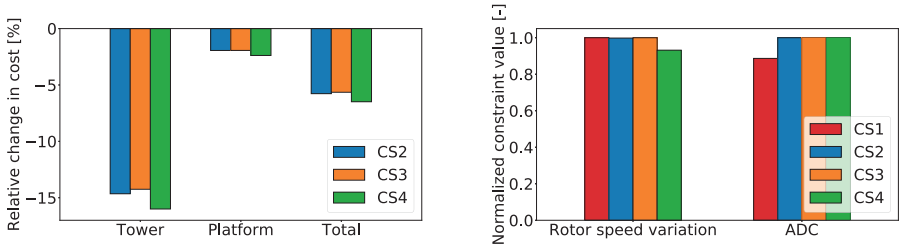

(a) Costs relative to CS1. **(b)** Rotor speed variation and ADC values.

Figure 4.15: Objective and constraint function values for optimized designs.

as previously discussed, it is expected that larger cost reductions could be achieved with CS4 if the rotor speed constraint is tightened.

Verification against nonlinear simulations in SIMA showed that the tower base fatigue damage was significantly overestimated for CS1, whereas good agreement was obtained with the other control strategies. The reason for the poor agreement was that the resulting aerodynamic damping for the platform pitch mode was much lower with this control strategy. Consequently, the resonant pitch response became very sensitive to the presence and amount of additional damping in the system, which was either not considered or underpredicted in the linear model. The overestimation of fatigue damage suggests that the cost reductions in Fig. 4.15(a) are highly optimistic, and that CS1 may yield a fatigue design similar to that with a nacelle velocity feedback controller. It also suggests that future optimization studies using the linearized model from the present work should consider more advanced control strategies than CS1, to limit the pitch response error.

4.3 Environmental modelling

Due to lack of site-specific data, or to limit the computational effort during the design process, conservative assumptions about the environmental loads are often used. The impact of different environmental modelling uncertainties on the fatigue reliability and associated design costs was assessed in **P5**, using an environmental model based on hindcast data from a realistic floating wind park site. In addition to the base case, four different environmental models were considered:

- Stochastic turbulence intensity described by the Weibull distribution from IEC (2005), rather than the 90 % design value.
- Inclusion of the wind directional distribution.

- Inclusion of the relative wind-wave direction distribution.

- A two-peak wave spectrum to account for swell.

The resulting equivalent fatigue factors with the different environmental models, based on Monte Carlo simulations on the linearized FWT model, are presented in Fig. 4.16(a). Here, the equivalent fatigue factor is defined as the maximum expected 20-year fatigue damage around the circumference, normalized by the base case results. The factors are shown for the fatigue-critical parts of the support structure, which consisted of the tower and upper part of the platform. For depths below approximately 10 m, shell buckling became the design driving constraint, and the differences in fatigue loads did not affect the design process.

The effect of turbulence and wind-wave misalignment varied significantly along the length of the structure due to differences in the relative importance of wind and wave response. The tower top response, which was almost exclusively governed by wind loads, was much more affected by the turbulence modelling than the tower base, and vice versa for the wind-wave misalignment. This also resulted in some location-dependent effects when the wind directional distribution was included. The inclusion of swell through a two-peaked wave spectrum had small impact on the fatigue reliability for the considered support structure.

Applying all the aforementioned environmental model uncertainties resulted in an almost constant reduction in fatigue damage of about 65 % along the length of the tower and upper part of the platform. This indicates that an additional safety factor on fatigue of about three is implicitly applied when these model uncertainties are neglected in the design process for such FWT structures.

Reductions in support structure costs with the different environmental models were quantified through re-design of the support structure, using a numerical optimization scheme as described in the previous sections. To account for the environmental modelling effects in the design optimization procedure, the equivalent fatigue factors from Fig. 4.16(a) were included in the applied fatigue safety factors along the tower and platform. The resulting cost reductions are shown in Fig. 4.16(b), where total cost reductions in the order of 5-11 % is observed. These numbers are only indicative, and depend on the platform concept, considered design constraints, and the metocean conditions at the actual wind park site.

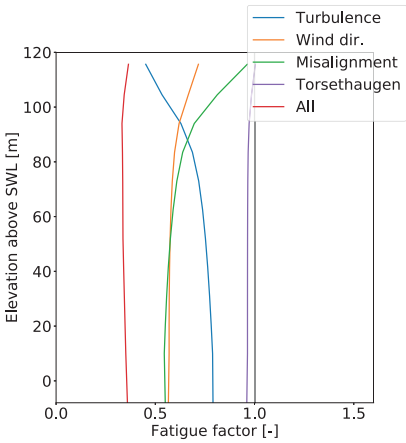

(a) Equivalent fatigue factors.

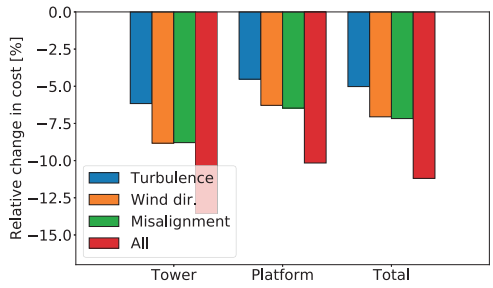

(b) Comparison of support structure costs for optimized designs.

Figure 4.16: Effect of environmental modelling on long-term fatigue and design costs.

4.4 Inspection schedule

This section considers derivation of cost-optimal DFFs, including costs related to construction and inspections during the operational lifetime. The required fatigue crack inspection interval for a FWT depends on the applied DFF, which results in trade-offs between CAPEX and OPEX. To minimize the cost of energy, the DFF resulting in the lowest lifetime costs should be applied. This issue was investigated in **P5**, based on probabilistic fracture mechanics and reliability updating using Bayes theorem. The study was performed with the three different set of DFFs described in Section 4.2.3. To evaluate lifetime costs of the considered designs, necessary inspection intervals with DFF1 and DFF2 to achieve the same reliability as DFF3 without inspections at the end of the service life were identified. The inspections were assumed to occur with fixed intervals for each design.

Figure 4.17(a) shows the accumulated reliability index over the service life of the system, assuming inspections with no detection of cracks every two and five years for DFF1 and DFF2, respectively. This corresponds to a total of nine and three inspections during the lifetime of the structure, which resulted in reliability indices within 5 % of DFF3 without inspections after 20 years.

Based on the results in Fig. 4.17(a), trade-offs between CAPEX and OPEX were derived. In Fig. 4.17(b), the lifetime costs are shown for different

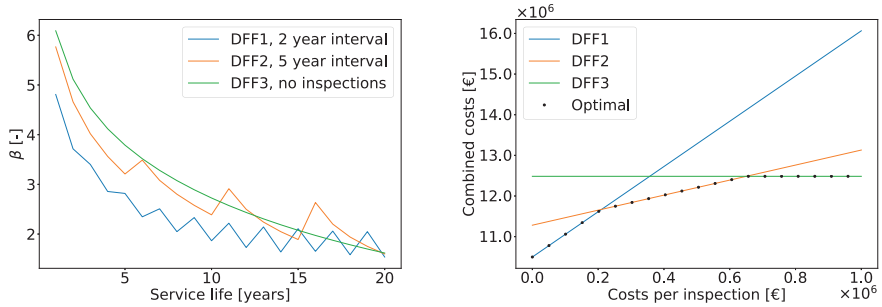

(a) System reliability index during service life, including the effect of inspections.

(b) Combined design and inspection costs comparison, r=0.05.

Figure 4.17: Reliability and total costs with different DFFs and inspection schedules.

values of the inspection costs, assuming a real interest rate of 5 %. In this particular case, DFF1 was the most cost-effective solution for costs per inspection lower than 210 000 € while DFF3 was the cost-optimal design for costs of more than 650 000 € per inspection. This corresponded to about 2 % and 6 % of the support structure costs with DFF1, respectively.

In the present work, higher DFFs were achieved by increasing the structural dimensions. The fatigue life could also be extended by reducing the SCF, which may be a more cost-effective option. However, the cost of improved fabrication tolerances or detail geometry is highly uncertain, and SCF reduction was therefore not considered.

Chapter 5

Conclusions and Recommendations for Future Work

This chapter summarizes the contributions of this thesis to the research community. Suggestions for future studies are also made, based on limitations identified in the current work.

5.1 Conclusions

This thesis has sought to improve the design process for FWTs through the development of efficient methods for global dynamic response analyses, and numerical design optimization techniques. The main focus has been on the support structure for 10 MW spar-type turbines, considering fatigue and ultimate loads. Some attention has also been given to the blade-pitch controller and mooring system, particularly related to coupling effects with the support structure.

A linearized aero-hydro-servo-elastic model with four structural DOFs was shown to yield acceptable accuracy for the support structure response with co-directional wind and waves. Nonlinear effects resulted in poor performance of the linearized model when the tower bending natural frequency was close to the 3P range. Some overestimation was also observed for the resonant platform pitch response, which caused the model to be conservative in general compared to nonlinear analyses. Analytical frequency-dependent aerodynamic damping and inertia coefficients were derived, which removed

the underestimation of the low-frequency response observed with constant damping coefficients.

A gradient-based optimization approach with analytic derivatives was used to perform integrated design optimization of the support structure, blade-pitch controller, and mooring system for a 10 MW spar FWT, including the scantling design of the hull, where the goal was to minimize the system costs and rotor speed variation. An hour-glass shape was found to be favourable for the platform below the wave zone, as it increased the effective rotational stiffness of the system and improved the low-frequency behaviour in pitch. The inclusion of structural hull design ensured a realistic distribution of material and proper penalization of designs with large drafts. Due to compliance with the platform, the tower took an unconventional shape, where the diameter increased from the base. Integrated optimization is needed to identify the optimal solution near the interface.

The optimized support structure was fully utilized with respect to fatigue along most of the tower length, as well as in the uppermost part of the platform. Below approximately 10 m below the SWL, shell buckling became design-driving due to the large hydrostatic pressure. The consistently high fatigue utilization in the upper part of the structure led to important system effects for the total fatigue reliability. By considering the support structure as a series system, an additional fatigue safety factor of two was needed for a system with eight fatigue-critical welds, to achieve the same reliability after 20 years as a single critical component. System effects may thus be important for cost-optimal designs with a given target safety level.

Trade-offs between rotor speed tracking, blade-pitch actuator use, and structural loads make controller design a challenging task, and due to important interaction effects, simultaneous design of the controller and support structure should be preferably be performed. The blade-pitch controller affected the fatigue loads in the tower and upper part of the platform due to damping of the resonant pitch response; however, because the critical extreme responses occurred in either below-rated or parked conditions, no effect was observed on the ULS design. Different control strategies were compared through integrated design optimization with constraints on rotor speed variation and blade-pitch actuator use. While appropriate values for these constraints are difficult to quantify, the methodology allowed for identification of optimal control parameters in a lifetime perspective, and fair comparison between different solutions.

Uncertainties in environmental input parameters used in global design ana-

lyses are often chosen based on conservative assumptions. The impact of these assumptions on the long-term fatigue reliability and associated costs of the support structure was assessed using Monte Carlo simulations and re-design of the tower and platform based on derived fatigue factors. Wind-wave misalignment, wind directionality, and stochastic turbulence intensity were all shown to have non-negligible effect on the long-term fatigue damage. The inclusion of all three resulted in an almost constant reduction in fatigue along the support structure length of about two-thirds, suggesting that an additional safety factor of three is inherent in the fatigue design when these effects are neglected.

5.2 Recommendations for future work

Based on the studies conducted in **P1-5**, the following suggestions are made for future work:

- *Alternative platform concepts:*
  The developed numerical design optimization methodology is only applicable for spar platforms, which imposes serious limitations on the design space for the floater. A more general description of the platform geometry would allow the optimizer to explore other parts of the design space, and possibly identify non-intuitive and more cost-effective solutions. This requires a numerical panel method for the hydrodynamic loads, with the support of gradient calculations. For structural optimization of a general platform shape, a more sophisticated finite element model, using e.g. shell elements, may be needed.

- *Nonlinear and transient events:*
  The linearized dynamic model developed in the present work cannot be used to analyse transient or highly nonlinear events. Because such conditions may be design-driving for certain parts of the system, it is recommended to focus on computationally efficient methods to include them in the design optimization process.

- *Improved cost models:*
  The optimal design from a numerical optimization process depends on the cost models. While material costs can be calculated in a straightforward manner, there are large uncertainties related to manufacturing, installation, maintenance, and decommissioning costs. If more reliable engineering cost models can be established, based on the actual lifetime costs of the system, this may have a large effect on the resulting cost-optimal designs.

- *Mooring system and power cable representation:*
  A more detailed description of the mooring system, including bridle lines, varying cross sections, and discrete components such as clump weights and buoys, would enable more complete and realistic optimization of the mooring design. Together with wind and wave directionality, such procedures could also consider the layout of the mooring system. A model describing the power cable dynamics would allow for simultaneous design optimization of the cable, including explicit constraints on the curvature.

- *Blade and drivetrain response:*
  A fully integrated FWT design optimization procedure must also consider simultaneous design of the rotor. This requires more detailed structural and aerodynamic models to accurately capture the blade and drivetrain response, as well as appropriate cost models and constraints for these subsystems.

- *Reliability-based design optimization:*
  FWTs are subjected to a stochastic environment, and uncertainties in loads and response are typically considered through partial safety factors. The design conservatism could be reduced through the application of probabilistic design, where the structure is optimized to minimize the cost for a given target probability of failure.

- *Farm-level design optimization:*
  Similarly to an integrated design optimization approach on the turbine level, design optimization considering farm-level effects could affect and improve the overall system behaviour. Important considerations include wake effects, total wind farm costs, system reliability effects, and possibly shared mooring lines or anchors.

Bibliography

N. Aggarwal, R. Manikandan, and N. Saha. Nonlinear short term extreme response of spar type floating offshore wind turbines. *Ocean Engineering*, 130:199–209, 2017. doi: 10.1016/j.oceaneng.2016.11.062.

T. Ashuri, M. B. Zaaijer, J. R. R. A. Martins, G. J. W. van Bussel, and G. A. M. van Kuik. Multidisciplinary design optimization of offshore wind turbines for minimum levelized cost of energy. *Renewable Energy*, 68:893–905, 2014. doi: 10.1016/j.renene.2014.02.045.

J. Azcona, D. Palacio, X. Munduate, L. González, and T. A. Nygaard. Impact of mooring lines dynamics on the fatigue and ultimate loads of three offshore floating wind turbines computed with IEC 61400-3 guideline. *Wind Energy*, 20:797–813, 2017. doi: 10.1002/we.2064.

E. E. Bachynski. *Design and dynamic analysis of tension leg platform wind turbines*. PhD thesis, Norwegian University of Science and Technology, 2014.

E. E. Bachynski and T. Moan. Linear and nonlinear analysis of tension leg platform wind turbines. In *Proceedings of the Twenty-second (2012) International Offshore and Polar Engineering Conference (ISOPE2012), Rhodes, Greece*, 2012.

E. E. Bachynski and T. Moan. Ringing loads on tension leg platform wind turbines. *Ocean Engineering*, 84:237–248, 2014. doi: 10.1016/j.oceaneng.2014.04.007.

E. E. Bachynski, M. Etemaddar, M. I. Kvittem, C. Luan, and T. Moan. Dynamic analysis of floating wind turbines during pitch actuator fault,

grid loss, and shutdown. *Energy Procedia*, 35:210–222, 2013. doi: 10.1016/j.egypro.2013.07.174.

E. E. Bachynski, M. I. Kvittem, C. Luan, and T. Moan. Wind-wave misalignment effects on floating wind turbines: motions and tower load effects. *Journal of Offshore Mechanics and Arctic Engineering*, 136, 2014. doi: 10.1115/1.4028028.

E. E. Bachynski, M. Thys, T. Sauder, V. Chabaud, and L. O. Sæther. Real-time hybrid model tests of a braceless semi-submersible wind turbine. Part II: experimental results. In *Proceedings of the ASME 2016 35th International Conference on Ocean, Offshore and Arctic Engineering (OMAE2016), Busan, South Korea*, 2016. doi: 10.1115/OMAE2016-54437.

C. Bak, F. Zahle, R. Bitsche, A. Yde, L. C. Henriksen, A. Natarajan, and M. H. Hansen. Description of the DTU 10 MW reference wind turbine. Technical Report DTU Wind Energy Report-I-0092, DTU Wind Energy, 2013.

J. G. Balchen, T. Andresen, and B. A. Foss. *Reguleringsteknikk [Control Engineering] (in Norwegian)*. Institutt for teknisk kybernetikk, NTNU, 2003.

L. Barj, S. Stewart, G. M. Stewart, M. Lackner, J. Jonkman, A. Robertson, and D. Matha. Wind/wave misalignment in the loads analysis of a floating offshore wind turbine. In *32nd ASME Wind Energy Symposium, National Harbor, Maryland*, 2014. doi: 10.2514/6.2014-0363.

I. Bayati, M. Belloli, and A. Facchinetti. Wind tunnel 2-DOF hybrid/HIL tests on the OC5 floating offshore wind turbine. In *Proceedings of the ASME 2017 36th International Conference on Ocean, Offshore and Arctic Engineering (OMAE2017), Trondheim, Norway*, 2017.

I. Bayati, A. Facchinetti, A. Fontanella, and M. Belloli. 6-DOF hydrodynamic modelling for wind tunnel hybrid/HIL tests of FOWT: the real-time challenge. In *Proceedings of the ASME 2018 37th International Conference on Ocean, Offshore and Arctic Engineering (OMAE2018), Madrid, Spain*, 2018. doi: 10.1115/OMAE2018-77804.

D. Benasciutti and R. Tovo. Spectral methods for lifetime prediction under wide-band stationary random processes. *International Journal of Fatigue*, 27:867–877, 2005. doi: 10.1016/j.ijfatigue.2004.10.007.

G. Benassai, A. Campanile, V. Piscopo, and A. Scamardella. Ultimate and accidental limit state design for mooring systems of floating offshore wind turbines. *Ocean Engineering*, 92:64–74, 2014. doi: 10.1016/j.oceaneng.2014.09.036.

P. A. Berthelsen, E. E. Bachynski, M. Karimirad, and M. Thys. Real-time hybrid model tests of a braceless semi-submersible wind turbine. Part III: calibration of a numerical model. In *Proceedings of the ASME 2016 35th International Conference on Ocean, Offshore and Arctic Engineering (OMAE2016), Busan, South Korea*, 2016. doi: 10.1115/OMAE2016-54640.

L. E. Borgman. Ocean wave simulation for engineering design. *Journal of the Waterways and Harbors Division*, 95(4):557–586, 1969.

S. Boyd and L. Vandenberghe. *Convex Optimization*. Cambridge University Press, 2004.

M. Brommundt, L. Krause, K. Merz, and M. Muskulus. Mooring system optimization for floating wind turbines using frequency domain analysis. *Energy Procedia*, 24:289–296, 2012. doi: 10.1016/j.egypro.2012.06.111.

M. L. Buhl. A new empirical relationship between thrust coefficient and induction factor for the turbulent windmill state. Technical Report NREL/TP-500-36834, National Renewable Energy Laboratory, 2005.

T. Burton, N. Jenkins, D. Sharpe, and E. Bossanyi. *Wind energy handbook*. Wiley, second edition, 2011.

P. K. Chaviaropoulos, A. Natarajan, and P. H. Jensen. Key performance indicators and target values for multi-megawatt offshore turbines. In *Proceedings of European Wind Energy Association Conference and Exhibition 2014 (EWEA 2014)*, 2014.

C.-T. Chen. *Linear system theory and design*. Oxford University Press, fourth edition, 2013.

K. H. Chew, K. Tai, E. Y. K. Ng, and M. Muskulus. Analytical gradient-based optimization of offshore wind turbine substructures under fatigue and extreme loads. *Marine Structures*, 47:23–41, 2016. doi: 10.1016/j.marstruc.2016.03.002.

G. F. Clauss and L. Birk. Hydrodynamic shape optimization of large offshore structures. *Applied Ocean Research*, 18(4):157–171, 1996. doi: 10.1016/S0141-1187(96)00028-4.

T. Dirlik. *Application of computers in fatigue analysis*. PhD thesis, University of Warwick, 1985.

DNV GL. Loads and site conditions for wind turbines. Technical Report DNVGL-ST-0437, DNV GL, 2016.

DNV GL. Modelling and analysis of marine operations. Technical Report DNVGL-RP-N103, DNV GL, 2017.

DNV GL. Floating wind turbine structures. Technical Report DNVGL-ST-0119, DNV GL, 2018a.

DNV GL. Support structures for wind turbines. Technical Report DNVGL-ST-0126, DNV GL, 2018b.

DNV GL. Environmental conditions and environmental loads. Technical Report DNVGL-RP-C205, DNV GL, 2019a.

DNV GL. Buckling Strength of Shells. Technical Report DNVGL-RP-C202, DNV GL, 2019b.

DNV GL. Fatigue design of offshore steel structures. Technical Report DNVGL-RP-C203, DNV GL, 2019c.

T. Duarte, A. J. Sarmento, and J. Jonkman. Effects of second-order hydrodynamic forces on floating offshore wind turbines. In *32nd ASME Wind Energy Symposium, National Harbor, Maryland*, 2014. doi: 10.2514/6.2014-0361.

O. M. Faltinsen. *Sea loads on ships and offshore structures*. Cambridge University Press, 1990.

J. Farkas and K. Jármai. *Optimum design of steel structures*. Springer, 2013.

T. Fischer, P. Rainey, E. Bossanyi, and M. Kühn. Study on control concepts suitable for mitigation of loads from misaligned wind and waves on offshore wind turbines supported on monopiles. *Wind Engineering*, 35(5): 561–574, 2011. doi: 10.1260/0309-524X.35.5.561.

P. A. Fleming, I. Pineda, M. Rossetti, A. D. Wright, and D. Arora. Evaluating methods for control of an offshore floating turbine. In *Proceedings of the ASME 2014 33rd International Conference on Ocean, Offshore and Arctic Engineering (OMAE2014), San Francisco, California, USA*, 2014. doi: 10.1115/OMAE2014-24107.

P. A. Fleming, A. Peiffer, and D. Schlipf. Wind turbine controller to mitigate structural loads on a floating wind turbine platform. *Journal of Offshore Mechanics and Arctic Engineering*, 141, 2019. doi: 10.1115/1.4042938.

I. Fylling and P. A. Berthelsen. WINDOPT- an optimization tool for floating support structures for deep water wind turbines. In *Proceedings of the ASME 2011 30th International Conference on Ocean, Offshore and Arctic Engineering (OMAE2011), Rotterdam, The Netherlands*, 2011. doi: 10.1115/OMAE2011-49985.

Z. Gao and T. Moan. Frequency-domain fatigue analysis of wide-band stationary Gaussian processes using a trimodal spectral formulation. *International Journal of Fatigue*, 30(10-11):1944–1955, 2008. doi: 10.1016/j.ijfatigue.2008.01.008.

A. J. Goupee, R. W. Kimball, and H. J. Dagher. Experimental observations of active blade pitch and generator control influence on floating wind turbine response. *Renewable Energy*, 104:9–19, 2017. doi: 10.1016/j.renene.2016.11.062. URL `http://dx.doi.org/10.1016/j.renene.2016.11.062`.

J. S. Gray, J. T. Hwang, J. R. R. A. Martins, K. T. Moore, and B. A. Naylor. OpenMDAO: an open-source framework for multidisciplinary design, analysis, and optimization. *Structural and Multidisciplinary Optimization*, 59:1075–1104, 2019. doi: 10.1007/s00158-019-02211-z.

A. Halfpenny. *Dynamic analysis of both on and offshore wind turbines in the frequency domain*. PhD thesis, University College London, 1998.

M. Hall, B. Buckham, and C. Crawford. Evolving offshore wind: a genetic algorithm-based support structure optimization framework for floating wind turbines. In *OCEANS 2013 MTS/IEEE Bergen: The Challenges of the Northern Dimension*, 2013. doi: 10.1109/OCEANS-Bergen.2013.6608173.

M. Hall, B. Buckham, and C. Crawford. Hydrodynamics-based floating wind turbine support platform optimization: a basis function approach. *Renewable Energy*, 66:559–569, 2014a. doi: 10.1016/j.renene.2013.12.035.

M. Hall, B. Buckham, and C. Crawford. Evaluating the importance of mooring line model fidelity in floating offshore wind turbine simulations. *Wind Energy*, 17:1835–1853, 2014b. doi: 10.1002/we.1669.

H. A. Haslum and O. M. Faltinsen. Alternative shape of spar platforms for use in hostile areas. In *Offshore Technology Conference*, 1999. doi: 10.4043/10953-ms.

J.-T. Horn, J. R. Krokstad, and B. J. Leira. Impact of model uncertainties on the fatigue reliability of offshore wind turbines. *Marine Structures*, 64: 174–185, 2019. doi: 10.1016/j.marstruc.2018.11.004.

IEA. Offshore wind outlook 2019. Technical report, International Energy Agency, 2019.

IEC. Wind turbines - part 1: design requirements. Technical Report IEC 61400-1, International Electrotechnical Commission, 2005.

IEC. Wind turbines - part 3: design requirements for offshore wind turbines. Technical Report IEC 61400-3, International Electrotechnical Commission, 2009.

K. Johannessen, T. S. Meling, and S. Haver. Joint Distribution for Wind and Waves in the Northern North Sea. *International Journal of Offshore and Polar Engineering*, 12(1):1–8, 2002.

N. Johnson, J. Jonkman, A. Wright, G. Hayman, and A. Robertson. Verification of floating offshore wind linearization functionality in OpenFAST. *Journal of Physics: Conference Series*, 1356, 2019. doi: 10.1088/1742-6596/1356/1/012022.

J. Jonkman. Influence of control on the pitch damping of a floating wind turbine. In *46th AIAA Aerospace Science Meeting and Exhibit, Reno, Nevada*, 2008. doi: 10.2514/6.2008-1306.

J. Jonkman and W. Musial. Offshore code comparison collaboration (OC3) for IEA task 23 offshore wind technology and deployment. Technical Report NREL/TP-5000-48191, National Renewable Energy Laboratory, 2010.

J. Jonkman, S. Butterfield, W. Musial, and G. Scott. Definition of a 5-MW reference wind turbine for offshore system development. Technical Report NREL/TP-500-38060, National Renewable Energy Laboratory, 2009.

J. M. Jonkman, A. D. Wright, G. J. Hayman, and A. N. Robertson. Full-system linearization for floating offshore wind turbines in OpenFAST. In *Proceedings of the ASME 2018 1st International Offshore Wind Technical Conference (IOWTC2018), San Francisco, California, USA*, 2018. doi: 10.1115/IOWTC2018-1025.

A. M. P. Jurado, M. Borg, and H. Bredmose. An efficient frequency-domain model for quick load analysis of floating offshore wind turbines. *Wind Energy Science*, 3(2):693–712, 2018. doi: 10.5194/wes-3-693-2018.

M. Karimi, M. Hall, B. Buckham, and C. Crawford. A multi-objective design optimization approach for floating offshore wind turbine support structures. *Journal of Ocean Engineering and Marine Energy*, 3(1):69–87, 2017. doi: 10.1007/s40722-016-0072-4.

M. Karimirad and T. Moan. Extreme dynamic structural response analysis of catenary moored spar wind turbine in harsh environmental conditions. *Journal of Offshore Mechanics and Arctic Engineering*, 133, 2011. doi: 10.1115/1.4003393.

G. Katsouris and A. Marina. Cost modelling of floating wind farms. Technical Report ECN-E–15- 078, ECN, 2016.

J. M. Kluger, T. P. Sapsis, and A. H. Slocum. A reduced-order, statistical linearization approach for estimating nonlinear floating wind turbine response statistics. In *Proceedings of the Twenty-sixth (2016) International Ocean and Polar Engineering Conference (ISOPE2016), Rhodes, Greece*, 2016.

B. J. Koo, M. H. Kim, and R. E. Randall. Mathieu instability of a spar platform with mooring and risers. *Ocean Engineering*, 31:2175–2208, 2004. doi: 10.1016/j.oceaneng.2004.04.005.

M. I. Kvittem and T. Moan. Frequency versus time domain fatigue analysis of a semisubmersible wind turbine tower. *Journal of Offshore Mechanics and Arctic Engineering*, 137, 2014. doi: 10.1115/1.4028340.

M. Lackner. Controlling platform motions and reducing blade loads for floating wind turbines. *Wind Engineering*, 33(6):541–553, 2009. doi: 10.1260/0309-524X.33.6.541.

A. B. Lambe and J. R. R. A. Martins. Extensions to the design structure matrix for the description of multidisciplinary design, analysis, and optimization processes. *Structural and Multidisciplinary Optimization*, 46: 273–284, 2012. doi: 10.1007/s00158-012-0763-y.

K. Larsen and P. C. Sandvik. Efficient methods for the calculation of dynamic mooring line tension. In *Proceedings of the First (1990) European Offshore Mechanics Symposium, Trondheim, Norway*, 1990.

T. J. Larsen and T. D. Hanson. A method to avoid negative damped low frequent tower vibrations for a floating, pitch controlled wind turbine. *Journal of Physics: Conference Series*, 75:012073, 2007. doi: 10.1088/1742-6596/75/1/012073.

C. F. Lee, E. E. Bachynski, and A. R. Nejad. Consequences of Load Mitigation Control Strategies for a Floating Wind Turbine. *Journal of Physics: Conference Series*, 2020.

M. Leimeister, A. Kolios, and M. Collu. Critical review of floating support structures for offshore wind farm deployment. *Journal of Physics: Conference Series*, 1104, 2018.

M. Leimeister, A. Kolios, M. Collu, and P. Thomas. Design optimization of the OC3 phase IV floating spar-buoy, based on global limit states. *Ocean Engineering*, 202, 2020. doi: 10.1016/j.oceaneng.2020.107186.

F. Lemmer, K. Müller, W. Yu, D. Schlipf, and P. W. Cheng. Optimization of floating offshore wind turbine platforms with a self-tuning controller. In *Proceedings of the ASME 2017 36th International Conference on Ocean, Offshore and Arctic Engineering (OMAE2017), Trondheim, Norway*, 2017. doi: 10.1115/OMAE2017-62038.

H. Lie and N. Sødahl. Simplified dynamic model for estimation of extreme anchor line tension. In *Offshore Australia, The 2nd Australian Oil, Gas & Petrochemical Exhibition and Conference, Melbourne, Australia*, 1993.

R. C. MacCamy and R. A. Fuchs. Wave forces on piles: a diffraction theory. Technical Report Technical Memorandum 69, Beach Erosion Board; Corps of Engineers, 1954.

H. O. Madsen, S. Krenk, and N. C. Lind. *Methods of structural safety*. Prentice-Hall, 1986.

H. O. Madsen, J. D. Sørensen, and R. Olesen. Optimal inspection planning for fatigue damage of offshore structures. In *Proceedings of ICOSSAR'89, the 5th International Conference on Structural Safety and Reliability, San Francisco, USA*, 1989.

J. F. Manwell, J. G. McGowan, and A. L. Rogers. *Wind energy explained*. Wiley, second edition, 2009.

S. Márquez-Domínguez and J. D. Sørensen. Fatigue reliability and calibration of fatigue design factors for offshore wind turbines. *Energies*, 5: 1816–1834, 2012. ISSN 19961073. doi: 10.3390/en5061816.

J. R. R. A. Martins. Perspectives on aerodynamic design optimization. In *AIAA Scitech 2020 Forum, Orlando, FL*, 2020. doi: 10.2514/6.2020-0043.

J. R. R. A. Martins and A. Ning. *Engineering design optimization*. Unpublished draft, 2020.

D. Matha, F. Sandner, C. Molins, A. Campos, and P. W. Cheng. Efficient preliminary floating offshore wind turbine design and testing methodologies and application to a concrete spar design. *Philosophical Transactions of the Royal Society A*, 373(20140350), 2015. doi: 10.1098/rsta.2014.0350.

K. Merz. A linear state-space model of an offshore wind turbine, implemented in the STAS wind power plant analysis program. Technical Report TR A7474, SINTEF Energy Research, 2015.

P. J. Moriarty and A. C. Hansen. AeroDyn theory manual. Technical Report NREL/TP-500-36881, National Renewable Energy Laboratory, 2005.

K. Müller, D. Matha, S. Tiedemann, R. Proskovics, and F. Lemmer. LIFES50+ D7.5: guidance on platform and mooring line selection, installation and marine operations. Technical report, University of Stuttgart, 2016.

K. Müller, F. Lemmer, and W. Yu. LIFES50+ D4.2: public definition of the two LIFES50+ 10MW floater concepts. Technical report, University of Stuttgart, 2018.

K. Müller, R. F. Guzmán, S. Zhou, M. Lerch, R. Proskovics, G. Pérez, I. Mendikoa, D. Matha, F. Borisade, J. Bhat, R. Scheffler, M. Thys, H. Bredmose, F. Madsen, and A. M. P. Jurado. LIFES50+ D7.11: design practice for 10MW+ FOWT suport structures. Technical report, University of Stuttgart, 2019.

W. Musial, S. Butterfield, and B. Ram. Energy from offshore wind. In *Offshore Technology Conference*, 2006. doi: 10.4043/18355-ms.

M. Muskulus. Simplified rotor load models and fatigue damage estimates for offshore wind turbines. *Philosophical Transactions of the Royal Society A*, 373(20140347), 2015. doi: 10.1098/rsta.2014.0347.

M. Muskulus and S. Schafhirt. Design optimization of wind turbine support structures - A review. *Journal of Ocean and Wind Energy*, 1(1):12–22, 2014.

A. Myhr and T. A. Nygaard. Load reductions and optimizations on tension-leg-buoy offshore wind turbine platforms. In *Proceedings of the Twenty-second (2012) International Offshore and Polar Engineering Conference (ISOPE2012), Rhodes, Greece*, 2012.

A. Naess. Technical note: on a rational approach to extreme value analysis. *Applied Ocean Research*, 6(3):173–174, 1984. doi: 10.1016/0141-1187(84)90007-5.

A. Naess and T. Moan. *Stochastic dynamics of marine structures*. Cambridge University Press, 2013.

A. R. Nejad, Z. Gao, and T. Moan. On long-term fatigue damage and reliability analysis of gears under wind loads in offshore wind turbine drivetrains. *International Journal of Fatigue*, 61:116–128, 2014. doi: 10.1016/j.ijfatigue.2013.11.023.

A. R. Nejad, E. E. Bachynski, M. I. Kvittem, C. Luan, Z. Gao, and T. Moan. Stochastic dynamic load effect and fatigue damage analysis of drivetrains in land-based and TLP, spar and semi-submersible floating wind turbines. *Marine Structures*, 42:137–153, 2015. doi: 10.1016/j.marstruc.2015.03.006.

A. R. Nejad, E. E. Bachynski, and T. Moan. Effect of axial acceleration on drivetrain responses in a spar-type floating wind turbine. *Journal of Offshore Mechanics and Arctic Engineering*, 141, 2019. doi: 10.1115/1.4041996.

J. N. Newman. *Marine hydrodynamics*. The MIT Press, 1977.

A. Ning and D. Petch. Integrated design of downwind land-based wind turbines using analytic gradients. *Wind Energy*, 19:2137–2152, 2016. doi: 10.1002/we.1972.

S. A. Ning. A simple solution method for the blade element momentum equations with guaranteed convergence. *Wind Energy*, 17(9):1327–1345, 2013. doi: 10.1002/we.1636.

J. Nocedal and S. J. Wright. *Numerical optimization*. Springer, second edition, 2006.

J. Oest, R. Sørensen, L. C. T. Overgaard, and E. Lund. Structural optimization with fatigue and ultimate limit constraints of jacket structures for large offshore wind turbines. *Structural and Multidisciplinary Optimization*, 55(3):779–793, 2017. doi: 10.1007/s00158-016-1527-x.

L. B. Pasamontes, F. G. Torres, D. Zwick, S. Schafhirt, and M. Muskulus. Support structure optimization for offshore wind Turbines with a genetic algorithm. In *Proceedings of the ASME 2014 33rd International Conference on Ocean, Offshore and Arctic Engineering (OMAE2014), San Francisco, California, USA*, 2014. doi: 10.1115/OMAE2014-24252.

M. Philippe, A. Babarit, and P. Ferrant. Comparison of time and frequency domain simulations of an offshore floating wind turbine. In *Proceedings of the ASME 2011 30th International Conference on Ocean, Offshore and Arctic Engineering (OMAE2011), Rotterdam, The Netherlands*, 2011. doi: 10.1115/OMAE2011-49722.

W. Popko, F. Vorpahl, A. Zuga, M. Kohlmeier, J. Jonkman, A. Robertson, T. J. Larsen, A. Yde, K. Sætertrø, K. M. Okstad, J. Nichols, T. A. Nygaard, Z. Gao, D. Manolas, K. Kim, Q. Yu, W. Shi, H. Park, A. Vásquez-Rojas, J. Dubois, D. Kaufer, P. Thomassen, M. J. de Ruiter, T. van der Zee, J. M. Peeringa, H. Zhiwen, and H. von Waaden. Offshore code comparison collaboration continuation (OC4), phase I - results of coupled simulations of an offshore wind turbine with jacket support structure. In *Proceedings of the Twenty-second (2012) International Offshore and Polar Engineering Conference (ISOPE2012), Rhodes, Greece*, 2012.

W. Popko, M. L. Huhn, A. Robertson, J. Jonkman, F. Wendt, K. Müller, M. Kretschmer, F. Vorpahl, T. R. Hagen, C. Galinos, J.-B. Le Dreff, P. Gilbert, B. Auriac, F. N. Villora, P. Schünemann, I. Bayati, M. Belloli, S. Oh, Y. Totsuka, J. Qvist, E. E. Bachynski, S. H. Sørum, P. E. Thomassen, H. Shin, F. Vittori, J. Galvan, C. Molins, P. Bonnet, T. van der Zee, R. Bergua, K. Wang, P. Fu, and J. Cai. Verification of a numerical model of the offshore wind turbine from the Alpha Ventus wind farm within OC5 phase III. In *Proceedings of the ASME 2018 37th International Conference on Ocean, Offshore and Arctic Engineering (OMAE2018), Madrid, Spain*, 2018.

W. Popko, A. Robertson, J. Jonkman, F. Wendt, P. Thomas, K. Müller, M. Kretschmer, T. R. Hagen, C. Galinos, J.-B. Le Dreff, P. Gilbert, B. Auriac, S. Oh, J. Qvist, S. H. Sørum, L. Suja-Thauvin, H. Shin, C. Molins, P. Trubat, P. Bonnet, R. Bergua, K. Wang, P. Fu, J. Cai, Z. Cai, A. Alexandre, and R. Harries. Validation of numerical models of the offshore wind turbine from the Alpha Ventus wind farm against full-scale measurements within OC5 phase III. In *Proceedings of the ASME 2019 38th International Conference on Ocean, Offshore and Arctic Engineering (OMAE2019), Glasgow, Scotland, UK*, 2019.

G. K. V. Ramachandran, L. Vita, A. Krieger, and K. Mueller. Design Basis for the Feasibility Evaluation of Four Different Floater Designs. *Energy Procedia*, 137:186–195, 2017. doi: 10.1016/j.egypro.2017.10.345.

L. Roald, J. Jonkman, A. Robertson, and N. Chokani. The effect of second-order hydrodynamics on floating offshore wind turbines. *Energy Procedia*, 35:253–264, 2013. doi: 10.1016/j.egypro.2013.07.178.

A. Robertson, J. Jonkman, F. Vorpahl, W. Popko, J. Qvist, L. Froyd, X. Chen, J. Azcona, E. Uzunoglu, C. G. Soares, C. Luan, H. Yutong, F. Pengcheng, A. Yde, T. Larsen, J. Nichols, R. Buils, L. Lei, T. A. Nygaard, D. Manolas, A. Heege, S. R. Vatne, H. Ormberg, T. Duarte, C. Godreau, H. F. Hansen, A. W. Nielsen, H. Riber, C. L. Cunff, F. Beyer, A. Yamaguchi, K. J. Jung, H. Shin, W. Shi, H. Park, M. Alves, and M. Guérinel. Offshore code comparison collaboration continuation within IEA wind task 30: phase II results regarding a floating semisubmersible wind system. In *Proceedings of the ASME 2014 33rd International Conference on Ocean, Offshore and Arctic Engineering (OMAE2014), San Francisco, California, USA*, 2014. doi: 10.1115/OMAE2014-24040.

A. N. Robertson, F. Wendt, J. M. Jonkman, W. Popko, H. Dagher, S. Gueydon, J. Qvist, F. Vittori, J. Azcona, E. Uzunoglu, C. G. Soares, R. Harries, A. Yde, C. Galinos, K. Hermans, J. B. de Vaal, P. Bozonnet, L. Bouy, I. Bayati, R. Bergua, J. Galvan, I. Mendikoa, C. B. Sanchez, H. Shin, S. Oh, C. Molins, and Y. Debruyne. OC5 project phase II: validation of global loads of the DeepCwind floating semisubmersible wind turbine. *Energy Procedia*, 137:38–57, 2017. doi: 10.1016/j.egypro.2017.10.333.

D. Roddier, C. Cermelli, A. Aubault, and A. Peiffer. Summary and conclusions of the full life-cycle of the WindFloat FOWT prototype project. *Proceedings of the ASME 2017 36th International Conference on Ocean, Offshore and Arctic Engineering (OMAE2017), Trondheim, Norway*, 2017. doi: 10.1115/OMAE2017-62561.

F. Sandner, D. Schlipf, D. Matha, and P. W. Cheng. Integrated optimization of floating wind turbine systems. In *Proceedings of the ASME 2014 33rd International Conference on Ocean, Offshore and Arctic Engineering (OMAE2014), San Francisco, California, USA*, 2014. doi: 10.1115/OMAE2014-24244.

T. Sauder, V. Chabaud, M. Thys, E. E. Bachynski, and L. O. Sæther. Real-time hybrid model tests of a braceless semi-submersible wind turbine. Part I: the hybrid approach. In *Proceedings of the ASME 2016*

35th International Conference on Ocean, Offshore and Arctic Engineering (OMAE2016), Busan, South Korea, 2016.

P. Sclavounos, C. Tracy, and S. Lee. Floating offshore wind turbines: responses in a seastate Pareto optimal designs and economic assessment. In *Proceedings of the ASME 27th International Conference on Offshore Mechanics and Arctic Engineering (OMAE2008), Estoril, Portugal*, 2008. doi: 10.1115/OMAE2008-57056.

SINTEF Ocean. RIFLEX user guide, 2016a.

SINTEF Ocean. SIMO user guide, 2016b.

B. Skaare, F. G. Nielsen, T. D. Hanson, R. Yttervik, O. Havmøller, and A. Rekdal. Analysis of measurements and simulations from the Hywind Demo floating wind turbine. *Wind Energy*, 18:1105–1122, 2015. doi: 10.1002/we.1750.

E. Smilden. *Structural control of offshore wind turbines - Increasing the role of control design in offshore wind farm development.* PhD thesis, Norwegian University of Science and Technology, 2019.

E. Smilden, E. E. Bachynski, A. J. Sørensen, and J. Amdahl. Site-specific controller design for monopile offshore wind turbines. *Marine Structures*, 61:503–523, 2018. doi: 10.1016/j.marstruc.2018.03.002.

A. Smith, T. Stehly, and W. Musial. 2014–2015 offshore wind technologies market report. Technical Report NREL/TP-5000-64283, National Renewable Energy Laboratory, 2015.

C. E. S. Souza and E. E. Bachynski. Changes in surge and pitch decay periods of floating wind turbines for varying wind speed. *Ocean Engineering*, 180:223–237, 2019. doi: 10.1016/j.oceaneng.2019.02.075.

C. E. S. Souza and E. E. Bachynski. Effects of hull flexibility on the structural dynamics of a tension leg platform floating wind turbine. *Journal of Offshore Mechanics and Arctic Engineering*, 142, 2020. doi: 10.1115/1.4044725.

A. Steinert, S. Ehlers, M. I. Kvittem, D. Merino, and M. Ebbesen. Cost assessment for a semi-submersible floating wind turbine with respect to the hydrodynamic response and tower base bending moments using particle swarm optimisation. In *Proceedings of the Twenty-sixth (2016) International Ocean and Polar Engineering Conference (ISOPE2016), Rhodes, Greece*, pages 419–426, 2016.

M. Strach-Sonsalla and M. Muskulus. Dynamics and design of floating wind turbines. In *Proceedings of the Twenty-sixth (2016) International Ocean and Polar Engineering Conference (ISOPE2016), Rhodes, Greece*, 2016.

G. I. Taylor. The spectrum of turbulence. *Proc. R. Soc. A*, 164:476–490, 1938.

The Carbon Trust. Floating offshore wind: market and technology review. Technical report, The Carbon Trust, 2015.

C. Tibaldi, M. H. Hansen, and L. C. Henriksen. Optimal tuning for a classical wind turbine controller. *Journal of Physics: Conference Series*, 555(012099), 2014. doi: 10.1088/1742-6596/555/1/012099.

C. Tibaldi, L. C. Henriksen, M. H. Hansen, and C. Bak. Wind turbine fatigue damage evaluation based on a linear model and a spectral method. *Wind Energy*, 19:1289–1306, 2016. doi: 10.1002/we.1898.

K. Torsethaugen. Model for double peaked wave spectrum. Technical Report STF22 A96204, SINTEF Civil and Envir. Engineering, 1996.

K. Torsethaugen and S. Haver. Simplified double peak spectral model for ocean waves. In *Proceedings of the Fourteenth (2004) International Ocean and Polar Engineering Conference (ISOPE2004), Toulon, France*, 2004.

C. Tracy. Parametric design of floating wind turbines. Master's thesis, Massachusetts Institute of Technology, 2007.

J. van der Tempel. *Design of support structures for offshore wind turbines.* PhD thesis, TU Delft, 2006.

G. J. van der Veen, I. J. Couchman, and R. O. Bowyer. Control of floating wind turbines. In *2012 American Control Conference, Fairmont Queen Elizabeth, Montreal, Canada*, pages 3148–3153, 2012. doi: 10.1109/acc.2012.6315120.

J. Velarde, C. Kramhøft, J. D. Sørensen, and G. Zorzi. Fatigue reliability of large monopiles for offshore wind turbines. *International Journal of Fatigue*, 134, 2020. doi: 10.1016/j.ijfatigue.2020.105487.

F. Vorpahl, H. Schwarze, T. Fischer, M. Seidel, and J. Jonkman. Offshore wind turbine environment, loads, simulation, and design. *WIREs Energy Environ*, 2:548–570, 2013. doi: 10.1002/wene.52.

E. N. Wayman, P. Sclavounos, S. Butterfield, J. Jonkman, and W. Musial. Coupled dynamic modeling of floating wind turbine systems. In *Offshore Technology Conference*, 2006. doi: 10.4043/18287-ms.

WindEurope. Floating offshore wind energy - a policy blueprint for Europe. Technical report, WindEurope, 2018.

WindEurope. Offshore wind in Europe - key trends and statistics 2019. Technical report, WindEurope, 2019.

A. S. Wise and E. E. Bachynski. Wake meandering effects on floating wind turbines. *Wind Energy*, 23:1266–1285, 2020. ISSN 10991824. doi: 10.1002/we.2485.

F. Zahle, C. Tibaldi, D. R. Verelst, C. Bak, R. Bitsche, and J. P. Blasques. Aero-elastic optimization of a 10 MW wind turbine. In *33rd ASME Wind Energy Symposium, American Institute of Aeronautics and Astronautics*, 2015. doi: 10.2514/6.2015-0491.

Appendix A

Appended Papers

Paper 1

A semi-analytical frequency domain model for efficient design evaluation of spar floating wind turbines

John Marius Hegseth and Erin E. Bachynski

Marine Structures, 2019

Marine Structures 64 (2019) 186–210

Contents lists available at ScienceDirect

Marine Structures

journal homepage: www.elsevier.com/locate/marstruc

A semi-analytical frequency domain model for efficient design evaluation of spar floating wind turbines

John Marius Hegseth*, Erin E. Bachynski

Department of Marine Technology, NTNU, 7491 Trondheim, Norway

ARTICLE INFO

Keywords:
Offshore wind
Design analysis
Frequency domain
Fatigue
Extreme response

ABSTRACT

A linear model for efficient design evaluation of spar floating wind turbines is presented, and verified against a nonlinear time domain model with regards to long-term fatigue and short-term extreme response for two different spar designs. The model uses generalized displacements and a semi-analytical approach to establish the equations of motion for the system, which are solved in the frequency domain. The results show agreement within ± 30% for the long-term fatigue considering operational conditions, however, the linear fatigue damage estimates are sensitive to the accuracy of the estimated natural frequency of the first bending mode. The results also suggest that a small number of environmental conditions can be simulated with a nonlinear time domain model to verify and possibly tune the linear model, which then can be used to run the full long-term analysis. Short-term extreme tower base bending moments and surge and pitch motions are observed to be nearly Gaussian above cut-out wind speed, as the response is dominated by wave forces. Consequently, the linear model is able to accurately capture the upcrossing rates, which are used to calculate the characteristic largest extreme response. For an operational case near rated wind speed, the response is somewhat non-Gaussian, which gives larger discrepancies between the linear and nonlinear models. However, due to large mean values in this condition, the total error in the extreme response is reduced, and reasonable agreement is achieved.

1. Introduction

The offshore wind industry has had significant growth over the last decade, and as a majority of the global wind resources are located in deeper waters, there has recently been an increased interest in floating wind turbines (FWTs). For floating wind farms to be economically feasible, cost-effective and reliable designs are needed. Design optimization of FWTs is a complex task, and due to interactions between aerodynamics, hydrodynamics, structural dynamics and control, coupled nonlinear time domain (TD) simulations are usually applied. As numerous load cases need to be analysed, the design process becomes computationally very expensive. It is therefore desirable to use simplified models, especially in preliminary design [1]. Frequency domain (FD) models provide an efficient way of performing dynamic simulations and are frequently used for floating structures in the offshore industry, usually in fatigue analyses [2]. Although less common in the offshore wind industry, design standards state that frequency domain analyses also can be used to calculate the fatigue loads for FWTs, if validation against time domain analyses or experiments is performed [3].

Several studies have investigated the applicability of FD models for FWTs. Typically, these models have considered first order hydrodynamic loads from potential theory and steady aerodynamic loads, and have been used to calculate response amplitude operators (RAOs) for the rigid body motions of the platform [4–7].

* Corresponding author.
E-mail address: john.m.hegseth@ntnu.no (J.M. Hegseth).

https://doi.org/10.1016/j.marstruc.2018.10.015
Received 10 August 2018; Received in revised form 2 October 2018; Accepted 30 October 2018

Nomenclature

α_2	Dirlik irregularity factor
β	Stiffness-proportional Rayleigh damping coefficient
Γ	Gamma function
ν_p	Expected rate of peaks
ρ	Water density
σ	Standard deviation
σ_x	Axial stress
ψ	Shape function
ω	Angular frequency
A	Cross sectional area
a	Hull radius
a_{11}	Transverse added mass per unit length
$\mathbf{B}$	Generalized damping matrix
B_{aero}	Aerodynamic damping
b_{visc}	Linearized viscous damping per unit length
C_d	Drag coefficient
D	Hull diameter
$\mathrm{d}F_W$	Wave excitation force per unit length
EI	Bending stiffness
$\mathbf{F}_\zeta$	Generalized wave load vector
F_T	Thrust force
$\mathbf{F}_U$	Generalized wind load vector
g	Gravitational acceleration
$\mathbf{H}_{ij}$	Transfer function from i to j
h	Water depth
I	Area moment of inertia
I_{RNA}	Inertia of RNA about the tower top
I_{wp}	Waterplane area moment of inertia
J'_n	Derivative of Bessel function of the first kind of order n
$\mathbf{K}$	Generalized stiffness matrix
K	Material property for SN curve
K_r	Hydrostatic restoring in pitch
K_t	Linear horizontal mooring stiffness
k	Wave number, thickness exponent for SN curve
L	Spar FWT draft
$\mathbf{M}$	Generalized mass matrix
M	Mass of spar including mooring system
M_{RNA}	Mass of RNA
M_T	Rotor moment
M_y	Bending moment about y-axis
m	Mass per unit length, slope of SN curve
m_n	n^{th} spectral moment
N	Axial force
r	Cross section outer radius
S_ζ	Wave spectrum
S_U	Wind spectrum
t	Wall thickness
t_{ref}	Reference thickness for SN curve
V	Hull displacement
x_m	Dirlik mean frequency
Y'_n	Derivative of Bessel function of the second kind of order n
z_B	Vertical centre of buoyancy
z_G	Vertical centre of gravity
z_{moor}	Vertical location of the fairleads
z_{TB}	Vertical location of the tower base
z_{top}	Vertical location of the tower top

Although useful information about the system may be found using only rigid body motions, the elasticity of the tower has been shown to significantly affect the global response of FWTs. Bachynski and Moan [8] compared a linear FD model with three rigid body modes to a nonlinear TD model for different tension leg platform wind turbine designs in both wave-only and combined wind-wave conditions. The study was later expanded to include turbulent wind excitation and aerodynamic damping [9], and concluded that the linear model was insufficient for design calculations, partly due to the rigid modelling of the tower. Kvittem and Moan [10] used a similar procedure to calculate tower base bending moments for a semi-submersible wind turbine, where the first bending mode of the tower was found from a free decay test and included using generalized coordinates. The contribution from the first bending mode on the tower base bending moment response was expressed as a dynamic amplification factor. The model was found to perform reasonably well in the 13 considered load cases, however, the fatigue damage was underestimated by up to 60% due to its exponential nature. A somewhat different approach was applied by Kluger et al. [11], who used statistical linearization to develop a FD model for the OC3 spar wind turbine [12]. The two first elastic tower modes were found for a fixed foundation and included in the analysis, and equivalent fatigue stress (EFS) at the tower base due to wave excitation and steady wind was calculated for 11 different environmental conditions. The results were compared to values from TD simulations reported by Matha [13], where the FD analysis was found to underestimate the total EFS by 12%.

Although earlier work has assessed the fatigue damage based on FD analyses for FWTs, these calculations have only been performed for a limited number of environmental conditions. Thus, little information exists regarding the accuracy of such models for a full long-term analysis. In addition, the design process must also consider the extreme response of the system, which can be a comprehensive task. Results from previous studies have shown that both the tower base bending moment [14] and global motions [15] for spar FWTs can be quite Gaussian in harsh environmental conditions, which suggests that a linear model also may be used to assess the extreme response in early stages of design. For a spar FWT, in addition to the ultimate stresses in the structure, the extreme surge and pitch response of the platform may be of interest, as these motions are important for loads on the mooring system and nacelle components, respectively.

In the present work, a semi-analytical FD approach is presented, where generalized degrees-of-freedom (DOFs) are used to describe the dynamic behaviour of the FWT. The system is linearized, and due to the simple geometry of the hull, closed-form expressions may be used for the hydrodynamic loads with good accuracy. This removes the need for a separate numerical hydrodynamic analysis, which significantly increases the computational efficiency. The aerodynamic loads are found numerically from TD simulations, and the forces are superimposed to find the total response. The approach is then compared to fully coupled nonlinear TD simulations for two different 10 MW spar FWT designs, considering long-term fatigue damage at the tower base, as well as short-term

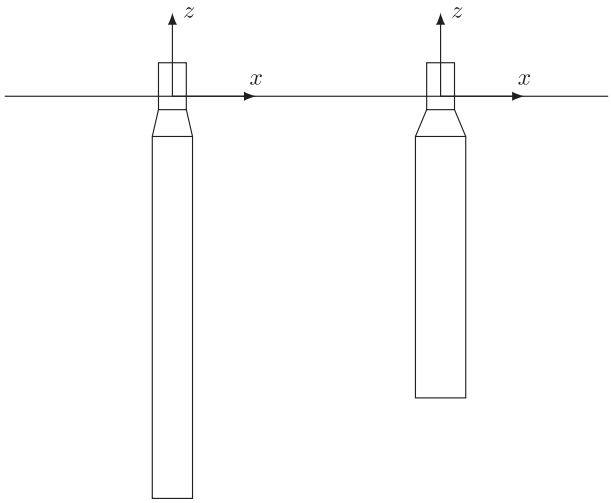

Fig. 1. Spar designs considered in the present work. Spar 1 (left) and spar 2 (right).

extreme values for the tower base bending moment and surge and pitch motions of the platform in selected conditions along the 50-year environmental contour. The linear FD model presented in the present work is not applicable for detailed analyses, but may complement state-of-the-art tools in early stages of design. The model can help the designer get a quick overview of the response of the system, and give indications of how the system responds to changes in the design parameters. It may also be used to identify critical load cases, which then can be analysed using coupled nonlinear TD analyses.

2. System description

2.1. Platform designs

The two spar buoys considered in the current work are shown in Fig. 1. The designs are based on the OC3-Hywind design [12] and consist of two cylinders with different diameters, connected by a linearly tapered section. The hull extends to a height of 10 m above still water level (SWL), where it is fixed to the tower. Spar 1 has the same draft as the original OC3 spar of 120 m, but with increased diameters to provide enough buoyancy to support a 10 MW wind turbine, and to match the tower base diameter. The large draft of the spar provides good stability and hydrodynamic performance, however, it limits the use to deep water, and complicates construction and towing to site. The draft of the second design (spar 2) was therefore reduced by 25%, which makes it more suitable for intermediate water depths. In addition to the draft reduction, the lower hull diameter was increased by 25% compared to spar 1, to achieve a sufficient amount of buoyancy.

The two designs are presented in Table 1, where values for the vertical centre of gravity (CoG) and moment of inertia are calculated by assuming that the hulls are partially filled with concrete ballast to achieve the correct draft, using a ballast density of 2600 kg/m^3, while a constant wall thickness of 6 cm is assumed for the steel hull. The water depth for both platforms is 320 m.

Table 1
Platform properties.

Parameter	Spar 1	Spar 2
Draft (m)	120.0	90.0
Elevation to tower base above SWL (m)	10.0	10.0
Depth to top of taper below SWL (m)	4.0	4.0
Depth to bottom of taper below SWL (m)	12.0	12.0
Diameter above taper (m)	8.3	8.3
Diameter below taper (m)	12.0	15.0
Mass including ballast (kg)	1.18E+7	1.33E+7
Displacement (m^3)	1.31E+4	1.49E+4
Moment of inertia about CoG (kgm^2)	6.53E+9	3.42E+9
Vertical CoG below SWL (m)	94.7	72.3
Vertical CoB below SWL (m)	62.0	47.8

Table 2
Main characteristics of the DTU 10 MW reference wind turbine [16].

Parameter	Value
Rated power	10 MW
Rotor orientation and configuration	Upwind, three blades
Rotor, hub diameter	178.3 m, 5.6 m
Hub height	119.0 m
Cut-in, rated, cut-out wind speed	4.0 m/s, 11.4 m/s, 25.0 m/s
Cut-in, rated rotor speed	6.0 rpm, 9.6 rpm
Overhang, shaft tilt, pre-cone	7.1 m, 5.0°, −2.5°
Rotor, nacelle, tower mass[a]	230.7 t, 446.0 t, 628.4 t

[a] Mass for original land-based tower.

2.2. DTU 10 MW wind turbine with modified tower

The spar buoys support the DTU 10 MW reference wind turbine [16], with the tower shortened by 10 m to achieve the same hub height as the onshore turbine at 119 m above SWL. The tower has a linearly tapered outer diameter and consists of ten sections with constant wall thickness in each section. In the modified tower, each section is shortened by 1 m, while the top and bottom diameters are kept unchanged. The key characteristics of the turbine are listed in Table 2.

The natural frequencies of the tower change when the turbine is placed on a floating substructure, and preliminary calculations showed that the natural frequency of the first bending mode for spar 2 was very close to the blade passing frequency at rated rotor speed. The wall thickness in all sections of the tower was therefore increased by 50% for spar 2, which moved the natural frequency above the 3P range.

2.3. Mooring system

The mooring system, described in Table 3, consists of three catenary lines spread symmetrically about the vertical axis. As in the OC3 project, a simplification is made in that the delta lines are removed, and lines with constant properties are instead used all the way up to the fairleads. A rotational spring is added to the model to ensure that the yaw stiffness from the mooring system is included. The fairleads are placed at a depth equal to the total CoG of the system including the wind turbine, in order to limit the coupling between surge and pitch motion. This results in a slightly stiffer mooring system for spar 2.

3. Time domain model

The fully coupled nonlinear aero-hydro-servo-elastic analyses are carried out in the time domain using the simulation workbench SIMA developed by SINTEF Ocean, which couples two computer codes: Riflex, a finite element solver developed for flexible beam elements; and SIMO, which calculates large volume hydrodynamic loads [17,18]. The spar buoys are modelled as six-DOF rigid bodies with first order wave forces found numerically from potential flow theory using WAMIT [19], combined with viscous forces from the drag term in Morison's equation, which are integated up to the instantaneous wave elevation. Second order potential flow forces are not considered in the model, as studies have shown that these loads have limited effect on the response for spar-type FWTs [20,21].

Bar elements with only axial stiffness are used to model the mooring lines, together with hydrodynamic loads from Morison's equation. The model thus includes the nonlinear restoring forces from the mooring system, as well as the dynamic behaviour of the mooring lines. The tower and blades are modelled using flexible beam elements.

The aerodynamic loads are calculated using blade element/momentum (BEM) theory, including Glauert correction, Prandtl hub and tip loss factors, dynamic stall, dynamic wake, skewed inflow and tower shadow. The code has previously been verified for FWTs [22,23]. As wind drag forces on the tower may become important at high wind speeds, this effect is included for the extreme response conditions using a drag force formulation with a drag coefficient of 0.7.

An external control system written in Java is used to modify the generator torque and blade pitch. In order to avoid pitch motion

Table 3
Mooring system properties.

Parameter	Spar 1	Spar 2
Radius to anchors (m)	855.2	855.2
Unstretched mooring line length (m)	902.2	902.2
Equivalent mooring line mass density (kg/m)	155.4	155.4
Equivalent mooring line axial stiffness (MN)	3.84E+8	3.84E+8
Fairlead depth below SWL (m)	77.2	56.3
Yaw spring stiffness (Nm/rad)	1.48E+8	1.48E+8

instability above rated wind speed due to negative feedback [24,25], the proportional and integral gains for the blade pitch are modified from the original controller. With the resulting gains, the controller has a natural frequency of 0.13 rad/s and a damping ratio of 0.7.

4. Frequency domain model

In the frequency domain model, a linear representation of the system is created as shown in Fig. 2. For simplicity, only the response in the xz-plane is considered in the present study. The platform is considered rigid, while the tower is modelled as a slender flexible beam. The rotor and nacelle assembly (RNA) is replaced by a point mass and inertia at the top of the tower, with resultant wind loads (thrust force, rotor pitching moment, and aerodynamic damping) acting on the tower top. The mooring system is represented by a linear spring at the position of the fairleads. As the structure is statically determinate, internal loads in the hull can be found by considering equilibrium between external, inertial, damping, restoring and internal reaction forces. In the present work, the tower base bending moment is the only internal load which is considered (see also Appendix A), but the method can easily be applied to other components.

Generalized displacements are used in combination with the principle of virtual work to establish the dynamic equations of motion [26], which are solved in the FD. In this procedure, the total response is described by a weighted combination of an arbitrary number of shape functions, ψ. The accuracy of the formulation thus depends on how well the actual displacement field is captured by the shape functions, which typically are chosen to represent the most important eigenmodes of the system.

Three generalized DOFs are included in the model, namely surge, pitch, and the first bending mode, as illustrated in Fig. 3. Orthogonal eigenmodes can be found numerically from the solution of the eigenvalue problem for a finite element (FE) model of the linearized system. However, as the shapes of the rigid body modes are known a priori, they are instead chosen as analytical functions for simplicity. In addition, to have global motions that are consistent with the TD model, the pitch mode is chosen as a rotation about the SWL. Using non-orthogonal modes introduces off-diagonal terms in the system matrices, however, these coupling effects are readily taken into account in the formulation.

The actual shape of the bending mode, on the other hand, is not known, and is therefore found from the eigenvalue solution. A third-order spline function is then fitted to the nodal displacements to have continuous expressions for the first and second order derivatives. The FE model used to solve the eigenvalue problem is based on the linearized system in Fig. 2 and does not include the blades, however, added mass on the hull is included using strip theory.

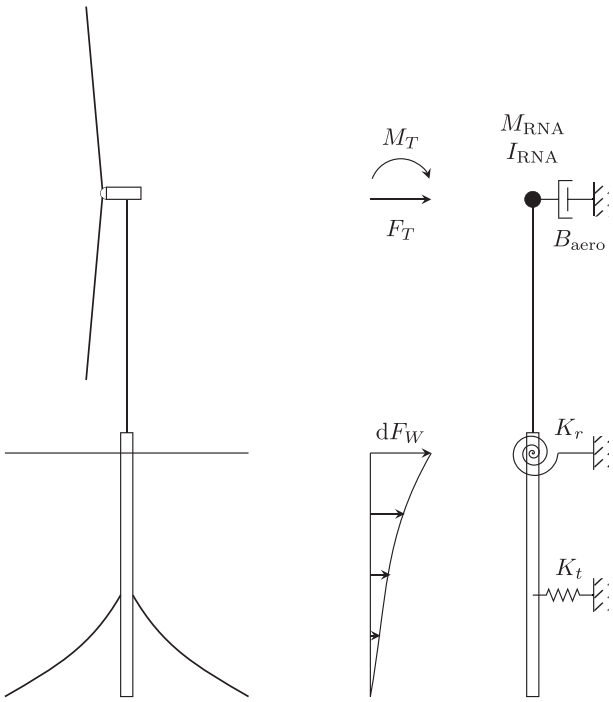

Fig. 2. Linear representation of the FWT system.

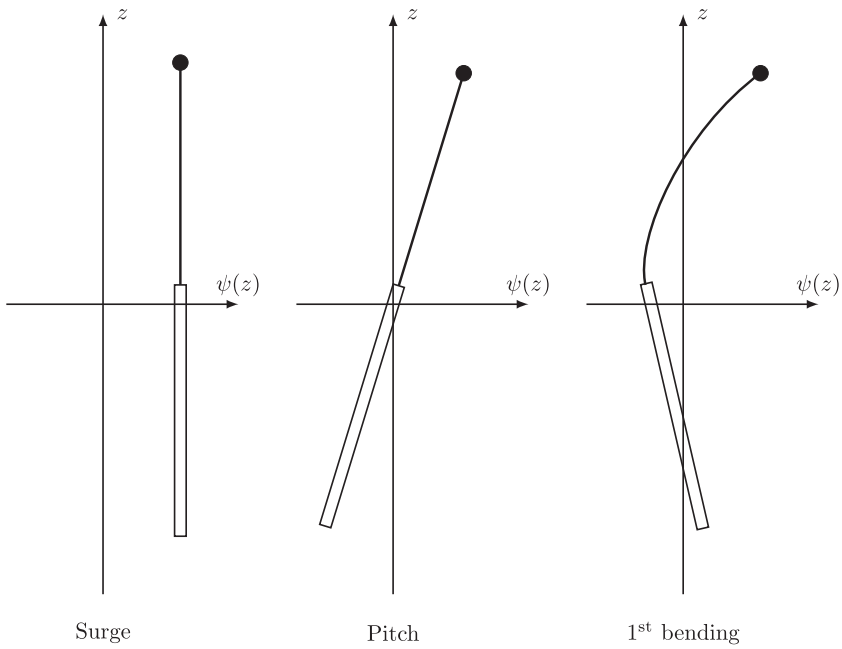

Fig. 3. DOFs considered in the analysis.

4.1. Load formulation

In order to predict the dynamic behaviour of the system, the inertia, damping, restoring and excitation forces on the structure need to be determined. Due to the simple and relatively slender geometry of the hull, the hydrodynamic loads on the floater can be simplified without significant loss of accuracy. The transverse added mass per unit length is approximated using the analytical expression for a 2D circular cylinder with diameter D in infinite fluid [27]:

$$a_{11}(z) = \rho\pi D^2(z)/4 \tag{1}$$

The linear wave excitation forces are taken from MacCamy-Fuchs theory [28]. The force per unit length, $\mathrm{d}F_W$, for a regular wave with unit amplitude is given by

$$\mathrm{d}F_W(z,\omega) = \frac{4\rho g}{k}\frac{\cosh k(z+h)}{\cosh kh} G\, e^{i(\omega t-\alpha)} \tag{2}$$

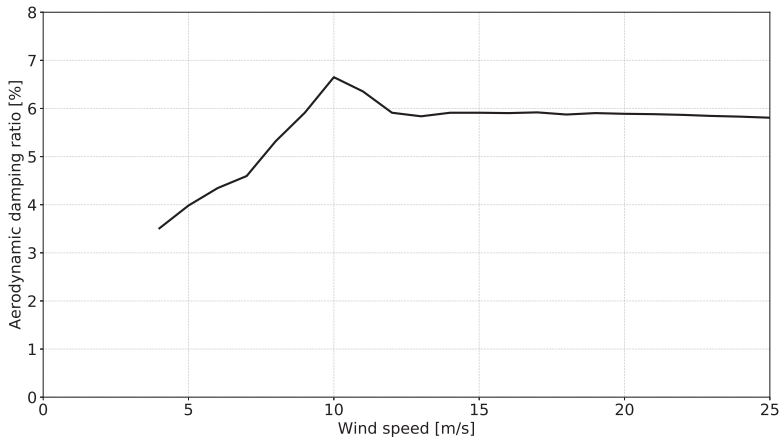

Fig. 4. Aerodynamic damping ratio for the first fore-aft mode of the land-based DTU 10 MW turbine as a function of wind speed.

where

$$G = \frac{1}{\sqrt{(J_1'(ka))^2 + (Y_1'(ka))^2}}, \quad \tan\alpha = \frac{J_1'(ka)}{Y_1'(ka)}. \tag{3}$$

For the aerodynamic loads, the BEM equations usually have to be solved in the TD [29], and there is no straight-forward way to establish linearized frequency-dependent wind forces. In the present study, the turbulent thrust force (F_T) and rotor moment (M_T) for different wind speeds are extracted from TD simulations on a fixed rotor in SIMA. The resulting time series are transformed to the FD using fast Fourier transform (FFT), and normalized with the incoming wind spectrum to create force transfer functions. In addition, the so-called aerodynamic damping, which arises due to the change in thrust force as a result of the nacelle's velocity, needs to be explicitly calculated, which can be done in various ways [29,30]. Here, the linearized damping is estimated following the procedure described by Bachynski [9]. Time domain simulations with a range of constant wind speeds are run on a fixed rotor, and the damping values are found as the change in thrust force for small variations in wind speed while the blade pitch and rotor speed are kept fixed:

$$B_{\text{aero}} = \frac{\mathrm{d}F_T}{\mathrm{d}U}. \tag{4}$$

The resulting aerodynamic damping values are shown as a function of mean wind speed in Fig. 4, presented as critical damping ratio for the first fore-aft tower mode of the original land-based DTU 10 MW turbine. The linearized aerodynamic damping applies to all generalized modes with nonzero deflection at the tower top, and the coefficient B_{aero} is varied with the mean wind speed. Damping caused by pure rotation of the rotor is not considered. It is assumed that any changes in aerodynamic forces that arise due to the motions of the FWT are captured by the aerodynamic damping term, which means that variations in control system outputs caused by platform motions are not considered in the model.

Rayleigh damping is used to model structural damping in the tower, with a stiffness-proportional coefficient $\beta = 0.007$ for both designs. For a given β, the damping ratio is proportional to the natural frequency, and using a constant value will thus reward stiffer designs, such as spar 2, without any physical reason. In an actual design process, the coefficient should therefore be continuously updated to keep the damping ratio constant. However, as the scope of the current work is not to perform design calculations, but rather to compare different modelling techniques, a constant coefficient is used for simplicity. The applied coefficient corresponds to a damping ratio of 0.9% and 1.2% at the first bending natural frequency for spar 1 and spar 2, respectively.

Viscous damping, which is important for the low-frequency surge response, is added based on stochastic linearization of the quadratic drag term in Morison's equation [31]:

$$\frac{1}{2}\rho C_d D(z)\dot{x}|\dot{x}| \approx \frac{1}{2}\rho C_d D(z)\sqrt{\frac{8}{\pi}}\sigma_{(\dot{x})}(z)\dot{x} = b_{\text{visc}}(z)\,\dot{x} \tag{5}$$

with a drag coefficient $C_d = 0.7$. The standard deviation of the velocity, $\sigma_{(\dot{x})}$, is found using an iteration scheme. Viscous wave excitation was found to be small compared to the wind excitation forces, and is therefore not included in the model. Wave radiation damping is also neglected. The aerodynamic drag forces on the tower, which only are included in the extreme response conditions, are taken into account in the linear model as a combination of a mean force, which is added directly, and a frequency-dependent force, which is found using stochastic linearization. Here, only the excitation forces are considered, meaning that the tower drag forces arising from the movement of the turbine are neglected.

The analytical solution for quasi-static horizontal tension in elastic catenary lines can be found in e.g. Faltinsen [32]. In order to find the linear mooring stiffness used in the model, K_t, this equation is differentiated numerically. The stiffness is calculated for the zero offset position of the hull in all environmental conditions, as the offset was found to have little effect on the results. However, updated stiffness values based on the actual mean position of the platform can easily be included. Mooring line excitation, damping and inertia are neglected in the model.

The hydrostatic restoring in pitch, which is applied as a rotational spring at the SWL, is found from

$$K_r = \rho g V z_B - M g z_G + \rho g I_{\text{wp}}. \tag{6}$$

4.2. Establishing the equations of motion

Using the vector containing the shape functions and the terms derived in the previous section, the generalized mass (including added mass), damping and stiffness matrices can be established [26]:

$$\mathbf{M} = \int_0^{z_{\text{top}}} m(z)\boldsymbol{\psi}(z)\boldsymbol{\psi}^{\top}(z)\mathrm{d}z + \int_{-L}^{0} [m(z) + a_{11}(z)]\boldsymbol{\psi}(z)\boldsymbol{\psi}^{\top}(z)\mathrm{d}z + M_{\text{RNA}}\boldsymbol{\psi}(z_{\text{top}})\boldsymbol{\psi}^{\top}(z_{\text{top}}) + I_{\text{RNA}}\boldsymbol{\psi}_{,z}(z_{\text{top}})\boldsymbol{\psi}_{,z}^{\top}(z_{\text{top}}) \tag{7}$$

$$\mathbf{B} = \beta \int_{z_{\text{TB}}}^{z_{\text{top}}} EI(z)\boldsymbol{\psi}_{,zz}(z)\boldsymbol{\psi}_{,zz}^{\top}(z)\mathrm{d}z + \int_{-L}^{0} b_{\text{visc}}(z)\boldsymbol{\psi}(z)\boldsymbol{\psi}^{\top}(z)\mathrm{d}z + B_{\text{aero}}\boldsymbol{\psi}(z_{\text{top}})\boldsymbol{\psi}^{\top}(z_{\text{top}}) \tag{8}$$

$$\mathbf{K} = \int_{z_{TB}}^{z_{top}} EI(z)\boldsymbol{\psi}_{,zz}(z)\boldsymbol{\psi}_{,zz}^{\top}(z)\mathrm{d}z + \int_{z_{TB}}^{z_{top}} N(z)\boldsymbol{\psi}_{,z}(z)\boldsymbol{\psi}_{,z}^{\top}(z)\mathrm{d}z + K_l\boldsymbol{\psi}(z_{moor})\boldsymbol{\psi}^{\top}(z_{moor}) + K_r\boldsymbol{\psi}_{,z}(0)\boldsymbol{\psi}_{,z}^{\top}(0), \tag{9}$$

where $N(z)$ is the axial force in the tower. The generalized wind and wave load vectors are found from

$$\mathbf{F}_U(\omega) = F_T(\omega)\boldsymbol{\psi}(z_{top}) + M_T(\omega)\boldsymbol{\psi}_{,z}(z_{top}) \tag{10}$$

$$\mathbf{F}_{\zeta}(\omega) = \int_{-L}^{0} dF_W(z,\omega)\boldsymbol{\psi}(z)\mathrm{d}z. \tag{11}$$

4.3. Frequency domain response

The transfer functions relating modal response to wave and wind input, $\mathbf{H}_{\zeta X}(\omega)$ and $\mathbf{H}_{UX}(\omega)$ respectively, are defined as

$$\mathbf{H}_{\zeta X}(\omega) = \mathbf{H}_{FX}(\omega)\mathbf{F}_{\zeta}(\omega),\ \ \mathbf{H}_{UX}(\omega) = \mathbf{H}_{FX}(\omega)\mathbf{F}_U(\omega) \tag{12}$$

where

$$\mathbf{H}_{FX}(\omega) = [-\omega^2\mathbf{M} + i\omega\mathbf{B} + \mathbf{K}]^{-1} \tag{13}$$

is the frequency response function matrix. Transfer functions between tower base bending moment and wind/wave input ($H_{\zeta M}(\omega)$ and $H_{UM}(\omega)$) are found by considering equilibrium between external, inertial, damping and internal forces. The complete equations may be found in Appendix A. As both the wind speed and wave elevation are considered to be stationary Gaussian processes within the short-term duration, the linear response will also be a stationary Gaussian process. The responses to wind and wave input are assumed to be independent; that is, there is no interaction between the responses at different frequencies. This is an assumption inherent in the linearization, and may not be equally applicable for all FWTs.

The response spectrum for an arbitrary response parameter ξ is then found by superimposing the wind and wave responses:

$$S_{\xi}(\omega) = |H_{\zeta\xi}(\omega)|^2 S_{\zeta}(\omega) + |H_{U\xi}(\omega)|^2 S_U(\omega), \tag{14}$$

while the variance is given as

$$\sigma_{(\xi)}^2 = \int_0^{\infty} S_{\xi}(\omega)\,\mathrm{d}\omega. \tag{15}$$

5. Dynamic simulations

5.1. Environmental conditions

The long-term fatigue assessment uses the joint probability distribution of metocean parameters given in Johannessen et al. [33]. Probability density functions (PDFs) for the parameters are shown in Fig. 5. IEC 61400-3 [34] prescribes a minimum bin size of 2 m/s for the wind speed, 0.5 m for wave heights, and 0.5 s for wave periods. Kvittem and Moan [35] performed a long-term fatigue analysis of a semi-submersible FWT, where damage sensitivities with regards to simulation length, bin size and number of samples were addressed. Based on their findings, the bin sizes for wave heights and wave periods in the present work are increased to 1 m and 1 s, respectively, and each condition is simulated using six 1-h realizations after removal of transients.

Long-term fatigue analyses used in design of FWTs should cover all relevant conditions over the lifetime of the structure, including operational, fault, idling, and survival conditions. The fatigue analysis presented in this study is limited to operational cases, which means that the mean wind speed is varied between 4 and 25 m/s, and the turbine is assumed to be operating normally. A total of 546 environmental conditions (ECs) are thus considered in the analysis, which corresponds to all ECs within 4–25 m/s with probability of occurrence greater than 10^{-4}. It is worth noting that, although not employed in the current fatigue comparison, the FD model also is applicable for wind speeds below cut-in or above cut-out, as long as only steady-state conditions are considered.

Three-dimensional turbulent wind time series are generated using TurbSim [36], assuming a Kaimal spectrum for IEC61400-1 class B turbines and a normal turbulence model. A power law profile with exponent 0.14 is used to model the vertical wind shear [34]. The same wind files are used both directly in the TD simulations, and to establish the wind thrust and rotor moment transfer functions used in the FD calculations, which are derived by taking the average values over the six seeds. The calculated transfer functions for each individual wind time series, as well as the average curves, are shown in Fig. 6 for 11 m/s mean wind speed, to illustrate the degree of variability between the realizations. Wave time series are generated using JONSWAP spectra with a peakedness parameter of 3.3. Co-directional waves and wind travelling in the positive x-direction are applied in all simulations, and no current is considered in the analysis.

Four ECs along the 50-year contour surface are selected to compare the short-term extreme response, as described in Table 4. In EC 1, the mean wind speed is close to the rated speed of the turbine, which gives the maximum thrust force on the rotor. EC 2 considers an operational condition near cut-out, while ECs 3 and 4 represent wind speeds above cut-out, where the turbine is parked

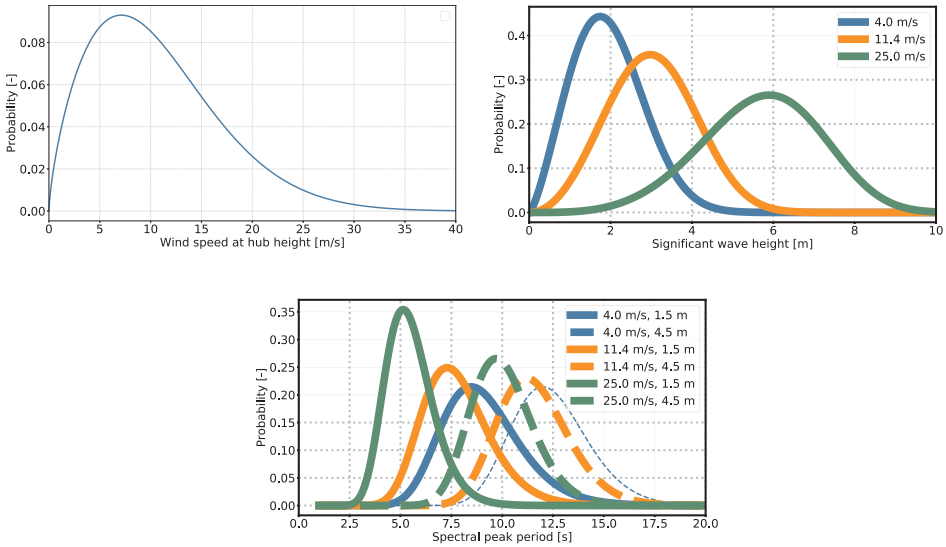

Fig. 5. Marginal distribution of 1-h wind speed, and conditional distributions of wave height and peak period. Based on Johannessen et al. [33].

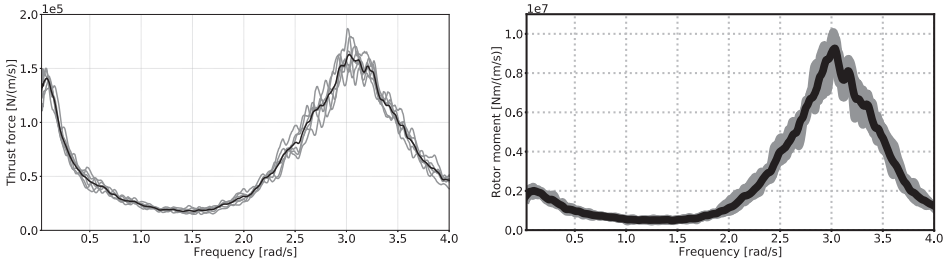

Fig. 6. Calculated transfer functions for aerodynamic excitation loads at 11 m/s mean wind speed. Six different wind realizations (grey) and average values (black).

and the blades are feathered. As for the fatigue analysis, 1-h simulations (excluding transients) are used in the extreme response comparison, but with 20 different random seeds for each condition. No fault conditions are considered, however, previous studies on blade pitch faults, grid loss and shutdown have shown that such events primarily affect the loads on the blades and shaft, and that the tower base fore-aft bending moment and global motions tend to be smaller than during fault-free conditions for spar-type FWTs [37,38].

5.2. Fatigue damage assessment

The fore-aft axial stress at the outer radius of the tower is calculated from

$$\sigma_x = \frac{N}{A} + \frac{M_y}{I} r. \tag{16}$$

Stress variations due to fluctuations in the axial force are found to be negligible compared to the moment-induced stress

Table 4
Environmental conditions for extreme response calculation.

Condition	1	2	3	4
Mean wind speed at hub height, U (m/s)	11.0	25.0	36.0	50.0
Significant wave height, H_s (m)	6.9	10.3	12.9	15.1
Spectral peak period, T_p (s)	10.0	12.5	14.0	16.0
Turbulence intensity at hub height, I (−)	0.18	0.14	0.13	0.12

variations, and are thus not included in the fatigue calculations. In the TD, rainflow counting is used together with SN curves and the Miner-Palmgren rule to estimate the fatigue damage, which is taken as the average value over the six realizations for each EC. In the FD, two different methods are considered:

1. Inverse Fourier transform (IFT)
2. Dirlik method

In the first method, 1-h stress time series are generated by performing IFT on the response spectrum with random phase angles. The fatigue damage is then calculated using rainflow counting and the Miner-Palmgren rule. The phase angles introduce randomness to the damage estimates, and the method is therefore performed with six different random seeds, as for the TD model. The average value is then used in the fatigue comparison.

The Dirlik method [39] uses the stress response spectrum and empirical factors to fit the PDF of the stress cycles to a combination of an exponential and two Rayleigh distributions, and the accuracy of the method is therefore dependent on how well the rainflow-count can be represented by these distributions. The expression for the fatigue damage during T seconds becomes [26]:

$$D_{\mathrm{DK}} = \frac{\nu_p T}{K}(2\sigma)^m\left(G_1 Q^m \Gamma(1+m) + (\sqrt{2})^m (G_2 R^m + G_3)\Gamma\left(1+\frac{m}{2}\right)\right)\left(\frac{t}{t_{\mathrm{ref}}}\right)^{mk} \tag{17}$$

where

$$G_1 = \frac{2(x_m - \alpha_2^2)}{1+\alpha_2^2},\ G_2 = \frac{1-\alpha_2-G_1+G_1^2}{1-R},\ G_3 = 1-G_1-G_2,\ Q = \frac{1.25(\alpha_2 - G_3 - G_2 R)}{G_1},\ R = \frac{\alpha_2 - x_m - G_1^2}{1-\alpha_2-G_1+G_1^2} \tag{18}$$

and

$$\alpha_2 = \frac{m_2}{\sqrt{m_0 m_4}},\ x_m = \frac{m_1}{m_0}\sqrt{\frac{m_2}{m_4}},\ \nu_p = \frac{1}{2\pi}\sqrt{\frac{m_4}{m_2}}. \tag{19}$$

Here, m_n is the n^{th} spectral moment, defined as:

$$m_n = \int_0^\infty \omega^n S(\omega)\mathrm{d}\omega. \tag{20}$$

The Dirlik method has previously been shown to give accurate results over a wide range of bandwidths for a stationary Gaussian process [40], and the closed-form expression makes it well-suited for efficient design optimization. However, the accuracy of the method deteriorates if the fatigue loads are dominated by a few frequency components [41].

The SN curve used for the tower base is the D curve in air taken from DNV-RP-C203 [42]. The curve is bilinear, i.e. the material parameters, and thus also the slope of the curve, change at a certain stress range. For the rainflow procedure, this is easily taken into account, however, the Dirlik method only allows for single-slope curves. Based on initial calculations, the Dirlik damage estimation is performed with material parameters valid for stress ranges above 52.63 MPa (fewer than 10^7 cycles).

5.3. Short-term extreme response

Several methods have been used to estimate the short-term extreme response of FWTs, such as the Gumbel method and Weibull tail method for global motions [15,43], and the Winterstein method for the tower base bending moment [14]. The present study uses the average upcrossing rate (AUR) method, see e.g. Naess and Gaidai [44], which previously has been shown to perform well for a bottom-fixed offshore wind turbine under combined wind and wave loading [45]. The AUR method is based on the assumption that upcrossings of high levels are statistically independent, which means that the number of upcrossings during time T will be Poisson distributed. The cumulative distribution function (CDF) of the extreme value Y may thus be written as

$$F_Y(y) = \exp\{-\nu^+(y)\,T\}, \tag{21}$$

where Y can represent an arbitrary response parameter, such as tower base bending moment, global motions of the platform, or mooring line tension. $\nu^+(y)$ is the mean upcrossing rate of level y, which can be estimated empirically from j simulated time series of length T_0:

$$\hat{\nu}^+(y) = \frac{1}{jT_0}\sum_{i=1}^{j} n_i^+(y;\,T_0) \tag{22}$$

where $n_i^+(y;\,T_0)$ is the number of upcrossings in time series i. Assuming that the appropriate asymptotic extreme value distribution for the considered response is the Gumbel distribution, the tail of the mean upcrossing rate may be written as

$$\nu^+(y) = q(y)\exp\{-a(y-b)^c\},\ y \geq y_0 \tag{23}$$

where $q(y)$ is slowly varying and can be approximated as a constant. The parameters a, b, c and q are then determined by fitting Eq. (23) to the empirical data, as described in detail by Saha and Naess [46]. This is done by minimizing the mean square error function:

$$F(a, b, c, q) = \sum_{i=1}^{N} w_i \left|\ln \hat{\nu}^+(y) - \ln q + a(y_i - b)^c\right|^2 \tag{24}$$

using the Levenberg-Marquardt least-squares optimization algorithm. w_i is a weight factor which puts more emphasis on the more reliable data points, and is found from the estimated 95% confidence interval.

The AUR method is also applicable for the linear model, where an analytical expression is available. For a stationary Gaussian process with zero mean, the upcrossing rate can be written as [26]:

$$\nu^+(y) = \nu^+(0) \exp\left\{-\frac{y^2}{2\sigma^2}\right\}, \tag{25}$$

where $\nu^+(0)$ is the mean zero-upcrossing rate, which can be found from the zeroth and second order spectral moments:

$$\nu^+(0) = \frac{1}{2\pi}\sqrt{\frac{m_2}{m_0}}. \tag{26}$$

The characteristic largest extreme response y_{1h}, i.e. the most probable maximum value in one hour, is used to compare the TD and FD models. The value is found approximately from the following relation:

$$F_Y(y_{1h}) = \mathrm{e}^{-1}. \tag{27}$$

6. Results

6.1. Natural periods

The natural periods of the linear system are estimated and compared to results from decay tests performed with the TD model in still water, as shown in Table 5. The decay tests are performed by releasing the platform from an offset position in the considered DOF, and the natural period is then found from the decaying motion. For the first bending mode, the hull is released together with the tower top, such that the coupling between platform pitch and tower bending is included.

The FD model slightly overestimates the natural periods, which for the rigid modes is found to mainly be a consequence of the simplified added mass formulation. The reason why the first bending natural frequency is better approximated for spar 1 than spar 2 can be understood by examining the eigenmodes. In Fig. 7, the bending mode from the linearized eigenvalue solution is compared to the mode shape found from a decay test in TD, where a bandpass filter around the natural frequency is used to extract the shape including one of the blades. Due to the increased stiffness of the tower in spar 2, the coupled blade-tower mode changes, and the blades undergo a larger amount of bending. The simplification of replacing the RNA by a point mass and inertia is thus less accurate than for spar 1, where the blades behave more like a rigid body in the first tower bending mode. The shape of the tower is, however, seemingly not affected by the blade behaviour, and both designs show good agreement between the decay tests and the eigenvalue solutions.

6.2. Fatigue damage

6.2.1. Linear and nonlinear estimates

Weighted 1-h fatigue damage is shown as a function of wind speed in Fig. 8. The linear predictions are seen to agree well with the TD results for spar 1, especially at wind speeds from 11 m/s and higher. For spar 2, the linear model is seen to overpredict the fatigue damage quite consistently by about 25–35%. The reasons for this overprediction are further explored in Section 6.2.2. The good agreement for spar 1 can be explained by the fact that the tower base bending moment is close to Gaussian in most of the considered environmental conditions, in particular at higher wind speeds, which are associated with larger waves. The response in these conditions is dominated by wave forces and by resonant motions, which tend to be Gaussian even for non-Gaussian loads [47].

A notable difference between the linear and nonlinear results for spar 1 is seen at 9 m/s, where the 3P frequency is very close to the natural frequency of the first bending mode, which leads to resonance and thus a significant increase in fatigue damage for the FD model. In TD, the resonance has a rather limited effect on the damage estimates, possibly due to nonlinearities in the model.

With a few exceptions, the IFT and Dirlik results agree well for all conditions in both designs. Compared to the TD model, the error in total fatigue damage is 10.6% (IFT) and 7.1% (Dirlik) for spar 1, and 30.4% (IFT) and 30.9% (Dirlik) for spar 2.

Table 5
Natural periods.

Mode	Spar 1		Spar 2	
	TD	FD	TD	FD
Surge (s)	120.55	122.22	116.80	121.67
Pitch (s)	35.48	36.39	38.29	39.81
1st bending (s)	2.41	2.42	1.79	1.85

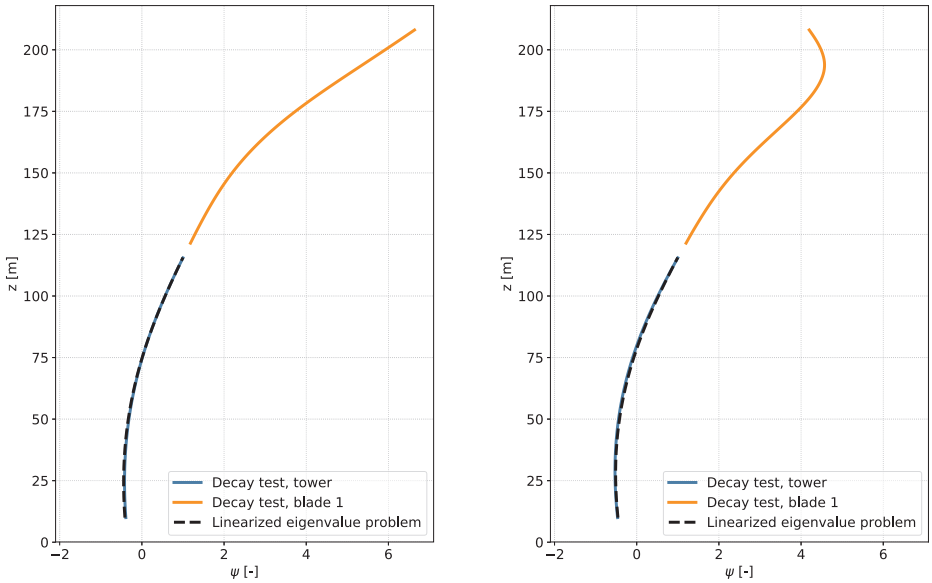

(a) Spar 1 (b) Spar 2

Fig. 7. Normalized bending mode shapes.

Scatter plots showing the calculated fatigue damage for each environmental condition in TD and FD are presented in Fig. 9, where the Dirlik results are used for the linear model. The solid black line indicates perfect agreement, while conservative FD predictions are found below the line.

The accuracy of the linear model is to a large extent insensitive to the amount of fatigue damage in the individual conditions, and the data follow a fairly straight line, with most points located within ± 10% of the line of best fit for both designs. For spar 1, this line, when neglecting the 9 m/s conditions, is very close to the diagonal. The 9 m/s results, although being highly overestimated by the linear model, are also seen to be reasonably consistent, as the ratio between the linear and nonlinear estimates is more or less constant with increasing damage.

For spar 2, all points are located below the 1:1 line, and as for spar 1, the conditions with the largest discrepancies between linear and nonlinear predictions are in general found at lower wind speeds (5–9 m/s). These wind speeds are associated with low sea states, and little excitation of the bending mode. The tower base bending moment is thus dominated by the low-frequency wind response, which is less accurately predicted by the linear model than the wave- and bending-frequency response. The low-frequency response in the linear model is also somewhat sensitive to how the thrust force spectrum is estimated, as reported by Kvittem and Moan [10]. It should be noted that these conditions are associated with relatively small bending moments, and their contribution to the total fatigue damage over the lifetime of the structure is thus not significant.

The limited scatter in the data for both designs suggest that it is possible to simulate a small number of environmental conditions in the TD to verify and, if necessary, calibrate a linear model which can be used to perform the full long-term analysis. The verification cases should cover the entire wind speed range, as resonance effects may have a large impact on the accuracy of the model. In addition, a 1 m/s interval for the wind speed bins may be needed to correctly capture the response around possible resonance wind speeds [35].

6.2.2. *Sensitivity to errors in natural frequency*

From the tower base stress spectra in Fig. 10, the reason for the general overprediction in fatigue damage by the linear model for spar 2 is obvious: the response in the region of the first bending mode is captured quite well by the linear model for spar 1, but is significantly overestimated for spar 2. The wave-frequency response is accurately estimated for both designs, whereas the low-frequency response is underpredicted at the pitch resonance frequency, mainly due to interaction between platform motion and the wind turbine controller in the TD model. Due to the limited number of cycles, however, the low-frequency response has little influence on the fatigue damage in the tower compared to the wave- and bending-frequency responses.

The overestimation of the response around the natural frequency of the first bending mode originates mainly from the small error in estimated natural period for the bending mode discussed in Section 6.1, as the wind excitation loads vary significantly with frequency in this region. In Fig. 11, the natural frequencies found from FD and TD are shown together with the transfer functions for thrust force and rotor moment at 21 m/s mean wind speed. From the figure, one clearly sees that the loads are reduced when the

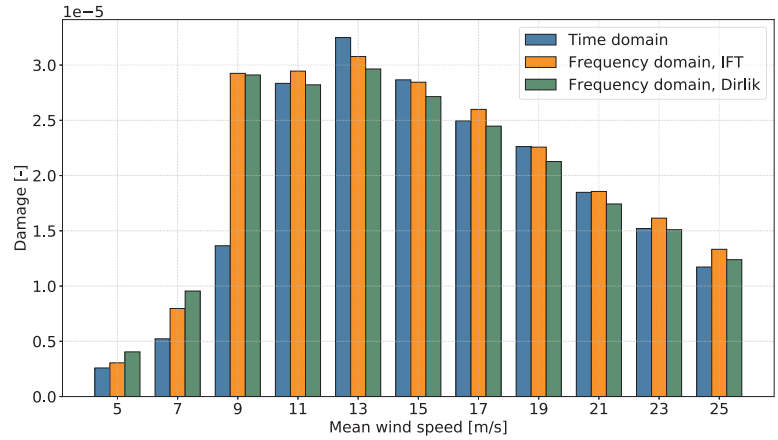

(a) Spar 1.

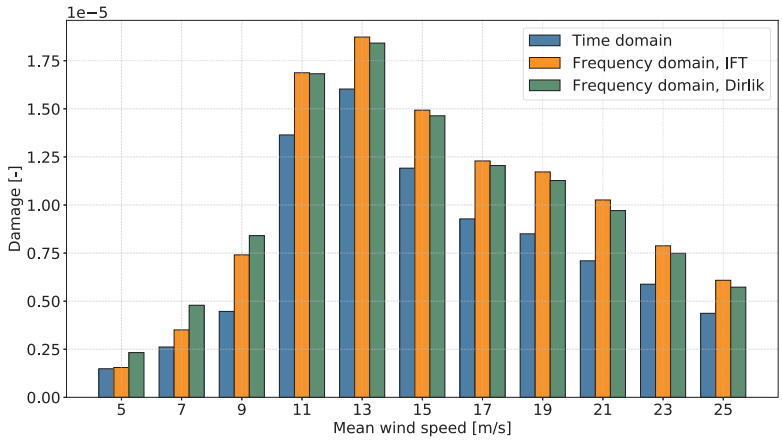

(b) Spar 2.

Fig. 8. 1-h weighted fatigue damage arranged by wind speed.

natural frequency for spar 2 is increased. The effect is most prominent for the rotor moment, which is about 25% lower at the TD natural frequency than at the natural frequency found from the linearized eigenvalue solution.

To quantify the importance of this error on the fatigue damage results, the natural period of the bending mode is shifted from 1.85 s to 1.79 s in the linear model by adding an artificial stiffness term, and the fatigue analysis is rerun. The results, presented in Fig. 12, show a large improvement at most wind speeds, and the total fatigue damage error is reduced by approximately 50%. This highlights the importance of having accurate estimates for the natural frequency and shape of the first bending mode, which is dependent on how well the RNA can be approximated as a rigid body. In an optimization process, the accuracy of the model simplification may vary as changes are made to the design, however, this can be taken into account by a straightforward calibration of the natural frequency in the linear model.

The eigenmode in tower bending depends on wind speed, due to increased blade stiffness caused by centrifugal forces and pitching of the blades, as well as changes in the mean platform pitch angle. This is illustrated in Fig. 13, where mode shapes from decay tests are shown for calm air and 21 m/s uniform wind. As a consequence, the natural frequency of the bending mode is slightly increased by 2–3% at higher wind speeds. In addition, the mode shape derivative at the tower top is reduced by up to 20%.

From Fig. 11, an increase in the natural frequency of the bending mode is seen to result in higher wind loads for spar 1. However, this effect is counteracted by the decrease in the tower top derivative, which reduces the generalized wind load caused by the rotor moment (see Eq. (10)). For spar 2, on the other hand, both effects reduce the wind excitation loads for the bending mode, and cause the tuned linear model to somewhat overestimate the fatigue damage at higher wind speeds, as observed in Fig. 12.

Regarding the bending-frequency response, it should also be mentioned that, even though no validation has been performed, the

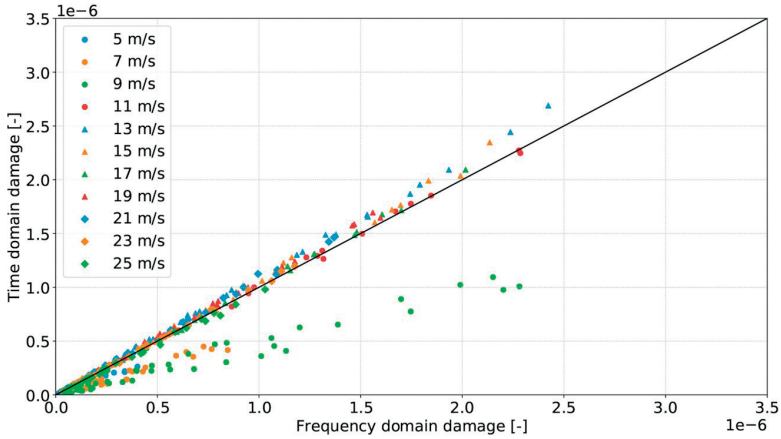

(a) Spar 1.

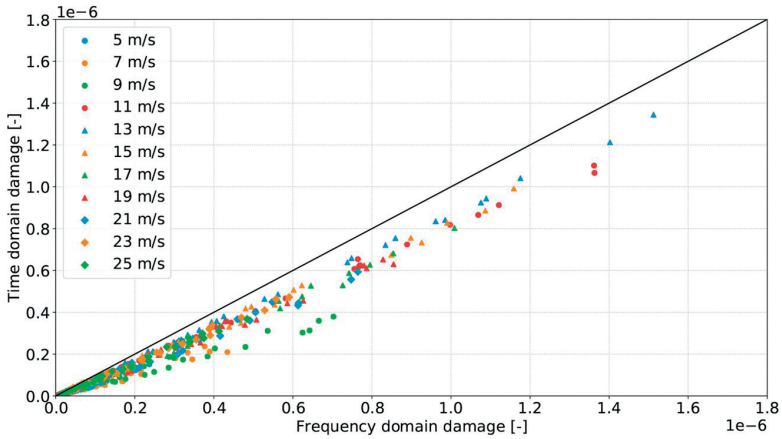

(b) Spar 2.

Fig. 9. Time and frequency domain fatigue damage for individual ECs.

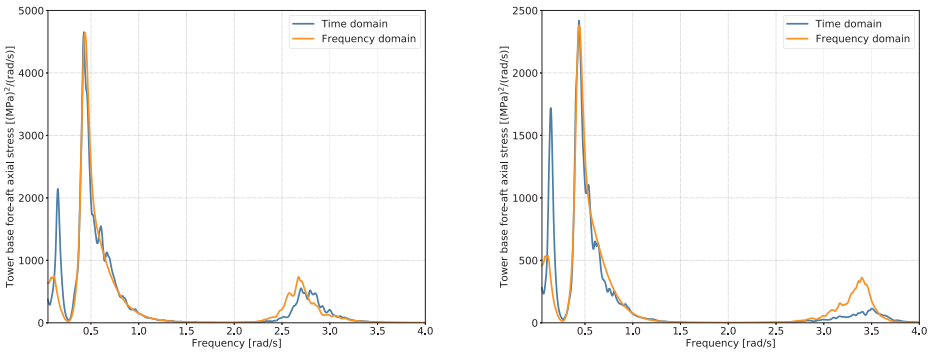

(a) Spar 1 (b) Spar 2

Fig. 10. Tower base stress response spectrum for $U = 21$ m/s, $H_s = 7.5$ m, $T_p = 14.5$ s.

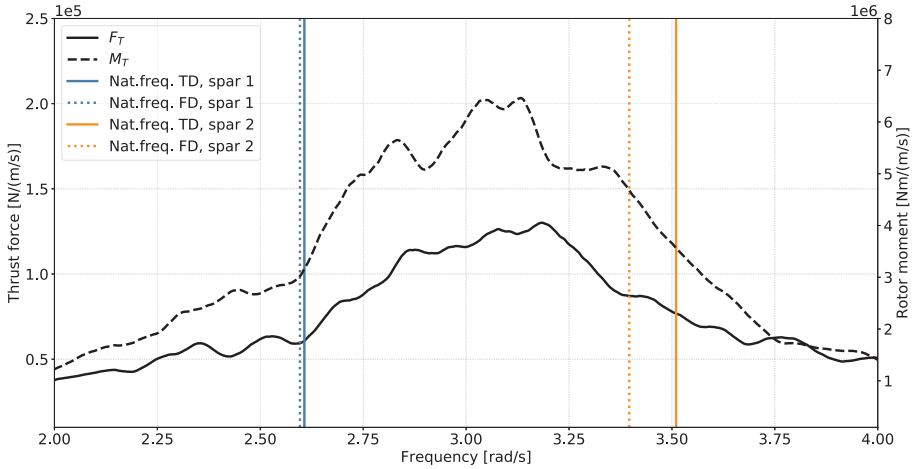

Fig. 11. Wind excitation transfer functions around first bending natural frequency, $U = 21$ m/s.

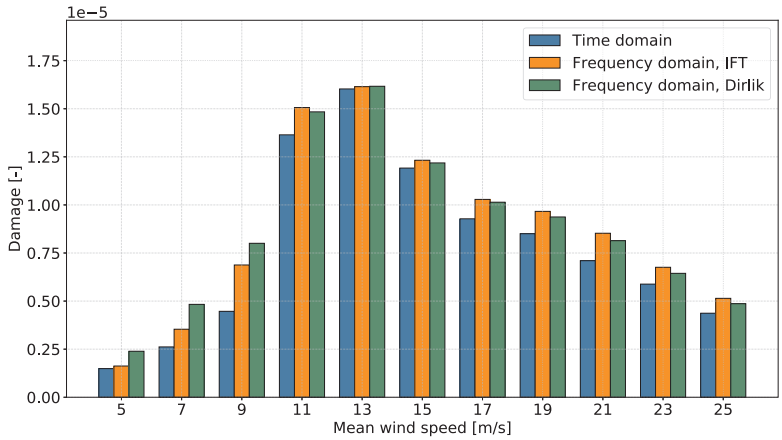

Fig. 12. 1-h weighted fatigue damage arranged by wind speed, spar 2 with tuned natural frequency for first bending mode.

present study assumes that the behaviour of the physical system is described correctly by the TD model. Full-scale measurements from the Hywind Demo FWT [48] have shown that the tower base bending moment response spectra contain energy around the first tower bending mode and that the numerical models thus capture real effects, however, the actual level of the response is sensitive to the modelling of the system, and may therefore not be correctly represented in the simulations.

6.3. Extreme value prediction

The short-term extreme response of the system in the four 50-year environmental conditions is calculated for the tower base bending moment, as well as for the surge and pitch motions of the platform. The results are presented in the following subsections.

6.3.1. Tower base bending moment

Response statistics for the tower base bending moment in the 50-year conditions are listed in Table 6. For a Gaussian process, the skewness is equal to zero, while the Pearson's kurtosis is equal to 3. The skewness and kurtosis values for the tower base bending moment suggest that the responses in EC 2–4 are very close to Gaussian, which is expected, as the bending moments in conditions above cut-out are completely dominated by wave loading, whereas the response in operational conditions with high wind speeds is governed by a combination of wave forces and resonance. The response in EC 1 exhibits some non-Gaussian behaviour due to the large aerodynamic thrust near rated wind speed, however, the degree of nonlinearity is small. In this context, it should also be emphasized that the TD model only includes first order wave loads, with the exception of viscous forces arising from the drag term in Morison's equation.

The standard deviations are accurately predicted by the linear model in all conditions, with relative errors between −2.9% and

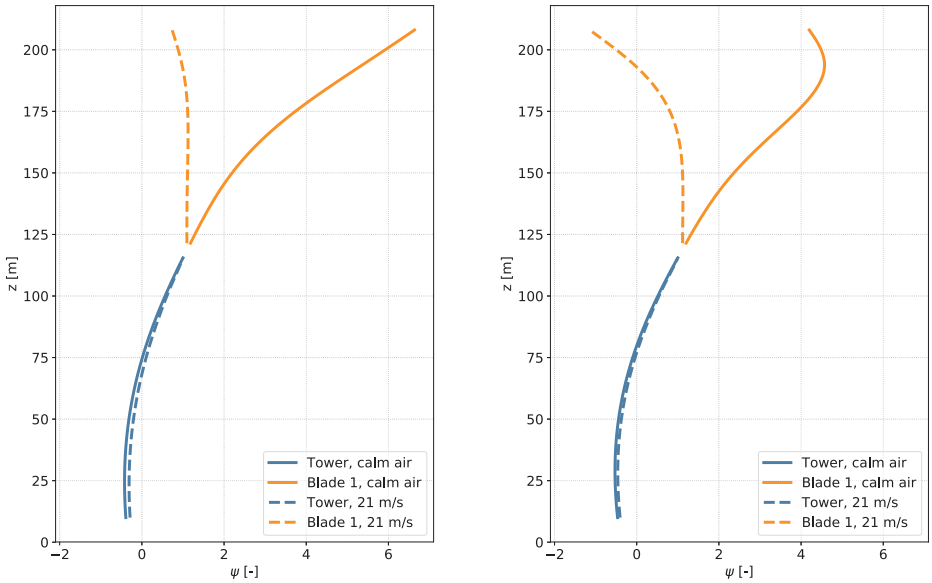

(a) Spar 1 (b) Spar 2

Fig. 13. Normalized bending mode shapes in calm air and for $U = 21$ m/s. Natural periods found from decay tests are 2.41 s (calm air) and 2.35 s (21 m/s) for spar 1, and 1.79 s (calm air) and 1.75 s (21 m/s) for spar 2.

Table 6
Tower base bending moment statistics, 50-year environmental conditions.

Model	Statistical quantity[a]	Spar 1				Spar 2			
		Condition				Condition			
		1	2	3	4	1	2	3	4
Time domain	Mean (MNm)	247.2	123.0	50.3	105.2	305.7	152.9	63.6	132.8
	Std.dev. (MNm)	89.1	101.0	106.5	118.8	103.8	106.2	115.5	129.7
	Skewness	−0.20	−0.03	−0.01	0.01	−0.30	−0.04	−0.01	0.01
	Kurtosis	3.03	3.00	3.00	3.01	3.13	3.00	3.01	3.01
Frequency domain	Mean (MNm)	260.8	127.8	52.3	101.3	329.4	161.4	66.5	128.9
	Std.dev. (MNm)	89.4	100.8	106.3	115.1	104.8	110.6	118.4	128.5

[a] Time domain results are averaged over 20 seeds.

4.1%. The mean moments are somewhat less accurate, with the largest errors of 5.5% (spar 1) and 7.8% (spar 2) occurring in EC 1, near rated wind speed, where also the largest mean values are found.

Empirical upcrossing rates are plotted together with optimized curve fits and Gaussian upcrossing rates based on the FD results in Figs. 14 and 15. The plots show the multiplication factor κ, which is related to the extreme response, y, through the relation

$$y = \mu + \kappa\sigma, \tag{28}$$

where μ and σ are the mean and standard deviation of the process. The characteristic largest 1-h extreme for a given environmental condition, which is used in the comparison, corresponds to an upcrossing rate of 2.78×10^{-4}.

The Gaussian upcrossing rates are seen to be conservative for EC 1, due to the slightly nonlinear behaviour which becomes more prominent as the bending moments increase. In the parked conditions, on the other hand, the response is linear also at lower upcrossing rates, and the empirical data are well-described by the linear model.

For spar 1, the FD solution is seen to follow the optimized curve fit closely in EC 2, however, larger discrepancies are observed for spar 2. The fact that the shape of the fitted curve is captured quite well, suggests that the error is related to the overprediction of the bending response discussed in the previous section. As the bending mode is located at a relatively high frequency, the response level has significant influence on the second order spectral moment. Consequently, the mean zero-upcrossing rate (see Eq. (26)) is overestimated by 29% compared to the TD model, which causes a right shift in the linear upcrossing rate curve as observed in Fig. 15b.

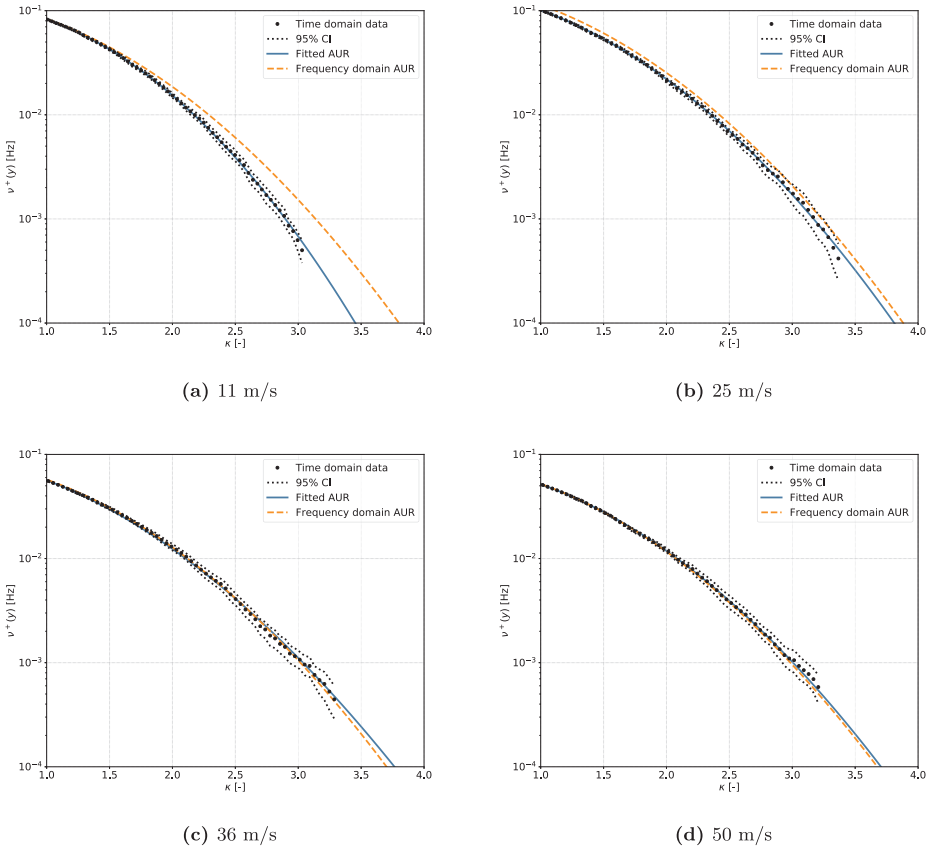

(a) 11 m/s (b) 25 m/s

(c) 36 m/s (d) 50 m/s

Fig. 14. Tower base bending moment upcrossing rates for spar 1.

The calculated 1-h extreme bending moments are listed in Table 7. The linear estimates give reasonably good approximations of the extreme response, particularly for EC 2–4, as indicated by the upcrossing results.

Due to the high mean value caused by the thrust force, the largest extreme response is found in EC 1. However, this may not be the case in general, and previous studies comparing short-term extremes in selected operational and survival conditions have shown that the largest tower base bending moments for a spar FWT can occur in storm conditions with extreme wind speeds [49,50]. The critical load cases may vary with floater design and turbine size, as it alters the ratio between wind and wave loads, and for long-term extremes, the probability of the conditions must be taken into account. The most critical operational condition is also not necessarily associated with maximum thrust force on the turbine. In a recent study by Sultania and Manuel [51], the largest 50-year tower base bending moment for a 5 MW spar FWT, considering only operational cases, was found for a mean wind speed of 21.7 m/s. This suggests that a wider range of environmental conditions should be considered in an actual design process.

6.3.2. Global motions

Tables 8 and 9 list extreme response statistics for surge and pitch, respectively. The global motions show similar behaviour to the tower base bending moments, but as a larger part of the response is located in the low-frequency range, there is less agreement between the TD and FD results for the standard deviations. The values are in general found to be underestimated by the linear model, with errors up to about 20% for both surge and pitch.

As for the bending moments, the upcrossing rates for the global motions (Appendix B) are accurately described by the Gaussian curves in EC 2–4, while the nonlinear behaviour in EC 1 results in conservative predictions by the linear model. For both spar designs, some slight nonlinearities are also seen at higher wind speeds, which causes the linear model to underestimate κ at lower upcrossing rates. The discrepancies are likely caused by the aerodynamic drag forces on the tower, which, although they mostly affect the mean position of the FWT, also become more important for the dynamic response as the wind speed increases. The good agreement for the surge motions in the parked conditions suggests that the viscous hydrodynamic forces on the hull contribute little to the motion response.

The resulting characteristic largest 1-h extreme values are listed in Tables 10 and 11. As expected, the most severe global motions are also found in EC 1. The pitch response, which shows the most pronounced non-Gaussian behaviour near rated wind speed, has the

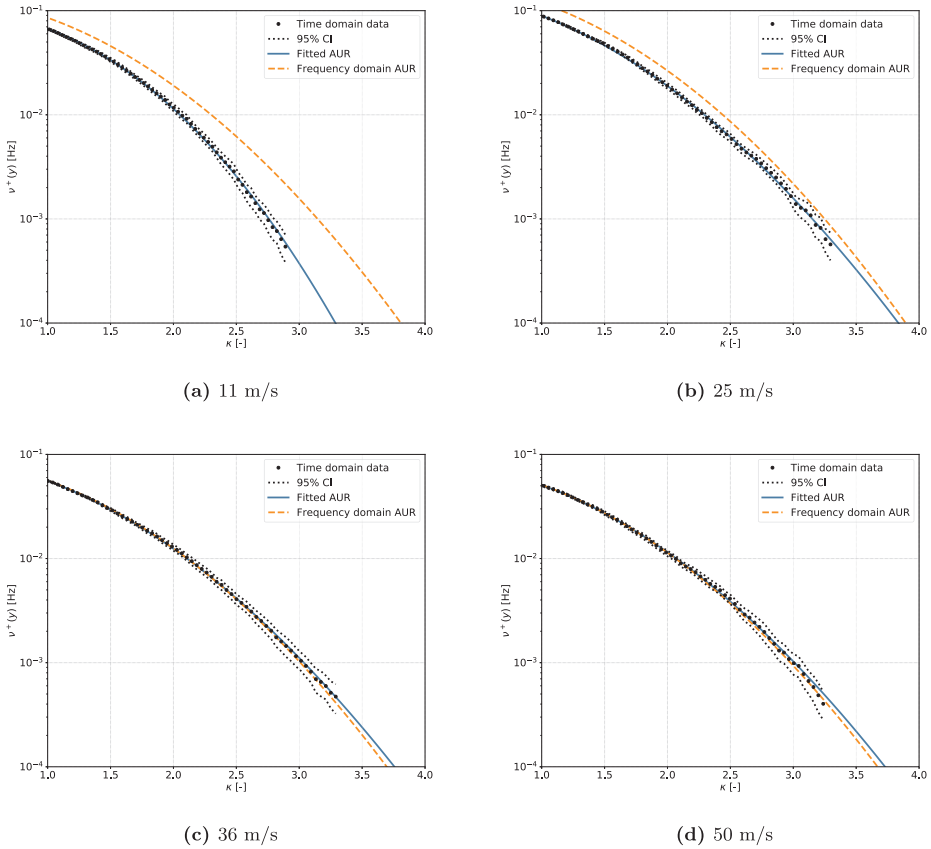

(a) 11 m/s (b) 25 m/s

(c) 36 m/s (d) 50 m/s

Fig. 15. Tower base bending moment upcrossing rates for spar 2.

Table 7
Characteristic largest extreme tower base bending moment y_{1h}, 50-year environmental conditions.

Model	Spar 1				Spar 2			
	Condition				Condition			
	1	2	3	4	1	2	3	4
Time domain (MNm)	534.2	480.6	418.7	509.8	624.1	529.6	462.6	577.4
Frequency domain (MNm)	575.7	491.7	415.4	491.3	699.3	562.0	469.9	563.3
Relative error (%)	7.8	2.3	−0.8	−3.6	12.0	6.1	1.6	−2.4

least accurate linear predictions in this condition. Large discrepancies are also seen in the most extreme wave condition (EC 4), mostly due to underestimation of the standard deviations in FD. For the surge motions, the extremes found from FD generally agree well with the TD simulations. Most notable are the results in EC 1, especially for spar 1, where the relative error between FD and TD is only −1%. However, this result is somewhat coincidental, as it is a consequence of the error in κ being almost exactly balanced out by the errors in μ and σ. Nonetheless, the results suggest that the extreme surge motions may be predicted with roughly the same accuracy as the tower base bending moments, despite larger discrepancies in the standard deviations, as the mean values account for a larger share of the total extreme response.

The accuracy of the linear model depends on the importance of nonlinearities in the system, which will vary with location, floater geometry, and different operational conditions. Therefore, the results presented here cannot be generalized to any FWT, and the FD model should be continuously verified against state-of-the-art tools during a design process. The agreement with nonlinear analyses also depends on how the system is represented in the TD model, and care should be taken to make sure that relevant nonlinearities are included.

Table 8
Platform surge response statistics, 50-year environmental conditions.

Model	Statistical quantity[a]	Spar 1				Spar 2			
		Condition				Condition			
		1	2	3	4	1	2	3	4
Time domain	Mean (m)	27.3	13.8	8.0	15.1	23.7	12.0	6.6	13.7
	Std.dev. (m)	6.9	2.4	2.9	4.6	6.2	2.2	2.7	3.9
	Skewness	−0.14	−0.02	0.05	−0.03	−0.13	−0.01	0.01	0.06
	Kurtosis	2.49	2.90	3.03	3.06	2.57	2.95	3.02	2.97
Frequency domain	Mean (m)	28.6	14.1	7.9	15.3	26.1	12.8	7.0	13.6
	Std.dev. (m)	5.4	2.3	2.5	3.5	5.2	2.2	2.5	3.5

[a] Time domain results are averaged over 20 seeds.

Table 9
Platform pitch response statistics, 50-year environmental conditions.

Model	Statistical quantity[a]	Spar 1				Spar 2			
		Condition				Condition			
		1	2	3	4	1	2	3	4
Time domain	Mean (deg)	6.7	3.4	1.7	3.4	9.2	4.6	2.2	4.4
	Std.dev. (deg)	1.8	1.0	1.2	1.7	2.4	1.3	1.3	2.1
	Skewness	−0.62	0.03	0.04	0.10	−0.72	0.03	0.03	0.10
	Kurtosis	3.37	2.90	3.02	2.99	3.54	2.92	2.99	3.02
Frequency domain	Mean (deg)	7.2	3.5	1.7	3.2	10.0	4.9	2.2	4.3
	Std.dev. (deg)	1.7	1.0	1.0	1.4	2.3	1.2	1.2	1.7

[a] Time domain results are averaged over 20 seeds.

Table 10
Characteristic largest extreme surge response y_{1h}, 50-year environmental conditions.

Model	Spar 1				Spar 2			
	Condition				Condition			
	1	2	3	4	1	2	3	4
Time domain (m)	44.2	21.4	17.8	29.4	38.6	19.0	15.7	26.4
Frequency domain (m)	43.8	21.4	16.1	26.6	40.7	20.0	15.1	24.9
Relative error (%)	−1.0	0.0	−9.5	−9.4	5.4	5.4	−3.6	−5.7

Table 11
Characteristic largest extreme pitch response y_{1h}, 50-year environmental conditions.

Model	Spar 1				Spar 2			
	Condition				Condition			
	1	2	3	4	1	2	3	4
Time domain (deg)	10.7	6.7	5.5	9.1	14.4	8.6	6.6	11.3
Frequency domain (deg)	12.3	6.6	5.0	7.7	16.7	8.7	6.0	9.8
Relative error (%)	14.8	−0.9	−9.4	−14.9	16.2	−4.9	−8.9	−13.2

7. Conclusions

A semi-analytical FD model has been developed, which allows for efficient preliminary design optimization of spar FWTs. The model has been verified against a fully coupled nonlinear TD model for two different 10 MW spar designs, with regards to fatigue damage in the tower base and short-term extreme response in both operational and survival conditions. The fatigue results show that the FD model is accurate in most environmental conditions, especially for spar 1, where the long-term fatigue damage is

overestimated by 7%. For spar 2, larger discrepancies are observed, and the linear model overpredicts the damage by approximately 30%. This is found to primarily be caused by errors in the response around the first bending mode, which is highly sensitive to the estimated natural frequency. The accuracy depends on how well the RNA can be approximated as a rigid body for the first bending mode, however, tuning the frequency by adding an artificial stiffness term can be performed in the case where the approximation leads to unacceptable errors.

For 9 m/s mean wind speed, the 3P frequency of the rotor coincides with the natural frequency of the first bending mode for spar 1, which leads to increased damage values and causes the linear model to significantly overpredict the response. The sensitivity with regards to wind speed also suggests that a finer discretization of the wind bins should be applied in a design process, to accurately capture the response around possible resonances. The accuracy of the linear model is found to be fairly independent of wave height and wave period, also for the wind speed which induces 3P resonance with the first tower bending frequency. This indicates that a small number of environmental conditions, which cover the full wind speed range, can be simulated with a TD model to verify and possibly tune the linear model, which then can be used to carry out the full long-term analysis.

The extreme response, both with regards to tower base bending moment and rigid body motions in surge and pitch, is seen to be nearly Gaussian near cut-out and in parked conditions, as it is dominated by wave forces. This results in good agreement for the linear model in these conditions. The largest extremes values are found in EC 1, near rated wind speed, which indicates that a wider range of environmental conditions may be important for the extreme response. The large aerodynamic forces in this condition also introduce some non-Gaussian behaviour, which causes the linear model to overestimate the multiplication factors (κ). However, as the mean values in this condition are relatively large, the inaccuracies in the total extreme response are reduced, and the total error in y_{1h} is within 16% for all considered responses in this condition. Regarding the standard deviations, good agreement between the linear and nonlinear models is obtained for the tower base bending moments, while larger discrepancies are seen for surge and pitch. The reason for this is that the global motions are more dependent on the low-frequency (wind-induced) response, which is less accurately captured by the linear model than the wave- and bending-frequency response. The TD model in the present study only includes first order wave forces, and could thus be improved by also considering higher order loads, which may be important for certain FWT concepts. The model should also be validated through comparisons with physical measurements.

The developed FD model is shown to be well-suited for preliminary design. It gives reasonable agreement with a fully coupled nonlinear TD model, both with regards to fatigue and extreme response, and the semi-analytical approach provides an efficient way to explore the design space. In addition, the closed-form expressions offers the possibility of using analytic gradients in a computer-aided optimization process. However, the efficiency of the model is partly due to the simple geometry of the platform, and the formulations are thus not valid for more complex platform designs, where more comprehensive numerical calculations may be necessary. Also, the approach is only applicable for steady-state conditions, and transient events, which also must be considered, cannot be analysed. Nonetheless, it can serve as a useful complement to more sophisticated models in the design process of spar-type FWTs, and significantly reduce the needed computational effort.

A Transfer functions

A.1 Wave elevation to tower base bending moment

The transfer function from wave elevation to tower base bending moment is given in Eq. (A.1). The equation considers bending moments due to inertial forces in the tower and RNA, aerodynamic damping forces, and gravitational forces.

$$\begin{aligned} H_{\zeta M}(\omega) = &- \int_{z_{\mathrm{TB}}}^{z_{\mathrm{top}}} m(z)\mathbf{H}_{\zeta\ddot{X}}^{\top}(\omega)\boldsymbol{\psi}(z)(z - z_{\mathrm{TB}})\mathrm{d}z - M_{\mathrm{RNA}}\mathbf{H}_{\zeta\ddot{X}}^{\top}(\omega)\boldsymbol{\psi}(z_{\mathrm{top}})(z_{\mathrm{top}} - z_{\mathrm{TB}}) \\ &- I_{\mathrm{RNA}}\mathbf{H}_{\zeta\ddot{X}}^{\top}(\omega)\boldsymbol{\psi}_{,z}(z_{\mathrm{top}}) - B_{\mathrm{aero}}\mathbf{H}_{\zeta\dot{X}}^{\top}(\omega)\boldsymbol{\psi}(z_{\mathrm{top}})(z_{\mathrm{top}} - z_{\mathrm{TB}}) \\ &+ \int_{z_{\mathrm{TB}}}^{z_{\mathrm{top}}} m(z)g\mathbf{H}_{\zeta X}^{\top}(\omega)[\boldsymbol{\psi}(z) - \boldsymbol{\psi}(z_{\mathrm{TB}})]\mathrm{d}z + M_{\mathrm{RNA}}g\mathbf{H}_{\zeta X}^{\top}(\omega)[\boldsymbol{\psi}(z_{\mathrm{top}}) - \boldsymbol{\psi}(z_{\mathrm{TB}})] \end{aligned} \tag{A.1}$$

A.2 Wind speed to tower base bending moment

The transfer function from wind speed to tower base bending moment is given in Eq. (A.2). The equation considers bending moments due to inertial forces in the tower and RNA, aerodynamic damping forces, gravitational forces, and wind excitation forces.

$$\begin{aligned} H_{UM}(\omega) = &- \int_{z_{\mathrm{TB}}}^{z_{\mathrm{top}}} m(z)\mathbf{H}_{U\ddot{X}}^{\top}(\omega)\boldsymbol{\psi}(z)(z - z_{\mathrm{TB}})\mathrm{d}z - M_{\mathrm{RNA}}\mathbf{H}_{U\ddot{X}}^{\top}(\omega)\boldsymbol{\psi}(z_{\mathrm{top}})(z_{\mathrm{top}} - z_{\mathrm{TB}}) \\ &- I_{\mathrm{RNA}}\mathbf{H}_{U\ddot{X}}^{\top}(\omega)\boldsymbol{\psi}_{,z}(z_{\mathrm{top}}) - B_{\mathrm{aero}}\mathbf{H}_{\zeta\dot{X}}^{\top}(\omega)\boldsymbol{\psi}(z_{\mathrm{top}})(z_{\mathrm{top}} - z_{\mathrm{TB}}) \\ &+ \int_{z_{\mathrm{TB}}}^{z_{\mathrm{top}}} m(z)g\mathbf{H}_{UX}^{\top}(\omega)[\boldsymbol{\psi}(z) - \boldsymbol{\psi}(z_{\mathrm{TB}})]\mathrm{d}z + M_{\mathrm{RNA}}g\mathbf{H}_{UX}^{\top}(\omega)[\boldsymbol{\psi}(z_{\mathrm{top}}) - \boldsymbol{\psi}(z_{\mathrm{TB}})] \\ &+ F_T(\omega)(z_{\mathrm{top}} - z_{\mathrm{TB}}) + M_T(\omega) \end{aligned} \tag{A.2}$$

B Upcrossing rates for global motions

B.1 Surge

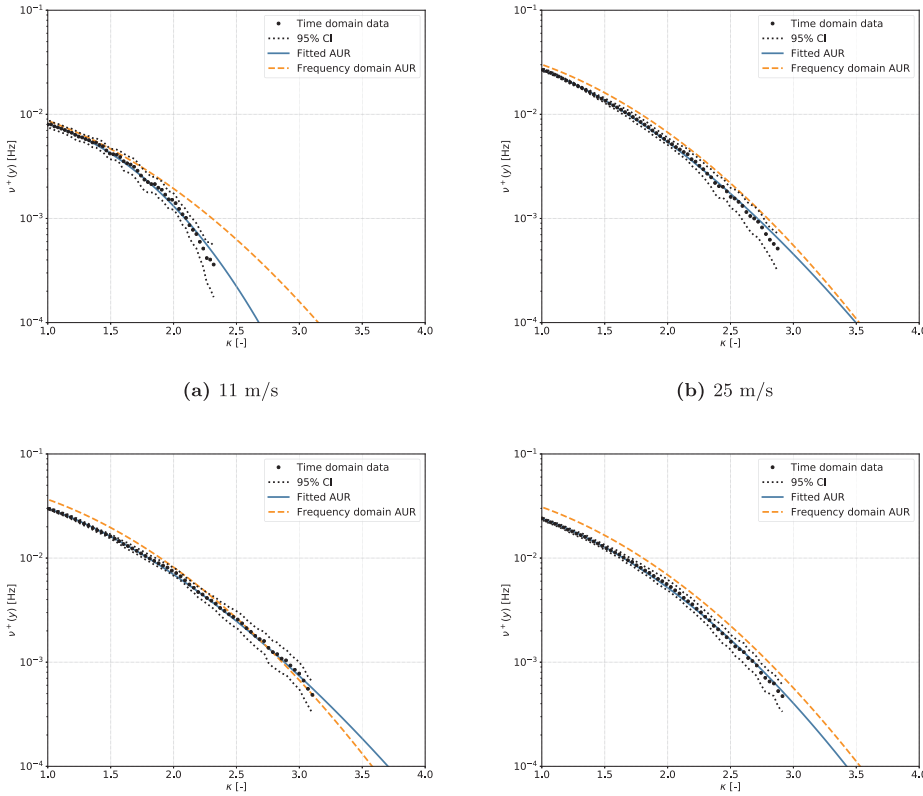

(a) 11 m/s **(b)** 25 m/s

(c) 36 m/s **(d)** 50 m/s

Figure B.1. Platform surge upcrossing rates for spar 1.

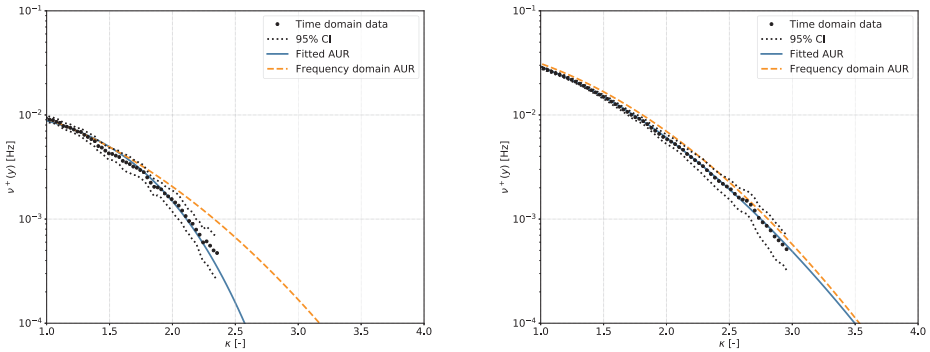

(a) 11 m/s **(b)** 25 m/s

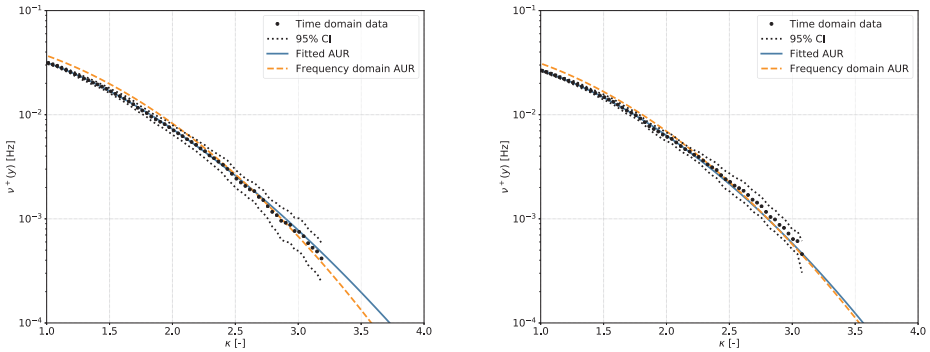

(c) 36 m/s **(d)** 50 m/s

Figure B.2. Platform surge upcrossing rates for spar 2.

B.2 Pitch

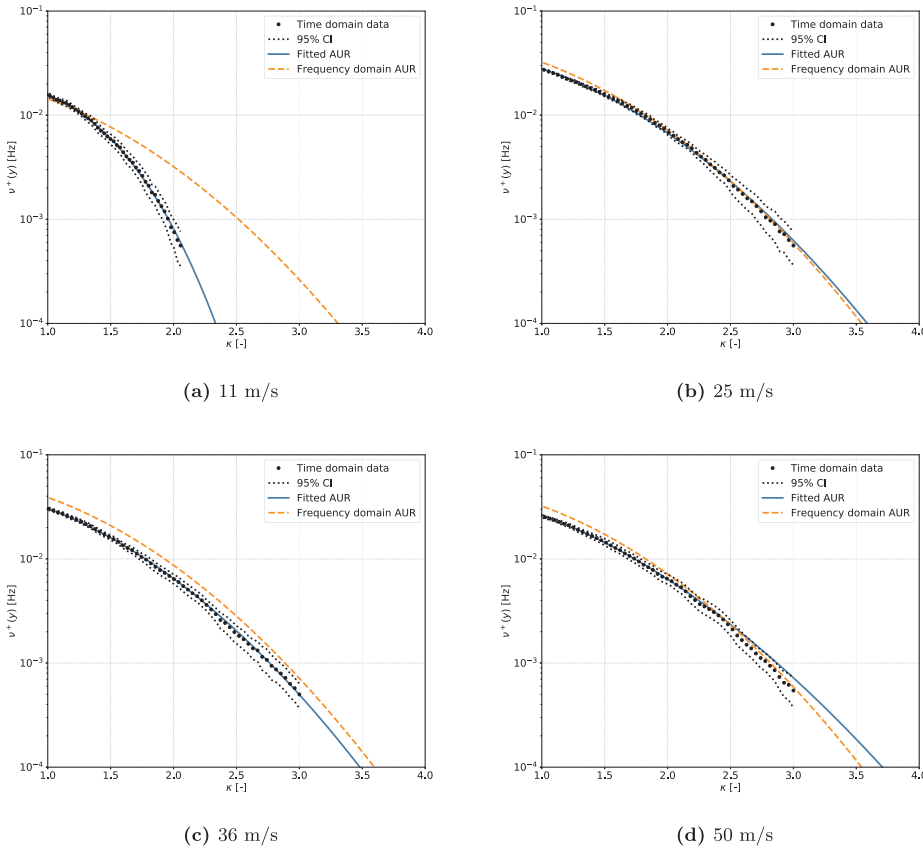

(a) 11 m/s **(b)** 25 m/s

(c) 36 m/s **(d)** 50 m/s

Figure B.3. Platform pitch upcrossing rates for spar 1.

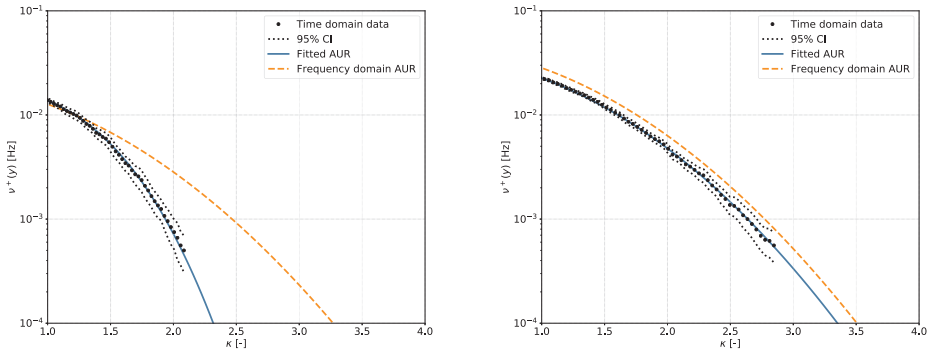

(a) 11 m/s (b) 25 m/s

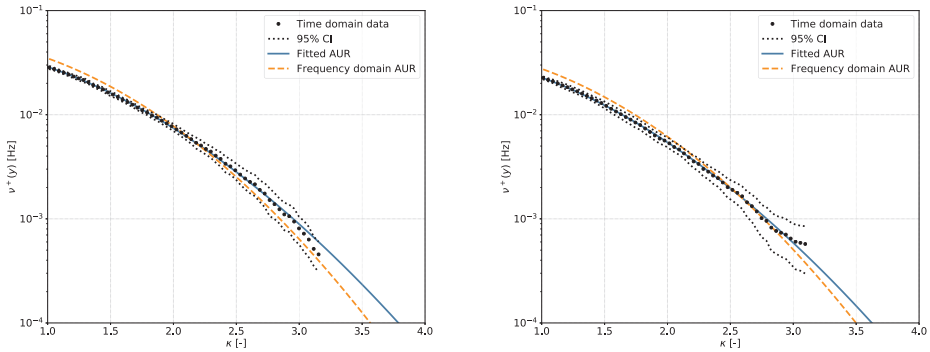

(c) 36 m/s (d) 50 m/s

Figure B.4. Platform pitch upcrossing rates for spar 2.

Funding

This research did not receive any specific grant from funding agencies in the public, commercial, or not-for-profit sectors.

References

[1] Strach-Sonsalla M, Muskulus M. Dynamics and design of floating wind turbines. Proceedings of the twenty-sixth (2016) international ocean and polar engineering conference (ISOPE2016), rhodes, Greece. 2016.
[2] DNV. Environmental Conditions and Environmental Loads. 2014. Tech. rep. DNV-RP-C205.
[3] DNV. Design of Floating Wind Turbine Structures. 2013. Tech. rep. OS-J103.
[4] Wayman EN, et al. Coupled dynamic modeling of floating wind turbine systems. Offshore technology conference. 2006.
[5] Sclavounos P, Tracy C, Lee S. Floating offshore wind turbines: responses in a seastate pareto optimal designs and economic assessment". proceedings of the ASME 27th international conference on offshore mechanics and arctic engineering (OMAE2008), estoril, Portugal. 2008.
[6] Philippe M, Babarit A, Ferrant P. Comparison of time and frequency domain simulations of an offshore floating wind turbine. Proceedings of the ASME 2011 30th international conference on ocean, offshore and arctic engineering (OMAE2011), rotterdam, The Netherlands. 2011.
[7] Wang K, et al. Frequency domain approach for the coupled analysis of floating wind turbine system. Ships Offshore Struct 2017;12(6):767–74.
[8] Bachynski EE, Moan T. Linear and nonlinear analysis of tension leg platform wind turbines. Proceedings of the twenty-second (2012) international offshore and polar engineering conference (ISOPE2012), rhodes, Greece. 2012.
[9] Bachynski EE. Design and dynamic analysis of tension leg platform wind turbines PhD thesis Norwegian University of Science and Technology; 2014
[10] Kvittem MI, Moan T. Frequency versus time domain fatigue analysis of a semisubmersible wind turbine tower. J Offshore Mech Arctic Eng 2014;137:1.
[11] Kluger JM, Sapsis TP, Slocum AH. A reduced-order, statistical linearization approach for estimating nonlinear floating wind turbine response statistics". Proceedings of the twenty- sixth (2016) international ocean and polar engineering conference (ISOPE2016), rhodes, Greece. 2016.
[12] Jonkman J. Definition of the Floating System for Phase IV of OC3. National Renewable Energy Laboratory; 2010. Tech. rep. NREL/TP-500-47535.
[13] Matha D. Model development and loads analysis of an offshore wind turbine on a tension leg platform, with a comparison to other floating turbine concepts MA thesis University of Colorado - Boulder; 2009
[14] Karimirad M, Moan T. Extreme dynamic structural response analysis of catenary moored spar wind turbine in harsh environmental conditions. J Offshore Mech Arctic Eng 2011;133.
[15] Aggarwal N, Manikandan R, Saha N. Nonlinear short term extreme response of spar type floating offshore wind turbines". Ocean Eng 2017;130:199–209.
[16] Bak C, et al. Description of the DTU 10 MW Reference Wind Turbine. 2013. Tech. rep. DTU Wind Energy Report-I-0092. DTU Wind Energy.

[17] MARINTEK. RIFLEX user guide. 2016.
[18] MARINTEK. SIMO user guide. 2016.
[19] Wamit Inc. WAMIT user manual. 2014.
[20] Roald L, et al. The effect of second-order hydrodynamics on floating offshore wind turbines. Energy Procedia 2013;35:253–64.
[21] Duarte T, Sarmento AJ, Jonkman J. Effects of second-order hydrodynamic forces on floating offshore wind turbines". 32nd ASME wind energy symposium, national harbor, Maryland. 2014.
[22] Ormberg H, Bachynski EE. Global analysis of floating wind turbines: code development, model sensitivity and benchmark study. Proceedings of the twenty-second (2012) international offshore and polar engineering conference (ISQPE2012), rhodes, Greece. 2012.
[23] Robertson A, et al. Offshore code comparison collaboration continuation within IEA wind task 30: phase II results regarding a floating semisubmersible wind system. Proceedings of the ASME 2014 33rd international conference on ocean, offshore and arctic engineering (OMAE2014), San Francisco, California, USA. 2014.
[24] Nielsen FG, Hanson TD, Skaare B. Integrated dynamic analysis of floating offshore wind turbines. Proceedings of OMAE 2006 25th international conference on offshore mechanics and arctic engineering, hamburg, Germany. 2006.
[25] Larsen TJ, Hanson TD. A method to avoid negative damped low frequent tower vibrations for a floating, pitch controlled wind turbine. J Phys Conf 2007;75. 012073.
[26] Naess A, Moan T. Stochastic dynamics of marine structures. Cambridge University Press; 2013.
[27] Newman JN. Marine hydrodynamics. The MIT Press; 1977.
[28] MacCamy RC, Fuchs RA. Wave Forces on Piles: a diffraction Theory Tech rep. Technical memorandum 69 Beach erosion board; Corps of Engineers; 1954.
[29] van der Tempel J. Design of support structures for offshore wind turbines" PhD thesis TU Delft; 2006
[30] Salzmann DJC, van der Tempel J. Aerodynamic damping in the design of support structures for offshore wind turbines". Proceedings of the offshore wind energy conference, copenhagen, Denmark. 2005.
[31] Borgman LE. Ocean wave simulation for engineering design. J Waterw Harb Div 1969;95(4):557–86.
[32] Faltinsen OM. Sea loads on ships and offshore structures. Cambridge University Press; 1990.
[33] Johannessen K, Meling TS, Haver S. Joint distribution for wind and waves in the Northern North sea. Int J Offshore Polar Eng 2002;12(1):1–8.
[34] IEC. Design requirements for Offshore Wind Turbines. 2009. Tech. rep. IEC 61400-3.
[35] Kvittem MI, Moan T. Time domain analysis procedures for fatigue assessment of a semi- submersible wind turbine. Mar Struct 2015;40:38–59.
[36] Jonkman BJ, Kilcher L. TurbSim user's guide: version 1.50 Tech. rep. NREL/TP-500-46198 National Renewable Energy Laboratory; 2009.
[37] Bachynski EE, et al. Dynamic analysis of floating wind turbines during pitch actuator fault, grid loss, and shutdown. Energy Procedia 2013;35:210–22.
[38] Jiang Z, Karimirad M, Moan T. Dynamic response analysis of wind turbines under blade pitch system fault, grid loss, and shutdown events. Wind Energy 2014;17:1385–409.
[39] Dirlik T. Application of computers in fatigue analysis" PhD thesis University of Warwick; 1985
[40] Gao Z, Moan T. Frequency-domain fatigue analysis of wide-band stationary Gaussian processes using a trimodal spectral formulation. Int J Fatig 2008;30:10–1. 1944–1955.
[41] Ragan P, Manuel L. Comparing estimates of wind turbine fatigue loads using time-domain and spectral methods". Wind Eng 2007;31(2):83–99.
[42] DNV. Fatigue Design of Offshore Steel Structures. 2010. Tech. rep. DNV-RP-C203.
[43] Aggarwal N, Manikandan R, Saha N. Predicting short term extreme response of spar offshore floating wind turbine". Procedia Eng 2015;116(1):47–55.
[44] Naess A, Gaidai O. Monte Carlo methods for estimating the extreme response of dynamical systems. J Eng Mech 2008;134(8):628–36.
[45] Saha N, et al. Short-term extreme response analysis of a jacket supporting an offshore wind turbine. Wind Energy 2014;17:87–104.
[46] Saha N, Naess A. Monte Carlo-based method for predicting extreme value statistics of uncertain structures. J Eng Mech 2010;136(12):1491–501.
[47] Kvittem MI, et al. Short-term fatigue analysis of semi-submersible wind turbine tower. Proceedings of the ASME 2011 30th international conference on ocean, offshore and arctic engineering (OMAE2011), rotterdam, The Netherlands. 2011.
[48] Skaare B, et al. Analysis of measurements and simulations from the Hywind Demo floating wind turbine. Wind Energy 2015;18:1105–22.
[49] Karimirad M, Moan T. Wave- and wind-induced dynamic response of a spar-type offshore wind turbine. J Waterw Port, Coast Ocean Eng 2012;138(1):920.
[50] Muliawan MJ, et al. Extreme responses of a combined spar-type floating wind turbine and floating wave energy converter (STC) system with survival modes. Ocean Eng 2013;65:7182.
[51] Sultania A, Manuel L. Reliability analysis for a spar-supported floating offshore wind turbine. Wind Eng 2018;42(1):51–65.

Paper 2

Frequency-dependent aerodynamic damping and inertia in linearized dynamic analysis of floating wind turbines

Carlos Eduardo S. Souza, John Marius Hegseth and Erin E. Bachynski

Journal of Physics: Conference Series, 2020

Frequency-Dependent Aerodynamic Damping and Inertia in Linearized Dynamic Analysis of Floating Wind Turbines

Carlos Eduardo S Souza, John Marius Hegseth and Erin E Bachynski

Department of Marine Technology, Norwegian University of Science and Technology, 7491 Trondheim, Norway

E-mail: carlos.souza@ntnu.no

Abstract. In frequency-domain (FD) models of floating wind turbines (FWT), it is common to regard the interaction between nacelle motions and thrust by means of a constant aerodynamic damping coefficient. This approach is effective at higher motions frequencies, but does not consider interactions between nacelle motions and the blade pitch control system. As a result, the motions and loads at frequencies closer to the controller bandwidth may be underpredicted. A remedy for this problem is to include the linearized thrust expression in the FD model, such that the dynamic effects related to control are considered. In this paper, these dynamic effects are related to frequency-dependent damping and inertia terms. Expressions for damping and inertia coefficients are obtained with two different methods, and then included in the FD model. The resulting responses are compared to those obtained with the constant damping coefficient method, and also with coupled time-domain simulations of a semi-submersible 10 MW FWT. The better performance of the FD model with frequency-dependent inertia and damping coefficients encourages the adoption of the linearized thrust approach for representing the interaction between nacelle motions, thrust and control system.

1. Introduction

Frequency-domain (FD) methods can be helpful in the design of floating wind turbines (FWTs), providing responses for a large number of loading conditions with relatively low computational time. Previous work has indicated that the response of FWTs in moderate environmental conditions may be estimated reasonably well using FD models [1, 2, 3]. However, their reliability depends on an accurate prediction of loads and interactions with linearized models.

An especially interesting interaction takes place between nacelle motions and the rotor thrust. Fluctuations in the nacelle's horizontal velocity provoke changes in the flow through the rotor, leading to oscillations in the rotor speed and thrust. An aerodynamic damping effect results from this interaction, and is normally included in FD models by means of a constant aerodynamic damping coefficient. This coefficient may be obtained from the thrust derivative w.r.t. the relative wind speed [1, 3, 4], or by means of decay simulations of the FWT under different incident wind speeds [2].

This method is convenient to implement due to its relative simplicity, and is normally adopted in combination with the frequency-dependent thrust obtained for a fixed wind turbine, installed on the top of the tower. A disadvantage of this approach is that the interactions of the nacelle

motions with the blade pitch control system are not considered, an effect that is known to reduce the damping or even render it negative [5, 6, 7], besides introducing an inertia effect [8]. As a consequence, the damping effect can be significantly overpredicted at frequencies close to the controller bandwidth, if the constant coefficient is used.

Control system effects can be included in an FD model by means of linearization of the thrust and torque. The rotor speed is then included as an additional degree of freedom, and the blade-pitch controller can be written in terms of the system states [9].

The objective of the present work is to relate the linearized thrust equations to the above-mentioned inertia and damping effects, providing a visualization of how those effects vary with wind speed and frequency for a given control system.

The aerodynamic inertia and damping coefficients are calculated both from the linearized thrust equations and from simulations where the nacelle is forced to oscillate with different frequencies, under uniform wind. The obtained coefficients are then included in an FD model of a semi-submersible 10 MW FWT. The responses predicted with the different methods for obtaining the coefficients are compared to coupled time-domain simulations, where the thrust is calculated with the blade element momentum (BEM) theory.

Section 2 presents the frequency domain model for the FWT; Section 3 introduces the thrust linearization procedure and provides formulations for the frequency-dependent aerodynamic inertia and damping coefficients; the time-domain simulations are explained in Section 4, and the results are presented in Section 5; final discussions and conclusions are provided in Section 6.

2. Frequency-domain analysis of FWT

The frequency domain model used in the present work consists of three degrees-of-freedom (DOFs), namely surge, heave, and pitch. The potential-theory hydrodynamic model is the same as the one adopted in the time-domain simulations, presented in Section 4. Viscous excitation is neglected, but viscous damping on the platform is added using stochastic linearization of the drag term in Morison's equation, where the standard deviation of the velocity along the length of the columns and pontoons is found using an iteration scheme.

The stiffness matrix includes both hydrostatic restoring and linearized mooring forces. The mooring stiffness matrix is a function of the mean offset, based on static equilibrium between mooring forces and mean thrust.

Transfer functions from wind speed to thrust force, $F_{UT}(\omega)$, are obtained for each mean wind speed as the squared root of the ratio between the spectrum of thrust time series, obtained from simulations with turbulent wind on a fixed turbine, and the incoming wind spectrum. The wind force vector is then found as

$$\mathbf{F}_U(\omega) = \begin{bmatrix} F_{UT}(\omega) & 0 & z_{hub}F_{UT}(\omega) \end{bmatrix}^\top , \tag{1}$$

where z_{hub} is the hub height above still water level (SWL). Transfer functions from wave and wind input to platform response, $\mathbf{H}_{\zeta X}(\omega)$ and $\mathbf{H}_{UX}(\omega)$ respectively, are expressed as

$$\mathbf{H}_{\zeta X}(\omega) = \mathbf{H}_{FX}(\omega)\mathbf{F}_\zeta(\omega),\ \mathbf{H}_{UX}(\omega) = \mathbf{H}_{FX}(\omega)\mathbf{F}_U(\omega)\,, \tag{2}$$

where

$$\mathbf{H}_{FX}(\omega) = \left[-\omega^2(\mathbf{M} + \mathbf{A}(\omega)) + i\omega\mathbf{B}(\omega) + \mathbf{K}\right]^{-1} \tag{3}$$

is the frequency response function matrix. After solving for the platform motions, the tower base bending moment response is found by considering dynamic equilibrium.

Using the wind and wave spectra, the response spectrum for an arbitrary response parameter ξ is then expressed as

$$S_\xi(\omega) = |H_{\zeta\xi}(\omega)|^2 S_\zeta(\omega) + |H_{U\xi}(\omega)|^2 S_U(\omega)\,. \tag{4}$$

3. Aerodynamic damping and inertia effects

The FD model described in Section 2 neglects the variations in the thrust caused by the FWT motions. The interactions between thrust and FWT motions are often represented by a constant damping coefficient, which is added to the matrix **B** in equation (3). This approach neglects the controller action. When the controller is included, its effect results in frequency-dependent damping and inertia coefficients, as shown further below.

3.1. Thrust linearization without controller

A common way to calculate the aerodynamic damping in FD models [1, 4, 3] is to linearize the thrust with respect to the relative wind speed at hub height, v, at different mean incoming wind speeds, U_w, considering no change in the blade pitch angle or rotor speed. Using a first order Taylor series expansion, the thrust is then expressed as

$$T = T_0 + \frac{\partial T}{\partial v}\Delta v\,. \tag{5}$$

Let the nacelle dynamics be represented by an 1-DOF, 1$^{\text{st}}$-order system:

$$m\ddot{x} + c\dot{x} + kx = T\,. \tag{6}$$

Uniform, non-turbulent wind is assumed for now. Recalling that $v = U_w - \dot{x}$, it is noted that $\Delta v = v - U_w = -\dot{x}$. Replacing (5) in (6), the damping effect becomes clear:

$$m\ddot{x} + \left(c + \frac{\partial T}{\partial v}\right)\dot{x} + kx = T_0\,, \tag{7}$$

and the coefficient, b_{aer}, can be expressed as

$$b_{aer} = \frac{\partial T}{\partial v}\,. \tag{8}$$

The damping effect estimated with this method considers the change in the steady-state thrust for a small perturbation in the uniform wind speed seen by the rotor, while neglecting the effect of the control system and rotor dynamics. Different coefficients are obtained for each incident wind velocity, but they are constant with respect to the nacelle frequency of oscillation. This method is relatively simple to use and normally provides satisfactory results when the turbine oscillates in a frequency range distant from the controller bandwidth. For lower frequencies of oscillation, interaction with the control system takes place and the damping coefficient dependence on frequency becomes more important.

3.2. Thrust linearization including controller

A more comprehensive method, which captures effects from the wind turbine controller, may be used by including the rotor speed DOF and control system in the FD model, and also linearizing the thrust with respect to rotor speed, Ω, and blade pitch angle, β:

$$T = T_0 + T_v\Delta v + T_\Omega\Delta\Omega + T_\beta\Delta\beta\,, \tag{9}$$

where the index indicates partial derivative w.r.t. the indicated variable, i.e., $A_B = \frac{\partial A}{\partial B}$. In order to find the damping coefficient, Equation (9) must be written in terms of $\dot{x}$ only. First, the aerodynamic torque, Q, is also given in its linearized version:

$$Q = Q_0 + Q_v\Delta v + Q_\Omega\Delta\Omega + Q_\beta\Delta\beta\,, \tag{10}$$

In addition, the rotor dynamics are given by

$$I_d\dot{\Omega} = Q - N_g E\,, \tag{11}$$

where I_d is the drivetrain inertia, N_g is the gear ratio and E is the electrical (generator) torque, here assumed as constant above rated wind speed. In equilibrium, $Q_0 = N_g E$, so replacing (10) in (11):

$$I_d\dot{\Omega} = Q_v\Delta v + Q_\Omega\Delta\Omega + Q_\beta\Delta\beta\,. \tag{12}$$

It is assumed that a PI controller commands the blade pitch angle, i.e.,

$$\Delta\beta = K_p\Delta\Omega + K_i\int\Delta\Omega dt\,, \tag{13}$$

where K_p and K_i are the proportional and integral controller gains. Equations (9) and (12) are now rewritten replacing $\Delta\beta$ as given in (13), and noting that $\Delta\Omega = \dot{\phi}$, where ϕ is the rotor azimuth angle:

$$T = T_0 - T_v\dot{x} + (T_\Omega + K_pT_\beta)\,\dot{\phi} + K_iT_\beta\phi\,, \tag{14}$$

$$I_d\ddot{\phi} - (Q_\Omega + K_pQ_\beta)\,\dot{\phi} - K_iQ_\beta\phi = -Q_v\dot{x}\,. \tag{15}$$

Assuming harmonic oscillation, Equation (15) can be written in the frequency domain, and the following transfer function between $x(\omega)$ and $\phi(\omega)$ is obtained:

$$\phi(\omega) = \frac{i\omega Q_v}{I_d\omega^2 + (Q_\Omega + K_pQ_\beta)\,i\omega + K_iQ_\beta}x(\omega) = C(\omega)x(\omega)\,. \tag{16}$$

The nacelle dynamics (Equation 6) are now written in terms of T as given in (14), and also expressed in the frequency domain, with $\phi(\omega)$ as given in (16):

$$\left\{-m\omega^2 + i\omega c + k + \underbrace{i\omega T_v - [(T_\Omega + K_pT_\beta)\,i\omega + K_iT_\beta]\,C(\omega)}_{-\omega^2 a_{aer}(\omega) + i\omega b_{aer}(\omega)}\right\}x(\omega) = T_0\,. \tag{17}$$

Based on the assumption that T responds harmonically to harmonic oscillations of the nacelle, the thrust can be written as a combination of terms proportional to the nacelle acceleration and velocity [8]. This assumption is further discussed in Section 3.3, but an immediate consequence is the definition of frequency-dependent, aerodynamic inertia and damping coefficients:

$$a_{aer}(\omega) = -\frac{1}{\omega^2}\,\mathrm{Re}\left\{i\omega T_v - [(T_\Omega + K_pT_\beta)\,i\omega + K_iT_\beta]\,C(\omega)\right\} \tag{18}$$

$$b_{aer}(\omega) = \frac{1}{\omega}\,\mathrm{Im}\left\{i\omega T_v - [(T_\Omega + K_pT_\beta)\,i\omega + K_iT_\beta]\,C(\omega)\right\} \tag{19}$$

3.3. Forced oscillations

The thrust and torque derivatives in Section 3 can be calculated analytically, based on the BEM equations, or numerically, using e.g. the central differences method. Both techniques assume that the thrust and torque respond immediately to changes in v, Ω and β, while in reality the time constants associated with rotor dynamics, aerodynamics, and control system, can be relevant when the nacelle moves at frequencies close to the controller bandwidth.

An alternative method to find the $a_{aer}(\omega)$ and $b_{aer}(\omega)$ coefficients is through simulations of forced nacelle oscillations, with aerodynamics calculated nonlinearly and under influence of

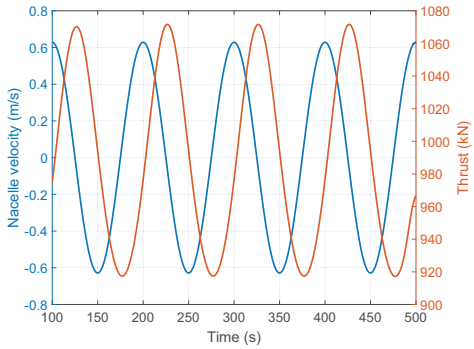

Figure 1: Thrust response to oscillations of the DTU 10 MW wind turbine, under constant incident wind speed of 13.0 m/s and period of oscillation of 100.0 s.

the control system. When the turbine oscillates harmonically, the thrust also oscillates nearly harmonically, but with a phase relative to the nacelle velocity. This can be seen in Figure 1, where the DTU 10 MW wind turbine is forced to oscillate with period 100.0 s and under constant incident wind speed of 13.0 m/s. The thrust can then be assumed to be composed of a mean plus an oscillating component:

$$T = T_0 + T_{osc}(U_w, \omega)\,. \tag{20}$$

Writing the nacelle velocity $\dot{x}$ as

$$\dot{x} = v_0 \cos(\omega t)\,, \tag{21}$$

the oscillating part of the thrust can then be assumed to be given by [8]

$$\begin{aligned} T_{osc} &= f_0 v_0 \cos(\omega t + \alpha) \\ &= f_0 \left[v_0 \cos(\omega t)\cos(\alpha) - v_0 \sin(\omega t)\sin(\alpha)\right] \\ &= f_0 \cos(\alpha)\dot{x} + \frac{f_0 \sin(\alpha)}{\omega}\ddot{x}\,. \end{aligned} \tag{22}$$

The amplifying factor f_0 and the phase α between nacelle velocity and thrust depend on the dynamic effects mentioned above, and are not straightforward to determine analytically. However, for a given turbine and control system they vary with the incident wind speed and frequency of oscillation, while motion amplitude does not seem to have a significant influence. They can therefore be obtained from forced oscillations covering the ranges of interest for both parameters. Fast Fourier transforms (FFTs) of the nacelle velocity and thrust are calculated, and f_0 and α can be directly obtained from the ratio between amplitudes or phases of both FFTs at the period of interest. Formulations for the aerodynamic inertia and damping coefficients are then directly determined from equation (23):

$$a_{aer}(U_w, \omega) = -\frac{f_0 \sin(\alpha)}{\omega}\,, \quad b_{aer}(U_w, \omega) = -f_0 \cos(\alpha)\,, \tag{23}$$

3.4. Coefficients calculation and comparison

The aerodynamic inertia and damping coefficients were obtained both from the linearized thrust and the forced oscillations method. For the former case, the thrust and torque derivatives were

obtained from the linearized BEM equations. For the latter, forced oscillations of the DTU 10 MW wind turbine were performed with a simulator which obtains aerodynamic loads from AeroDyn [10], updates the blade pitch angle based on the same controller strategy presented in Section 4, and updates the rotor speed based on the rotor dynamics as in Equation (11). Oscillation periods varied from 20.0 s to 130.0 s, and uniform wind with the three velocities in Table 3 was considered. The BEM formulation with dynamic stall is adopted for the AeroDyn calculations.

The coefficients obtained with both approaches are shown in Figures 2 and 3. In spite of the oscillatory character of the curves obtained with the oscillation method, the agreement between both methods looks satisfactory, especially for higher wind velocities. The inertia effect is of the order of 1% of the mass of typical FWTs, resulting in negligible consequences for the surge dynamics. The contribution to the moment of inertia in pitch is however considerable, due to the nacelle height. Important changes in the pitch natural period can then result, as shown in [8]. The constant damping coefficients as obtained in equation (5) are also plotted in Fig. 3, showing that the discrepancy w.r.t. the frequency-dependent coefficients is larger for lower frequencies and higher wind velocities.

3.5. The aerodynamic inertia and damping effects on the FWT dynamics

It was already shown that the fluctuations in the aerodynamic thrust resulting from the nacelle motions may be treated as frequency-dependent inertia and damping effects. The derivation assumed non-turbulent wind, under the hypothesis that the fluctuations in the apparent wind flow in the rotor due to turbulence can be decoupled from those caused by the nacelle motions.

Under the same assumption, the fluctuations in the thrust due to nacelle oscillations can now be added to the FD model presented in Section 2. This is done by noting that, from Equations (22) and (23), the oscillating component of the thrust can be written as

$$T_{osc} = -a_{aer}\ddot{x} - b_{aer}\dot{x}\,. \tag{24}$$

The following aerodynamic and damping matrices, $\mathbf{A_{aer}}$ and $\mathbf{B_{aer}}$, are then defined:

$$\mathbf{A_{aer}}(\omega) = \begin{bmatrix} a_{aer}(\omega) & 0 & a_{aer}(\omega)z_{hub} \\ 0 & 0 & 0 \\ a_{aer}(\omega)z_{hub} & 0 & a_{aer}(\omega)z_{hub}^2 \end{bmatrix}, \quad \mathbf{B_{aer}}(\omega) = \begin{bmatrix} b_{aer}(\omega) & 0 & b_{aer}(\omega)z_{hub} \\ 0 & 0 & 0 \\ b_{aer}(\omega)z_{hub} & 0 & b_{aer}(\omega)z_{hub}^2 \end{bmatrix}. \tag{25}$$

$\mathbf{A_{aer}}$ and $\mathbf{B_{aer}}$ are now summed to $\mathbf{A}$ and $\mathbf{B}$ in equation (3), which includes the effect of nacelle motion in the FD analysis.

4. Simulations

The platform considered is the OO-Star 10 MW [11], a semi-submersible concept designed for the LIFES50+ project. The main properties are summarized in Table 1. The potential-theory hydrodynamic loads are generated with WADAM, and viscosity is added in form of the Morison drag term. The platform is installed at a water depth of 130.0 m, and the mooring system consists on a simplified 3-catenary line arrangement, which differs from the original of taut lines with clump weights.

The DTU 10 MW turbine (Table 2) is installed at the top of the tower, at a height of 118.4 m. The blade-pitch controller corresponds to the PI formulation of Equation (13), i.e., the power error contribution of the original controller [12] is not included. The controller gains are tuned such that its bandwidth is below the pitch natural period, and a gain scheduling strategy corrects the gains according to the current blade pitch angle.

The time-domain simulations were performed with SIMA, a workbench which allows for coupled analyses between floating bodies and slender elements [14, 15]. The platform, nacelle

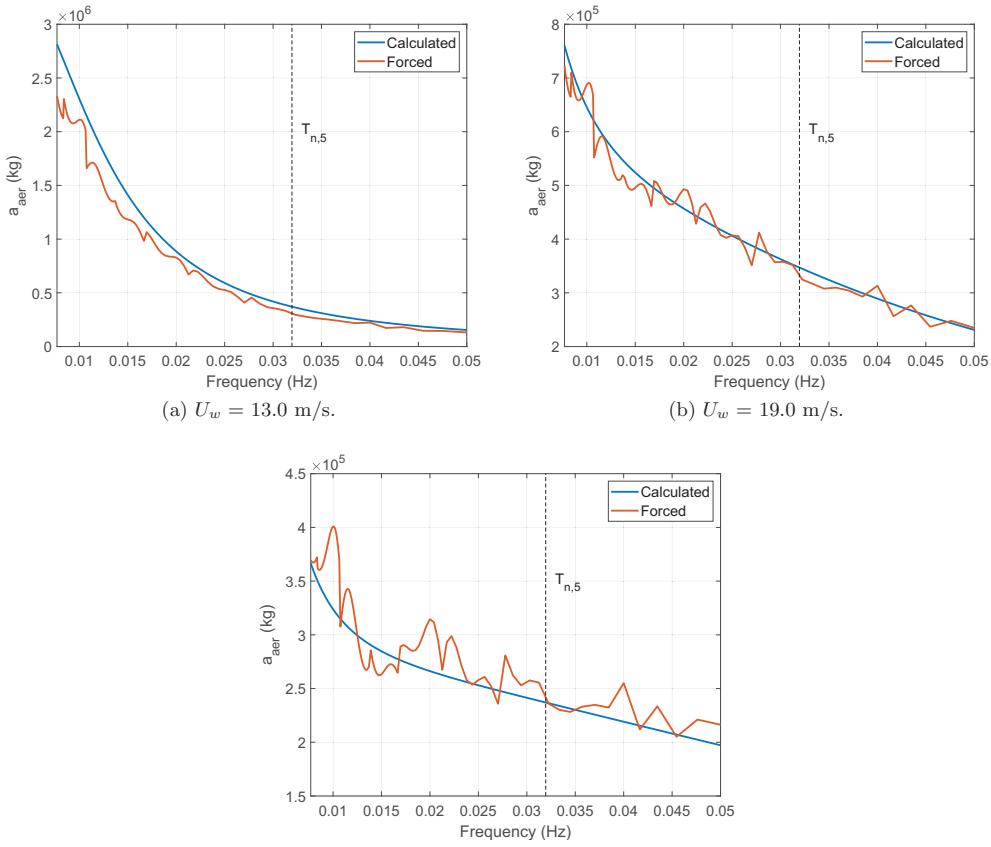

(a) $U_w = 13.0$ m/s.

(b) $U_w = 19.0$ m/s.

(c) $U_w = 25.0$ m/s.

Figure 2: Aerodynamic inertia coefficients, calculated with the linearized approach or obtained from the forced oscillations method.

Draft, D (m)	22.0
Total mass, m_{tot} (kg)	2.36×10^7
Center of gravity, VCG (m)	-7.9
Surge nat. per., T_1 (s)	181.8
Pitch nat. per., T_5 (s)	31.3

Table 1: Main properties of the OO-Star 10 MW FWT [11].

and hub are modeled as rigid bodies, while the blades, tower and mooring lines are modeled as flexible structures, with finite elements. The aerodynamics are based on the BEM theory, with dynamic stall and dynamic wake effects based on Øye's models [16]. Hub and tip losses are modeled with the Prandtl factor, and Glauerts correction is applied for high induction factors. The environmental conditions are listed in Table 3. Turbulent wind was generated with TurbSim [17], using the IEC Kaimal spectrum with turbulence characteristic B (moderate). A JONSWAP

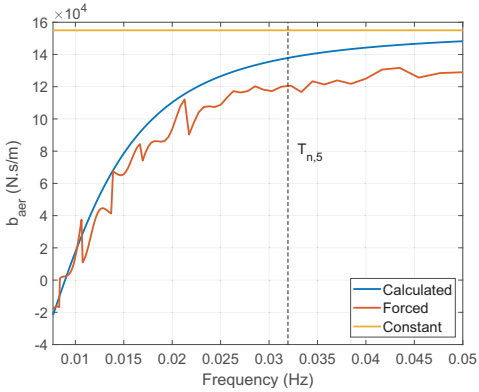

(a) $U_w = 13.0$ m/s.

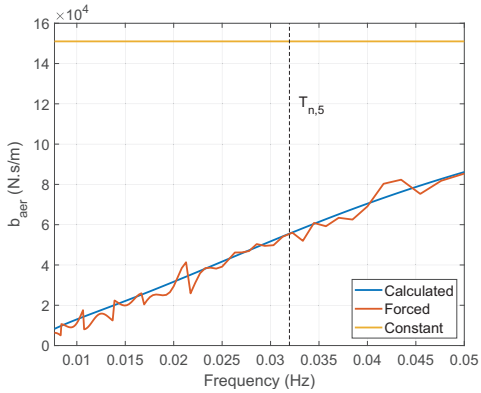

(b) $U_w = 19.0$ m/s.

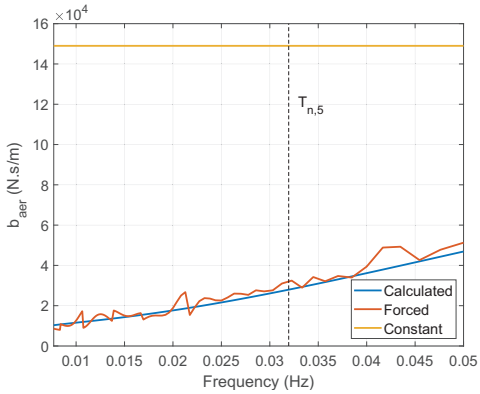

(c) $U_w = 25.0$ m/s.

Figure 3: Aerodynamic damping coefficients, calculated with the linearized approach (both constant and frequency-dependent) or obtained from the forced oscillations method.

Rotor radius, R (m)	89.2
Rated rotor speed, Ω_0 (rad/s)	1.0
Drivetrain inertia, I_d (kg.m^2)	1.6×10^8
Gear ratio, N_g (-)	50
Rotor-nacelle assemble mass, m_{RNA} (kg)	6.7×10^5
Proportional controller gain, K_p (s)	0.1794
Integral controller gain, K_i (-)	0.0165

Table 2: Main properties of the DTU 10MW wind turbine [13]. The controller gains refer to $\beta = 0°$.

wave spectrum with a γ factor of 3.3 was used to describe the sea state. The simulations lasted for one hour, which showed to provide a sufficient number of LF oscillations for the analysis. Only one realization of each condition was considered.

	U_w (m/s)	H_s (m)	T_p (s)
C1	13.0	2.7	10.3
C2	19.0	4.0	11.1
C3	25.0	5.8	12.1

Table 3: Environmental conditions.

5. Results

Figure 4 shows the frequency-domain pitch response for the three conditions in Table 3, obtained with time-domain simulations in SIMA; and with the FD model from Section 2, using the different approaches for including the aerodynamic damping and inertia effects, as presented in Section 3. When the constant damping coefficient from Equation (8) is adopted, the method is referred to as *FD constant*; with the frequency-dependent inertia and damping coefficients as given by Equations (18) and (19), the approach is named *FD calculated*; and when the coefficients are obtained from the forced harmonic oscillations, as in Equation (23), the *FD forced* identifier is adopted.

The curves indicate that the adoption of a constant damping coefficient overestimates the damping effect at lower frequencies, resulting in significantly underpredicted resonant response for frequencies below 0.05 Hz. When frequency-dependent coefficients are adopted, however, the situation is the opposite: the damping effect is underestimated, resulting in higher response for lower frequencies. Using the coefficients based on the forced oscillations leads to improved results in comparison with those obtained from the linearized thrust equations, in terms of the pitch motion standard deviation (Table 4). All three methods perform equivalently in the wave-frequency range (0.05-0.15 Hz), where the response is underpredicted due to the absence of viscous excitation in the FD model.

Similar conclusions can be obtained regarding the tower-base bending moment (Figure 5). The most remarkable difference in comparison with the plots for the pitch response is for $U_w = 13.0$ m/s (Figure 5a), which shows a persistent underprediction for all the three FD models for frequencies above 0.04 Hz. The errors in predicted tower base bending moment, shown in Table 4, are in general lower than for the pitch motion, since wave-frequency and 3p loads also influence the tower-base bending moment, and are less affected by the damping dependence of frequency. The accuracy is satisfactory for calculated and, especially, forced methods.

Figure 6 compares the low-frequency responses in pitch, for $U_w = 19.0$ m/s, when the inertia effect is included or disregarded. The FD model with damping coefficient obtained from forced oscillations is adopted, but only the blue curve includes the inertia coefficient – resulting in a peak period about 2.5 s longer then when the inertia effect is not considered.

6. Conclusion

A method was developed to illustrate the importance of including the interaction between the nacelle motions and thrust in the frequency-domain representation of a FWT. The thrust fluctuations resulting from nacelle motions can be interpreted as frequency-dependent inertia and damping effects, which challenges the traditional approach of adopting a constant aerodynamic damping coefficient.

Expressions were derived for the respective coefficients based both on a linearized expression for the thrust and on forced oscillations of a wind turbine in the time domain. The obtained coefficients were included in a 3 DOF FD model of the OOstar semi-submersible FWT. Comparisons were made between the models using a constant aerodynamic damping coefficient, the frequency-dependent inertia and damping coefficients obtained in two different ways, and

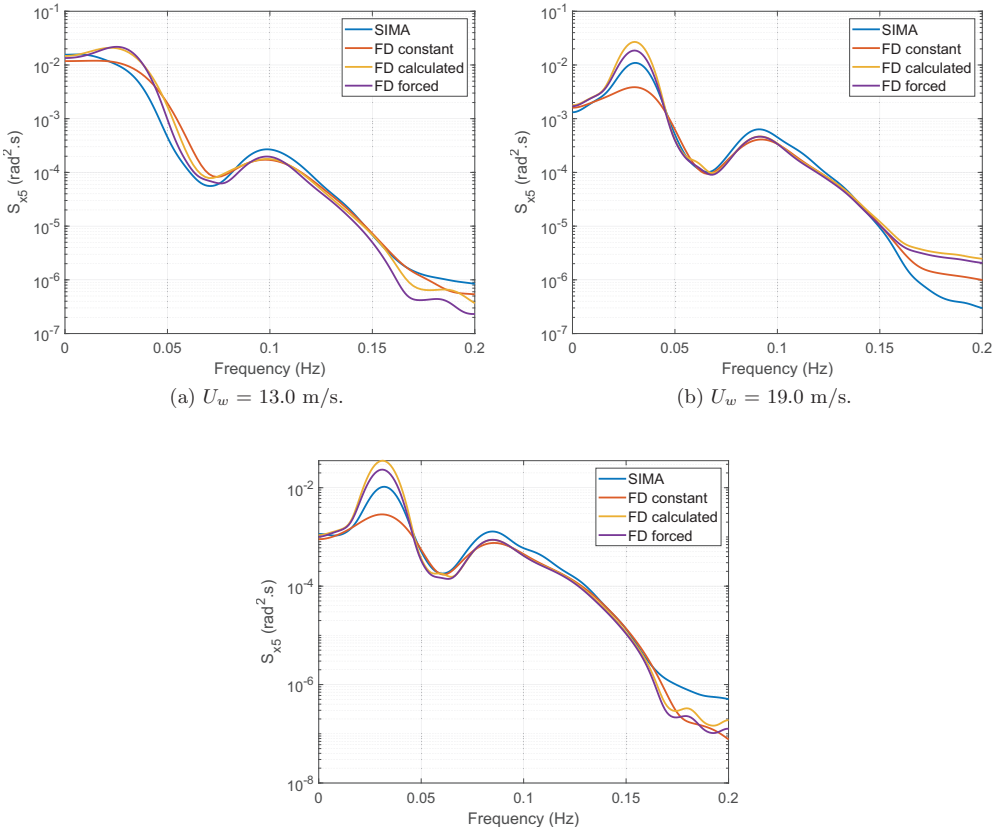

(a) $U_w = 13.0$ m/s.

(b) $U_w = 19.0$ m/s.

(c) $U_w = 25.0$ m/s.

Figure 4: Frequency-domain platform pitch response – comparison between SIMA simulations and frequency-domain analyses with different approaches for calculating the aerodynamic inertia and damping.

time-domain simulations. Both platform pitch motion and tower base bending moment were analyzed. It was observed that the constant damping coefficient underestimates the responses in the frequency range of the FWT surge and pitch natural frequencies.

The frequency-dependent coefficients, on the other hand, overestimated the response in the same frequency range, but are closer to the time-domain predictions. The aerodynamic inertia was shown to increase the pitch natural period by about 2.5 s, for a mean incident wind speed of 19.0 m/s. The differences between using coefficients based on the linearized thrust or on the forced oscillations were not very significant, but a slightly better agreement of the LF responses with the time-domain simulations was attained with the latter.

The introduction of inertia and damping coefficients was chosen for its didactic interest, but the adoption of a linearized thrust as in Equation (9) in a FD model is a simpler and equivalent approach to include the interaction between nacelle motion and thrust, with due consideration of controller and rotor dynamic effects.

In any case, a better agreement of the LF response should still be pursued. Other linearization

Condition	FD constant (%)	FD calculated (%)	FD forced (%)
C1	-0.2	+23.7	+21.8
C2	-24.8	+38.0	+20.0
C3	-29.6	+55.0	+30.6

Table 4: Error in pitch standard deviation compared to time domain simulations.

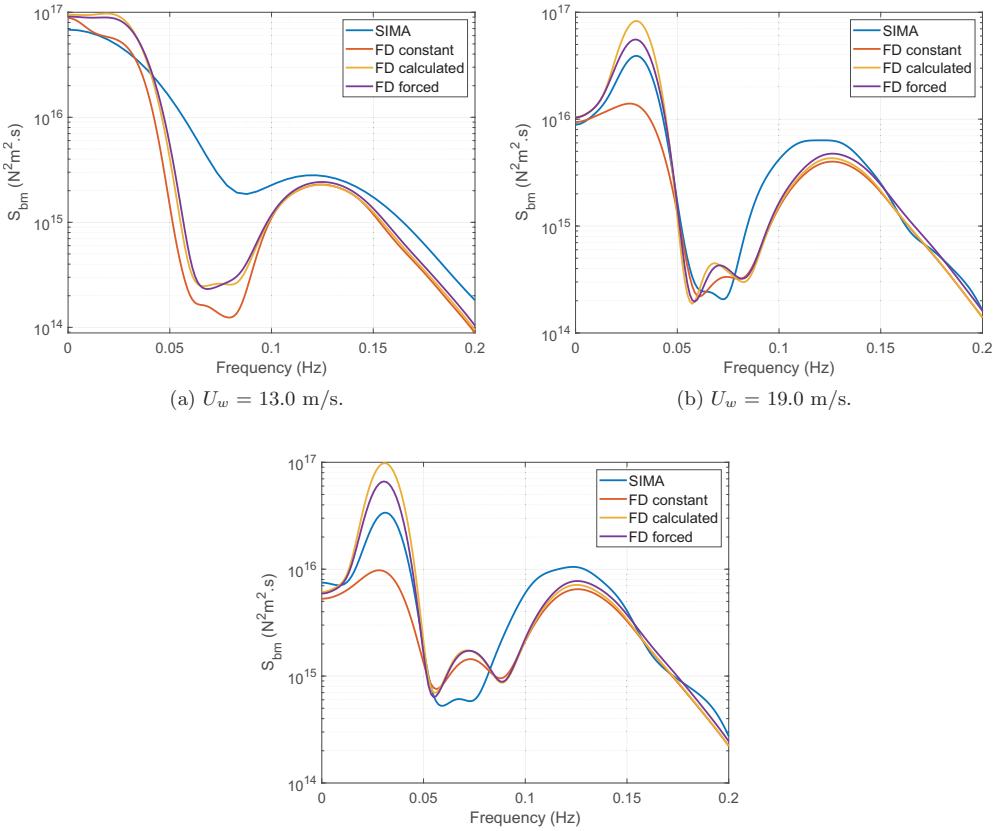

(a) $U_w = 13.0$ m/s.

(b) $U_w = 19.0$ m/s.

(c) $U_w = 25.0$ m/s.

Figure 5: Frequency-domain tower base bending moment – comparison between SIMA simulations and frequency-domain analyses with different approaches for calculating the aerodynamic inertia and damping.

methods could be attempted, trying to preserve effects other than those obtained with the partial derivatives of thrust and torque w.r.t. relative wind velocity, rotor speed and blade-pitch angle.

Condition	FD constant (%)	FD calculated (%)	FD forced (%)
C1	-7.1	+13.0	+10.7
C2	-29.8	+15.1	+2.9
C3	-33.0	+19.2	+5.3

Table 5: Error in tower base bending moment standard deviation compared to time domain simulations.

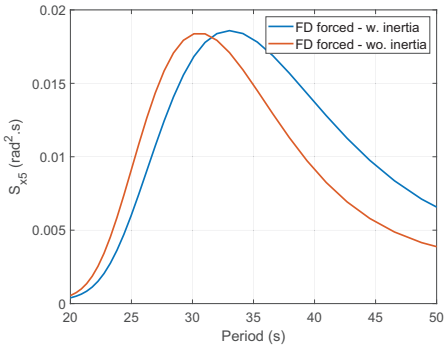

Figure 6: Pitch response estimated in the frequency domain for $U_w = 19.0$ m/s, with aerodynamic damping estimated using the forced oscillations method and with/without considering the aerodynamic inertia effect.

References

[1] Kvittem MI, Moan T. Frequency Versus Time Domain Fatigue Analysis of a Semisubmersible Wind Turbine Tower. Journal of Offshore Mechanics and Arctic Engineering. 2015 Feb;137(1):011901–011901–11. Available from: http://dx.doi.org/10.1115/1.4028340.

[2] Pegalajar-Jurado A, Borg M, Bredmose H. An efficient frequency-domain model for quick load analysis of floating offshore wind turbines. Wind Energy Science. 2018;3(2):693–712. Available from: https://www.wind-energ-sci.net/3/693/2018/.

[3] Hegseth JM, Bachynski EE. A semi-analytical frequency domain model for efficient design evaluation of spar floating wind turbines. Marine Structures. 2019;64:186 – 210. Available from: http://www.sciencedirect.com/science/article/pii/S0951833918303149.

[4] Bachynski EE. Design and dynamic analysis of tension leg platform wind turbines [Ph.D. thesis]. Norwegian University of Science and Technology. Trondheim, Norway; 2014.

[5] Nielsen F, Hanson T, Skaare B. Integrated dynamic analysis of floating offshore wind turbines. In: Proceedings of the ASME 2016 25th International Conference on Offshore Mechanics and Arctic Engineering; 2006. .

[6] Larsen TJ, Hanson TD. A method to avoid negative damped low frequent tower vibrations for a floating, pitch controlled wind turbine. Journal of Physics: Conference Series. 2007 jul;75:012073. Available from: https://doi.org/10.1088%2F1742-6596%2F75%2F1%2F012073.

[7] Jonkman JM. Influence of control on the pitch damping of a floating wind turbine. In: Proceedings of the ASME Wind Energy Symposium; 2008. .

[8] Souza CES, Bachynski EE. Changes in surge and pitch decay periods of floating wind turbines for varying wind speed. Ocean Engineering. 2019;180:223 – 237. Available from: http://www.sciencedirect.com/science/article/pii/S0029801818315932.

[9] Goupee AJ, Kimball RW, Dagher HJ. Experimental observations of active blade pitch and generator control influence on floating wind turbine response. Renewable Energy. 2017;104:9 – 19.

[10] Moriarty PJ, Hansen AC. AeroDyn Theory Manual. Denver, Colorado: National Renewable Energy

Laboratory; 2005. NREL/EL-500-36881.
[11] Müller K, Lemmer F, Yu W. LIFES50+ - D4.2 Public Definition of the Two LIFES50+ 10MW Floater Concepts. University of Stuttgart; 2018.
[12] Hansen MH, Henriksen LC. Basic DTU Wind Energy controller. Technical University of Denmark; 2019. DTU Wind Energy E No. 0028.
[13] Bak C, Zahle F, Bitsche R, Kim T, Yde A, Henriksen LC, et al. Description of the DTU 10 MW Reference Wind Turbine. DTU Wind Energy; 2013. DTU Wind Energy Report-I-0092.
[14] SINTEF OCEAN. RIFLEX - Theory manual; 2016.
[15] SINTEF OCEAN. SIMO - Theory manual; 2016.
[16] Hansen MOL. Aerodynamics of Wind Turbines. Earthscan; 2013.
[17] Jonkman BJ, Kilcher L. TurbSim User's Guide: version 1.06.00. National Renewable Energy Laboratory; 2012.

Paper 3

Integrated design optimization of spar floating wind turbines

John Marius Hegseth, Erin E. Bachynski and Joaquim R. R. A. Martins

Marine Structures, 2020

Marine Structures 72 (2020) 102771

Contents lists available at ScienceDirect

Marine Structures

journal homepage: http://www.elsevier.com/locate/marstruc

Integrated design optimization of spar floating wind turbines

John Marius Hegseth [a,*], Erin E. Bachynski [a], Joaquim R.R.A. Martins [b]

[a] Department of Marine Technology, NTNU, 7491, Trondheim, Norway
[b] Department of Aerospace Engineering, University of Michigan, Ann Arbor, MI, 48109, USA

ARTICLE INFO

Keywords:
Offshore wind energy
Floating wind turbines
Integrated design
Gradient-based optimization

ABSTRACT

A linearized aero-hydro-servo-elastic floating wind turbine model is presented and used to perform integrated design optimization of the platform, tower, mooring system, and blade-pitch controller for a 10 MW spar floating wind turbine. Optimal design solutions are found using gradient-based optimization with analytic derivatives, considering both fatigue and extreme response constraints, where the objective function is a weighted combination of system cost and power quality. Optimization results show that local minima exist both in the soft-stiff and stiff-stiff range for the first tower bending mode and that a stiff-stiff tower design is needed to reach a solution that satisfies the fatigue constraints. The optimized platform has a relatively small diameter in the wave zone to limit the wave loads on the structure and an hourglass shape far below the waterline. The shape increases the restoring moment and natural frequency in pitch, which leads to improved behaviour in the low-frequency range. The importance of integrated optimization is shown in the solutions for the tower and blade-pitch control system, which are clearly affected by the simultaneous design of the platform. State-of-the-art nonlinear time-domain analyses show that the linearized model is conservative in general, but reasonably accurate in capturing trends, suggesting that the presented methodology is suitable for preliminary integrated design calculations.

1. Introduction

Floating wind turbines (FWTs) are complex multidisciplinary systems, which makes design optimization a challenging and time consuming task. Different components, such as the wind turbine control system, tower, platform, and mooring system, are typically designed separately in a sequential manner; however, due to strong coupling between the disciplines, this often leads to suboptimal solutions at the overall system level. It is therefore desirable to use an integrated optimization approach where the components are designed simultaneously while considering all relevant disciplines. Multidisciplinary design optimization (MDO) techniques can be used to solve such problems [1].

A large body of literature exists on the topic of FWT design, often using parametric studies to assess the behaviour of the system. Tracy [2] performed simplified frequency-domain analyses to evaluate a large variety of FWT designs. Bachynski and Moan [3] used spreadsheet calculations together with fully coupled time-domain simulations to analyse different design parameters for five tension leg platform (TLP) wind turbines. Gilloteaux and Bozonnet [4] examined the response of cylinder-shaped FWTs with different geometries.

An early study on hydrodynamic shape optimization of offshore structures using computer-aided optimization was carried out by

* Corresponding author.
E-mail address: john.m.hegseth@ntnu.no (J.M. Hegseth).

https://doi.org/10.1016/j.marstruc.2020.102771
Received 5 November 2019; Received in revised form 29 March 2020; Accepted 30 March 2020

Clauss and Birk [5], and more recently, these techniques have also been applied in the design of FWT systems. Brommundt et al. [6] optimized the catenary mooring system for a semi-submersible FWT using frequency-domain analyses. The model included the directionality of the environmental loads and thus also considered the layout of the mooring lines. Hall et al. [7] performed single- and multi-objective hull shape and mooring line optimization for different platform concepts spanning all stability classes and found that the Pareto front was dominated by relatively complex platforms with several legs and taut mooring lines. The work was later extended by Karimi et al. [8], using an updated dynamic model and a new optimization algorithm, which significantly affected the derived optimal solutions. Myhr and Nygaard [9] used time-domain simulations and two extreme load cases to optimize the structural design of a tension leg buoy and found that the wave forces could be significantly reduced if the cylindrical platform section in the wave zone was replaced with a space frame. Muskulus and Schafhirt [10] offers a comprehensive review of wind turbine support structure optimization.

Despite gradient-based optimization being desirable due to its efficiency, especially for large design spaces [10], most of the work on FWT design optimization has been performed using gradient-free methods. This is likely due to the difficult task of computing accurate gradients. One exception is Fylling and Berthelsen [11], who optimized the hull shape, mooring lines and power cable for a spar FWT using a gradient-based approach with numerical gradients obtained using finite differences.

The aforementioned studies consider the design of the platform, mooring system, or both, but the tower, rotor, and control system are considered fixed during the optimization. Because the design process must consider the energy production and not only the cost of the FWT system, the control system should preferably be integrated in the optimization procedure [12]. Numerical optimization of a land-based wind turbine controller has been performed by Tibaldi et al. [13], but little exists in the literature concerning FWTs. A first step in this direction was made by Lemmer et al. [14], who optimized four main dimensions of a three-column semi-submersible FWT, where the controller was automatically tuned in each design iteration using a linear quadratic regulator (LQR). The optimization sought to minimize a combination of material costs and damage-equivalent loads in the tower for seven operational conditions, with a constraint on the static pitch angle at rated thrust.

A limitation of previous work on FWT design optimization is that the large-volume platform is considered rigid in the design analyses. In addition, the tower design is typically not considered in the optimization process. Since turbines are getting larger, the flexibility of the platform is becoming increasingly important and may need to be considered to obtain the correct global behaviour of the system. The elasticity of the platform affects both the shape and the natural frequency of the structure's eigenmodes, which may influence the tower response.

To address these issues, the current work develops an integrated optimization process that considers the tower and platform design simultaneously, and captures the coupling effects between the two subsystems. A flexible hull, combined with distributed hydrodynamic forces, also enables the structural design of the platform to be integrated in the global optimization loop. A computationally efficient low-fidelity model is used to analyse the linearized aero-hydro-servo-elastic dynamics of a 10 MW spar FWT in the frequency domain. The model is implemented in the OpenMDAO framework [15], which enables efficient gradient-based optimization using analytic gradients. The spar platform, tower, mooring system, and control system are then optimized in an integrated fashion, considering both fatigue and extreme response constraints, where a weighted combination of system cost and power quality is employed as the objective function. Finally, the results are verified against nonlinear time-domain analyses. The rotor design is not modified during the optimization, since the model is considered unsuitable for local blade response. The design optimization of wind turbine rotors is considered to be outside the scope of the current work, but has been considered separately [16–18].

Since the presented design optimization methodology is based on a simplified dynamic model, its main purpose is to help designers in the preliminary design phase. Due to the computational efficiency of the model, it can also be used to quickly get insight into the system behaviour, and to study the effect of changes in system parameters on the dynamic response and resulting design solutions. Detailed design would require more accurate nonlinear analyses incurring a much greater computational cost.

The paper is organized as follows. The linear FWT model used to perform the integrated design analyses is presented in Section 2. In Section 3, the optimization problem is summarized and the design variables, constraints, and objective function are described in detail. The results from the optimization study are presented and discussed in Section 4, and the optimized design solutions are verified using a high-fidelity simulation tool. Finally, the findings are summarized in Section 5.

2. FWT model

The coupled dynamics of FWTs are typically analysed using nonlinear time-domain analyses, which capture the complex interactions between aerodynamics, hydrodynamics, structural dynamics, and control. For a design optimization procedure that requires several iterations to converge, each involving a large number of load cases, the process becomes computationally prohibitive. Simplified models are therefore needed, especially in the conceptual design phase, where large parts of the design space are explored to identify possible solutions.

The present design optimization study considers a spar buoy that supports the DTU 10 MW reference wind turbine [19] at a water depth of 320 m. The steel hull is partially filled with concrete ballast to achieve the correct draft, using a ballast density of 2600 kg/m^3. The interface with the tower is located 10 m above the still water line (SWL), while the hub height is 119 m above the SWL. A catenary mooring system consisting of three lines spread symmetrically about the vertical axis is used for station-keeping. For simplicity, the so-called crowfeet (or delta lines) are removed, and lines with constant cross-sectional properties are used. The yaw motions of the platform are not included in the linearized model.

Only the response in the x-z-plane is considered in the current work, and co-directional waves and wind travelling in the positive x-direction are applied in all simulations. An overview of the FWT system, including the mooring system layout, is shown in Fig. 1.

2.1. Linearized system formulation

The system is linearized to obtain the equations of motion, which are solved in the frequency domain. The model is expressed in state-space form, and consists of a structural part and a control system part, which are connected to obtain the complete closed-loop aero-hydro-servo-elastic model in Section 2.4. The linearized system considers perturbations in the state and input variables, **x** and **u** respectively, about the operational point:

$$\mathbf{x} = \mathbf{x}_0 + \Delta\mathbf{x}, \quad \mathbf{u} = \mathbf{u}_0 + \Delta\mathbf{u}. \tag{1}$$

The dynamic equations of motion are then expressed as

$$\Delta\dot{\mathbf{x}} = \mathbf{A}\Delta\mathbf{x} + \mathbf{B}\Delta\mathbf{u}, \tag{2}$$

where **A** is the state matrix, and **B** is the input matrix. In the rest of this work, the Δ sign is omitted for brevity.

2.2. Structural model

2.2.1. Platform and turbine

The structural model for the platform and turbine considers four degrees-of-freedom (DOFs), as shown in Fig. 2. The equations of motion for the three support structure DOFs (surge, pitch, and the first bending mode of the tower and platform) are derived by using generalized displacements similar to Hegseth and Bachynski [20], but using a flexible hull. Hydrodynamic excitation loads are found from MacCamy–Fuchs theory, while the added mass is based on analytical 2D coefficients. Radiation damping is neglected, while viscous damping is computed using a stochastic linearization of the drag term in Morison's equation. The three support structure DOFs are gathered in the vector $\boldsymbol{\xi} = [\xi_1 \quad \xi_5 \quad \xi_7]^\top$. The differential equation for the rotor speed, $\dot{\phi}$, considers only rigid body dynamics and thus neglects the torsional DOF of the shaft:

$$I_D\,\ddot{\phi} = Q_A - N_{gear}Q_G. \tag{3}$$

Here, I_D is the rotor and drivetrain inertia, Q_A is the aerodynamic torque, N_{gear} is the gear ratio, and Q_G is the generator torque.

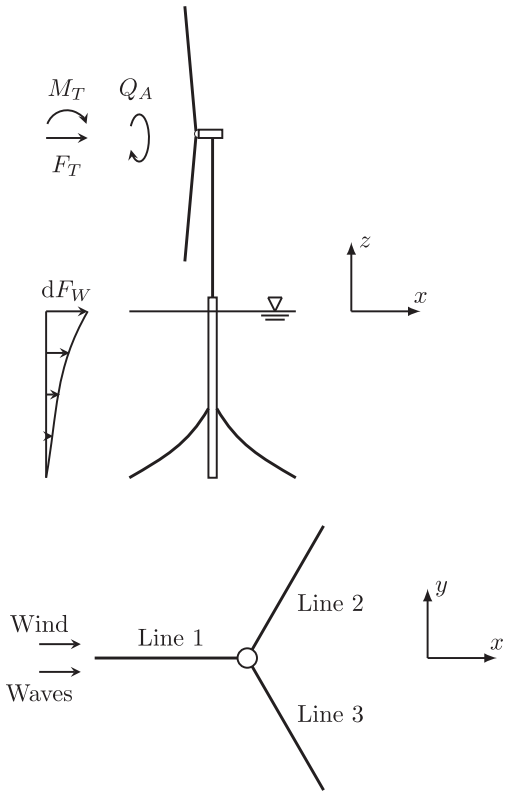

Fig. 1. Overview of the FWT system.

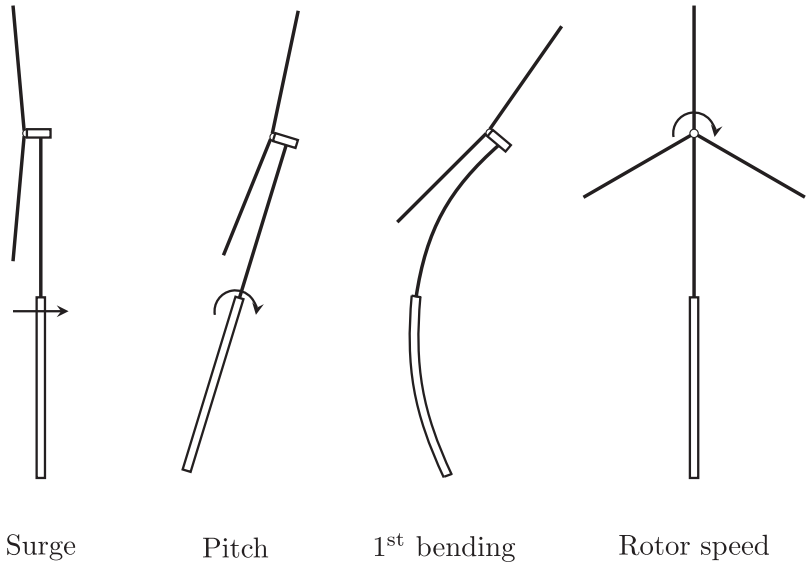

Fig. 2. Structural DOFs considered in the model.

For each wind-wave condition, the linearization point for the system is found from static equilibrium when the system is subjected to the mean environmental loads. In addition to the mean aerodynamic loads on the rotor, the static component of the aerodynamic quadratic drag force on the tower is included.

Although the linearized model presented here may yield reasonably accurate estimates for the global response of the tower, platform and mooring lines, it is not considered suitable for blade design, which typically involves nonlinear analyses in the time domain. One exception is Merz [21], who performed conceptual blade design for a stall-regulated offshore wind turbine using linear frequency-domain analyses. Because modern wind turbine blades are made of composite materials, and because they are more sensitive to local aerodynamic effects than the support structure and mooring system, including the blade design would require significant enhancements to the aerodynamic and structural models presented here, which is outside the scope of the current work. In addition, previous studies on FWTs have indicated that transient fault conditions, which cannot be analysed with the presented methodology, may be critical for extreme blade loads [22,23]. The blade response is therefore not considered in the model; instead, the aerodynamic forces are applied as resultant loads on the tower top.

With the structural DOFs described above, the state vector is defined as

$$\mathbf{x}_s = \begin{bmatrix} \boldsymbol{\xi} \\ \dot{\boldsymbol{\xi}} \\ \phi \end{bmatrix}. \tag{4}$$

The inputs to the structural system consist of both control system outputs and disturbances due to environmental loads, which are separated in two different vectors $\mathbf{u}_{sc}$ and $\mathbf{u}_{sd}$. The control input vector is written as

$$\mathbf{u}_{sc} = \begin{bmatrix} Q_G \\ \theta \end{bmatrix}, \tag{5}$$

where θ is the collective blade pitch angle, which is found from the control system model, together with the generator torque. The current implementation neglects the dynamics of the generator and pitch actuator systems, and the generator torque and blade pitch are thus instantaneously set to their reference values at each time step.

The wind speed varies over the rotor disk; however, because only the resultant aerodynamic loads at the tower top are of interest in the analysis, it is desirable to express the wind input using a single scalar variable. This is achieved by expressing a rotor effective wind speed for each of the three resultant forces in Fig. 1. The rotor effective wind speed is a spatially constant wind speed that yields the same resultant forces on the rotor as the full wind field and may therefore be considered as a weighted average of the wind speed seen by the different blade elements. The disturbance vector is expressed as

$$\mathbf{u}_{sd} = \begin{bmatrix} v_{F_T} & v_{M_T} & v_{Q_A} & F_{W,1} & F_{W,5} & F_{W,7} \end{bmatrix}^\top, \tag{6}$$

where v_{F_T}, v_{M_T} and v_{Q_A} are the effective wind speeds for thrust, tilting moment and aerodynamic torque, respectively, which are derived in Section 2.5.2. $F_{W,n}$ represents the generalized wave excitation force in support structure DOF n, found from MacCamy–Fuchs theory. The resulting system is written as:

$$\dot{\mathbf{x}}_s = \mathbf{A}_s\mathbf{x}_s + \mathbf{B}_{sc}\mathbf{u}_{sc} + \mathbf{B}_{sd}\mathbf{u}_{sd}, \tag{7a}$$

$$\mathbf{y}_s = \mathbf{C}_s\mathbf{x}_s, \tag{7b}$$

where the state matrix is found from the total mass (**M**, including hydrodynamic added mass), stiffness (**K**), and damping (**D**) matrices for the system

$$\mathbf{A}_s = \begin{bmatrix} \mathbf{0} & \mathbf{I} \\ -\mathbf{M}^{-1}\mathbf{K} & -\mathbf{M}^{-1}\mathbf{D} \end{bmatrix} \tag{8}$$

The input matrices $\mathbf{B}_{sc}$ and $\mathbf{B}_{sd}$ relate control inputs and disturbances to forces on the structural DOFs, while the output matrix for the structural model, $\mathbf{C}_s$, is chosen such that the rotor speed is the single output to match the control system input:

$$\mathbf{C}_s = [0 \quad 0 \quad 0 \quad 0 \quad 0 \quad 0 \quad 1]. \tag{9}$$

2.2.2. Mooring system

The response of the mooring lines is calculated using the simplified dynamic frequency-domain model described by Larsen and Sandvik [24] and later extended by Lie and Sødahl [25]. Here, the lines are modelled as a single DOF system, as shown in Fig. 3.

The dynamic tension in the line can then be derived as

$$T_D = k_E[x(t) - u(t)] = c^*|\dot{u}(t)|\dot{u}(t) + k_G u(t) + \omega^2 m^* x(t), \tag{10}$$

where $u(t)$ is the generalized displacement of the line, found from a quasi-static analysis where the upper end is displaced two times the standard deviation of the platform motion from the equilibrium position (significant motion). The geometric stiffness (k_G) is found as the secant stiffness when the line is moved from equilibrium to the position of significant motion. The generalized inertia coefficient (m^*) and damping coefficient (c^*) are found using the quasi-static line configuration as the shape function. The linearized damping coefficient (c_L) is computed using the stochastic linearization

$$c^*|\dot{u}(t)|\dot{u}(t) \approx c^*\sqrt{\frac{8}{\pi}}\sigma_{(\dot{u})}\dot{u}(t) = c_L\dot{u}(t), \tag{11}$$

where $\sigma_{(\dot{u})}$ denotes the standard deviation of $\dot{u}$. Because Eq. (10) can be considered to be a variant of Morison's equation, non-Gaussian extremes for the dynamic mooring line tension can be found from the normalized maxima distribution of the Morison force, which consists of a Rayleigh distribution for low probability levels and an exponential distribution for high probability levels [25]:

$$F_Y(y) = \begin{cases} 1 - \exp\left[-\left(3k^2+1\right)\dfrac{y^2}{2}\right], & 0 \le y \le y_0 \\ 1 - \exp\left[-\dfrac{\sqrt{3k^2+1}}{2k}\left(y - \dfrac{y_0}{2}\right)\right], & y \ge y_0, \end{cases} \tag{12}$$

where $y = T_D/\sigma_{(T_D)}$ is the normalized tension, and

$$y_0 = \frac{1}{2k\sqrt{3k^2+1}}. \tag{13}$$

The parameter k is a measure of the relative importance of drag and inertia forces.

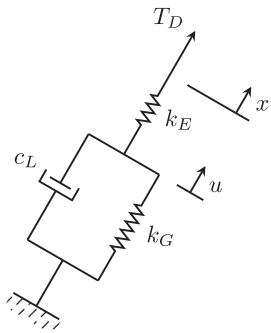

Fig. 3. Simplified dynamic mooring line model as illustrated by Lie and Sødahl [25].

2.3. Control system model

The baseline linear control system follows the generic approach for variable-speed pitch-controlled wind turbines [26]. The approach uses two independent controllers: a generator-torque controller for below-rated wind speeds and a collective blade-pitch controller for above-rated wind speeds. Typically, these types of controllers also include transition strategies to ensure smooth switchovers between regions; however, for simplicity, this is not included in the current implementation. In both control regimes, the control system is described with the following first-order system

$$\dot{\mathbf{x}}_c = \mathbf{A}_c\mathbf{x}_c + \mathbf{B}_c\mathbf{u}_c, \tag{14a}$$

$$\mathbf{y}_c = \mathbf{C}_c\mathbf{x}_c, \tag{14b}$$

where the rotor speed is the only input, and the outputs are the generator torque and the blade pitch angle:

$$\mathbf{u}_c = [\dot{\phi}], \quad \mathbf{y}_c = \begin{bmatrix} Q_G \\ \theta \end{bmatrix}. \tag{15}$$

First, the rotor speed is filtered through a first-order low-pass filter with corner frequency ω_{lp} to avoid high-frequency excitation of the control system

$$\mathbf{A}_c = \begin{bmatrix} 0 & 1 \\ 0 & -\omega_{lp} \end{bmatrix}, \quad \mathbf{B}_c = \begin{bmatrix} 0 \\ \omega_{lp} \end{bmatrix}, \quad \mathbf{x}_c = \begin{bmatrix} \phi_{lp} \\ \dot{\phi}_{lp} \end{bmatrix}, \tag{16}$$

where $\dot{\phi}_{lp}$ is the low-pass filtered rotor speed. Below the rated wind speed, the generator torque is set to be proportional to the square of the rotor speed to balance the aerodynamic torque and thus maintain the optimal tip-speed ratio, which maximizes the power output. Above the rated wind speed, the generator torque is kept constant at the rated torque, and a PI controller is used to modify the collective blade pitch angle:

$$\mathbf{C}_c = \begin{bmatrix} 0 & 2K\dot{\phi}_0 \\ 0 & 0 \end{bmatrix} (\text{below rated}), \tag{17}$$

$$\mathbf{C}_c = \begin{bmatrix} 0 & 0 \\ \eta_k k_i & \eta_k k_p \end{bmatrix} (\text{above rated}).$$

Here, K is the generator torque constant, η_k is the gain-scheduling parameter, while k_i and k_p are the integral and proportional gains of the PI controller, respectively.

2.4. Closed-loop system

The structural and control system models can be written as a single closed-loop system by setting $\mathbf{y_s} = \mathbf{u_c}$ and $\mathbf{u}_{sc} = \mathbf{y_c}$:

$$\dot{\mathbf{x}} = \mathbf{A}\mathbf{x} + \mathbf{B}\mathbf{u}_{sd}, \tag{18a}$$

$$\mathbf{y} = \mathbf{C}\mathbf{x}, \tag{18b}$$

where

$$\mathbf{A} = \begin{bmatrix} \mathbf{A}_s & \mathbf{B}_{sc}\mathbf{C}_c \\ \mathbf{B}_c\mathbf{C}_s & \mathbf{A}_c \end{bmatrix}, \quad \mathbf{B} = \begin{bmatrix} \mathbf{B}_{sd} \\ \mathbf{0} \end{bmatrix}, \quad \mathbf{x} = \begin{bmatrix} \mathbf{x_s} \\ \mathbf{x_c} \end{bmatrix}, \tag{19}$$

and $\mathbf{C}$ is set to the identity matrix. The closed-loop system is then transformed to the frequency domain. The transfer matrix between disturbances and outputs for a frequency ω is defined as:

$$\mathbf{H}(\omega) = \mathbf{C}(i\omega\mathbf{I} - \mathbf{A})^{-1}\mathbf{B}. \tag{20}$$

The cross-spectral density matrix of the response vector $\mathbf{y}$ can be calculated from

$$\mathbf{S}_\mathbf{y}(\omega) = \mathbf{H}(\omega)\mathbf{S}_\mathbf{u}(\omega)\mathbf{H}(\omega)^H, \tag{21}$$

where $(\cdot)^H$ denotes the conjugate transpose [27]. The variance spectra of $\mathbf{y}$ are then found along the diagonal of $\mathbf{S}_\mathbf{y}(\omega)$.

The cross spectral density matrix ($\mathbf{S}_\mathbf{u}(\omega)$) is used for the load process and has the following structure

$$\mathbf{S}_\mathbf{u}(\omega) = \begin{bmatrix} \mathbf{S}_{\text{wind}}(\omega) & \mathbf{0} \\ \mathbf{0} & \mathbf{S}_{\text{wave}}(\omega) \end{bmatrix} \tag{22}$$

The off-diagonal terms above are zero because the wind and wave processes are assumed to be uncorrelated [28].

The resulting response spectra are applied, together with dynamic equilibrium, to find the bending moment response along the

tower and platform. The fatigue damage is then calculated at selected locations using the Dirlik method [29].

The extreme response of the support structure is computed using the average upcrossing rate (AUR) method [30]. Assuming that the response process is stationary and Gaussian with zero mean, the cumulative distribution function (CDF) of the extreme value Y for an arbitrary response parameter can be written as [27].

$$F_Y(y) = \exp\left\{ -\nu^+(0)\ T \exp\left(-\frac{y^2}{2\sigma^2} \right) \right\}, \tag{23}$$

where $\nu^+(0)$ is the mean zero-upcrossing rate, which can be found from the zeroth- and second-order spectral moments:

$$\nu^+(0) = \frac{1}{2\pi} \sqrt{\frac{m_2}{m_0}}. \tag{24}$$

The n^{th} spectral moment is defined as:

$$m_n = \int_0^\infty \omega^n S(\omega) \mathrm{d}\omega. \tag{25}$$

The most probable maximum value in 1 h, y_{1h}, is used in the design constraints related to extreme response. The value is approximated using:

$$F_Y(y_{1h}) = \mathrm{e}^{-1}. \tag{26}$$

The mean value of the response process is then added to y_{1h} to obtain the total extreme value. We have used this methodology to compute fatigue damage in the tower base, as well as extreme surge, pitch, and tower base bending moment response, for two 10 MW spar FWT designs in previous work [20]. We found this methodology to yield good agreement within ± 30% for long-term fatigue and ± 15% for short-term extremes when compared to nonlinear time-domain simulations.

2.5. Aerodynamic forces

2.5.1. Linearized BEM theory

The aerodynamic forces on the blades are computed using blade-element momentum (BEM) theory [31,32]. A quasi-steady formulation is used, meaning that dynamic wake and dynamic stall effects are neglected. The Glauert correction and hub and tip loss factors are included in the model. The normal and tangential inflow velocities for a blade section at radius r are defined as:

$$V_n = v\ (1 - a_n), \tag{27a}$$

$$V_t = \dot{\phi}\ r\ (1 + a_t), \tag{27b}$$

where v is the relative wind speed, and a_n and a_t are the normal and tangential induction factors, respectively. In the analyses, induction factors for the different blade sections are found from pre-calculated lookup tables as functions of blade pitch angle and tip speed ratio. The inflow velocity W and inflow angle φ seen by the blade element are then expressed as

$$W = \sqrt{V_n^2 + V_t^2}, \tag{28a}$$

$$\varphi = \tan^{-1} \frac{V_n}{V_t}. \tag{28b}$$

The angle of attack is the difference between the inflow angle and the element's combined pitch and twist angle:

$$\alpha = \varphi - (\theta + \beta). \tag{29}$$

Here, β is the twist angle. The lift and drag forces can then be computed using tabulated lift and drag coefficients

$$L = \frac{1}{2} \rho c W^2 C_l(\alpha), \tag{30a}$$

$$D = \frac{1}{2} \rho c W^2 C_d(\alpha). \tag{30b}$$

The normal and tangential forces relative to the rotor plane are found from a coordinate system transformation

$$F_n = L \cos\varphi + D \sin\varphi \tag{31a}$$

$$F_t = L \sin\varphi - D \cos\varphi. \tag{31b}$$

The blade root loads of interest, i.e., the flapwise shear force F_y, the flapwise bending moment M_z, and the edgewise bending moment M_y, are found by integrating the loads over the length of the blade

$$F_y = \int_0^R F_n \, \mathrm{d}r, \tag{32a}$$

$$M_z = \int_0^R r \, F_n \, \mathrm{d}r, \tag{32b}$$

$$M_y = \int_0^R r \, F_t \, \mathrm{d}r. \tag{32c}$$

As seen in Eqs. (27)–(32), the aerodynamic forces are nonlinear functions of wind speed, rotor speed, and blade pitch angle. To obtain linear forces that can be applied in the simplified FWT model, the blade root forces are linearized using a first order Taylor expansion:

$$F_y \approx F_{y0} + F_{y,v}\Delta v + F_{y,\dot{\phi}}\Delta\dot{\phi} + F_{y,\theta}\Delta\theta, \tag{33a}$$

$$M_z \approx M_{z0} + M_{z,v}\Delta v + M_{z,\dot{\phi}}\Delta\dot{\phi} + M_{z,\theta}\Delta\theta, \tag{33b}$$

$$M_y \approx M_{y0} + M_{y,v}\Delta v + M_{y,\dot{\phi}}\Delta\dot{\phi} + M_{y,\theta}\Delta\theta, \tag{33c}$$

where the subscripts after the commas denote partial derivative with respect to the variable, i.e.,

$$A_{x,y} = \frac{\partial A_x}{\partial y}. \tag{34}$$

2.5.2. Rotor effective wind speed

A rotor effective wind speed is used to describe the incoming wind field. The effective wind speed is dependent on the type of resultant load (thrust force, tilting moment, or aerodynamic torque), as well as the mean wind speed.

As shown by Halfpenny [33], the (single sided) cross-spectral density of the rotationally sampled wind speed for two blade elements j and k can be written as:

$$S_v^{(jk)}(\omega) = \sum_{n=-\infty}^{\infty} \mathrm{e}^{in\psi} K_n^{(jk)}(|\omega - n\dot{\phi}|)\, S_U(|\omega - n\dot{\phi}|), \tag{35}$$

where $S_U(\omega)$ is the incoming wind spectrum, ψ is the azimuth angle between the elements, and K_n is the n^{th} Fourier coefficient of the coherence function γ, which is Fourier expanded in the rotor plane:

$$K_n^{(jk)}(\omega) = \frac{1}{\pi}\int_0^{\pi} \gamma\left(\omega, d_{jk}\right)\cos(n\theta)\,\mathrm{d}\theta. \tag{36}$$

The coherence function for two points with separation distance d and frequency f (in Hz) is taken from IEC [34] and expressed as

$$\gamma(f,d) = \exp\left(-12\left[\left(\frac{fd}{U_{\mathrm{hub}}}\right)^2 + \left(\frac{0.12d}{L_c}\right)^2\right]^{0.5}\right), \tag{37}$$

where U_{hub} is the mean hub-height wind speed and L_c is a coherence scale parameter.

The forces on each blade element can then be found from the rotationally sampled wind speed and weight factors relating wind speed to forces on the element. These weight factors are the partial derivatives of the blade element forces in Eq. (31) with respect to wind speed. When summing the forces on the blade elements to obtain the total tower top loads, cancellation of harmonics results in peaks at multiples of three of the rotor frequency (i.e., 3P, 6P, 9P, etc.) for the resultant force spectra. In the current work, harmonics higher than 3P are neglected. Tower shadow and wind shear are not included.

The spectra for the effective wind speeds are calculated from the resultant force spectra and the total weight factors over the rotor:

$$S_{v_{F_T}}(\omega) = \frac{S_{F_T}(\omega)}{\left(3\,F_{y,v}\right)^2}, \tag{38a}$$

$$S_{v_{M_T}}(\omega) = \frac{S_{M_T}(\omega)}{\left(\frac{3}{2}\,M_{z,v}\right)^2}, \tag{38b}$$

$$S_{v_{Q_A}}(\omega) = \frac{S_{Q_A}(\omega)}{\left(3\,M_{y,v}\right)^2}. \tag{38c}$$

The wind load submatrix in Eq. (22), $\mathbf{S}_{\mathrm{wind}}(\omega)$, can then be found simply by observing which harmonics of the wind are shared by

the different load components. As shown by Halfpenny [33], the thrust force and aerodynamic torque on the turbine are perfectly correlated, since they share all harmonics, and completely uncorrelated from the tilting moment. This is because they have no harmonics in common.

2.5.3. Resultant aerodynamic forces

Following the derivation of weight factors in the previous section, the relation between derivatives of the blade root forces and resultant forces on the rotor becomes evident:

$$F_{T,v} = 3\, F_{y,v}, \tag{39a}$$

$$M_{T,v} = \frac{3}{2}\, M_{z,v}, \tag{39b}$$

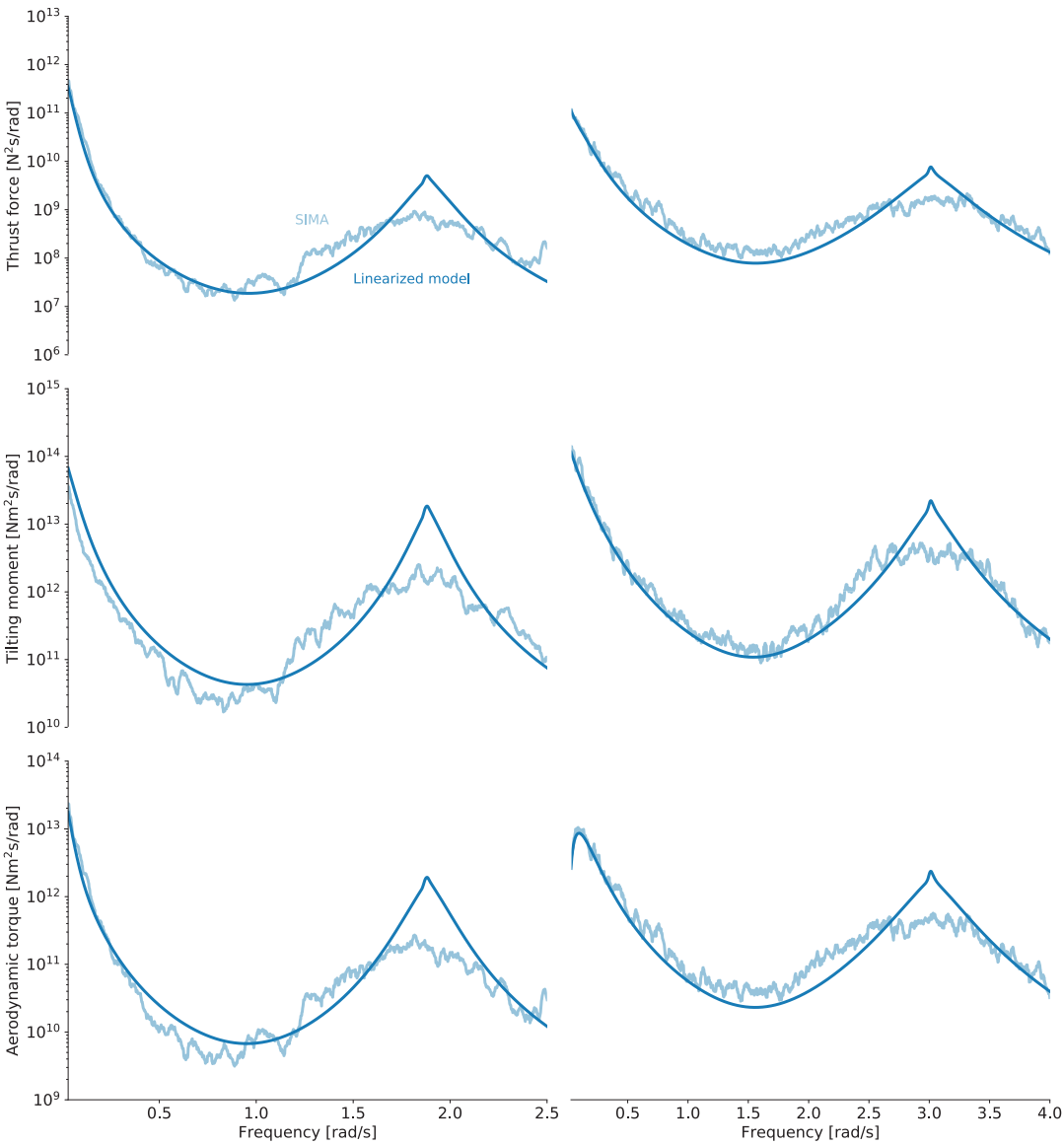

Fig. 4. Comparison of spectra for resultant aerodynamic loads on the tower top. Mean wind speeds of 7 m/s (left) and 15 m/s (right).

$$Q_{A,v} = 3\, M_{y,v}. \tag{39c}$$

The same relations hold for the derivatives with respect to the rotor speed and blade pitch angle; however, a change in rotor speed or collective blade pitch angle affects all parts of the rotor plane equally, and perturbations in these variables therefore do not contribute to the tilting moment. The total resultant aerodynamic forces are thus expressed as:

$$F_T \approx F_{T0} + F_{T,v}\Delta v + F_{T,\dot{\phi}}\Delta\dot{\phi} + F_{T,\theta}\Delta\theta, \tag{40a}$$

$$M_T \approx M_{T0} + M_{T,v}\Delta v, \tag{40b}$$

$$Q_A \approx Q_{A0} + Q_{A,v}\Delta v + Q_{A,\dot{\phi}}\Delta\dot{\phi} + Q_{A,\theta}\Delta\theta. \tag{40c}$$

2.5.4. Verification

To verify the linearized aerodynamic formulation, the resultant tower top loads are compared to results from nonlinear time-domain simulations performed using the SIMA software developed by SINTEF Ocean, which couples the RIFLEX [35] and SIMO [36] programs. Here, the blades are modelled using nonlinear beam elements, and the aerodynamic loads on the blades are computed using BEM theory with a Glauert correction, hub and tip loss factors, dynamic wake, dynamic stall, and tower shadow. The three-dimensional turbulent wind field is created using TurbSim [37], where the vertical wind shear is modelled by the power law with an exponent of 0.14 [38].

Fig. 4 shows the comparison for a fixed turbine with the control system active for mean wind speeds of 7 and 15 m/s. The results show overall good agreement, with the exception of frequencies close to the 3P frequency, where the linear model overestimates the loads. This discrepancy may be due to the assumption of constant rotor speed in the effective wind speed formulation, which causes the linear model to overestimate the response of the 1st bending mode (and thus the fatigue damage in the structure) if the natural frequency is close to the blade passing frequency. However, this is not expected to significantly affect the results from the optimization, because it is highly unlikely that the optimizer will converge to a design solution with the first bending frequency within the 3P range.

2.6. Environmental conditions

The fatigue design should consider all relevant environmental conditions (ECs) over the lifetime of the structure; however, to limit the computational effort, 30 ECs are used to evaluate the long-term fatigue performance in the present work. The mean wind speeds range from 1 to 30 m/s with 1 m/s steps. For each mean wind speed, the most probable values for the significant wave height and spectral peak period are used. These values, as well as the probability associated with each condition, are found from the joint probability distribution presented by Johannessen et al. [39], and shown in Fig. 5. The probabilities are normalized to achieve a total probability of unity, i.e.,

$$\sum_{i=1}^{N_{EC}} p_i = 1, \tag{41}$$

where N_{EC} is the number of ECs considered in the analysis, and p_i is the probability of condition i.

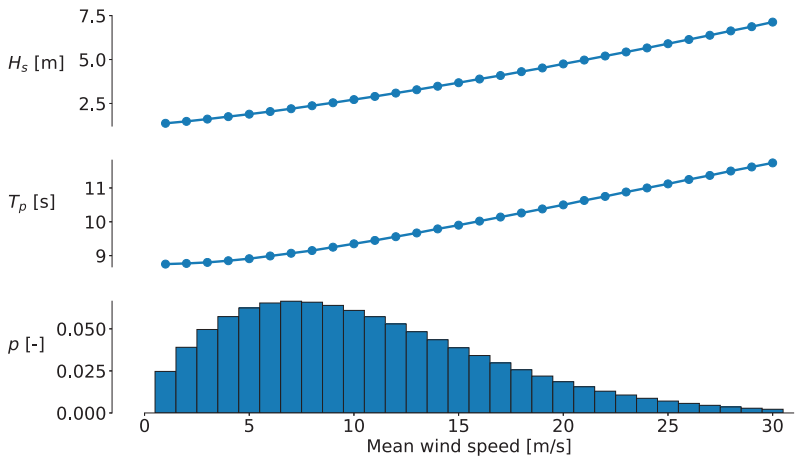

Fig. 5. Significant wave heights, spectral peak periods, and normalized probabilities associated with mean hub height wind speeds applied in the fatigue calculations.

The three ECs described in Table 1, which are located on the 50-year contour surface, are selected to evaluate the extreme response. In EC 1, the mean wind speed is close to the rated speed of the turbine, which yields the maximum thrust force on the rotor. EC 2 considers an operational condition with above-rated wind speed, while EC 3 represents a wind speed above cut-out, where the turbine is parked and the blades are feathered.

For all ECs, a Kaimal spectrum for IEC class B turbines and a normal turbulence model (NTM) [34] are used to describe the incoming wind.

3. Optimization problem

The present optimization study considers the design of four different subsystems simultaneously:

1. Spar platform
2. Wind turbine tower
3. Mooring system
4. Blade-pitch control system

The formulation of the optimization problem is described in the following subsections.

3.1. Framework

The FWT model is implemented in OpenMDAO [15], which is an open-source framework for multidisciplinary design, analysis and optimization. A modular approach is utilized, where smaller units of code (components) are connected to form the larger and more complex multidisciplinary model. Inputs, outputs, and partial derivatives for each component are given to the framework, which handles the data transfer between different parts of the code, performs the analysis, and calculates the total system derivatives needed by the optimizer [40]. To analyse a large number of load cases in an efficient manner, the code is parallelized using MPI.

The design is optimized using a gradient-based approach where analytic derivatives are computed for the coupled model. Analytic gradient computation requires significant implementation effort, but offers increased computational efficiency and accuracy compared to finite-difference approximations. The total derivatives are computed using the adjoint method, whose cost is independent of the number of design variables [41]. With the current model, which has 80 inputs and 18 outputs, the run time for the gradient computation is roughly 4× the analysis time, where a single wind-wave condition runs in approximately 5 s on a standard laptop. The model layout and data dependencies are illustrated using an extended design structure matrix (XDSM) [42] in Fig. B.1 in Appendix B.

The SNOPT algorithm [43] is used to solve the optimization problem. SNOPT uses a sequential quadratic programming (SQP) approach to solve nonlinear constrained optimization problems, and is connected to OpenMDAO using the pyOptSparse interface [44].

Because gradient-based methods have the problem of potentially getting stuck in local minima if the objective function is multi-modal, the optimization is run starting from several initial design points.

3.2. Objective

Ideally, a FWT design optimization procedure should try to minimize the levelized cost of energy (LCOE), which is the lifetime costs of the system divided by the total energy production. However, because the LCOE depends on numerous unknown parameters that cannot be included properly in an engineering optimization model, simpler objectives are needed. A common choice is the weight or the associated material costs of the system, but cost functions that do not take into account production cost components, such as welding, are considered unrealistic [10]. In addition, a measure of the power production performance should be included. The amount of produced energy will mostly depend on the wind farm site and is unlikely to vary much with the design of the FWT system. Another relevant performance measure is the quality of the power delivered by the turbine, which describes how much the energy output fluctuates. High-quality power, which has low variability in the output, is desirable, and its value for a given design is proportional to the variation in rotor speed. The objective function used in the present work is thus a weighted combination of two parameters: the system costs, C_{total}, which cover material and manufacturing, and the weighted average of the rotor speed standard deviation, $\sigma_{(\dot{\phi})}$, which is a measure of the power quality:

$$f = w_1 C_{\text{total}} + w_2 \sigma_{(\dot{\phi})}. \tag{42}$$

Table 1
Environmental conditions for extreme response calculations.

Condition	1	2	3
Mean wind speed at hub height, U (m/s)	11.0	21.0	50.0
Significant wave height, H_s (m)	7.5	9.9	15.1
Spectral peak period, T_p (s)	12.0	14.0	16.0
Turbulence intensity at hub height, I (–)	0.18	0.14	0.12

The relative importance is controlled by the weight factors w_1 and w_2, where $w_1 + w_2 = 1; w_1, w_2 \in [0, 1]$. Because the monetary cost of reduced power quality is difficult to quantify, the optimization is run with different values for the weight factors, to assess the trade-off between the two sub-objectives.

The total cost of the system is

$$C_{\text{total}} = C_{\text{spar}} + C_{\text{tower}} + C_{\text{moor}}, \tag{43}$$

where C_{spar}, C_{tower} and C_{moor} are the costs of the platform, tower, and mooring system, respectively. The platform and tower costs take into consideration both material and manufacturing, using cost models from Farkas and Jármai [45]. Costs related to installation, maintenance, and decommissioning are not included. The cost of the platform (and similarly for the tower) is expressed as

$$C_{\text{spar}} = k_m M_{\text{spar}} + k_f \sum_i T_i, \tag{44}$$

where k_m is the steel cost factor, M_{spar} is the steel mass of the hull, and k_f is the fabrication cost per unit time. T_i is the time spent at fabrication stage i, expressed as a function of the geometry. The manufacturing costs include forming of plate elements into shells, assembly, welding, and painting. The ratio between the material and fabrication cost factors, k_m/k_f, depends on the labour cost, which varies with the fabrication site. In the present work a ratio of 1.0 is assumed, which is a typical value for West European labour [45]. Based on numbers from Teillant et al. [46], the cost of structural steel is about 80 times the cost of concrete ballast (per kg). The cost of ballast is therefore neglected in the current work.

Many different estimates for the cost of steel for floating support structures can be found in the literature, spanning from 1.0 €/kg (only material [47]) to 4.5 €/kg (including manufacturing and assembly [14]). Here, the steel cost factor, k_m, is assumed to have a value of 2.7 €/kg, which is approximately the same as the value used by Fylling and Berthelsen [11]. The mooring line costs are expressed as a function of weight, with a price of 3–4.5 €/kg, depending on the grade [48]. In the present work, steel grade R4 with an associated cost of 3.5 €/kg is assumed, which results in mooring line costs that are about 5–10% of the support structure costs. The relative importance of mooring and support structure costs, which is somewhat uncertain, may affect the optimization results due to trade-off effects; however, preliminary analyses indicate that the system is fairly insensitive to the cost distribution.

The weighted average of the rotor speed standard deviation, used in Eq. (42), is computed by summing the values from each of the 30 FLS conditions described in Section 2.6, weighted by the probability of the condition:

$$\sigma_{(\dot{\phi})} = \sum_{i=1}^{N_{\text{EC}}} p_i \sigma_{(\dot{\phi}),i}, \tag{45}$$

where $\sigma_{(\dot{\phi}),i}$ is the rotor speed standard deviation for condition i.

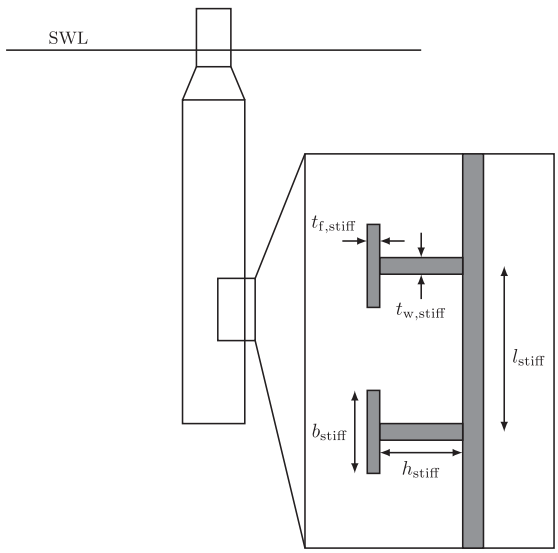

Fig. 6. Scantling design parameters.

3.3. Design variables

3.3.1. Spar platform

In the design process, the hull is discretized using ten sections in the vertical direction. The length of each section, as well as the diameter and wall thickness at each connecting node are included as design variables in the optimization. The diameter and wall thickness are assumed to vary linearly within each element. The number of elements that must be welded together during production is assumed to be equal to the number of hull sections, and is thus independent of the section lengths.

In addition, the study considers the scantling design of the hull. The spar platform is assumed to be equipped with circumferential T-ring stiffeners, which are described by five variables: the thickness and length of the web and flange, and the distance between the stiffeners. This is illustrated in Fig. 6. The ring stiffener variables are assumed to be constant within each section of the hull, and a material density of 7850 kg/m^3 is used for all components.

3.3.2. Tower

Similarly to the platform, the tower is parameterized as ten sections with linearly interpolated cross sectional properties. The section lengths are kept fixed during the optimization to achieve the same hub height as the original DTU 10 MW turbine at 119 m above SWL. Here, each section has a length of 10.5 m, except for the uppermost section, which has a length of 11.13 m. The design variables are the diameter and wall thickness for each section, and the inner structure in the tower is not considered. Because secondary structures in the tower are not modelled, the material density is increased to 8500 kg/m^3 to achieve a more realistic tower mass [19].

3.3.3. Mooring system

The mooring system optimization includes four design variables: the mooring line diameter, the depth of the fairleads below the SWL, the total length of the lines, and the horizontal distance between fairlead and anchor. Because the analyses only consider the 2D response of the turbine with co-directional wind and waves, the layout of the mooring system in the horizontal plane is not considered in the study.

The mooring line diameter affects both the mass and stiffness properties of the lines. The equations for the submerged weight and axial stiffness, w_{moor} and EA_{moor} respectively, are taken from Barltrop [49]:

$$w_{\mathrm{moor}} = 0.1875\, D_{\mathrm{moor}}^2 \quad [\mathrm{N/m}] \tag{46}$$

and

$$EA_{\mathrm{moor}} = 90000\, D_{\mathrm{moor}}^2 \quad [\mathrm{N}], \tag{47}$$

where D_{moor} is expressed in mm.

Table 2
Design variables used in the study.

Description	Symbol	Number of variables	Units
Spar diameter	D_{spar}	11	m
Spar wall thickness	t_{spar}	11	m
Spar length	L_{spar}	10	m
Ring stiffener flange thickness	$t_{f,\mathrm{stiff}}$	4	m
Ring stiffener web thickness	$t_{w,\mathrm{stiff}}$	4	m
Ring stiffener flange width	b_{stiff}	4	m
Ring stiffener web height	h_{stiff}	4	m
Ring stiffener distance	l_{stiff}	4	m
Tower diameter	D_{tower}	11	m
Tower wall thickness	t_{tower}	11	m
Mooring line diameter	D_{moor}	1	m
Fairlead depth	z_{moor}	1	m
Mooring line length	L_{moor}	1	m
Horizontal distance from fairlead to anchor	x_{moor}	1	m
Proportional gain of blade-pitch controller	k_p	1	rad·s/rad
Integral gain of blade-pitch controller	k_i	1	rad/rad

3.3.4. Control system

The control system optimization considers the proportional and integral gains of the blade-pitch PI controller. Although more advanced control strategies are not employed in the present work, they could be implemented with their associated parameters as design variables within the present framework, as long as the system can be reasonably accurately represented by a linear control model. A relevant example is the well-known "negative damping problem" related to the blade-pitch controller above rated wind speed, which can induce instabilities in the platform motions of the system [50]. A suggested way to resolve this issue is to use a feedback term proportional to the nacelle velocity [51] or platform pitch velocity [52] to manipulate the rotor speed set point. The velocity feedback gain could then be incorporated as a design variable in the optimization process.

3.3.5. Summary

Concatenating the design variables for each of the subsystems described in the previous sections would result in a total of 110 design variables. To reduce the required computational effort, the number of design variables is decreased by introducing B-splines for the ring stiffener parameters. B-splines use a pre-defined number of control points, which we set to $n_{cp} = 4$, to produce smooth distributions for the parameters. The remaining support structure design variable vectors are kept at their original sizes, because we found this to result in better optimization convergence. Thus, the optimization problem was reduced to the 80 design variables detailed in Table 2.

3.4. Constraints

The present optimization study includes constraints related both to fatigue (FLS) and ultimate (ULS) limit states for the system. In addition, a number of restrictions are added to avoid non-physical or infeasible design solutions, as detailed below. These may not be stated explicitly in design standards, but are chosen here based on common practice or engineering judgment.

3.4.1. Spar platform

The fatigue damage in the hull is calculated at each node using SN curves and the Dirlik method. The D curve with cathodic protection developed by DNV GL [53] is applied together with a design fatigue factor (DFF) of 3.0. This DFF is higher than the minimum required value given by DNV GL [54], but corresponds to the DFF for a normal safety class in the previous DNV standard [55]. The lifetime of the FWT system is chosen to be 20 years, and the fatigue design constraint that needs to be satisfied is thus expressed as

$$D_{\text{tot}} \leq \frac{1.0}{\text{DFF}}, \tag{48}$$

where D_{tot} is the total fatigue damage in 20 years:

$$D_{\text{tot}} = N_{20} \sum_{i=1}^{N_{\text{EC}}} p_i D_i. \tag{49}$$

Here, N_{20} is the number of short term conditions in 20 years, and D_i is the fatigue damage in condition i.
Hull buckling is assessed using design criteria stated by DNV GL [56], where the following buckling modes are considered:

1. Shell buckling: Buckling of shell plating between ring stiffeners
2. Panel ring buckling: Buckling of shell plating including ring stiffeners
3. Column buckling: Buckling of the cylinder as a column

For shells, the stability requirement is given by

$$\sigma_{j,\text{Sd}} \leq f_{\text{ksd}}, \tag{50}$$

where $\sigma_{j,\text{Sd}}$ is the design equivalent von Mises stress, and f_{ksd} is the design shell buckling strength. To avoid panel ring buckling, several requirements must be met. The cross sectional area of the ring frame, A_{stiff}, must satisfy

$$A_{\text{stiff}} \geq \left(\frac{2}{Z_l^2} + 0.06\right) l_{\text{stiff}}\, t_{\text{spar}}, \tag{51}$$

where Z_l is a curvature parameter. Also, the effective moment of inertia of the ring frame, I_{stiff}, must satisfy

$$I_{\text{stiff}} \geq I_x + I_{xh} + I_h, \tag{52}$$

where the terms on the right hand side are the minimum required moments of inertia for cylindrical shells subjected to axial, bending, or both (I_x), torsion, shear, or both (I_{xh}), and external hydrostatic pressure (I_h). Because the ballast inside the platform is assumed to be solid, the horizontal pressure from the ballast, which counteracts the external pressure, is not accounted for in the buckling calculations [54]. To avoid local buckling of the ring frame, the web height is limited to

$$h_{\text{stiff}} \leq 1.35\, t_{\text{w,stiff}} \sqrt{\frac{E}{f_y}}. \tag{53}$$

The torsional buckling of the ring frame need not be considered if

$$b_{\text{stiff}} \geq \frac{7 h_{\text{stiff}}}{\sqrt{10 + \frac{E}{f_y}\frac{h_{\text{stiff}}}{r}}}, \tag{54}$$

where E is the Young's modulus, and r is the mid-plane shell radius. The yield stress, f_y, is set to 355 MPa. To avoid assessing column buckling, the following equation should be satisfied

$$\left(\frac{kL_C}{i_C}\right)^2 \leq 2.5\frac{E}{f_y}, \tag{55}$$

where k is the effective length factor (set to 1.0), L_C is the total length of the cylinder, and i_C is the radius of gyration for the cylinder section. For the hull buckling, a load factor $\gamma_F = 1.35$ is applied on the environmental loads [54], while the material factor, γ_M, is given by the following equation [54]:

$$\gamma_M = \begin{cases} 1.10, & \bar{\lambda}_s < 0.5 \\ 0.80 + 0.60\,\bar{\lambda}_s, & 0.5 \leq \bar{\lambda}_s \leq 1.0 \\ 1.40, & \bar{\lambda}_s > 1.0, \end{cases} \tag{56}$$

where $\bar{\lambda}_s$ is the reduced shell slenderness defined in DNV GL [56].

The buoyancy forces should be equal to the total weight of the system, which is achieved by filling the inside of the platform with concrete ballast from the bottom until equilibrium is reached. In addition, the platform is limited to have a maximum pitch angle of no more than 15° in any of the extreme ECs. A maximum offset requirement of 32 m, which corresponds to 10% of the water depth, is also applied to avoid breakage of the power cable. These constraints are based on common industry practice and should be verified before they are used in an actual design process.

Another potentially constrained response parameter is the nacelle acceleration, which has been frequently considered in design optimization of FWTs, either as a constraint [11,57] or as part of the objective function [7,8]. The rationale behind setting a limit on the maximum acceleration at the nacelle is typically related to reduced loads on the drivetrain; however, a recent study by Nejad et al. [58] found that the accelerations at the tower top were not a good indicator for either maximum or fatigue loads on the main bearings of the gearbox. This parameter is therefore not considered in the present work.

The heave response is not calculated in the model and is therefore not constrained, but the natural period in heave is limited to minimum 25 s to avoid the possibility of heave resonance in the wave frequency range. Here, the added mass in heave is approximated as the value for a 3D circular disc provided by DNV GL [59], with the same diameter as the bottom of the platform.

Another issue relevant for spar platforms is the phenomenon known as Mathieu instability, which can occur when the pitch restoring moment varies harmonically due to large heave motions [60]. Haslum and Faltinsen [61] reported that unstable solutions occur when the ratio between the heave motion and the pitch natural frequency is 0.5, 1.0, 1.5, or 2.0. Mathieu instability is avoided in the current work by placing a constraint on the ratio between the natural periods in heave and pitch, to prevent it from reaching a value close to one of the critical ratios.

The presented model is only strictly valid for hull sections with vertical walls. However, the diameter varies with the platform nodes, and abrupt changes in geometry are unwanted due to fatigue performance. Therefore, the sections are conical in reality. To avoid platform shapes where the physics are not captured correctly by the model, a maximum taper angle of 10° is applied as a constraint for each section.

To limit the computational effort, constraints that must be satisfied along the length of the platform, such as the fatigue and buckling constraints, are aggregated using Kreisselmeier–Steinhauser (KS) functions [62,63]. This is also done for constraints that must be satisfied in each of the 50-year conditions.

3.4.2. Tower

The fatigue damage in the tower is assessed in the same way as described for the platform, but with the D curve in air and DFF = 2.0 [55].

Tower buckling is assessed using Eurocode 3 [64], assuming that the tower is stiffened between each section to reduce the buckling length. For each tower section, the following equation must be satisfied

$$\sigma_x \leq \frac{\sigma_{cr}}{\gamma_M \gamma_F}, \tag{57}$$

where σ_x is the axial stress on the outer radius of the tower, σ_{cr} is the critical buckling stress, and γ_F and γ_M are load and material factors, respectively. The factors applied in the current work are $\gamma_M = 1.1$ [65] and $\gamma_F = 1.35$ [54]. To ensure a smooth transition between the platform and tower, the tower base diameter and wall thickness are set equal to the diameter and wall thickness at the platform top. As for the hull, KS functions are used to aggregate the constraints.

3.4.3. Mooring system

Two constraints are applied to the mooring system: the maximum mooring line tension should not exceed the breaking strength of the chain, and the tension at the anchor should be purely horizontal. The first constraint is expressed as [54]

$$T_d \leq 0.95\, S_{\text{mbs}}, \tag{58}$$

where S_{mbs} is the minimum breaking strength and T_d is the design tension,

$$T_d = \gamma_{\text{mean}}\, T_{c,\text{mean}} + \gamma_{\text{dyn}}\, T_{c,\text{dyn}}. \tag{59}$$

Here, $T_{c,\text{mean}}$ and $T_{c,\text{dyn}}$ are the characteristic mean tension and the characteristic dynamic tension in the 50-year condition, respectively, and $\gamma_{\text{mean}} = 1.3$ and $\gamma_{\text{dyn}} = 1.75$ are the load factors for the normal safety class [54]. The minimum breaking strength is computed using

$$S_{\text{mbs}} = c\, D_{\text{moor}}^2 (44 - 0.08 D_{\text{moor}}), \tag{60}$$

where c is a constant dependent on the mooring chain grade [66].

The second constraint is based on the assumption that the anchors are not designed to take vertical forces, which requires the mooring lines to have sufficient length to avoid uplift at the anchors in all relevant ULS conditions [67]. The constraint limits the maximum experienced offset at the fairleads to be less than the critical value, which is found from an iteration scheme where the offset is increased until the effective length of the mooring line equals the total line length.

3.4.4. Control system

For certain combinations of the PI controller gains, the FWT system may become unstable. This is avoided by adding a requirement that the closed-loop poles of the system should have negative real parts, which ensures stability [68]. Analyzing the poles of the linearized system is not an exact method for determination of stability; Sandner et al. [69] found that a spar FWT with gains that gave poles in the right half plane still showed reasonable performance in nonlinear simulations. However, this analysis provides a starting point for a more detailed design of the control system.

4. Results

The results of the optimization study, presented in the following subsections, are divided into six parts. First, we discuss the multimodality of the design space, and identify local minima. Trade-off effects between the two sub-objectives in Eq. (42) are then assessed by running the optimization problem stated in Section 3 with different weight factors. Subsequently, a single combination of weight factors is selected, and the resulting optimized design of the support structure, mooring system, and controller is described in detail. Finally, the design is verified using nonlinear time domain simulations.

4.1. Soft-stiff and stiff-stiff tower design

The fatigue damage in the support structure increases significantly if the natural frequency of the first tower bending mode coincides with the blade passing frequency, and the optimizer will therefore try to move the tower mode away from the 3P range. The direction that the mode is moved during the optimization will depend on the initial design, as illustrated in Fig. 7. Due to the "barrier" created by the blade passing frequency, the optimizer will not be able to move over to the stiff-stiff range if the initial design has a soft-stiff tower, and vice versa.

Initial studies performed in this work showed that the tower mode had to be placed in the stiff-stiff range for the optimization problem to converge to a feasible solution, because the optimizer was unable to find a design that satisfied the fatigue constraints in the

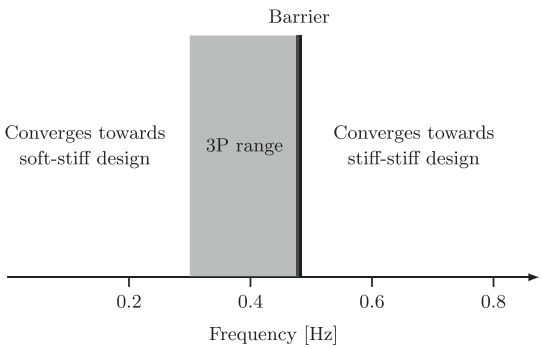

Fig. 7. Impact of initial tower bending natural frequency on optimization results.

soft-stiff range. Although these results suggest that it is challenging to design such a FWT system with a soft-stiff tower, it should not be treated as proof that a solution does not exist. The design analyses are based on a simplified model and a reduced set of ECs for the long-term fatigue calculations, which may give inaccurate results for certain combinations of parameters. In addition, more advanced control strategies, such as a speed exclusion zone to prevent tower resonance in the below-rated regime, could improve the fatigue behaviour. More detailed studies of potential designs are therefore needed to conclude whether a feasible soft-stiff tower design is possible.

4.2. Trade-offs between system costs and power quality

To assess the trade-offs between costs and power quality for the system, the optimization is performed with different values for the weight factors in Eq. (42). Here, the rotor speed standard deviation is normalized by the value achieved with the land-based DTU 10 MW wind turbine and the original controller [70], found from nonlinear time domain analyses using SIMA. The land-based weighted average rotor speed standard deviation is found to be 0.043 rad/s. Because the present work considers a floating system with a simplified controller, the rotor speed variations are expected to be larger than the land-based reference value.

The results, shown in Fig. 8, suggest that a significant reduction in rotor speed variation can be achieved with relatively small increases in the total costs. However, these results are dependent on the environmental conditions that drives the extreme response. The reduction in rotor speed variation is primarily achieved by modifying the blade-pitch controller gains, but for both platform motions and buckling loads in the support structure, the below-rated 50-year condition (EC 1) yields the largest response. Therefore, the blade-pitch controller does not affect the extreme response of the system, and the trade-off effects are limited to the response in the above-rated fatigue conditions, where a faster controller (and thus better rotor speed tracking) leads to an increase in the fatigue loads and consequently to an increase in material costs.

In the following sections, the results are presented for the case shown with a black circle in Fig. 8, which corresponds to $w_1 = 7\times 10^{-8}$ and $w_2 = (1 - 7\times 10^{-8})$ in Eq. (42).

4.3. Platform and tower

The optimized tower and platform design, including fatigue and buckling utilization, is shown in Fig. 9. For the hull, the value for the most critical buckling mode is shown.

The probable reason for the relatively small platform diameter in the wave zone is to reduce the wave loads on the structure. Because a smaller diameter increases the axial stress for a given bending moment, and because the fatigue loads in this part of the structure are large, a large wall thickness is needed in this area to satisfy the FLS design criteria. Fatigue is the critical failure mode down to a depth of approximately 10 m, beyond which buckling due to hydrostatic pressure becomes the constraint driving the design.

Below the wave zone, the hull exhibits an hourglass shape, with maximum and minimum values for the diameter approximately 32 m and 56 m below the SWL, respectively. The sharp edges located where the diameter reaches its maximum and minimum and the constant gradient between them is a result of the maximum taper angle constraint being active for most of the platform sections. The constraint is a consequence of the simplified hydrodynamic and structural formulations, and its value is based solely on engineering judgment. The results indicate that the performance of the platform can be further improved if this constraint is relaxed, which might require a more comprehensive numerical model and possibly more information about the effect of the platform shape on the manufacturing costs.

The hourglass shape serves several purposes that are beneficial for the platform dynamics. The large diameter just below the wave

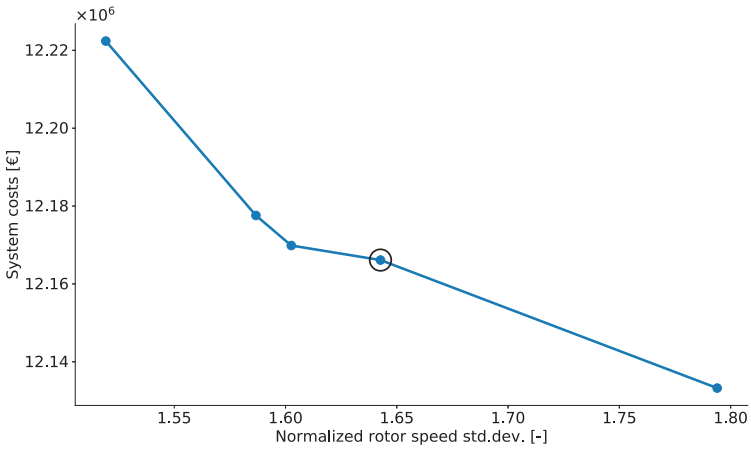

Fig. 8. Trade-offs between rotor speed variation and system costs in the multiobjective optimization.

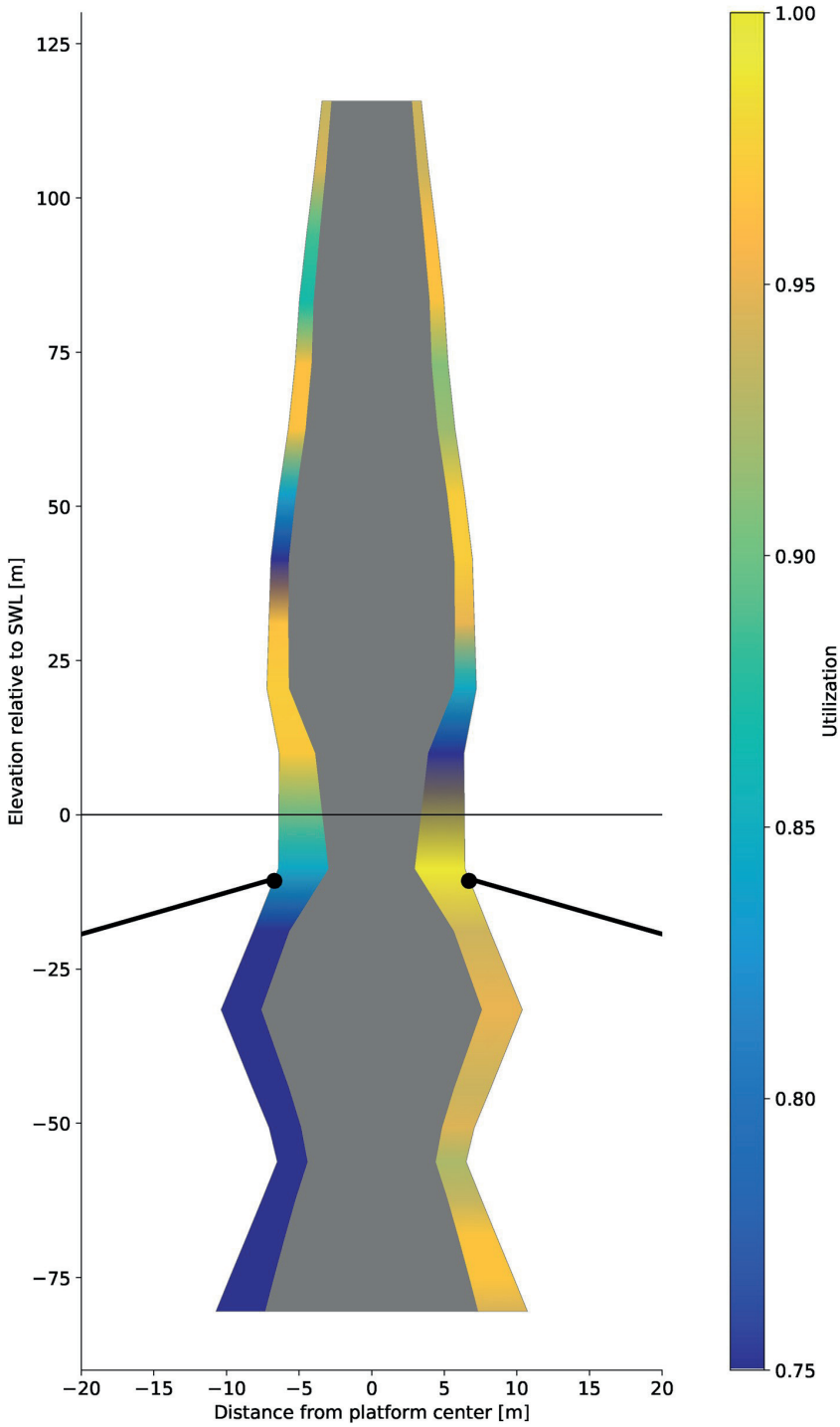

Fig. 9. Optimized tower and platform design with fatigue utilization (left) and buckling utilization (right). The wall thickness is scaled by a factor of 40 relative to the diameter for visualization purposes.

zone raises the centre of buoyancy (CoB), and because spar platforms achieve most of their restoring moment in roll and pitch from the distance between the CoB and the total centre of gravity (CoG), this effectively increases the rotational stiffness of the system.

The increase in diameter near the bottom of the spar can be explained by two factors. First, because the hull is filled with concrete ballast from the bottom until equilibrium between weight and buoyancy is reached, a consequence of the increased diameter is that a larger share of the required ballast can be placed near the bottom, which lowers the platform CoG. Second, the increased surface area at the bottom increases the added mass and thus the natural period in heave, which is constrained from below to avoid resonance in the wave-frequency range. One effect of increasing the restoring moment is that the natural period in pitch is reduced. At higher frequencies, there is less energy in the wind (less turbulence) and thus less excitation around the natural frequency as well.

The lower draft compared to other designs, such as the 5 MW OC3-Hywind design [71], is advantageous from a material cost point of view, because the high hydrostatic pressure at large depths requires thick-walled sections. Although costs related to installation are not a part of the objective in the current optimization scheme, a shallower draft is also favourable with respect to assembly and towing to site, which is one of the challenges related to spar buoys.

Both the maximum platform pitch constraint of 15° and the maximum offset constraint of 32 m in the 50-year conditions are active for the optimized design. The critical condition for both constraints is EC 1, where the mean wind speed is close to rated. The static pitch angle at rated thrust for the optimized design is 7.7°. The key characteristics for the optimized spar platform are listed in Table 3, while natural periods for the system in calm air are listed in Table 4. Distributed properties for the optimized platform and tower are given in Tables 10 and 11 in Appendix A.

Surprisingly, the diameter of the tower increases from the base and reaches its maximum at a height of 20.5 m above the SWL. This is uncommon for wind turbine towers, which typically are widest at the bottom and taper gradually towards the nacelle. The reason for this unconventional design is related to the integrated optimization approach, which takes into account the cost and performance of the tower and platform simultaneously. In general, within the limits set by the buckling constraints, the most cost-effective way to achieve the required fatigue performance for a given tower section is to increase the diameter and decrease the wall thickness. However, at the tower base, the diameter also has to match the diameter at the top of the platform, which should be reduced to limit the wave loads on the structure. The result of these conflicting influences is that the optimized tower starts with a smaller-than-optimal diameter at the base and consequently larger-than-optimal wall thickness (from the point of view of an isolated tower), before the diameter is increased and the wall thickness is significantly reduced.

The spar platform has clearly separated areas where the design is driven by either fatigue or ultimate loads because of the large bending moments in the wave zone and high hydrostatic pressure in the lower parts. Unlike the spar platform, both tower constraints are dominated by bending moments. Consequently, the optimizer is able to find a tower design where both the FLS and ULS constraints are close to the limit along the whole length. Table 5 lists the main parameters of the optimized tower, where the elevations to the tower base and tower top are fixed during the optimization.

In Fig. 10, the optimized tower design is compared to the tower of the OO-Star Wind Floater Semi 10 MW, which was part of the LIFES50+ project [72]. The comparison shows that the present design in general has a larger diameter and a smaller wall thickness than the OO-Star tower. Comparing the overall tower properties, the mass of the tower optimized in the present work is approximately 24% lower than the OO-Star tower, despite using a slightly larger effective mass density (8500 vs. 8243 kg/m^3). The natural frequency of the first fore-aft tower bending mode (with flexible substructure) is 0.8 Hz and 0.59 Hz for the optimized tower and the OO-Star tower, respectively, which places them both well within the stiff-stiff range. One drawback with the large diameter in the tower presented here is that tower shadow effects, which are not considered in the model, become more prominent. This may in turn lead to increased loads on the blades and increased 3P excitation on the tower, which could complicate the design process.

The optimized scantling design parameters are shown in Fig. 11. All five variables follow the same pattern, where a reduced distance between stiffeners results in smaller required stiffener size. In general, the most critical buckling mode driving the ring stiffener design is the buckling of the shell plating.

4.4. Control system

The optimized control system parameters for different weight factors are plotted against the resulting power quality in Fig. 12. Increasing the gains results in a faster controller, leading to lower variation in the rotor speed.

To assess the importance of integrating the controller in the FWT design loop, the optimization procedure is repeated with the control parameters k_p and k_i fixed at their initial values, as shown in Table 6. The values are those obtained by Hegseth and Bachynski [20], where a simple detuning procedure was used to reduce the bandwidth of the original DTU 10 MW controller [70] and thus place

Table 3
Optimized platform properties (without tower and turbine).

Parameter	Value	Units
Draft	80.4	m
Mass including ballast	1.57×10^7	kg
Displacement	1.72×10^4	m^3
Moment of inertia about CoG	4.66×10^9	kgm^2
Vertical CoG below SWL	66.0	m
Vertical CoB below SWL	42.9	m

Table 4
Natural periods for the optimized FWT system.

Mode	Value	Units
Surge	144.7	s
Pitch	34.4	s
Heave	25.0	s
1st bending	1.25	s

Table 5
Optimized tower properties.

Parameter	Value	Units
Elevation to tower base above SWL	10.0	m
Elevation to tower top above SWL	115.63	m
Total mass	9.5×10^5	kg
Vertical CoG above SWL	49.1	m
Moment of inertia about CoG	7.46×10^8	kgm^2

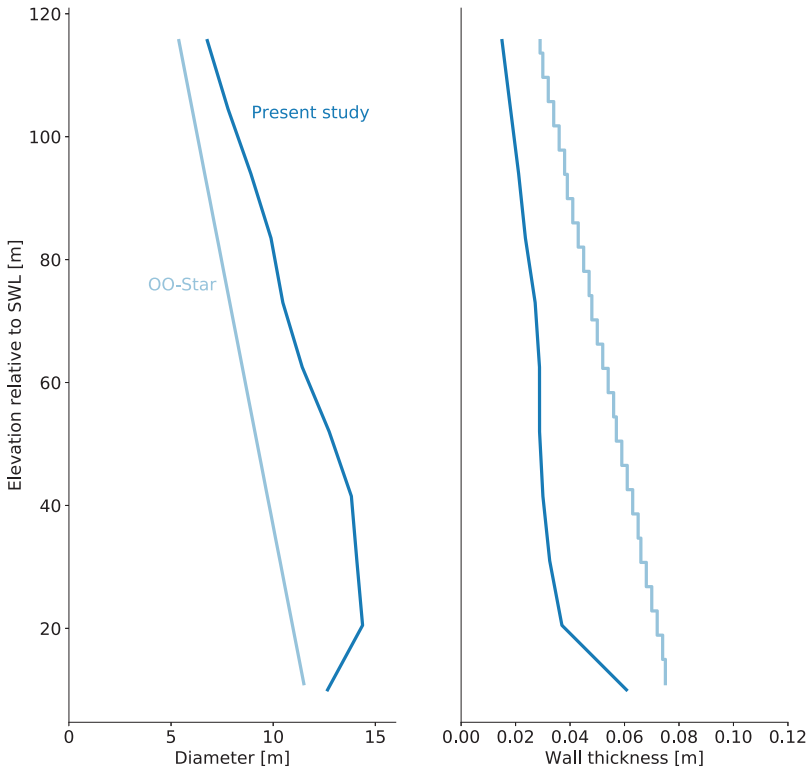

Fig. 10. Comparison of optimized tower design with LIFES50+ OO-Star Wind Floater.

it below the platform pitch natural frequency, while the damping ratio was kept constant.

The cost and power quality for the optimized solutions with and without the controller (for the same objective function weights) are shown in Table 7. Using the initial detuned controller results in both slightly higher costs, due to larger fatigue loads in the tower, and larger rotor speed variation. Although the actual numbers depend on the values used for the gains and thus are only valid for this particular example, it shows that neglecting the controller in the structural design process may lead to more expensive solutions with lesser performance.

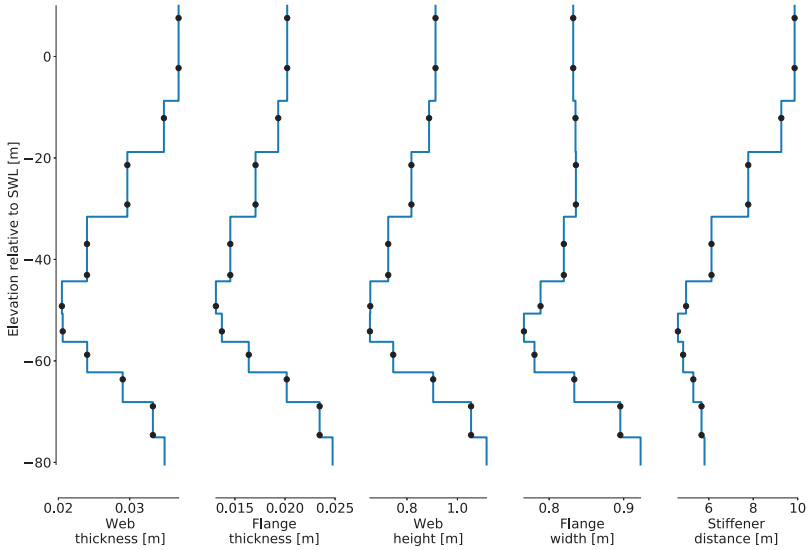

Fig. 11. Optimized ring stiffener parameters. The black dots show a possible stiffener layout.

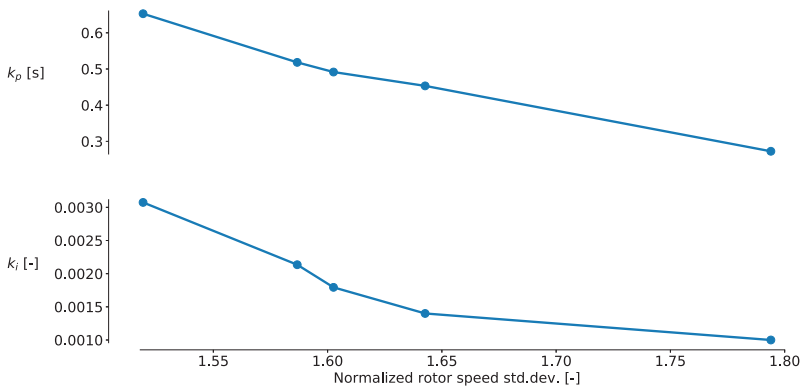

Fig. 12. Optimized blade-pitch controller gains plotted against resulting rotor speed variation.

Table 6
Fixed control system parameters.

Parameter	Value	Units
k_p	0.1794	rad·s/rad
k_i	0.0165	rad/rad

Table 7
Objective function values with and without controller included in the optimization.

	System cost [10_6 €]	Normalized rotor speed std.dev. [−]
With controller	12.17	1.65
Without controller	12.19	1.82
Difference	0.2%	10.9%

4.5. Mooring system

The optimized mooring system parameters are listed in Table 8. The most critical ULS condition for both mooring system constraints is found to be EC 1, as for the maximum offset and pitch angle constraints in Section 4.3. This is due to the large thrust forces in this condition. The optimized solution consists of relatively long mooring lines to meet the requirement of no uplift at the anchors. The line length and thus the material costs of the system, could be significantly reduced if vertically loaded anchors were used; however, these types of anchors are more expensive to install [73]. More information about the total costs of the mooring system, including installation and anchoring, would be needed to identify the most cost-effective solution.

Based on the results presented here, the significance of designing the mooring system simultaneously with the platform is not as clear as for the tower or control system. Although the mass of the platform and tower affect the natural period in surge and subsequently the level of excitation around resonance, the surge response is mostly governed by the rotor and mooring system design and is to a large degree independent from the design of the support structure. The most important coupling effects between the support structure and mooring system are related to the location of the fairleads, which influences the surge-pitch coupling and thus the pitch response of the platform. The fairlead position also affects the fatigue damage in the hull because the mooring forces contribute to the internal loads in the platform. Another coupling effect is that low-frequency mooring line dynamics, which is dependent on the platform motions, will induce damping for the low-frequency platform response [74]. However, this coupling effect is not considered in the present work.

The delta connections are omitted from the mooring system in the present model, and the yaw response of the platform is neglected in the analysis. Since one of the main tasks of the mooring system for a spar FWT is to limit yaw motions [75], the optimized mooring design presented here may have to be modified to obtain satisfactory performance for the platform response. In addition, common mooring line components that can improve the system behaviour, such as buoys or clump weights, can not be modelled with the current methodology and are not considered.

4.6. Design verification

The proposed design optimization approach is verified by analysing initial and optimized designs using nonlinear aero-hydro-servo-elastic time-domain simulations in SIMA. Here, the tower, hull, and blades are modelled using nonlinear beam elements. Hydrodynamic loads in the horizontal direction are applied on the platform using MacCamy–Fuchs theory, together with viscous forces from the drag term in Morison's equation. In heave, the hydrodynamic loads are limited to buoyancy forces integrated up to the instantaneous free surface and added mass on the lower end of the platform, meaning that Froude–Krylov and diffraction forces are neglected. Since the heave response is not considered in the linearized model, and the first order wave excitation in heave is small, this is deemed acceptable for the present work.

Bar elements with only axial stiffness are used to model the mooring lines, and hydrodynamic loads on the lines are computed using Morison's equation. A rotational spring is added to the model to ensure that the yaw stiffness from the mooring system is included, using a spring stiffness of 1.48×10^8 Nm/rad. The aerodynamic loads on the rotor are computed using BEM theory as described in Section 2.5.4, and viscous drag forces on the tower are included.

The fatigue performance of the tower and hull is assessed by analysing the 30 FLS conditions using six 1-h realizations. Rainflow counting and the Miner–Palmgren rule are used to estimate the fatigue damage, which is taken as the average value over the six seeds. The extreme response, i.e., the most probable maximum value in 1 h in the 50-year conditions, is found using the AUR method, where the function describing the upcrossing rate is fitted to the empirical data [76]. 1-h simulations with 20 different random seeds are used for each 50-year condition.

The initial design is based on the "Spar 1" design obtained by Hegseth and Bachynski [20], but with 60% increase in wall thickness and 40% increase in diameter along the hull and tower to place the first tower mode in the stiff-stiff range. This FWT system has not been through a proper design process and does not represent a realistic solution. The purpose of including it in the verification is not to use it as a benchmark for the optimized design, but rather to show that the presented methodology is able to capture real trends.

Fatigue and buckling utilization factors from the nonlinear time-domain analyses are shown in Fig. 13 and Fig. 14 for the initial and optimal designs, respectively. For the initial design, the fatigue damage values are overestimated by the linear model in the wave zone and lower parts of the tower, where the largest utilization factors are found. This is primarily due to limitations in the Dirlik calculations in the current work, which assumes a single-slope SN curve valid for high-cycle fatigue. Therefore, this assumption becomes less accurate for designs with large damage values, where there is also a significant contribution from low-cycle fatigue. The buckling utilization factors agree very well, suggesting that the extreme response in this condition is relatively linear.

For the optimized designs, the fatigue damage and buckling utilization factors in the tower agree reasonably well with the results from the linearized model, which is usually conservative. This is primarily due to the overestimation of the platform pitch response in the linear model, which become more prominent in extreme conditions. Because the pitch response for the initial design is in general much smaller than for the optimized solution and thus contributes less to the bending moments in the structure, this effect is not seen for the initial design results in Fig. 13.

There is a notable difference between the linear and nonlinear models for the fatigue damage at the tower top in Fig. 14, where the accumulated damage based on time-domain simulations in SIMA is about twice as high. We believe this to be a consequence of somewhat non-Gaussian bending moment response at the tower top, which causes the accuracy of the Dirlik method to deteriorate. For the rest of the tower, the response is close to Gaussian, which earlier has been shown to result in good agreement between the Dirlik method and rainflow counting for spar FWTs [20].

Table 8
Optimized mooring system parameters.

Parameter	Value	Units
D_{moor}	0.081	m
z_{moor}	− 10.7	m
L_{moor}	1433.0	m
x_{moor}	1497.2	m

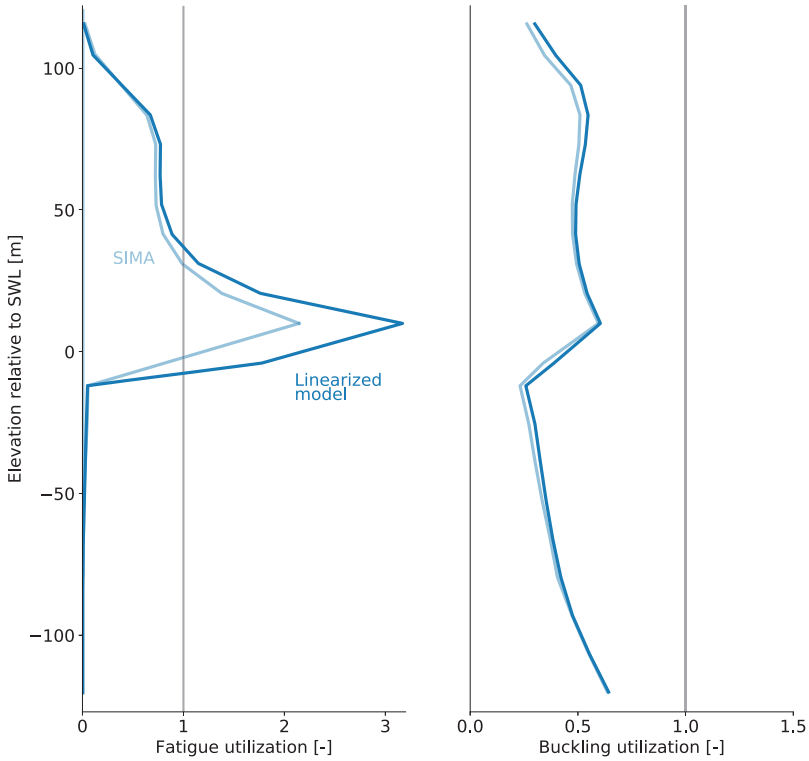

Fig. 13. Comparison of fatigue and buckling utilization factors, initial design.

Almost perfect agreement is observed for the hull buckling, despite the overprediction of the bending moments by the linear model. The reason for this is that the hydrostatic pressure, which is easily obtained without error, is the most important load component for buckling of the shell plating in the hull.

The extreme values for the offset, pitch angle, and mooring tension are listed in Table 9. The linearized model overestimates the platform motions, mainly because the aerodynamic loads are linearized and the mooring line damping is neglected. The mooring tension, on the other hand, is underestimated by the linear model, which also predicts a 4% decrease in the extreme value from initial to optimized design that is not observed in the nonlinear model.

5. Conclusions

A linearized aero-hydro-servo-elastic FWT model has been developed and used to optimize the design of the platform, tower, mooring system, and blade-pitch controller for a 10 MW spar FWT. The goal of the optimization is to minimize a weighted combination of the system costs and rotor speed variation, which is used as a measure of the power quality.

The results of the optimization depend on the initial tower design because a local minimum exist in both the soft-stiff and stiff-stiff range for the first bending mode. Initial analyses suggest that feasible soft-stiff tower designs may be challenging to achieve for these types of FWT systems, since no solution that satisfied the FLS constraints was identified by the optimizer. However, including more advanced control strategies could improve the fatigue behaviour in the soft-stiff range, and potentially result in a different global minimum for the problem.

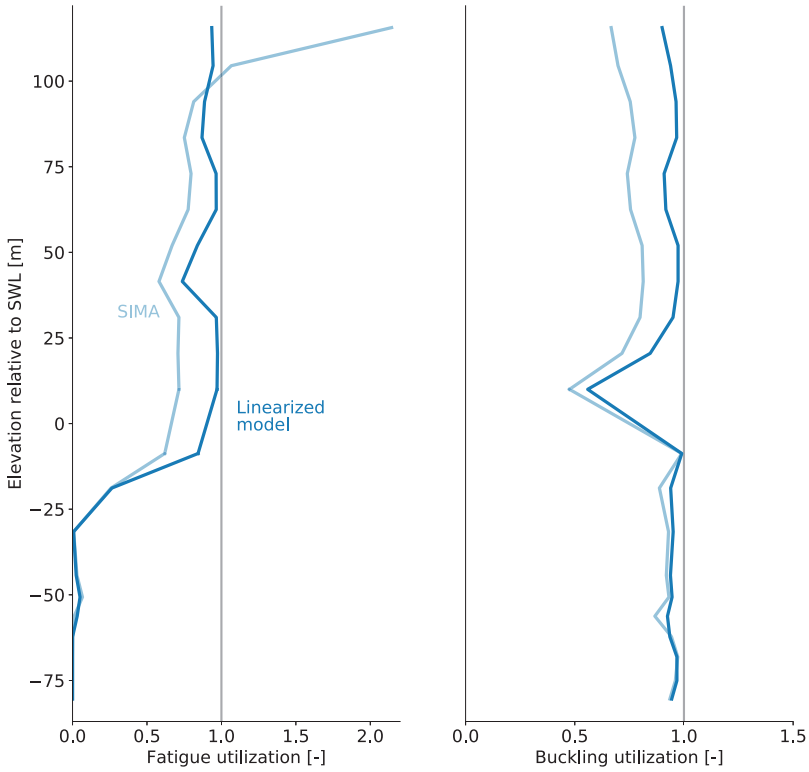

Fig. 14. Comparison of fatigue and buckling utilization factors, optimized design.

Table 9
Comparison of extreme response constraints.

Model	Initial design			Optimized design		
	Surge	Pitch	Mooring tension	Surge	Pitch	Mooring tension
Linear	35.1 m	7.0 deg	6.15×10^6 N	32.0 m	15.0 deg	5.91×10^6 N
Nonlinear	29.4 m	5.9 deg	6.68×10^6 N	27.1 m	11.3 deg	6.68×10^6 N

The platform adopts an hourglass shape below the wave zone, where the diameter is kept small to limit the wave loads on the structure. The hourglass shape maximizes the distance between the CoB and the CoG, which increases the restoring moment and natural frequency in pitch and consequently improves the behaviour in the low-frequency range for the platform pitch response. The large bottom diameter also increases the added mass in heave, which helps place the natural frequency outside the wave-frequency range.

The importance of integrated design is evident in the optimized solutions for the tower and blade-pitch control system, where the interaction with the platform clearly affects the design. For the tower, the integrated optimization results in an unconventional design where the diameter increases from the tower base, because the base diameter is constrained to match the diameter at the upper end of the platform. Varying the weight factors in the multi-objective optimization primarily affected the control system variables, which governed the trade-offs between rotor speed variation and fatigue damage in the support structure (and thus the material costs). Optimizing with fixed gains from a simple detuning procedure resulted in 0.2% higher cost and 10.5% larger rotor speed standard deviation compared to the integrated solution.

The loads on the drivetrain are not considered in the present optimization study because there is a lack of response parameters that can serve as proxies for the drivetrain performance with the current methodology. If such parameters are identified, additional terms may be included in a multi-objective optimization approach to penalize designs with unfavourable drivetrain response. As discussed in Section 3.2, finding appropriate weights for the different sub-objectives is challenging, and sensitivity studies would be needed to assess trade-offs between the variables. This would in turn increase the computational effort.

The use of linear analyses in the frequency domain imposes important limitations on the computations, since nonlinear and

transient effects are not captured. The accuracy of the model, and thus its applicability in design optimization studies, is therefore dependent on the importance of these effects. Also, the proposed methodology is only applicable for spar platforms, which limits the choices of the optimizer. A more general description of the platform geometry, which requires more comprehensive models for the hydrodynamics and structural dynamics, would allow the optimization to explore other parts of the design space and possibly identify more cost-effective solutions.

The feasibility of the optimized design is verified using state-of-the-art simulations, which show that the simplified model gives reasonably accurate predictions for both fatigue and extreme response. In general, the linearized model is conservative, especially for the platform pitch motions, which tended to be more nonlinear than the internal loads in the support structure. The main reason for the overprediction is likely to be the linearization of the aerodynamic loads.

The proposed methodology is shown to be suitable for preliminary design, where it can provide a starting design for later and more detailed design phases. The integration of several subsystems in a single design optimization process clearly affects the results and improves the overall system behaviour. The methodology can be extended to account for additional concepts, parameters, and load cases, which may help identify novel design solutions.

Declaration of competing interest

The authors declare that they have no known competing financial interests or personal relationships that could have appeared to influence the work reported in this paper.

Acknowledgements

Financial support from the Research Council of Norway (NFR) through project number 274827 - “Green Energy at Sea” is gratefully acknowledged. The first author is grateful to John Jasa for helpful discussions regarding the OpenMDAO implementation.

A. Distributed Properties for the Optimized Platform and Tower

Table 10
Distributed platform properties.

Elevation above SWL [m]	Outer diameter [m]	Wall thickness [m]
− 80.427	21.365	0.084
− 75.064	19.505	0.075
− 68.117	17.055	0.064
− 62.249	15.003	0.056
− 56.242	12.940	0.051
− 50.677	14.070	0.054
− 44.312	16.314	0.061
− 31.584	20.681	0.068
− 18.829	16.212	0.060
− 8.741	12.784	0.085
10.000	12.660	0.061

Table 11
Distributed tower properties.

Elevation above SWL [m]	Outer diameter [m]	Wall thickness [m]
10.000	12.660	0.061
20.500	14.377	0.037
31.000	14.096	0.033
41.500	13.827	0.030
52.000	12.742	0.029
62.500	11.422	0.029
73.000	10.473	0.027
83.500	9.892	0.024
94.000	8.904	0.021
104.500	7.789	0.018
115.630	6.774	0.015

B. XDSM Diagram

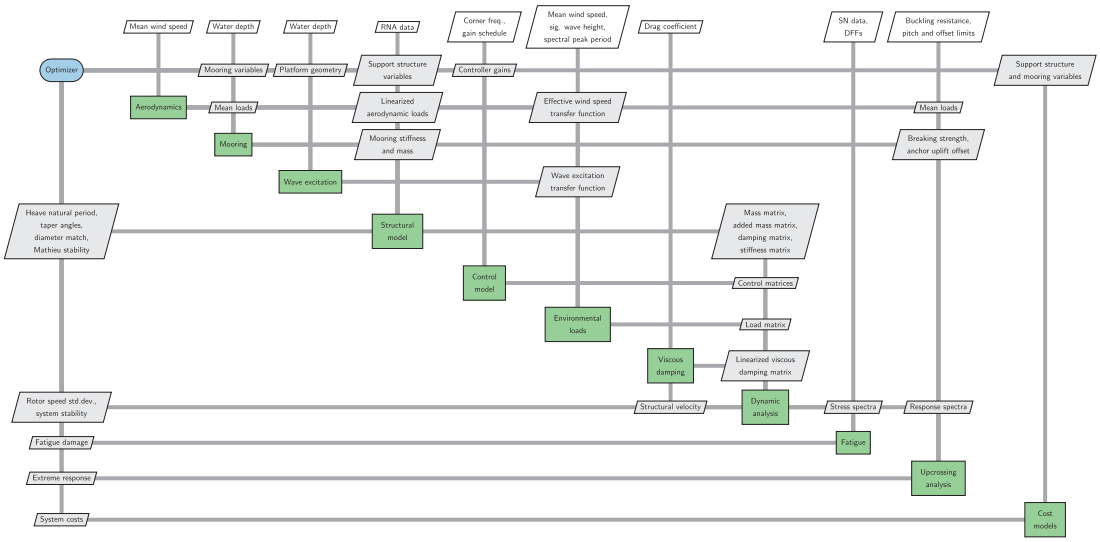

Fig. B.1. XDSM diagram showing the model layout and data dependencies. Rounded blue box is the optimizer, green boxes are analysis models, gray parallelograms are data, white parallelograms are fixed input parameters, and gray lines represent data dependencies. The data moves from top to bottom and left to right in the upper triangular part, and from bottom to top and right to left in the lower triangular part. See Lambe and Martins [42] for more details on how to interpret this figure.

References

[1] Martins JRRA, Lambe AB. Multidisciplinary design optimization: a survey of architectures. AIAA J 2013;51(9):2049–75. https://doi.org/10.2514/1.J051895.

[2] Tracy C. Parametric design of floating wind turbines. Master's thesis. Massachusetts Institute of Technology; 2007.

[3] Bachynski EE, Moan T. Design considerations for tension leg platform wind turbines. Mar Struct 2012;29:89–114. https://doi.org/10.1016/j.marstruc.2012.09.001.

[4] Gilloteaux J-C, Bozonnet P. Parametric analysis of a cylinder-like shape floating platform dedicated to multi-megawatt wind turbine. In: Proceedings of the twenty-fourth (2014) international ocean and polar engineering conference (ISOPE2014). Korea: Busan; 2014.

[5] Clauss GF, Birk L. Hydrodynamic shape optimization of large offshore structures. Appl Ocean Res 1996;18(4):157–71. https://doi.org/10.1016/S0141-1187(96)00028-4.

[6] Brommundt M, Krause L, Merz K, Muskulus M. Mooring system optimization for floating wind turbines using frequency domain analysis. Energy Procedia 2012;24:289–96. https://doi.org/10.1016/j.egypro.2012.06.111.

[7] Hall M, Buckham B, Crawford C. Evolving offshore wind: a genetic algorithm-based support structure optimization framework for floating wind turbines. In: OCEANS 2013 MTS/IEEE bergen: the challenges of the Northern dimension; 2013. https://doi.org/10.1109/OCEANS-Bergen.2013.6608173.

[8] Karimi M, Hall M, Buckham B, Crawford C. A multi-objective design optimization approach for floating offshore wind turbine support structures. J Ocean Eng Mar Energy 2017;3(1):69–87. https://doi.org/10.1007/s40722-016-0072-4.

[9] Myhr A, Nygaard TA. Load reductions and optimizations on tension-leg-buoy offshore wind turbine platforms. In: Proceedings of the twenty-second (2012) international offshore and polar engineering conference (ISOPE2012), Rhodes, Greece; 2012.

[10] Muskulus M, Schafhirt S. Design optimization of wind turbine support structures - a review. J Ocean Wind Energy 2014;1(1):12–22.

[11] Fylling I, Berthelsen PA. WINDOPT- an optimization tool for floating support structures for deep water wind turbines. In: Proceedings of the ASME 2011 30th international conference on ocean, offshore and Arctic engineering (OMAE2011), Rotterdam, The Netherlands; 2011. https://doi.org/10.1115/OMAE2011-49985.

[12] Strach-Sonsalla M, Muskulus M. Dynamics and design of floating wind turbines. In: Proceedings of the twenty-sixth (2016) international ocean and polar engineering conference (ISOPE2016), Rhodes, Greece; 2016.

[13] Tibaldi C, Hansen MH, Henriksen LC. Optimal tuning for a classical wind turbine controller. J Phys Conf 2014;555(12099). https://doi.org/10.1088/1742-6596/555/1/012099.

[14] Lemmer F, Müller K, Yu W, Schlipf D, Cheng PW. Optimization of floating offshore wind turbine platforms with a self-tuning controller. In: Proceedings of the ASME 2017 36th international conference on ocean, offshore and Arctic engineering (OMAE2017), trondheim, Norway; 2017. https://doi.org/10.1115/OMAE2017-62038.

[15] Gray JS, Hwang JT, Martins JRRA, Moore KT, Naylor BA. OpenMDAO: an open-source framework for multidisciplinary design, analysis, and optimization. Struct Multidiscip Optim 2019;59:1075–104. https://doi.org/10.1007/s00158-019-02211-z.

[16] Ashuri T, Zaaijer MB, Martins JRRA, van Bussel GJW, van Kuik GAM. Multidisciplinary design optimization of offshore wind turbines for minimum levelized cost of energy. Renew Energy 2014;68:893–905. https://doi.org/10.1016/j.renene.2014.02.045.

[17] Ashuri T, Martins JRRA, Zaaijer MB, van Kuik GAM, van Bussel GJW. Aeroservoelastic design definition of a 20 MW common research wind turbine model. Wind Energy 2016;19:2071–87. https://doi.org/10.1002/we.1970.

[18] Madsen MH Aa, Zahle F, Sørensen NN, Martins JRRA. Multipoint high-fidelity CFD-based aerodynamic shape optimization of a 10 MW wind turbine. Wind Energy Sci 2019;4:163–92. https://doi.org/10.5194/wes-4-163-2019. ISSN 23667451.

[19] Bak C, Zahle F, Bitsche R, Yde A, Henriksen LC, Natarajan A, Hansen MH. Description of the DTU 10 MW reference wind turbine. Technical Report DTU Wind Energy Report-I-0092. DTU Wind Energy; 2013.
[20] Hegseth JM, Bachynski EE. A semi-analytical frequency domain model for efficient design evaluation of spar floating wind turbines. Mar Struct 2019;64:186–210. https://doi.org/10.1016/j.marstruc.2018.10.015.
[21] Merz K. Conceptual design of a stall-regulated rotor for a deepwater offshore wind turbine. PhD thesis. Norwegian University of Science and Technology; 2011.
[22] Bachynski EE, Etemaddar M, Kvittem MI, Luan C, Moan T. Dynamic analysis of floating wind turbines during pitch actuator fault, grid loss, and shutdown. Energy Procedia 2013;35:210–22. https://doi.org/10.1016/j.egypro.2013.07.174.
[23] Jiang Z, Karimirad M, Moan T. Dynamic response analysis of wind turbines under blade pitch system fault, grid loss, and shutdown events. Wind Energy 2014;17:1385–409. https://doi.org/10.1002/we.1639.
[24] Larsen K, Sandvik PC. Efficient methods for the calculation of dynamic mooring line tension. In: Proceedings of the first (1990) European offshore mechanics symposium, trondheim, Norway; 1990.
[25] Lie H, Sødahl N. Simplified dynamic model for estimation of extreme anchor line tension. In: Offshore Australia, the 2nd Australian oil, gas & petrochemical exhibition and conference, Melbourne, Australia; 1993.
[26] Jonkman J, Butterfield S, Musial W, Scott G. Definition of a 5-MW reference wind turbine for offshore system development. Technical Report NREL/TP-500-38060. National Renewable Energy Laboratory; 2009.
[27] Naess A, Moan T. Stochastic dynamics of marine structures. Cambridge University Press; 2013.
[28] DNV GL. Loads and site conditions for wind turbines. Technical Report DNVGL-ST-0437. DNV GL; 2016.
[29] Dirlik T. Application of computers in fatigue analysis. PhD thesis. University of Warwick; 1985.
[30] Naess A, Gaidai O. Monte Carlo methods for estimating the extreme response of dynamical systems. J Eng Mech 2008;134(8):628–36. https://doi.org/10.1061/(ASCE)0733-9399 (2008)134:8(628).
[31] Burton T, Jenkins N, Sharpe D, Bossanyi E. Wind energy handbook. second ed. Wiley; 2011.
[32] Manwell JF, McGowan JG, Rogers AL. Wind energy explained. second ed. Wiley; 2009.
[33] Halfpenny A. Dynamic analysis of both on and offshore wind turbines in the frequency domain. PhD thesis. University College London; 1998.
[34] IEC. Wind turbines - part 1: design requirements. Technical Report IEC 61400-1. International Electrotechnical Commission; 2005.
[35] SINTEF Ocean. RIFLEX user guide. 2016.
[36] SINTEF Ocean. SIMO user guide. 2016.
[37] Jonkman BJ, Kilcher L. TurbSim user's guide: version 1.50. Technical Report NREL/TP-500-46198. National Renewable Energy Laboratory; 2009.
[38] IEC. Wind turbines - part 3: design requirements for offshore wind turbines. Technical Report IEC 61400-3. International Electrotechnical Commission; 2009.
[39] Johannessen K, Meling TS, Haver S. Joint distribution for wind and waves in the Northern North Sea. Int J Offshore Polar Eng 2002;12(1):1–8.
[40] Hwang JT, Martins JRRA. A computational architecture for coupling heterogeneous numerical models and computing coupled derivatives. ACM Trans Math Softw 2018;44(4). https://doi.org/10.1145/3182393.
[41] Martins JRRA, Hwang JT. Review and unification of methods for computing derivatives of multidisciplinary computational models. AIAA J 2013;51(11):2582–99. https://doi.org/10.2514/1.J052184. ISSN 00011452.
[42] Lambe AB, Martins JRRA. Extensions to the design structure matrix for the description of multidisciplinary design, analysis, and optimization processes. Struct Multidiscip Optim 2012;46:273–84. https://doi.org/10.1007/s00158-012-0763-y.
[43] Gill PE, Murray W, Saunders MA. SNOPT: an SQP algorithm for large-scale constrained optimization. SIAM J Optim 2002;12(4):979–1006. https://doi.org/10.1137/S0036144504446096.
[44] Perez RE, Jansen PW, Martins JRRA. pyOpt: A Python-based object-oriented framework for nonlinear constrained optimization. Struct Multidiscip Optim 2012;45(1):101–18. https://doi.org/10.1007/s00158-011-0666-3.
[45] Farkas J, Jármai K. Optimum design of steel structures. Springer; 2013.
[46] Teillant B, Krügel K, Guérinel M, Vicente M, Debruyne Y, Malerba F, Gradowski M, Roveda S, Neumann F, Noorloos HV, Schuitema R, Gomes R, Henriques J, Gato L, Combourieu A, Neau A, Borgarino B, Doussal J-C, Philippe M, Moretti G, Fontana M. WETFEET wave energy transition to future by evolution of engineering and technology D2.3: engineering challenges related to full scale and large deployment implementation of the proposed breakthroughs. WavEC Offshore Renewables; 2016. Technical report.
[47] Myhr A, Bjerkseter C, Ågotnes A, Nygaard TA. Levelised cost of energy for offshore floating wind turbines in a life cycle perspective. Renew Energy 2014;66:714–28. https://doi.org/10.1016/j.renene.2014.01.017.
[48] Larsen K. Personal communication. 2019.
[49] Barltrop N. Floating structures: a guide for design and analysis. Oilfield Publications Inc.; 1998.
[50] Larsen TJ, Hanson TD. A method to avoid negative damped low frequent tower vibrations for a floating, pitch controlled wind turbine. J Phys Conf Ser 2007;75:012073. https://doi.org/10.1088/1742-6596/75/1/012073.
[51] van der Veen GJ, Couchman IJ, Bowyer RO. Control of floating wind turbines. In: 2012 American control conference. Montreal, Canada: Fairmont Queen Elizabeth; 2012. p. 3148–53. https://doi.org/10.1109/acc.2012.6315120.
[52] Lackner M. Controlling platform motions and reducing blade loads for floating wind turbines. Wind Eng 2009;33(6):541–53. https://doi.org/10.1260/0309-524X.33.6.541.
[53] DNV GL. Fatigue design of offshore steel structures. Technical Report DNVGL-RP-C203. DNV GL; 2019.
[54] DNV GL. Floating wind turbine structures. Technical Report DNVGL-ST-0119. DNV GL; 2018.
[55] DNV. Design of floating wind turbine structures. Technical Report DNV-OS-J103. DNV; 2013.
[56] DNV GL. Buckling strength of shells. Technical Report DNVGL-RP-C202. DNV GL; 2019.
[57] Steinert A, Ehlers S, Kvittem MI, Merino D, Ebbesen M. Cost assessment for a semi-submersible floating wind turbine with respect to the hydrodynamic response and tower base bending moments using particle swarm optimisation. In: Proceedings of the twenty-sixth (2016) international ocean and polar engineering conference (ISOPE2016), Rhodes, Greece; 2016. p. 419–26.
[58] Nejad AR, Bachynski EE, Moan T. Effect of axial acceleration on drivetrain responses in a spar-type floating wind turbine. J Offshore Mech Arctic Eng 2019;141. https://doi.org/10.1115/1.4041996.
[59] DNV GL. Modelling and analysis of marine operations. Technical Report DNVGL-RP-N103. DNV GL; 2017.
[60] Koo BJ, Kim MH, Randall RE. Mathieu instability of a spar platform with mooring and risers. Ocean Eng 2004;31:2175–208. https://doi.org/10.1016/j.oceaneng.2004.04.005.
[61] Haslum HA, Faltinsen OM. Alternative shape of spar platforms for use in hostile areas. In: Offshore technology conference; 1999. https://doi.org/10.4043/10953-ms.
[62] Kreisselmeier G, Steinhauser R. Systematic control design by optimizing a vector performance index. In: International federation of active controls symposium on computer-aided design of control systems, Zurich, Switzerland; 1979. https://doi.org/10.1016/s1474-6670(17)65584-8.
[63] Lambe AB, Kennedy GJ, Martins JRRA. An evaluation of constraint aggregation strategies for wing box mass minimization. Struct Multidiscip Optim 2017;55:257–77. https://doi.org/10.1007/s00158-016-1495-1.
[64] European Committee for Standardization. Eurocode 3: design of steel structures, part 1-6: strength and stability of shell structures. Technical Report EN 1993-1-6: 2007. European Committee for Standardization; 2007.
[65] DNV GL. Support structures for wind turbines. Technical Report DNVGL-ST-0126. DNV GL; 2018.
[66] DNV GL. Offshore mooring chain. Technical Report DNVGL-OS-E302. DNV GL; 2018.
[67] DNV GL. Position mooring. Technical Report DNVGL-OS-E301. DNV GL; 2018.
[68] Chen C-T. Linear system theory and design. fourth ed. Oxford University Press; 2013.

[69] Sandner F, Schlipf D, Matha D, Cheng PW. Integrated optimization of floating wind turbine systems. In: Proceedings of the ASME 2014 33rd international conference on ocean, offshore and Arctic engineering (OMAE2014), san Francisco, California, USA; 2014. https://doi.org/10.1115/OMAE2014-24244.
[70] Hansen MH, Henriksen LC. Basic DTU wind energy controller. Technical Report DTU Wind Energy Report-E-0018. DTU Wind Energy; 2013.
[71] Jonkman J. Definition of the floating system for phase IV of OC3. Technical Report NREL/TP-500-47535. National Renewable Energy Laboratory; 2010.
[72] Müller K, Lemmer F, Yu W. LIFES50+ D4.2: public definition of the two LIFES50+ 10MW floater concepts. Technical report. University of Stuttgart; 2018.
[73] Musial W, Butterfield S, Boone A. Feasibility of floating platform systems for wind turbines. In: 23rd ASME wind energy symposium, Reno, Nevada, USA; 2004. https://doi.org/10.2514/6.2004-1007.
[74] Lie H, Gao Z, Moan T. Mooring line damping estimation by a simplified dynamic model. In: Proceedings of OMAE 2007 26h international conference on offshore mechanics and Arctic engineering, san Diego, California, USA; 2007. https://doi.org/10.1115/OMAE2007-29155.
[75] Skaare B, Nielsen FG, Hanson TD, Yttervik R, Havmøller O, Rekdal A. Analysis of measurements and simulations from the Hywind Demo floating wind turbine. Wind Energy 2015;18:1105–22. https://doi.org/10.1002/we.1750.
[76] Saha N, Naess A. Monte Carlo-based method for predicting extreme value statistics of uncertain structures. J Eng Mech 2010;136(12):1491–501. https://doi.org/10.1061/(ASCE)EM.1943-7889.0000194.

Paper 4

Design optimization of spar floating wind turbines considering different control strategies

John Marius Hegseth, Erin E. Bachynski and Joaquim R. R. A. Martins

Accepted to: Journal of Physics: Conference Series, 2020

Design Optimization of Spar Floating Wind Turbines Considering Different Control Strategies

John Marius Hegseth[1], **Erin E. Bachynski**[1], **Joaquim R. R. A. Martins**[2]

[1] Department of Marine Technology, NTNU, 7491 Trondheim, Norway

[2] Department of Aerospace Engineering, University of Michigan, Ann Arbor, MI 48109, USA

E-mail: john.m.hegseth@ntnu.no

Abstract. One of the challenges related to the design of floating wind turbines (FWTs) is the strong interactions between the controller and the support structure, which may result in an unstable system. Several control strategies have been proposed to improve the dynamic behaviour, all of which result in trade-offs between structural loads, rotor speed variation, and blade pitch actuator use, which makes controller design a challenging task. Due to the interactions, simultaneous design of the controller and support structure should be performed to properly identify and compare different solutions. In the present work, integrated design optimization of the blade-pitch controller and support structure is performed for a 10 MW spar FWT, considering four different control strategies, to evaluate the effect of the controller on the structural design and associated costs. The introduction of velocity feedback control reduces the platform pitch response and consequently the fatigue loads in the tower, which leads to a decrease in the tower costs compared to a simple PI controller. Low-pass filtering of the nacelle velocity signal to remove the wave-frequency components results in reduced rotor speed variation, but offers only small improvements in costs, likely due to the limited wave-frequency response for the considered designs. Comparisons with nonlinear time-domain simulations show that the linearized model is able to capture trends with acceptable accuracy, but that significant overpredictions may occur for the platform pitch response.

1. Introduction

For floating wind turbines (FWTs), the performance of the control system generally depends on the support structure design and vice versa. A well-known interaction between the blade pitch controller and platform motions is the introduction of negative damping above rated wind speed [1]. While detuning the controller gains such that the bandwidth is reduced achieves stability, this results in poorer rotor speed tracking performance [1, 2]. Several alternative methods have also been suggested to resolve the issue, such as introducing a feedback term proportional to the pitch velocity [3] or nacelle velocity [4, 5] to manipulate the generator speed reference. For these types of feedback control, Fleming et al. [6] also suggested to remove the wave-frequency components from the velocity signal, as this reduced the tower loads. All of these control strategies result in trade-offs between structural loads, rotor speed variation, and blade pitch actuator use, which vary with different environmental conditions. Therefore, identifying optimal control parameters is a challenging task.

Due to the strong interactions, simultaneous design of the controller and support structure should be performed to have a fair comparison between different solutions. A step toward simultaneous design was made by Lemmer et al. [7], who optimized the main dimensions of a three-column semi-submersible FWT. They minimized a combination of material costs and damage-equivalent loads in the tower for seven operational conditions, with a constraint on the static pitch angle at rated thrust. The controller was tuned at each design iteration using a linear quadratic regulator (LQR) approach. To properly identify and compare optimal solutions, the integrated control and structural designs should, however, be evaluated over the lifetime of the system, considering actual design limits. The purpose of the present study is to perform integrated design optimization of the blade-pitch controller and support structure for

a 10 MW FWT, considering long-term fatigue damage and extreme response constraints, to evaluate the effect of different control strategies on the structural design and associated costs.

2. Linearized FWT dynamics

2.1. FWT definition

The present study perfoms the design optimization of a spar buoy that supports the DTU 10 MW reference wind turbine [8] at a water depth of 320 m. The steel hull is partially filled with concrete ballast to achieve the correct draft, using a ballast density of 2600 kg/m^3. The interface with the tower is located 10 m above the still water line (SWL), while the hub height is 119 m above the SWL. A catenary mooring system consisting of three lines spread symmetrically about the vertical axis is used for station-keeping. Only the response in the xz-plane is considered in the current work, and co-directional waves and wind travelling in the positive x-direction are applied in all simulations. An overview of the FWT system is shown in Fig. 1.

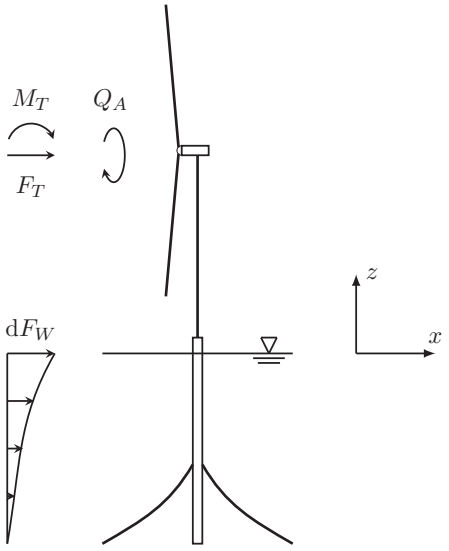

Figure 1: Overview of the FWT system.

2.2. Linearized equations of motion

The system is linearized and expressed in state-space form, and consists of a structural part and a control system part, which are connected to obtain the complete closed-loop aero-hydro-servo-elastic model as described by Hegseth et al. [9]. For each wind-wave condition, the operational point is found from static equilibrium when the system is subjected to the mean wind loads. The linearized system considers perturbations in the state and input variables, $\mathbf{x}$ and $\mathbf{u}$ respectively, about the operational point:

$$\mathbf{x} = \mathbf{x_0} + \Delta\mathbf{x}, \quad \mathbf{u} = \mathbf{u_0} + \Delta\mathbf{u}. \tag{1}$$

The dynamic equations of motion are then expressed as

$$\Delta\dot{\mathbf{x}} = \mathbf{A}\Delta\mathbf{x} + \mathbf{B}\Delta\mathbf{u}, \tag{2}$$

where $\mathbf{A}$ is the state matrix and $\mathbf{B}$ is the input matrix.

2.3. Structural model

The structural model for the platform and turbine considers four degrees-of-freedom (DOFs), namely surge, pitch, first tower/platform bending mode, and rotor speed. The equations of motions for the former three are found from generalized displacements similar to Hegseth and Bachynski [10], but using a flexible hull to ensure a correct natural frequency for the first bending mode, while a rigid drivetrain and rotor is assumed for the rotor dynamics. The structural state vector is thus written as

$$\mathbf{x}_s = \begin{bmatrix} \xi_1 & \xi_5 & \xi_7 & \dot{\xi}_1 & \dot{\xi}_5 & \dot{\xi}_7 & \dot{\varphi} \end{bmatrix}^\top, \tag{3}$$

where ξ_n represents generalized support structure DOF n, and $\dot{\varphi}$ is the rotor speed.

Hydrodynamic excitation loads on the hull are described by MacCamy–Fuchs theory, and transverse added mass is based on analytical 2D coefficients. Radiation damping is neglected, while viscous damping is found from stochastic linearization of the drag term in Morison's equation.

Wind loads on the rotor are derived from linearized BEM theory with the incoming wind field described by the Kaimal spectrum and an exponential coherence function for the longitudinal wind

velocity component [11]. The blades are considered rigid in the model, and the aerodynamic forces on the rotor are applied as resultant loads at the tower top. In addition, the static component of the aerodynamic quadratic drag force on the tower is included.

The inputs to the structural system consist of both control system outputs and disturbances due to environmental loads. The control input vector contains the references for the generator torque (Q_G) and the collective blade pitch angle (θ), and is defined as

$$\mathbf{u}_{sc} = [Q_G \quad \theta]^\top . \tag{4}$$

The disturbance vector contains rotor-effective wind speeds for thrust, tilting moment and aerodynamic torque, and generalized wave excitation forces for each support structure DOF, i.e.

$$\mathbf{u}_{sd} = [v_{F_T} \quad v_{M_T} \quad v_{Q_A} \quad F_{W,1} \quad F_{W,5} \quad F_{W,7}]^\top . \tag{5}$$

2.4. Controller description

The baseline linear control system consists of a generator-torque controller and a collective blade-pitch controller, which work independently in below-rated and above-rated wind speeds, respectively. Below rated wind speed, the generator torque is set to be proportional to the square of the rotor speed to maintain the optimal tip-speed ratio. Above rated wind speed, the generator torque is kept constant, and four different strategies are considered for the blade-pitch controller:

- CS1: Gain-scheduled PI controller
- CS2: Gain-scheduled PI controller + platform pitch velocity feedback
- CS3: Gain-scheduled PI controller + nacelle velocity feedback
- CS4: Gain-scheduled PI controller + nacelle velocity feedback + low-pass filter

For feedback control using platform pitch or nacelle velocity, we use the modified rotor speed reference, $\dot{\varphi}_0'$, defined by Lackner [3]:

$$\dot{\varphi}_0' = \dot{\varphi}_0(1 + k_f \dot{x}_f) \tag{6}$$

where $\dot{\varphi}_0$ is the nominal rotor speed reference, k_f is the velocity feedback gain, and $\dot{x}_f$ is either the platform pitch velocity or the nacelle velocity. An updated expression for the rotor speed error can then be established as

$$\Delta\dot{\varphi}' = \dot{\varphi} - \dot{\varphi}_0' = \Delta\dot{\varphi} - \dot{\varphi}_0 k_f \dot{x}_f, \tag{7}$$

where $\Delta\dot{\varphi}$ is the nominal rotor speed error. In CS4, the nacelle velocity signal is passed through a first order low-pass filter to remove the wave-frequency components before it is fed back to the blade-pitch controller.

2.5. Response calculations

The structural and control system models are written as a single closed-loop system, which is solved in the frequency domain. Dynamic force equilibrium is then used together with the response spectra to calculate the bending moment response along the tower.

The fatigue damage is calculated at selected locations in the tower using the Dirlik method [12], while the extreme response of the support structure is found using the AUR method, where the most probable maximum value in one hour is used in the design constraints. The model has earlier been verified against fully coupled nonlinear time domain simulations in SIMA [9].

The rotor speed tracking performance is evaluated using the weighted average of the rotor speed standard deviation, which is found by summing the values from each short-term condition that is considered, weighted by their associated probabilities:

$$\sigma_{(\dot{\varphi})} = \sum_{i=1}^{N_{EC}} p_i \sigma_{(\dot{\varphi}),i}. \tag{8}$$

Here, N_{EC} is the number of short-term conditions, $\sigma_{(\dot{\varphi}),i}$ is the rotor speed standard deviation in condition i, and p_i is the probability of the condition.

To evaluate blade-pitch actuator fatigue, the actuator duty cycle (ADC) was defined in Kendall et al. [13] as the total number of degrees pitched divided by the total simulation time. Although ADC cannot be used as an absolute measure of the actuator fatigue damage, it is suitable for comparison of different control strategies. The normalized ADC, which is used in the current work, is defined by Bottasso et al. [14] as

$$\mathrm{ADC}_i = \frac{1}{T}\int_0^T \frac{|\dot{\theta}_i(t)|}{\dot{\theta}_{\max}}\mathrm{d}t, \tag{9}$$

where $\dot{\theta}_i$ is the blade pitch rate in condition i, T is the total simulation time, and $\dot{\theta}_{\max}$ is the maximum allowable blade pitch rate, which for the DTU 10 MW is equal to 10 deg/s.

If the process is ergodic, the ADC can be expressed using the expected value:

$$\mathrm{ADC}_i = \frac{1}{\dot{\theta}_{\max}} E\left[|\dot{\theta}_i(t)|\right]. \tag{10}$$

Assuming that the blade pitch rate is Gaussian, the expected value can be calculated as

$$E\left[|\dot{\theta}_i(t)|\right] = \sqrt{\frac{2}{\pi}}\sigma_{(\dot{\theta}),i}. \tag{11}$$

For the linearized model, the ADC can thus be derived from the blade pitch rate standard deviation. The weighted average ADC used in the design optimization is then found similarly as in Eq. (8).

2.6. Environmental conditions

Fifteen different ECs are used to evaluate the long-term fatigue performance in the present work. The conditions span mean wind speeds from 1-30 m/s with 2 m/s step, and for each mean wind speed, the most probable values for the significant wave height and spectral peak period are used. These values, as well as the associated probabilities of occurrence, are found from the joint probability distribution derived by Johannessen et al. [15], and shown in Fig. 2.

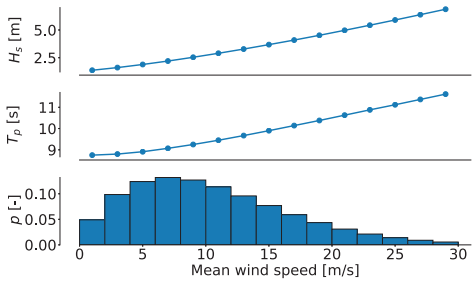

Figure 2: Significant wave heights, spectral peak periods, and normalized probabilities applied in the fatigue calculations.

Three ECs, described in Table 1, along the 50-year contour surface, are selected to evaluate the extreme response. EC 1 and 2 represent operational wind speeds above rated, while EC 3 considers an extreme storm condition, where the turbine is parked with feathered blades. For all ECs, the IEC Class B normal turbulence model (NTM) [11] is used for the incoming wind, while the waves are described by a JONSWAP spectrum with a peakedness parameter of 3.3.

3. Optimization problem

The FWT model is implemented in OpenMDAO [16], which is an open-source framework for multidisciplinary design, analysis, and optimization. The design is optimized using a gradient-based approach, where the derivatives of the model are computed analytically using coupled adjoints. The optimization problem is solved using the SNOPT algorithm [17], which uses a sequential quadratic programming (SQP) approach, through the pyOptSparse Python interface [18].

3.1. Objective function

The objective function used in the present work is the combined cost of the platform and tower, C_{spar} and C_{tower} respectively:

$$f = C_{\mathrm{spar}} + C_{\mathrm{tower}}. \tag{12}$$

Table 1: Environmental conditions for extreme response calculations.

Condition	1	2	3
Mean wind speed at hub height, U (m/s)	13.0	21.0	50.0
Significant wave height, H_s (m)	8.1	9.9	15.1
Spectral peak period, T_p (s)	14.0	15.0	16.0
Turbulence intensity at hub height, I (-)	0.17	0.14	0.12

The costs consider both material and manufacturing, using the cost models developed by Farkas and Jármai [19]. Costs related to installation, maintenance, and decommissioning are not included. The cost of the platform (and similarly of the tower) is expressed as

$$C_{spar} = k_m M_{\text{spar}} + k_f \sum_i T_i, \tag{13}$$

where k_m is the steel cost factor, M_{spar} is the steel mass of the hull, and k_f is the fabrication cost per unit time. T_i is the time spent at fabrication stage i, expressed as a function of the geometry. The steel cost factor, k_m, is assumed to have a value of 2.7 €/kg, while the ratio between the material and fabrication cost factors, k_m/k_f, is set to 1.0, which is a typical value for West European labour [19]. The cost of the concrete ballast is neglected in the current work.

3.2. Design variables

Both the platform and tower are discretized into ten sections along the length. For the tower, the diameter and wall thickness at the nodes connecting the sections are set as design variables. The length of the tower sections is kept fixed during the optimization, to maintain the original hub height.

The structural design of the spar platform is primarily governed by buckling loads, which for most parts of the hull are dominated by the hydrostatic pressure. The structural design of the platform is therefore not considered in the study, and only the diameter at the platform nodes and the length of each section are included in the design optimization. The wall thickness is expressed as a function of depth, based on the optimized structural design from Hegseth et al. [9]. This ensures a proper mass distribution, and penalizes designs with large drafts and consequently high external pressure loads, which require increased use of material. The mooring system design is kept fixed during the optimization.

For the control system, the optimization considers the proportional (k_p) and integral (k_i) gains for the blade-pitch controller, as well as the velocity feedback gain (k_f) for the pitch and nacelle velocity feedback control. For CS4, the corner frequency of the nacelle velocity low-pass filter (ω_f) is also included.

3.3. Constraints

The fatigue damage at each tower node is evaluated using an SN curve approach, where the D curve in air from DNV-RP-C203 [20] is applied together with a design fatigue factor (DFF) of 2.0 [21], and the lifetime of the FWT system is chosen to be 20 years. The fatigue design constraints are thus expressed as

$$D_{tot} = N_{20} \sum_{i=1}^{N_{\text{EC}}} p_i D_i \leq \frac{1.0}{\text{DFF}}, \tag{14}$$

where D_{tot} is the total fatigue damage in 20 years, N_{20} is the number of short term conditions in 20 years, and D_i is the fatigue damage in condition i.

Tower buckling is assessed using Eurocode 3 [22], assuming that the tower is stiffened between each section to reduce the buckling length. To ensure a smooth transition between the platform and tower, the tower base diameter is set to be equal to the diameter at the platform top. Both fatigue and buckling constraints are aggregated using Kreisselmeier–Steinhauser (KS) functions [23].

The maximum platform pitch angle in the considered 50-year conditions is limited to 15°. Although the heave response is not included in the model, heave resonance in the wave frequency range is avoided by placing a lower limit of 25 s on the heave natural period. The added mass in heave is approximated as the value for a 3D circular disc with the same diameter as the platform bottom [24].

The presented model is valid strictly for hull sections with vertical walls, and a maximum taper angle of 10° is therefore applied as a constraint for each section of the platform, to avoid shapes where the physics are not captured correctly. Offset constraints are not considered, as the surge response is mostly governed by the rotor and mooring system design.

Appropriate upper limits for the rotor speed variation and blade-pitch actuator use are difficult to quantify. The constraints are therefore based on values taken from the land-based DTU 10 MW wind turbine with the original controller [25], where the weighted average rotor speed standard deviation and ADC are found from nonlinear time domain analyses using the simulation tool SIMA. Initial analyses found that the rotor speed variation obtained with the land-based turbine was unrealistic for the floating system with the simplified controllers considered in the present work. To enlarge the feasible region of the design space, the constraints for both the rotor speed variation and the ADC are scaled by a factor of 1.5 compared to the land-based values, as shown in Table 2.

4. Results

4.1. Optimized designs

The optimized support structure design for CS1 is illustrated in Fig. 3. The hourglass shape taken by the platform below the wave zone increases the distance between the center of buoyancy and the center of gravity, which leads to increased pitch restoring stiffness, while the relatively large diameter at the bottom results in larger added mass and consequently longer natural period in heave. For the upper part of the platform and intersection with the tower, the optimizer finds a balance between a small diameter, which is desirable with regards to hydrodynamic loads, and a large diameter, which (together with a small wall thickness) is the most cost-effective way to achieve the required fatigue life.

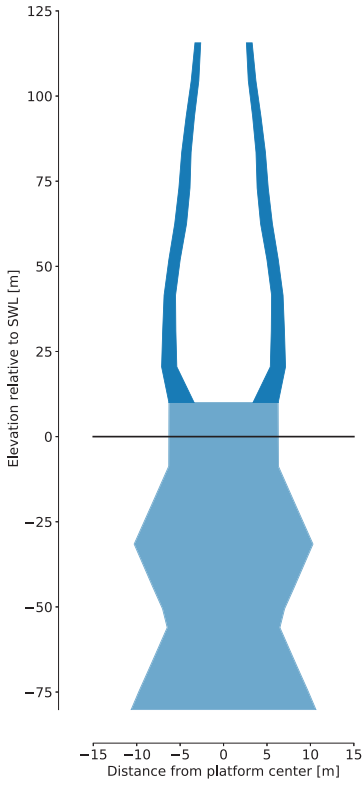

Figure 3: Optimized support structure design for CS1. The wall thickness in the tower is scaled by a factor of 40 relative to the diameter for illustration purposes.

The optimized tower diameter and wall thickness distributions for the different control strategies are plotted in Fig. 4. All four solutions follow the same trends, and the effect of velocity feedback control is most visible for the wall thickness, where the values for CS2-4 are approximately 20 % lower than for the simple PI controller (CS1) along most of the tower length. The reduced wall thickness is enabled by a decrease in the fatigue loads for these controllers, which is the design-driving constraint for the tower. For all four control strategies, the 15° pitch angle constraint is also active; however, as the 50-year storm condition with parked turbine (EC3) is found to be the critical load case for extreme response, this constraint is not affected by the controller.

The improved fatigue performance can be understood by examining the response spectra for the optimized designs. In Fig. 5a, the tower base bending moment spectra are shown for a mean wind speed of 15 m/s. Large differences are seen around the pitch natural frequency at 0.15 rad/s, where the velocity feedback controllers increase the aerodynamic damping and thus reduce the response. The low-pass filtering of the nacelle velocity removes the wave-frequency range from the signal, which results in a higher optimal velocity feedback gain and nearly eliminates the tower base bending moment response

Table 2: Land-based and applied constraint values for the rotor speed variation and blade-pitch actuator use.

Variable	Land-based value	Constraint value
$\sigma_{(\dot{\varphi})}$ [rad/s]	4.22E-2	6.33E-2
ADC [-]	5.10E-3	7.65E-3

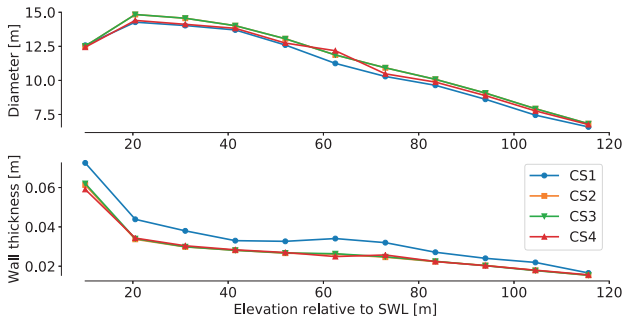

Figure 4: Tower diameter and wall thickness for optimized designs.

arising from resonant pitch motions. The wave-frequency bending moments, on the other hand, is unaffected by the control strategy. The blade pitch spectra in Fig. 5b show how the larger PI gains in the velocity feedback controllers result in overall increased actuator use, with the exception of the pitch natural frequency, as well as the wave-frequency band for CS4.

The optimized costs of the tower, platform, and tower plus platform for CS2-4 are shown in Fig. 6a, compared to the optimized costs for CS1. The majority of the cost reductions come from the tower, due to the improved fatigue behaviour, whereas the platform is less affected due to the fixed costs related to buckling resistance and the 15° pitch angle constraint. However, because a lighter tower results in a lower overall center of gravity, the platform pitch response is somewhat improved, and a small reduction in platform costs of about 2 % is also observed. Because the platform accounts for 70-75 % of the total costs for the considered designs, the resulting total cost reduction is approximately 6 %.

The resulting rotor speed standard deviations and ADCs, normalized by their maximum allowable values from Table 2, are shown in Fig. 6b. For each control strategy, there exists a limit where no further reduction in cost can be achieved by increasing the actuator use. This limit is higher for the velocity feedback controllers than for a controller using only the rotor speed error as input, which causes the ADC constraint to be inactive at the optimum for CS1. A larger ADC may result in higher probability of fatigue failure for the actuator bearings, and therefore more detailed design considering the lifetime of the system should be performed to determine appropriate values for this constraint.

For the rotor speed variation, better performance is achieved with CS4 than with the other control strategies. Since there is a trade-off between rotor speed variation and structural loads (and thus costs) as previously discussed, it is expected that larger cost reductions can be achieved with CS4 if the rotor speed constraint is tightened.

Some limitations to this work should be noted. The standard deviation in steady-state conditions is used as the only measure of the rotor speed tracking performance, and extreme rotor speed excursions due to gusts are not considered. The effect of the controllers on surge motions, drivetrain response, mooring line tension, or blade response has also not been studied. In addition, the performance of the FWT system could likely be further improved by also adding individual pitch control or modifications to the torque controller, which have not been examined in the present work.

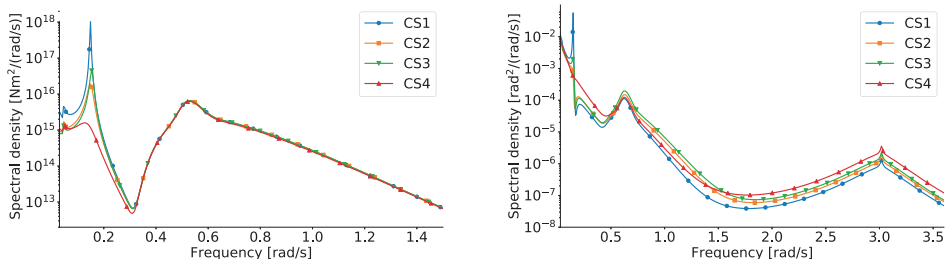

(a) Tower base bending moment. **(b)** Blade pitch.

Figure 5: Response spectra, 15 m/s mean wind speed.

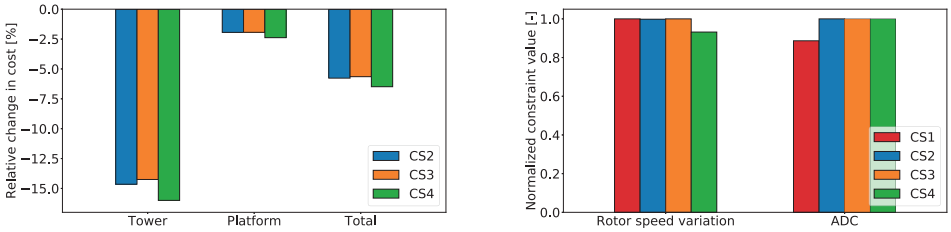

(a) Costs relative to CS1. **(b)** Rotor speed variation and ADC values.

Figure 6: Objective and constraint function values for optimized designs.

4.2. Sequential versus multidisciplinary optimization

In the presented methodology, the platform, tower, and blade-pitch controller are optimized simultaneously. This approach, commonly known as multidisciplinary design optimization (MDO) [26], is preferred for coupled systems, where a sequential optimization process in general leads to suboptimal solutions on the overall system level [27]. To assess the importance of integrated design, results using MDO are compared to a sequential optimization for CS4, where the controller and support structure are optimized separately. For the sequential approach, the control parameters are first optimized to minimize the rotor speed variation, with constraints on system stability and ADC. All support structure parameters are kept constant and structural constraints are not considered. The support structure is then optimized for minimum cost, keeping the controller parameters fixed at their optimized values from the previous step. This procedure is repeated until the system has converged. Since this method results in different objective functions for the two sequential problems, a multi-objective approach is utilized for the MDO study, where a combination of costs and rotor speed variation is minimized with different relative weighting.

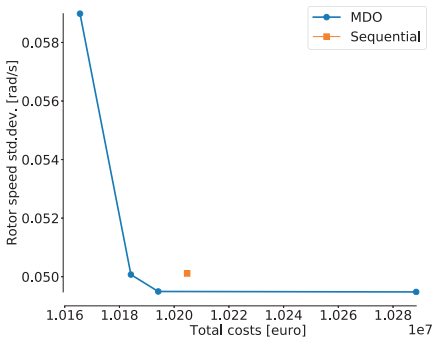

Figure 7: MDO vs. sequential optimization.

Figure 7 shows the MDO Pareto front together with the optimal solution from the sequential approach. The results confirm that improved designs can be achieved with integrated optimization; however, the differences are small. For the same rotor speed variation, using MDO results in

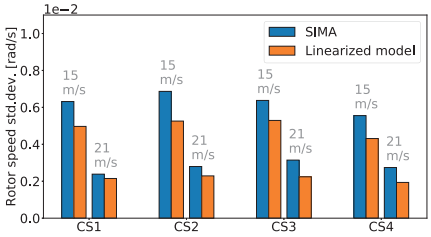

(a) Weighted rotor speed variation.

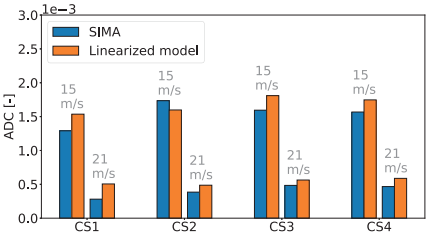

(b) Weighted ADC.

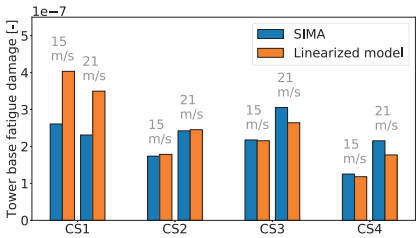

(c) Weighted tower base 1-h fatigue damage.

Figure 8: Comparison of response parameters with SIMA.

approximately 0.5 % reduction in the costs of the tower, or 0.2 % in total costs. Although small coupling effects are seen for the considered optimization problem, larger differences are expected in cases where the controller has a greater effect on the structural response.

4.3. Verification

The optimized controller designs are verified through fully coupled nonlinear time-domain simulations using SIMA, where two different ECs above rated wind speed are simulated with each control strategy for a specified support structure design. Comparisons with the linearized model for different response parameters, weighted by the probability of each condition, are shown in Fig. 8.

The linearized model is seen to mostly follow the trends observed in the nonlinear simulations, but some errors are present. The largest errors are observed for the tower base fatigue damage, which is significantly overestimated for CS1, whereas good agreement is obtained with the other control strategies. The reason for the poor agreement is that the aerodynamic (and thus the overall) damping for the platform pitch mode is much lower with this control strategy. Consequently, the resonant pitch response becomes very sensitive to the presence and amount of additional damping in the system, which is either not considered or underpredicted in the linear model. This disagreement was also observed for a linearized model of the 10 MW OO-Star semisubmersible in Souza et al. [28], which used a control strategy similar to CS1. The overestimation of fatigue damage means that the optimized tower design for CS1 is more conservative than for the other control strategies, suggesting that the cost reductions in Fig. 6a are highly optimistic, and that CS1 may yield a fatigue design similar to that with a nacelle velocity feedback controller. It also suggests that future optimization studies using the linearized model should consider more advanced control strategies than CS1, to limit the pitch response error.

In addition, the rotor speed standard deviation is consistently underestimated by about 20 % for all four control strategies. This disagreement could be taken into consideration in the optimization process by adjusting the constraint value.

5. Concluding remarks

The design of the platform, tower, and blade-pitch control system for a 10 MW spar FWT was optimized simultaneously using a linearized aero-hydro-servo-elastic model and gradient-based optimization with

analytic derivatives. The goal has been to minimize the material and manufacturing costs of the support structure, with constraints on tower fatigue damage and buckling, extreme platform pitch motions, rotor speed variation, and blade-pitch actuator use, considering four different strategies for the blade-pitch controller.

The effect of the controller on the structural response was limited to the fatigue damage in the tower, since the storm condition with parked turbine was found to govern the extreme responses of the system considered here. The reduction in tower loads for the velocity feedback controllers compared to the simple PI control system was a consequence of lower platform pitch response, which led to a reduction in the wall thickness required to satisfy the long-term fatigue damage constraint. Consequently, the tower costs were reduced, and also the platform costs due to better dynamic performance. Although low-pass filtering of the nacelle velocity signal did not offer significant cost reductions, this control strategy also saw a reduction in rotor speed variation, since the constraint was inactive at the optimum. It is also expected that the effect of this filter will be more prominent for FWT concepts with larger wave-frequency response.

Comparisons with nonlinear time-domain simulations showed that the linearized model in general is able to capture trends with acceptable accuracy, but that the platform pitch response can be significantly overpredicted for designs with low aerodynamic damping if contributions from other sources of damping are small. This was the case for CS1, which indicates that the cost reductions achieved for CS2-4 are considerably overestimated. For the velocity feedback controllers, which increases the amount of aerodynamic damping induced by the control system, this problem was not observed, and good agreement was achieved.

The presented approach is useful for conceptual FWT design, where it can be used to quickly explore the design space before resorting to higher fidelity tools for detailed subsystem analysis and design. The model captures important interactions between the controller and support structure, and enables assessment of trade-off effects in a lifetime perspective. Further, the methodology can be extended to account for additional design parameters and load cases, which may help identify novel design solutions.

References

[1] T. J. Larsen and T. D. Hanson. “A Method to Avoid Negative Damped Low Frequent Tower Vibrations for a Floating, Pitch Controlled Wind Turbine”. In: *Journal of Physics: Conference Series* 75 (2007), p. 012073.

[2] J. Jonkman. “Influence of Control on the Pitch Damping of a Floating Wind Turbine”. In: *46th AIAA Aerospace Science Meeting and Exhibit, Reno, Nevada*. 2008.

[3] M. Lackner. “Controlling Platform Motions and Reducing Blade Loads for Floating Wind Turbines”. In: *Wind Engineering* 33.6 (2009), pp. 541–553.

[4] G. J. van der Veen, I. J. Couchman, and R. O. Bowyer. “Control of floating wind turbines”. In: *2012 American Control Conference, Fairmont Queen Elizabeth, Montreal, Canada*. 2012, pp. 3148–3153.

[5] P. A. Fleming et al. “Evaluating Methods for Control of an Offshore Floating Turbine”. In: *Proceedings of the ASME 2014 33rd International Conference on Ocean, Offshore and Arctic Engineering (OMAE2014), San Francisco, California, USA*. 2014.

[6] P. A. Fleming, A. Peiffer, and D. Schlipf. “Wind Turbine Controller to Mitigate Structural Loads on a Floating Wind Turbine Platform”. In: *Journal of Offshore Mechanics and Arctic Engineering* 141 (2019).

[7] F. Lemmer et al. “Optimization of Floating Offshore Wind Turbine Platforms With a Self-Tuning Controller”. In: *Proceedings of the ASME 2017 36th International Conference on Ocean, Offshore and Arctic Engineering (OMAE2017), Trondheim, Norway*. 2017.

[8] C. Bak et al. *Description of the DTU 10 MW Reference Wind Turbine*. Tech. rep. DTU Wind Energy Report-I-0092. DTU Wind Energy, 2013.

[9] J. M. Hegseth, E. E. Bachynski, and J. R. R. A. Martins. “Integrated design optimization of spar floating wind turbines”. In: *Marine Structures* 72 (2020).

[10] J. M. Hegseth and E. E. Bachynski. “A semi-analytical frequency domain model for efficient design evaluation of spar floating wind turbines”. In: *Marine Structures* 64 (2019), pp. 186–210.

[11] IEC. *Wind Turbines - Part 1: Design Requirements*. Tech. rep. IEC 61400-1. 2005.

[12] T. Dirlik. “Application of Computers in Fatigue Analysis”. PhD thesis. University of Warwick, 1985.

[13] L. Kendall et al. “Application of Proportional-Integral and Disturbance Accommodating Control to Variable Speed Variable Pitch Horizontal Axis Wind Turbines”. In: *Wind Engineering* 21.1 (1997), pp. 21–38.

[14] C. L. Bottasso et al. “Optimization-based study of bend-twist coupled rotor blades for passive and integrated passive/active load alleviation”. In: *Wind Energy* 16 (2013), pp. 1149–1166.

[15] K. Johannessen, T. S. Meling, and S. Haver. “Joint Distribution for Wind and Waves in the Northern North Sea”. In: *International Journal of Offshore and Polar Engineering* 12.1 (2002), pp. 1–8.

[16] J. S. Gray et al. “OpenMDAO: An open-source framework for multidisciplinary design, analysis, and optimization”. In: *Structural and Multidisciplinary Optimization* 59 (2019), pp. 1075–1104.

[17] P. E. Gill, W. Murray, and M. A. Saunders. “SNOPT: an SQP Algorithm for Large-Scale Constrained Optimization”. In: *SIAM Journal on Optimization* 12.4 (2002), pp. 979–1006.

[18] R. E. Perez, P. W. Jansen, and J. R. R. A. Martins. “pyOpt: A Python-Based Object-Oriented Framework for Nonlinear Constrained Optimization”. In: *Structural and Multidisciplinary Optimization* 45.1 (2012), pp. 101–118.

[19] J. Farkas and K. Jármai. *Optimum Design of Steel Structures*. Springer, 2013.

[20] DNV. *Fatigue Design of Offshore Steel Structures*. Tech. rep. DNV-RP-C203. 2010.

[21] DNV. *Design of Floating Wind Turbine Structures*. Tech. rep. DNV-OS-J103. 2013.

[22] European Committee for Standardization. *Eurocode 3: Design of Steel Structures, Part 1-6: Strength and Stability of Shell Structures*. Tech. rep. EN 1993-1-6: 2007. 2007.

[23] G. Kreisselmeier and R. Steinhauser. “Systematic Control Design by Optimizing a Vector Performance Index”. In: *International Federation of Active Controls Symposium on Computer-Aided Design of Control Systems, Zurich, Switzerland*. 1979.

[24] DNV. *Modelling and Analysis of Marine Operations*. Tech. rep. DNV-RP-H103. 2011.

[25] M. H. Hansen and L. C. Henriksen. *Basic DTU Wind Energy controller*. Tech. rep. DTU Wind Energy Report-E-0018. 2013.

[26] J. R. R. A. Martins and A. B. Lambe. “Multidisciplinary Design Optimization: A Survey of Architectures”. In: *AIAA Journal* 51.9 (2013), pp. 2049–2075.

[27] M. Muskulus and S. Schafhirt. “Design optimization of wind turbine support structures-A review”. In: *Journal of Ocean and Wind Energy* 1.1 (2014), pp. 12–22.

[28] C. E. S. Souza, J. M. Hegseth, and E. E. Bachynski. “Frequency-dependent aerodynamic damping and inertia in linearized dynamic analysis of floating wind turbines”. In: *Journal of Physics: Conference Series* 1452.012040 (2020).

Paper 5

Effect of environmental modelling and inspection strategy on the optimal design of floating wind turbines

John Marius Hegseth, Erin E. Bachynski and Bernt J. Leira

Submitted to: Reliability Engineering and System Safety, 2020

This article is awaiting submission and is therefore not included

Appendix B

Formulation of Rotor Effective Wind Speed

As shown by Halfpenny (1998), the (single sided) cross spectral density of the rotationally sampled wind speed for two blade elements j and k may be written:

$$S_v^{(jk)}(\omega) = \sum_{n=-\infty}^{\infty} \mathrm{e}^{in\psi} K_n^{(jk)}(|\omega - n\dot{\varphi}|)\, S_U(|\omega - n\dot{\varphi}|), \tag{B.1}$$

where $S_U(\omega)$ is the incoming wind spectrum, ψ is the azimuth angle between the elements, and K_n is the n^{th} Fourier coefficient of the coherence function γ, which is Fourier expanded in the rotor plane:

$$K_n^{(jk)}(\omega) = \frac{1}{\pi} \int_0^{\pi} \gamma(\omega, d_{jk}) \cos(n\theta)\, \mathrm{d}\theta. \tag{B.2}$$

The coherence function for two points with separation distance d and frequency f in Hz is taken from IEC (2005) and expressed as

$$\gamma(f, d) = \exp\left(-12\left[\left(\frac{fd}{U_{\mathrm{hub}}}\right)^2 + \left(\frac{0.12d}{L_c}\right)^2\right]^{0.5}\right), \tag{B.3}$$

where U_{hub} is the mean hub-height wind speed and L_c is a coherence scale parameter.

Using Eq. (B.1), the wind speed seen by each blade element can be found, and used together with aerodynamic derivatives to calculate blade root

forces and subsequently resultant rotor loads. For a three-bladed turbine with n_b blade elements on each blade, $\mathbf{S}_v(\omega)$ is a $3n_b$ x $3n_b$ matrix with the following structure:

$$\mathbf{S}_v(\omega) = \begin{bmatrix} \mathbf{S}_{v,11}(\omega) & \mathbf{S}_{v,12}(\omega) & \mathbf{S}_{v,13}(\omega) \\ \mathbf{S}_{v,21}(\omega) & \mathbf{S}_{v,22}(\omega) & \mathbf{S}_{v,23}(\omega) \\ \mathbf{S}_{v,31}(\omega) & \mathbf{S}_{v,32}(\omega) & \mathbf{S}_{v,33}(\omega) \end{bmatrix} \tag{B.4}$$

However, if only the resultant loads are of interest, and the blades are identical, the calculations can be simplified by defining a single 'effective' blade, and the cross spectral density matrix for the effective blade can be found from the auto-spectral density for one of the blades in Eq. (B.4). For the thrust force and aerodynamic torque, which is the sum of the blade root shear force F_y and edgewise bending moment M_y respectively, the same formulation can be used:

$$\overline{\mathbf{S}}_v(\omega) = 3^2 \sum_{n=-\infty}^{\infty} \overline{\mathbf{S}}_{v,n}(\omega), \tag{B.5}$$

where

$$\overline{\mathbf{S}}_{v,n}(\omega) = \begin{cases} \mathbf{K}_n(|\omega - n\dot{\varphi}|)\, S_U(|\omega - n\dot{\varphi}|), & n \in \{..., -6, -3, 0, 3, 6, ...\} \\ 0, & \text{otherwise,} \end{cases} \tag{B.6}$$

and $\mathbf{K}_n$ only considers elements on the same blade. For the tilting moment, the effective blade formulation is somewhat different, as the azimuth angle of the blade affects the contribution from the blade root moment on the resultant load. The contribution from the flapwise blade root moment on the rotor titling moment is proportional to $\cos(\dot{\varphi}t)$, and the cross spectral density matrix thus becomes:

$$\overline{\mathbf{S}}_v(\omega) = \left(\frac{3}{2}\right)^2 \sum_{n=-\infty}^{\infty} \overline{\mathbf{S}}_{v,n}(\omega), \tag{B.7}$$

where

$$\overline{\mathbf{S}}_{v,n}(\omega) = \begin{cases} \mathbf{K}_n(|\omega - (n+1)\dot{\varphi}|)\, S_U(|\omega - (n+1)\dot{\varphi}|), & n \in \{..., -7, -4, -1, 2, 5, ...\} \\ \mathbf{K}_n(|\omega - (n-1)\dot{\varphi}|)\, S_U(|\omega - (n-1)\dot{\varphi}|), & n \in \{..., -5, -2, 1, 4, 7, ...\} \\ 0, & \text{otherwise} \end{cases} \tag{B.8}$$

As seen from the non-zero terms in Eqs. (B.6) and (B.8), the cancellation of harmonics with a three-bladed turbine results in peaks at multiples of three of the rotor frequency (i.e. 3P, 6P, 9P, etc.) for the resultant loads. The tower top load spectra can be found by pre- and post-multiplying $\overline{\mathbf{S}}_v(\omega)$ with the weight factors for each element, i.e. factors that relate wind speed to the aerodynamic loads on the element:

$$S_{F_T}(\omega) = \mathbf{W}_{F_T}^{\top}\, \overline{\mathbf{S}}_v(\omega)\, \mathbf{W}_{F_T} \tag{B.9a}$$

$$S_{M_T}(\omega) = \mathbf{W}_{M_T}^{\top}\, \overline{\mathbf{S}}_v(\omega)\, \mathbf{W}_{M_T} \tag{B.9b}$$

$$S_{Q_A}(\omega) = \mathbf{W}_{Q_A}^{\top}\, \overline{\mathbf{S}}_v(\omega)\, \mathbf{W}_{Q_A}. \tag{B.9c}$$

Here,

$$\mathbf{W}_{F_T} = \begin{bmatrix} F_{n,v}(r_1)\Delta r \\ F_{n,v}(r_2)\Delta r \\ \cdot \\ F_{n,v}(r_N)\Delta r \end{bmatrix},\ \mathbf{W}_{M_T} = \begin{bmatrix} r_1\, F_{n,v}(r_1)\Delta r \\ r_2\, F_{n,v}(r_2)\Delta r \\ \cdot \\ r_N\, F_{n,v}(r_N)\Delta r \end{bmatrix},\ \mathbf{W}_{Q_A} = \begin{bmatrix} r_1\, F_{t,v}(r_1)\Delta r \\ r_2\, F_{t,v}(r_2)\Delta r \\ \cdot \\ r_N\, F_{t,v}(r_N)\Delta r \end{bmatrix}. \tag{B.10}$$

The spectra for the effective wind speeds can be calculated from the tower top load spectra and the total weight factors over the rotor:

$$S_{v_{F_T}}(\omega) = \frac{S_{F_T}(\omega)}{(3\, F_{y,v})^2} \tag{B.11a}$$

$$S_{v_{M_T}}(\omega) = \frac{S_{M_T}(\omega)}{\left(\frac{3}{2}\, M_{z,v}\right)^2} \tag{B.11b}$$

$$S_{v_{Q_A}}(\omega) = \frac{S_{Q_A}(\omega)}{(3\, M_{y,v})^2}. \tag{B.11c}$$

The cross spectral density matrix for the wind loads can be found by observing which harmonics of the wind are shared by the different load components. As shown by Halfpenny (1998), the thrust force and aerodynamic torque on the turbine are perfectly correlated, as they share all harmonics, and completely uncorrelated from the tilting moment, as they have no harmonics in common.

Previous PhD theses published at the Department of Marine Technology (earlier: Faculty of Marine Technology) NORWEGIAN UNIVERSITY OF SCIENCE AND TECHNOLOGY

Report No.	Author	Title
	Kavlie, Dag	Optimization of Plane Elastic Grillages, 1967
	Hansen, Hans R.	Man-Machine Communication and Data-Storage Methods in Ship Structural Design, 1971
	Gisvold, Kaare M.	A Method for non-linear mixed -integer programming and its Application to Design Problems, 1971
	Lund, Sverre	Tanker Frame Optimalization by means of SUMT-Transformation and Behaviour Models, 1971
	Vinje, Tor	On Vibration of Spherical Shells Interacting with Fluid, 1972
	Lorentz, Jan D.	Tank Arrangement for Crude Oil Carriers in Accordance with the new Anti-Pollution Regulations, 1975
	Carlsen, Carl A.	Computer-Aided Design of Tanker Structures, 1975
	Larsen, Carl M.	Static and Dynamic Analysis of Offshore Pipelines during Installation, 1976
UR-79-01	Brigt Hatlestad, MK	The finite element method used in a fatigue evaluation of fixed offshore platforms. (Dr.Ing. Thesis)
UR-79-02	Erik Pettersen, MK	Analysis and design of cellular structures. (Dr.Ing. Thesis)
UR-79-03	Sverre Valsgård, MK	Finite difference and finite element methods applied to nonlinear analysis of plated structures. (Dr.Ing. Thesis)
UR-79-04	Nils T. Nordsve, MK	Finite element collapse analysis of structural members considering imperfections and stresses due to fabrication. (Dr.Ing. Thesis)
UR-79-05	Ivar J. Fylling, MK	Analysis of towline forces in ocean towing systems. (Dr.Ing. Thesis)
UR-80-06	Nils Sandsmark, MM	Analysis of Stationary and Transient Heat Conduction by the Use of the Finite Element Method. (Dr.Ing. Thesis)
UR-80-09	Sverre Haver, MK	Analysis of uncertainties related to the stochastic modeling of ocean waves. (Dr.Ing. Thesis)
UR-81-15	Odland, Jonas	On the Strength of welded Ring stiffened cylindrical Shells primarily subjected to axial Compression
UR-82-17	Engesvik, Knut	Analysis of Uncertainties in the fatigue Capacity of

		Welded Joints
UR-82-18	Rye, Henrik	Ocean wave groups
UR-83-30	Eide, Oddvar Inge	On Cumulative Fatigue Damage in Steel Welded Joints
UR-83-33	Mo, Olav	Stochastic Time Domain Analysis of Slender Offshore Structures
UR-83-34	Amdahl, Jørgen	Energy absorption in Ship-platform impacts
UR-84-37	Mørch, Morten	Motions and mooring forces of semi submersibles as determined by full-scale measurements and theoretical analysis
UR-84-38	Soares, C. Guedes	Probabilistic models for load effects in ship structures
UR-84-39	Aarsnes, Jan V.	Current forces on ships
UR-84-40	Czujko, Jerzy	Collapse Analysis of Plates subjected to Biaxial Compression and Lateral Load
UR-85-46	Alf G. Engseth, MK	Finite element collapse analysis of tubular steel offshore structures. (Dr.Ing. Thesis)
UR-86-47	Dengody Sheshappa, MP	A Computer Design Model for Optimizing Fishing Vessel Designs Based on Techno-Economic Analysis. (Dr.Ing. Thesis)
UR-86-48	Vidar Aanesland, MH	A Theoretical and Numerical Study of Ship Wave Resistance. (Dr.Ing. Thesis)
UR-86-49	Heinz-Joachim Wessel, MK	Fracture Mechanics Analysis of Crack Growth in Plate Girders. (Dr.Ing. Thesis)
UR-86-50	Jon Taby, MK	Ultimate and Post-ultimate Strength of Dented Tubular Members. (Dr.Ing. Thesis)
UR-86-51	Walter Lian, MH	A Numerical Study of Two-Dimensional Separated Flow Past Bluff Bodies at Moderate KC-Numbers. (Dr.Ing. Thesis)
UR-86-52	Bjørn Sortland, MH	Force Measurements in Oscillating Flow on Ship Sections and Circular Cylinders in a U-Tube Water Tank. (Dr.Ing. Thesis)
UR-86-53	Kurt Strand, MM	A System Dynamic Approach to One-dimensional Fluid Flow. (Dr.Ing. Thesis)
UR-86-54	Arne Edvin Løken, MH	Three Dimensional Second Order Hydrodynamic Effects on Ocean Structures in Waves. (Dr.Ing. Thesis)
UR-86-55	Sigurd Falch, MH	A Numerical Study of Slamming of Two-Dimensional Bodies. (Dr.Ing. Thesis)
UR-87-56	Arne Braathen, MH	Application of a Vortex Tracking Method to the Prediction of Roll Damping of a Two-Dimension Floating Body. (Dr.Ing. Thesis)

UR-87-57	Bernt Leira, MK	Gaussian Vector Processes for Reliability Analysis involving Wave-Induced Load Effects. (Dr.Ing. Thesis)
UR-87-58	Magnus Småvik, MM	Thermal Load and Process Characteristics in a Two-Stroke Diesel Engine with Thermal Barriers (in Norwegian). (Dr.Ing. Thesis)
MTA-88-59	Bernt Arild Bremdal, MP	An Investigation of Marine Installation Processes – A Knowledge - Based Planning Approach. (Dr.Ing. Thesis)
MTA-88-60	Xu Jun, MK	Non-linear Dynamic Analysis of Space-framed Offshore Structures. (Dr.Ing. Thesis)
MTA-89-61	Gang Miao, MH	Hydrodynamic Forces and Dynamic Responses of Circular Cylinders in Wave Zones. (Dr.Ing. Thesis)
MTA-89-62	Martin Greenhow, MH	Linear and Non-Linear Studies of Waves and Floating Bodies. Part I and Part II. (Dr.Techn. Thesis)
MTA-89-63	Chang Li, MH	Force Coefficients of Spheres and Cubes in Oscillatory Flow with and without Current. (Dr.Ing. Thesis
MTA-89-64	Hu Ying, MP	A Study of Marketing and Design in Development of Marine Transport Systems. (Dr.Ing. Thesis)
MTA-89-65	Arild Jæger, MH	Seakeeping, Dynamic Stability and Performance of a Wedge Shaped Planing Hull. (Dr.Ing. Thesis)
MTA-89-66	Chan Siu Hung, MM	The dynamic characteristics of tilting-pad bearings
MTA-89-67	Kim Wikstrøm, MP	Analysis av projekteringen for ett offshore projekt. (Licenciat-avhandling)
MTA-89-68	Jiao Guoyang, MK	Reliability Analysis of Crack Growth under Random Loading, considering Model Updating. (Dr.Ing. Thesis)
MTA-89-69	Arnt Olufsen, MK	Uncertainty and Reliability Analysis of Fixed Offshore Structures. (Dr.Ing. Thesis)
MTA-89-70	Wu Yu-Lin, MR	System Reliability Analyses of Offshore Structures using improved Truss and Beam Models. (Dr.Ing. Thesis)
MTA-90-71	Jan Roger Hoff, MH	Three-dimensional Green function of a vessel with forward speed in waves. (Dr.Ing. Thesis)
MTA-90-72	Rong Zhao, MH	Slow-Drift Motions of a Moored Two-Dimensional Body in Irregular Waves. (Dr.Ing. Thesis)
MTA-90-73	Atle Minsaas, MP	Economical Risk Analysis. (Dr.Ing. Thesis)
MTA-90-74	Knut-Aril Farnes, MK	Long-term Statistics of Response in Non-linear Marine Structures. (Dr.Ing. Thesis)
MTA-90-75	Torbjørn Sotberg, MK	Application of Reliability Methods for Safety Assessment of Submarine Pipelines. (Dr.Ing.

		Thesis)
MTA-90-76	Zeuthen, Steffen, MP	SEAMAID. A computational model of the design process in a constraint-based logic programming environment. An example from the offshore domain. (Dr.Ing. Thesis)
MTA-91-77	Haagensen, Sven, MM	Fuel Dependant Cyclic Variability in a Spark Ignition Engine - An Optical Approach. (Dr.Ing. Thesis)
MTA-91-78	Løland, Geir, MH	Current forces on and flow through fish farms. (Dr.Ing. Thesis)
MTA-91-79	Hoen, Christopher, MK	System Identification of Structures Excited by Stochastic Load Processes. (Dr.Ing. Thesis)
MTA-91-80	Haugen, Stein, MK	Probabilistic Evaluation of Frequency of Collision between Ships and Offshore Platforms. (Dr.Ing. Thesis)
MTA-91-81	Sødahl, Nils, MK	Methods for Design and Analysis of Flexible Risers. (Dr.Ing. Thesis)
MTA-91-82	Ormberg, Harald, MK	Non-linear Response Analysis of Floating Fish Farm Systems. (Dr.Ing. Thesis)
MTA-91-83	Marley, Mark J., MK	Time Variant Reliability under Fatigue Degradation. (Dr.Ing. Thesis)
MTA-91-84	Krokstad, Jørgen R., MH	Second-order Loads in Multidirectional Seas. (Dr.Ing. Thesis)
MTA-91-85	Molteberg, Gunnar A., MM	The Application of System Identification Techniques to Performance Monitoring of Four Stroke Turbocharged Diesel Engines. (Dr.Ing. Thesis)
MTA-92-86	Mørch, Hans Jørgen Bjelke, MH	Aspects of Hydrofoil Design: with Emphasis on Hydrofoil Interaction in Calm Water. (Dr.Ing. Thesis)
MTA-92-87	Chan Siu Hung, MM	Nonlinear Analysis of Rotordynamic Instabilities in Highspeed Turbomachinery. (Dr.Ing. Thesis)
MTA-92-88	Bessason, Bjarni, MK	Assessment of Earthquake Loading and Response of Seismically Isolated Bridges. (Dr.Ing. Thesis)
MTA-92-89	Langli, Geir, MP	Improving Operational Safety through exploitation of Design Knowledge - an investigation of offshore platform safety. (Dr.Ing. Thesis)
MTA-92-90	Sævik, Svein, MK	On Stresses and Fatigue in Flexible Pipes. (Dr.Ing. Thesis)
MTA-92-91	Ask, Tor Ø., MM	Ignition and Flame Growth in Lean Gas-Air Mixtures. An Experimental Study with a Schlieren System. (Dr.Ing. Thesis)
MTA-86-92	Hessen, Gunnar, MK	Fracture Mechanics Analysis of Stiffened Tubular Members. (Dr.Ing. Thesis)

MTA-93-93	Steinebach, Christian, MM	Knowledge Based Systems for Diagnosis of Rotating Machinery. (Dr.Ing. Thesis)
MTA-93-94	Dalane, Jan Inge, MK	System Reliability in Design and Maintenance of Fixed Offshore Structures. (Dr.Ing. Thesis)
MTA-93-95	Steen, Sverre, MH	Cobblestone Effect on SES. (Dr.Ing. Thesis)
MTA-93-96	Karunakaran, Daniel, MK	Nonlinear Dynamic Response and Reliability Analysis of Drag-dominated Offshore Platforms. (Dr.Ing. Thesis)
MTA-93-97	Hagen, Arnulf, MP	The Framework of a Design Process Language. (Dr.Ing. Thesis)
MTA-93-98	Nordrik, Rune, MM	Investigation of Spark Ignition and Autoignition in Methane and Air Using Computational Fluid Dynamics and Chemical Reaction Kinetics. A Numerical Study of Ignition Processes in Internal Combustion Engines. (Dr.Ing. Thesis)
MTA-94-99	Passano, Elizabeth, MK	Efficient Analysis of Nonlinear Slender Marine Structures. (Dr.Ing. Thesis)
MTA-94-100	Kvålsvold, Jan, MH	Hydroelastic Modelling of Wetdeck Slamming on Multihull Vessels. (Dr.Ing. Thesis)
MTA-94-102	Bech, Sidsel M., MK	Experimental and Numerical Determination of Stiffness and Strength of GRP/PVC Sandwich Structures. (Dr.Ing. Thesis)
MTA-95-103	Paulsen, Hallvard, MM	A Study of Transient Jet and Spray using a Schlieren Method and Digital Image Processing. (Dr.Ing. Thesis)
MTA-95-104	Hovde, Geir Olav, MK	Fatigue and Overload Reliability of Offshore Structural Systems, Considering the Effect of Inspection and Repair. (Dr.Ing. Thesis)
MTA-95-105	Wang, Xiaozhi, MK	Reliability Analysis of Production Ships with Emphasis on Load Combination and Ultimate Strength. (Dr.Ing. Thesis)
MTA-95-106	Ulstein, Tore, MH	Nonlinear Effects of a Flexible Stern Seal Bag on Cobblestone Oscillations of an SES. (Dr.Ing. Thesis)
MTA-95-107	Solaas, Frøydis, MH	Analytical and Numerical Studies of Sloshing in Tanks. (Dr.Ing. Thesis)
MTA-95-108	Hellan, Øyvind, MK	Nonlinear Pushover and Cyclic Analyses in Ultimate Limit State Design and Reassessment of Tubular Steel Offshore Structures. (Dr.Ing. Thesis)
MTA-95-109	Hermundstad, Ole A., MK	Theoretical and Experimental Hydroelastic Analysis of High Speed Vessels. (Dr.Ing. Thesis)
MTA-96-110	Bratland, Anne K., MH	Wave-Current Interaction Effects on Large-Volume Bodies in Water of Finite Depth. (Dr.Ing. Thesis)
MTA-96-111	Herfjord, Kjell, MH	A Study of Two-dimensional Separated Flow by a Combination of the Finite Element Method and

		Navier-Stokes Equations. (Dr.Ing. Thesis)
MTA-96-112	Æsøy, Vilmar, MM	Hot Surface Assisted Compression Ignition in a Direct Injection Natural Gas Engine. (Dr.Ing. Thesis)
MTA-96-113	Eknes, Monika L., MK	Escalation Scenarios Initiated by Gas Explosions on Offshore Installations. (Dr.Ing. Thesis)
MTA-96-114	Erikstad, Stein O., MP	A Decision Support Model for Preliminary Ship Design. (Dr.Ing. Thesis)
MTA-96-115	Pedersen, Egil, MH	A Nautical Study of Towed Marine Seismic Streamer Cable Configurations. (Dr.Ing. Thesis)
MTA-97-116	Moksnes, Paul O., MM	Modelling Two-Phase Thermo-Fluid Systems Using Bond Graphs. (Dr.Ing. Thesis)
MTA-97-117	Halse, Karl H., MK	On Vortex Shedding and Prediction of Vortex-Induced Vibrations of Circular Cylinders. (Dr.Ing. Thesis)
MTA-97-118	Igland, Ragnar T., MK	Reliability Analysis of Pipelines during Laying, considering Ultimate Strength under Combined Loads. (Dr.Ing. Thesis)
MTA-97-119	Pedersen, Hans-P., MP	Levendefiskteknologi for fiskefartøy. (Dr.Ing. Thesis)
MTA-98-120	Vikestad, Kyrre, MK	Multi-Frequency Response of a Cylinder Subjected to Vortex Shedding and Support Motions. (Dr.Ing. Thesis)
MTA-98-121	Azadi, Mohammad R. E., MK	Analysis of Static and Dynamic Pile-Soil-Jacket Behaviour. (Dr.Ing. Thesis)
MTA-98-122	Ulltang, Terje, MP	A Communication Model for Product Information. (Dr.Ing. Thesis)
MTA-98-123	Torbergsen, Erik, MM	Impeller/Diffuser Interaction Forces in Centrifugal Pumps. (Dr.Ing. Thesis)
MTA-98-124	Hansen, Edmond, MH	A Discrete Element Model to Study Marginal Ice Zone Dynamics and the Behaviour of Vessels Moored in Broken Ice. (Dr.Ing. Thesis)
MTA-98-125	Videiro, Paulo M., MK	Reliability Based Design of Marine Structures. (Dr.Ing. Thesis)
MTA-99-126	Mainçon, Philippe, MK	Fatigue Reliability of Long Welds Application to Titanium Risers. (Dr.Ing. Thesis)
MTA-99-127	Haugen, Elin M., MH	Hydroelastic Analysis of Slamming on Stiffened Plates with Application to Catamaran Wetdecks. (Dr.Ing. Thesis)
MTA-99-128	Langhelle, Nina K., MK	Experimental Validation and Calibration of Nonlinear Finite Element Models for Use in Design of Aluminium Structures Exposed to Fire. (Dr.Ing. Thesis)
MTA-99-	Berstad, Are J., MK	Calculation of Fatigue Damage in Ship Structures.

129		(Dr.Ing. Thesis)
MTA-99-130	Andersen, Trond M., MM	Short Term Maintenance Planning. (Dr.Ing. Thesis)
MTA-99-131	Tveiten, Bård Wathne, MK	Fatigue Assessment of Welded Aluminium Ship Details. (Dr.Ing. Thesis)
MTA-99-132	Søreide, Fredrik, MP	Applications of underwater technology in deep water archaeology. Principles and practice. (Dr.Ing. Thesis)
MTA-99-133	Tønnessen, Rune, MH	A Finite Element Method Applied to Unsteady Viscous Flow Around 2D Blunt Bodies With Sharp Corners. (Dr.Ing. Thesis)
MTA-99-134	Elvekrok, Dag R., MP	Engineering Integration in Field Development Projects in the Norwegian Oil and Gas Industry. The Supplier Management of Norne. (Dr.Ing. Thesis)
MTA-99-135	Fagerholt, Kjetil, MP	Optimeringsbaserte Metoder for Ruteplanlegging innen skipsfart. (Dr.Ing. Thesis)
MTA-99-136	Bysveen, Marie, MM	Visualization in Two Directions on a Dynamic Combustion Rig for Studies of Fuel Quality. (Dr.Ing. Thesis)
MTA-2000-137	Storteig, Eskild, MM	Dynamic characteristics and leakage performance of liquid annular seals in centrifugal pumps. (Dr.Ing. Thesis)
MTA-2000-138	Sagli, Gro, MK	Model uncertainty and simplified estimates of long term extremes of hull girder loads in ships. (Dr.Ing. Thesis)
MTA-2000-139	Tronstad, Harald, MK	Nonlinear analysis and design of cable net structures like fishing gear based on the finite element method. (Dr.Ing. Thesis)
MTA-2000-140	Kroneberg, André, MP	Innovation in shipping by using scenarios. (Dr.Ing. Thesis)
MTA-2000-141	Haslum, Herbjørn Alf, MH	Simplified methods applied to nonlinear motion of spar platforms. (Dr.Ing. Thesis)
MTA-2001-142	Samdal, Ole Johan, MM	Modelling of Degradation Mechanisms and Stressor Interaction on Static Mechanical Equipment Residual Lifetime. (Dr.Ing. Thesis)
MTA-2001-143	Baarholm, Rolf Jarle, MH	Theoretical and experimental studies of wave impact underneath decks of offshore platforms. (Dr.Ing. Thesis)
MTA-2001-144	Wang, Lihua, MK	Probabilistic Analysis of Nonlinear Wave-induced Loads on Ships. (Dr.Ing. Thesis)
MTA-2001-145	Kristensen, Odd H. Holt, MK	Ultimate Capacity of Aluminium Plates under Multiple Loads, Considering HAZ Properties. (Dr.Ing. Thesis)
MTA-2001-146	Greco, Marilena, MH	A Two-Dimensional Study of Green-Water

		Loading. (Dr.Ing. Thesis)
MTA-2001-147	Heggelund, Svein E., MK	Calculation of Global Design Loads and Load Effects in Large High Speed Catamarans. (Dr.Ing. Thesis)
MTA-2001-148	Babalola, Olusegun T., MK	Fatigue Strength of Titanium Risers – Defect Sensitivity. (Dr.Ing. Thesis)
MTA-2001-149	Mohammed, Abuu K., MK	Nonlinear Shell Finite Elements for Ultimate Strength and Collapse Analysis of Ship Structures. (Dr.Ing. Thesis)
MTA-2002-150	Holmedal, Lars E., MH	Wave-current interactions in the vicinity of the sea bed. (Dr.Ing. Thesis)
MTA-2002-151	Rognebakke, Olav F., MH	Sloshing in rectangular tanks and interaction with ship motions. (Dr.Ing. Thesis)
MTA-2002-152	Lader, Pål Furset, MH	Geometry and Kinematics of Breaking Waves. (Dr.Ing. Thesis)
MTA-2002-153	Yang, Qinzheng, MH	Wash and wave resistance of ships in finite water depth. (Dr.Ing. Thesis)
MTA-2002-154	Melhus, Øyvin, MM	Utilization of VOC in Diesel Engines. Ignition and combustion of VOC released by crude oil tankers. (Dr.Ing. Thesis)
MTA-2002-155	Ronæss, Marit, MH	Wave Induced Motions of Two Ships Advancing on Parallel Course. (Dr.Ing. Thesis)
MTA-2002-156	Økland, Ole D., MK	Numerical and experimental investigation of whipping in twin hull vessels exposed to severe wet deck slamming. (Dr.Ing. Thesis)
MTA-2002-157	Ge, Chunhua, MK	Global Hydroelastic Response of Catamarans due to Wet Deck Slamming. (Dr.Ing. Thesis)
MTA-2002-158	Byklum, Eirik, MK	Nonlinear Shell Finite Elements for Ultimate Strength and Collapse Analysis of Ship Structures. (Dr.Ing. Thesis)
IMT-2003-1	Chen, Haibo, MK	Probabilistic Evaluation of FPSO-Tanker Collision in Tandem Offloading Operation. (Dr.Ing. Thesis)
IMT-2003-2	Skaugset, Kjetil Bjørn, MK	On the Suppression of Vortex Induced Vibrations of Circular Cylinders by Radial Water Jets. (Dr.Ing. Thesis)
IMT-2003-3	Chezhian, Muthu	Three-Dimensional Analysis of Slamming. (Dr.Ing. Thesis)
IMT-2003-4	Buhaug, Øyvind	Deposit Formation on Cylinder Liner Surfaces in Medium Speed Engines. (Dr.Ing. Thesis)
IMT-2003-5	Tregde, Vidar	Aspects of Ship Design: Optimization of Aft Hull with Inverse Geometry Design. (Dr.Ing. Thesis)
IMT-	Wist, Hanne Therese	Statistical Properties of Successive Ocean Wave

2003-6		Parameters. (Dr.Ing. Thesis)
IMT-2004-7	Ransau, Samuel	Numerical Methods for Flows with Evolving Interfaces. (Dr.Ing. Thesis)
IMT-2004-8	Soma, Torkel	Blue-Chip or Sub-Standard. A data interrogation approach of identity safety characteristics of shipping organization. (Dr.Ing. Thesis)
IMT-2004-9	Ersdal, Svein	An experimental study of hydrodynamic forces on cylinders and cables in near axial flow. (Dr.Ing. Thesis)
IMT-2005-10	Brodtkorb, Per Andreas	The Probability of Occurrence of Dangerous Wave Situations at Sea. (Dr.Ing. Thesis)
IMT-2005-11	Yttervik, Rune	Ocean current variability in relation to offshore engineering. (Dr.Ing. Thesis)
IMT-2005-12	Fredheim, Arne	Current Forces on Net-Structures. (Dr.Ing. Thesis)
IMT-2005-13	Heggernes, Kjetil	Flow around marine structures. (Dr.Ing. Thesis
IMT-2005-14	Fouques, Sebastien	Lagrangian Modelling of Ocean Surface Waves and Synthetic Aperture Radar Wave Measurements. (Dr.Ing. Thesis)
IMT-2006-15	Holm, Håvard	Numerical calculation of viscous free surface flow around marine structures. (Dr.Ing. Thesis)
IMT-2006-16	Bjørheim, Lars G.	Failure Assessment of Long Through Thickness Fatigue Cracks in Ship Hulls. (Dr.Ing. Thesis)
IMT-2006-17	Hansson, Lisbeth	Safety Management for Prevention of Occupational Accidents. (Dr.Ing. Thesis)
IMT-2006-18	Zhu, Xinying	Application of the CIP Method to Strongly Nonlinear Wave-Body Interaction Problems. (Dr.Ing. Thesis)
IMT-2006-19	Reite, Karl Johan	Modelling and Control of Trawl Systems. (Dr.Ing. Thesis)
IMT-2006-20	Smogeli, Øyvind Notland	Control of Marine Propellers. From Normal to Extreme Conditions. (Dr.Ing. Thesis)
IMT-2007-21	Storhaug, Gaute	Experimental Investigation of Wave Induced Vibrations and Their Effect on the Fatigue Loading of Ships. (Dr.Ing. Thesis)
IMT-2007-22	Sun, Hui	A Boundary Element Method Applied to Strongly Nonlinear Wave-Body Interaction Problems. (PhD Thesis, CeSOS)
IMT-2007-23	Rustad, Anne Marthine	Modelling and Control of Top Tensioned Risers. (PhD Thesis, CeSOS)
IMT-2007-24	Johansen, Vegar	Modelling flexible slender system for real-time simulations and control applications
IMT-2007-25	Wroldsen, Anders Sunde	Modelling and control of tensegrity structures.

		(PhD Thesis, CeSOS)
IMT-2007-26	Aronsen, Kristoffer Høye	An experimental investigation of in-line and combined inline and cross flow vortex induced vibrations. (Dr. avhandling, IMT)
IMT-2007-27	Gao, Zhen	Stochastic Response Analysis of Mooring Systems with Emphasis on Frequency-domain Analysis of Fatigue due to Wide-band Response Processes (PhD Thesis, CeSOS)
IMT-2007-28	Thorstensen, Tom Anders	Lifetime Profit Modelling of Ageing Systems Utilizing Information about Technical Condition. (Dr.ing. thesis, IMT)
IMT-2008-29	Refsnes, Jon Erling Gorset	Nonlinear Model-Based Control of Slender Body AUVs (PhD Thesis, IMT)
IMT-2008-30	Berntsen, Per Ivar B.	Structural Reliability Based Position Mooring. (PhD-Thesis, IMT)
IMT-2008-31	Ye, Naiquan	Fatigue Assessment of Aluminium Welded Box-stiffener Joints in Ships (Dr.ing. thesis, IMT)
IMT-2008-32	Radan, Damir	Integrated Control of Marine Electrical Power Systems. (PhD-Thesis, IMT)
IMT-2008-33	Thomassen, Paul	Methods for Dynamic Response Analysis and Fatigue Life Estimation of Floating Fish Cages. (Dr.ing. thesis, IMT)
IMT-2008-34	Pákozdi, Csaba	A Smoothed Particle Hydrodynamics Study of Two-dimensional Nonlinear Sloshing in Rectangular Tanks. (Dr.ing.thesis, IMT/ CeSOS)
IMT-2007-35	Grytøyr, Guttorm	A Higher-Order Boundary Element Method and Applications to Marine Hydrodynamics. (Dr.ing.thesis, IMT)
IMT-2008-36	Drummen, Ingo	Experimental and Numerical Investigation of Nonlinear Wave-Induced Load Effects in Containerships considering Hydroelasticity. (PhD thesis, CeSOS)
IMT-2008-37	Skejic, Renato	Maneuvering and Seakeeping of a Singel Ship and of Two Ships in Interaction. (PhD-Thesis, CeSOS)
IMT-2008-38	Harlem, Alf	An Age-Based Replacement Model for Repairable Systems with Attention to High-Speed Marine Diesel Engines. (PhD-Thesis, IMT)
IMT-2008-39	Alsos, Hagbart S.	Ship Grounding. Analysis of Ductile Fracture, Bottom Damage and Hull Girder Response. (PhD-thesis, IMT)
IMT-2008-40	Graczyk, Mateusz	Experimental Investigation of Sloshing Loading and Load Effects in Membrane LNG Tanks Subjected to Random Excitation. (PhD-thesis, CeSOS)
IMT-2008-41	Taghipour, Reza	Efficient Prediction of Dynamic Response for Flexible amd Multi-body Marine Structures. (PhD-

		thesis, CeSOS)
IMT-2008-42	Ruth, Eivind	Propulsion control and thrust allocation on marine vessels. (PhD thesis, CeSOS)
IMT-2008-43	Nystad, Bent Helge	Technical Condition Indexes and Remaining Useful Life of Aggregated Systems. PhD thesis, IMT
IMT-2008-44	Soni, Prashant Kumar	Hydrodynamic Coefficients for Vortex Induced Vibrations of Flexible Beams, PhD thesis, CeSOS
IMT-2009-45	Amlashi, Hadi K.K.	Ultimate Strength and Reliability-based Design of Ship Hulls with Emphasis on Combined Global and Local Loads. PhD Thesis, IMT
IMT-2009-46	Pedersen, Tom Arne	Bond Graph Modelling of Marine Power Systems. PhD Thesis, IMT
IMT-2009-47	Kristiansen, Trygve	Two-Dimensional Numerical and Experimental Studies of Piston-Mode Resonance. PhD-Thesis, CeSOS
IMT-2009-48	Ong, Muk Chen	Applications of a Standard High Reynolds Number Model and a Stochastic Scour Prediction Model for Marine Structures. PhD-thesis, IMT
IMT-2009-49	Hong, Lin	Simplified Analysis and Design of Ships subjected to Collision and Grounding. PhD-thesis, IMT
IMT-2009-50	Koushan, Kamran	Vortex Induced Vibrations of Free Span Pipelines, PhD thesis, IMT
IMT-2009-51	Korsvik, Jarl Eirik	Heuristic Methods for Ship Routing and Scheduling. PhD-thesis, IMT
IMT-2009-52	Lee, Jihoon	Experimental Investigation and Numerical in Analyzing the Ocean Current Displacement of Longlines. Ph.d.-Thesis, IMT.
IMT-2009-53	Vestbøstad, Tone Gran	A Numerical Study of Wave-in-Deck Impact usin a Two-Dimensional Constrained Interpolation Profile Method, Ph.d.thesis, CeSOS.
IMT-2009-54	Bruun, Kristine	Bond Graph Modelling of Fuel Cells for Marine Power Plants. Ph.d.-thesis, IMT
IMT 2009-55	Holstad, Anders	Numerical Investigation of Turbulence in a Sekwed Three-Dimensional Channel Flow, Ph.d.-thesis, IMT.
IMT 2009-56	Ayala-Uraga, Efren	Reliability-Based Assessment of Deteriorating Ship-shaped Offshore Structures, Ph.d.-thesis, IMT
IMT 2009-57	Kong, Xiangjun	A Numerical Study of a Damaged Ship in Beam Sea Waves. Ph.d.-thesis, IMT/CeSOS.
IMT 2010-58	Kristiansen, David	Wave Induced Effects on Floaters of Aquaculture Plants, Ph.d.-thesis, CeSOS.

IMT 2010-59	Ludvigsen, Martin	An ROV-Toolbox for Optical and Acoustic Scientific Seabed Investigation. Ph.d.-thesis IMT.
IMT 2010-60	Hals, Jørgen	Modelling and Phase Control of Wave-Energy Converters. Ph.d.thesis, CeSOS.
IMT 2010- 61	Shu, Zhi	Uncertainty Assessment of Wave Loads and Ultimate Strength of Tankers and Bulk Carriers in a Reliability Framework. Ph.d. Thesis, IMT/ CeSOS
IMT 2010-62	Shao, Yanlin	Numerical Potential-Flow Studies on Weakly-Nonlinear Wave-Body Interactions with/without Small Forward Speed, Ph.d.thesis,CeSOS.
IMT 2010-63	Califano, Andrea	Dynamic Loads on Marine Propellers due to Intermittent Ventilation. Ph.d.thesis, IMT.
IMT 2010-64	El Khoury, George	Numerical Simulations of Massively Separated Turbulent Flows, Ph.d.-thesis, IMT
IMT 2010-65	Seim, Knut Sponheim	Mixing Process in Dense Overflows with Emphasis on the Faroe Bank Channel Overflow. Ph.d.thesis, IMT
IMT 2010-66	Jia, Huirong	Structural Analysis of Intect and Damaged Ships in a Collission Risk Analysis Perspective. Ph.d.thesis CeSoS.
IMT 2010-67	Jiao, Linlin	Wave-Induced Effects on a Pontoon-type Very Large Floating Structures (VLFS). Ph.D.-thesis, CeSOS.
IMT 2010-68	Abrahamsen, Bjørn Christian	Sloshing Induced Tank Roof with Entrapped Air Pocket. Ph.d.thesis, CeSOS.
IMT 2011-69	Karimirad, Madjid	Stochastic Dynamic Response Analysis of Spar-Type Wind Turbines with Catenary or Taut Mooring Systems. Ph.d.-thesis, CeSOS.
IMT - 2011-70	Erlend Meland	Condition Monitoring of Safety Critical Valves. Ph.d.-thesis, IMT.
IMT – 2011-71	Yang, Limin	Stochastic Dynamic System Analysis of Wave Energy Converter with Hydraulic Power Take-Off, with Particular Reference to Wear Damage Analysis, Ph.d. Thesis, CeSOS.
IMT – 2011-72	Visscher, Jan	Application of Particla Image Velocimetry on Turbulent Marine Flows, Ph.d.Thesis, IMT.
IMT – 2011-73	Su, Biao	Numerical Predictions of Global and Local Ice Loads on Ships. Ph.d.Thesis, CeSOS.
IMT – 2011-74	Liu, Zhenhui	Analytical and Numerical Analysis of Iceberg Collision with Ship Structures. Ph.d.Thesis, IMT.
IMT – 2011-75	Aarsæther, Karl Gunnar	Modeling and Analysis of Ship Traffic by Observation and Numerical Simulation. Ph.d.Thesis, IMT.

Imt – 2011-76	Wu, Jie	Hydrodynamic Force Identification from Stochastic Vortex Induced Vibration Experiments with Slender Beams. Ph.d.Thesis, IMT.
Imt – 2011-77	Amini, Hamid	Azimuth Propulsors in Off-design Conditions. Ph.d.Thesis, IMT.
IMT – 2011-78	Nguyen, Tan-Hoi	Toward a System of Real-Time Prediction and Monitoring of Bottom Damage Conditions During Ship Grounding. Ph.d.thesis, IMT.
IMT- 2011-79	Tavakoli, Mohammad T.	Assessment of Oil Spill in Ship Collision and Grounding, Ph.d.thesis, IMT.
IMT- 2011-80	Guo, Bingjie	Numerical and Experimental Investigation of Added Resistance in Waves. Ph.d.Thesis, IMT.
IMT- 2011-81	Chen, Qiaofeng	Ultimate Strength of Aluminium Panels, considering HAZ Effects, IMT
IMT- 2012-82	Kota, Ravikiran S.	Wave Loads on Decks of Offshore Structures in Random Seas, CeSOS.
IMT- 2012-83	Sten, Ronny	Dynamic Simulation of Deep Water Drilling Risers with Heave Compensating System, IMT.
IMT- 2012-84	Berle, Øyvind	Risk and resilience in global maritime supply chains, IMT.
IMT- 2012-85	Fang, Shaoji	Fault Tolerant Position Mooring Control Based on Structural Reliability, CeSOS.
IMT- 2012-86	You, Jikun	Numerical studies on wave forces and moored ship motions in intermediate and shallow water, CeSOS.
IMT- 2012-87	Xiang ,Xu	Maneuvering of two interacting ships in waves, CeSOS
IMT- 2012-88	Dong, Wenbin	Time-domain fatigue response and reliability analysis of offshore wind turbines with emphasis on welded tubular joints and gear components, CeSOS
IMT- 2012-89	Zhu, Suji	Investigation of Wave-Induced Nonlinear Load Effects in Open Ships considering Hull Girder Vibrations in Bending and Torsion, CeSOS
IMT- 2012-90	Zhou, Li	Numerical and Experimental Investigation of Station-keeping in Level Ice, CeSOS
IMT- 2012-91	Ushakov, Sergey	Particulate matter emission characteristics from diesel enignes operating on conventional and alternative marine fuels, IMT
IMT- 2013-1	Yin, Decao	Experimental and Numerical Analysis of Combined In-line and Cross-flow Vortex Induced Vibrations, CeSOS

IMT-2013-2	Kurniawan, Adi	Modelling and geometry optimisation of wave energy converters, CeSOS
IMT-2013-3	Al Ryati, Nabil	Technical condition indexes doe auxiliary marine diesel engines, IMT
IMT-2013-4	Firoozkoohi, Reza	Experimental, numerical and analytical investigation of the effect of screens on sloshing, CeSOS
IMT-2013-5	Ommani, Babak	Potential-Flow Predictions of a Semi-Displacement Vessel Including Applications to Calm Water Broaching, CeSOS
IMT-2013-6	Xing, Yihan	Modelling and analysis of the gearbox in a floating spar-type wind turbine, CeSOS
IMT-7-2013	Balland, Océane	Optimization models for reducing air emissions from ships, IMT
IMT-8-2013	Yang, Dan	Transitional wake flow behind an inclined flat plate-----Computation and analysis, IMT
IMT-9-2013	Abdillah, Suyuthi	Prediction of Extreme Loads and Fatigue Damage for a Ship Hull due to Ice Action, IMT
IMT-10-2013	Ramìrez, Pedro Agustìn Pèrez	Ageing management and life extension of technical systems- Concepts and methods applied to oil and gas facilities, IMT
IMT-11-2013	Chuang, Zhenju	Experimental and Numerical Investigation of Speed Loss due to Seakeeping and Maneuvering. IMT
IMT-12-2013	Etemaddar, Mahmoud	Load and Response Analysis of Wind Turbines under Atmospheric Icing and Controller System Faults with Emphasis on Spar Type Floating Wind Turbines, IMT
IMT-13-2013	Lindstad, Haakon	Strategies and measures for reducing maritime CO2 emissons, IMT
IMT-14-2013	Haris, Sabril	Damage interaction analysis of ship collisions, IMT
IMT-15-2013	Shainee, Mohamed	Conceptual Design, Numerical and Experimental Investigation of a SPM Cage Concept for Offshore Mariculture, IMT
IMT-16-2013	Gansel, Lars	Flow past porous cylinders and effects of biofouling and fish behavior on the flow in and around Atlantic salmon net cages, IMT
IMT-17-2013	Gaspar, Henrique	Handling Aspects of Complexity in Conceptual Ship Design, IMT
IMT-18-2013	Thys, Maxime	Theoretical and Experimental Investigation of a Free Running Fishing Vessel at Small Frequency of Encounter, CeSOS
IMT-19-2013	Aglen, Ida	VIV in Free Spanning Pipelines, CeSOS

IMT-1-2014	Song, An	Theoretical and experimental studies of wave diffraction and radiation loads on a horizontally submerged perforated plate, CeSOS
IMT-2-2014	Rogne, Øyvind Ygre	Numerical and Experimental Investigation of a Hinged 5-body Wave Energy Converter, CeSOS
IMT-3-2014	Dai, Lijuan	Safe and efficient operation and maintenance of offshore wind farms ,IMT
IMT-4-2014	Bachynski, Erin Elizabeth	Design and Dynamic Analysis of Tension Leg Platform Wind Turbines, CeSOS
IMT-5-2014	Wang, Jingbo	Water Entry of Freefall Wedged – Wedge motions and Cavity Dynamics, CeSOS
IMT-6-2014	Kim, Ekaterina	Experimental and numerical studies related to the coupled behavior of ice mass and steel structures during accidental collisions, IMT
IMT-7-2014	Tan, Xiang	Numerical investigation of ship's continuous- mode icebreaking in leverl ice, CeSOS
IMT-8-2014	Muliawan, Made Jaya	Design and Analysis of Combined Floating Wave and Wind Power Facilities, with Emphasis on Extreme Load Effects of the Mooring System, CeSOS
IMT-9-2014	Jiang, Zhiyu	Long-term response analysis of wind turbines with an emphasis on fault and shutdown conditions, IMT
IMT-10-2014	Dukan, Fredrik	ROV Motion Control Systems, IMT
IMT-11-2014	Grimsmo, Nils I.	Dynamic simulations of hydraulic cylinder for heave compensation of deep water drilling risers, IMT
IMT-12-2014	Kvittem, Marit I.	Modelling and response analysis for fatigue design of a semisubmersible wind turbine, CeSOS
IMT-13-2014	Akhtar, Juned	The Effects of Human Fatigue on Risk at Sea, IMT
IMT-14-2014	Syahroni, Nur	Fatigue Assessment of Welded Joints Taking into Account Effects of Residual Stress, IMT
IMT-1-2015	Bøckmann, Eirik	Wave Propulsion of ships, IMT
IMT-2-2015	Wang, Kai	Modelling and dynamic analysis of a semi-submersible floating vertical axis wind turbine, CeSOS
IMT-3-2015	Fredriksen, Arnt Gunvald	A numerical and experimental study of a two-dimensional body with moonpool in waves and current, CeSOS
IMT-4-2015	Jose Patricio Gallardo Canabes	Numerical studies of viscous flow around bluff bodies, IMT

IMT-5-2015	Vegard Longva	Formulation and application of finite element techniques for slender marine structures subjected to contact interactions, IMT
IMT-6-2015	Jacobus De Vaal	Aerodynamic modelling of floating wind turbines, CeSOS
IMT-7-2015	Fachri Nasution	Fatigue Performance of Copper Power Conductors, IMT
IMT-8-2015	Oleh I Karpa	Development of bivariate extreme value distributions for applications in marine technology,CeSOS
IMT-9-2015	Daniel de Almeida Fernandes	An output feedback motion control system for ROVs, AMOS
IMT-10-2015	Bo Zhao	Particle Filter for Fault Diagnosis: Application to Dynamic Positioning Vessel and Underwater Robotics, CeSOS
IMT-11-2015	Wenting Zhu	Impact of emission allocation in maritime transportation, IMT
IMT-12-2015	Amir Rasekhi Nejad	Dynamic Analysis and Design of Gearboxes in Offshore Wind Turbines in a Structural Reliability Perspective, CeSOS
IMT-13-2015	Arturo Jesùs Ortega Malca	Dynamic Response of Flexibles Risers due to Unsteady Slug Flow, CeSOS
IMT-14-2015	Dagfinn Husjord	Guidance and decision-support system for safe navigation of ships operating in close proximity, IMT
IMT-15-2015	Anirban Bhattacharyya	Ducted Propellers: Behaviour in Waves and Scale Effects, IMT
IMT-16-2015	Qin Zhang	Image Processing for Ice Parameter Identification in Ice Management, IMT
IMT-1-2016	Vincentius Rumawas	Human Factors in Ship Design and Operation: An Experiential Learning, IMT
IMT-2-2016	Martin Storheim	Structural response in ship-platform and ship-ice collisions, IMT
IMT-3-2016	Mia Abrahamsen Prsic	Numerical Simulations of the Flow around single and Tandem Circular Cylinders Close to a Plane Wall, IMT
IMT-4-2016	Tufan Arslan	Large-eddy simulations of cross-flow around ship sections, IMT

IMT-5-2016	Pierre Yves-Henry	Parametrisation of aquatic vegetation in hydraulic and coastal research,IMT
IMT-6-2016	Lin Li	Dynamic Analysis of the Instalation of Monopiles for Offshore Wind Turbines, CeSOS
IMT-7-2016	Øivind Kåre Kjerstad	Dynamic Positioning of Marine Vessels in Ice, IMT
IMT-8-2016	Xiaopeng Wu	Numerical Analysis of Anchor Handling and Fish Trawling Operations in a Safety Perspective, CeSOS
IMT-9-2016	Zhengshun Cheng	Integrated Dynamic Analysis of Floating Vertical Axis Wind Turbines, CeSOS
IMT-10-2016	Ling Wan	Experimental and Numerical Study of a Combined Offshore Wind and Wave Energy Converter Concept
IMT-11-2016	Wei Chai	Stochastic dynamic analysis and reliability evaluation of the roll motion for ships in random seas, CeSOS
IMT-12-2016	Øyvind Selnes Patricksson	Decision support for conceptual ship design with focus on a changing life cycle and future uncertainty, IMT
IMT-13-2016	Mats Jørgen Thorsen	Time domain analysis of vortex-induced vibrations, IMT
IMT-14-2016	Edgar McGuinness	Safety in the Norwegian Fishing Fleet – Analysis and measures for improvement, IMT
IMT-15-2016	Sepideh Jafarzadeh	Energy effiency and emission abatement in the fishing fleet, IMT
IMT-16-2016	Wilson Ivan Guachamin Acero	Assessment of marine operations for offshore wind turbine installation with emphasis on response-based operational limits, IMT
IMT-17-2016	Mauro Candeloro	Tools and Methods for Autonomous Operations on Seabed and Water Coumn using Underwater Vehicles, IMT
IMT-18-2016	Valentin Chabaud	Real-Time Hybrid Model Testing of Floating Wind Tubines, IMT
IMT-1-2017	Mohammad Saud Afzal	Three-dimensional streaming in a sea bed boundary layer
IMT-2-2017	Peng Li	A Theoretical and Experimental Study of Wave-induced Hydroelastic Response of a Circular Floating Collar
IMT-3-2017	Martin Bergström	A simulation-based design method for arctic maritime transport systems

IMT-4-2017	Bhushan Taskar	The effect of waves on marine propellers and propulsion
IMT-5-2017	Mohsen Bardestani	A two-dimensional numerical and experimental study of a floater with net and sinker tube in waves and current
IMT-6-2017	Fatemeh Hoseini Dadmarzi	Direct Numerical Simualtion of turbulent wakes behind different plate configurations
IMT-7-2017	Michel R. Miyazaki	Modeling and control of hybrid marine power plants
IMT-8-2017	Giri Rajasekhar Gunnu	Safety and effiency enhancement of anchor handling operations with particular emphasis on the stability of anchor handling vessels
IMT-9-2017	Kevin Koosup Yum	Transient Performance and Emissions of a Turbocharged Diesel Engine for Marine Power Plants
IMT-10-2017	Zhaolong Yu	Hydrodynamic and structural aspects of ship collisions
IMT-11-2017	Martin Hassel	Risk Analysis and Modelling of Allisions between Passing Vessels and Offshore Installations
IMT-12-2017	Astrid H. Brodtkorb	Hybrid Control of Marine Vessels – Dynamic Positioning in Varying Conditions
IMT-13-2017	Kjersti Bruserud	Simultaneous stochastic model of waves and current for prediction of structural design loads
IMT-14-2017	Finn-Idar Grøtta Giske	Long-Term Extreme Response Analysis of Marine Structures Using Inverse Reliability Methods
IMT-15-2017	Stian Skjong	Modeling and Simulation of Maritime Systems and Operations for Virtual Prototyping using co-Simulations
IMT-1-2018	Yingguang Chu	Virtual Prototyping for Marine Crane Design and Operations
IMT-2-2018	Sergey Gavrilin	Validation of ship manoeuvring simulation models
IMT-3-2018	Jeevith Hegde	Tools and methods to manage risk in autonomous subsea inspection,maintenance and repair operations
IMT-4-2018	Ida M. Strand	Sea Loads on Closed Flexible Fish Cages
IMT-5-2018	Erlend Kvinge Jørgensen	Navigation and Control of Underwater Robotic Vehicles

IMT-6-2018	Bård Stovner	Aided Intertial Navigation of Underwater Vehicles
IMT-7-2018	Erlend Liavåg Grotle	Thermodynamic Response Enhanced by Sloshing in Marine LNG Fuel Tanks
IMT-8-2018	Børge Rokseth	Safety and Verification of Advanced Maritime Vessels
IMT-9-2018	Jan Vidar Ulveseter	Advances in Semi-Empirical Time Domain Modelling of Vortex-Induced Vibrations
IMT-10-2018	Chenyu Luan	Design and analysis for a steel braceless semi-submersible hull for supporting a 5-MW horizontal axis wind turbine
IMT-11-2018	Carl Fredrik Rehn	Ship Design under Uncertainty
IMT-12-2018	Øyvind Ødegård	Towards Autonomous Operations and Systems in Marine Archaeology
IMT-13-2018	Stein Melvær Nornes	Guidance and Control of Marine Robotics for Ocean Mapping and Monitoring
IMT-14-2018	Petter Norgren	Autonomous Underwater Vehicles in Arctic Marine Operations: Arctic marine research and ice monitoring
IMT-15-2018	Minjoo Choi	Modular Adaptable Ship Design for Handling Uncertainty in the Future Operating Context
MT-16-2018	Ole Alexander Eidsvik	Dynamics of Remotely Operated Underwater Vehicle Systems
IMT-17-2018	Mahdi Ghane	Fault Diagnosis of Floating Wind Turbine Drivetrain- Methodologies and Applications
IMT-18-2018	Christoph Alexander Thieme	Risk Analysis and Modelling of Autonomous Marine Systems
IMT-19-2018	Yugao Shen	Operational limits for floating-collar fish farms in waves and current, without and with well-boat presence
IMT-20-2018	Tianjiao Dai	Investigations of Shear Interaction and Stresses in Flexible Pipes and Umbilicals
IMT-21-2018	Sigurd Solheim Pettersen	Resilience by Latent Capabilities in Marine Systems
IMT-22-2018	Thomas Sauder	Fidelity of Cyber-physical Empirical Methods. Application to the Active Truncation of Slender Marine Structures
IMT-23-2018	Jan-Tore Horn	Statistical and Modelling Uncertainties in the Design of Offshore Wind Turbines

IMT-24-2018	Anna Swider	Data Mining Methods for the Analysis of Power Systems of Vessels
IMT-1-2019	Zhao He	Hydrodynamic study of a moored fish farming cage with fish influence
IMT-2-2019	Isar Ghamari	Numerical and Experimental Study on the Ship Parametric Roll Resonance and the Effect of Anti-Roll Tank
IMT-3-2019	Håkon Strandenes	Turbulent Flow Simulations at Higher Reynolds Numbers
IMT-4-2019	Siri Mariane Holen	Safety in Norwegian Fish Farming – Concepts and Methods for Improvement
IMT-5-2019	Ping Fu	Reliability Analysis of Wake-Induced Riser Collision
IMT-6-2019	Vladimir Krivopolianskii	Experimental Investigation of Injection and Combustion Processes in Marine Gas Engines using Constant Volume Rig
IMT-7-2019	Anna Maria Kozlowska	Hydrodynamic Loads on Marine Propellers Subject to Ventilation and out of Water Condition.
IMT-8-2019	Hans-Martin Heyn	Motion Sensing on Vessels Operating in Sea Ice: A Local Ice Monitoring System for Transit and Stationkeeping Operations under the Influence of Sea Ice
IMT-9-2019|	Stefan Vilsen	Method for Real-Time Hybrid Model Testing of Ocean Structures – Case on Slender Marine Systems
IMT-10-2019	Finn-Christian W. Hanssen	Non-Linear Wave-Body Interaction in Severe Waves
IMT-11-2019	Trygve Olav Fossum	Adaptive Sampling for Marine Robotics
IMT-12-2019	Jørgen Bremnes Nielsen	Modeling and Simulation for Design Evaluation
IMT-13-2019	Yuna Zhao	Numerical modelling and dyncamic analysis of offshore wind turbine blade installation
IMT-14-2019	Daniela Myland	Experimental and Theoretical Investigations on the Ship Resistance in Level Ice
IMT-15-2019	Zhengru Ren	Advanced control algorithms to support automated offshore wind turbine installation
IMT-16-2019	Drazen Polic	Ice-propeller impact analysis using an inverse propulsion machinery simulation approach
IMT-17-2019	Endre Sandvik	Sea passage scenario simulation for ship system performance evaluation

IMT-18-2019	Loup Suja-Thauvin	Response of Monopile Wind Turbines to Higher Order Wave Loads
IMT-19-2019	Emil Smilden	Structural control of offshore wind turbines – Increasing the role of control design in offshore wind farm development
IMT-20-2019	Aleksandar-Sasa Milakovic	On equivalent ice thickness and machine learning in ship ice transit simulations
IMT-1-2020	Amrit Shankar Verma	Modelling, Analysis and Response-based Operability Assessment of Offshore Wind Turbine Blade Installation with Emphasis on Impact Damages
IMT-2-2020	Bent Oddvar Arnesen Haugaløkken	Autonomous Technology for Inspection, Maintenance and Repair Operations in the Norwegian Aquaculture
IMT-3-2020	Seongpil Cho	Model-based fault detection and diagnosis of a blade pitch system in floating wind turbines
IMT-4-2020	Jose Jorge Garcia Agis	Effectiveness in Decision-Making in Ship Design under Uncertainty
IMT-5-2020	Thomas H. Viuff	Uncertainty Assessment of Wave-and Current-induced Global Response of Floating Bridges
IMT-6-2020	Fredrik Mentzoni	Hydrodynamic Loads on Complex Structures in the Wave Zone
IMT-7-2020	Senthuran Ravinthrakumar	Numerical and Experimental Studies of Resonant Flow in Moonpools in Operational Conditions
IMT-8-2020	Stian Skaalvik Sandøy	Acoustic-based Probabilistic Localization and Mapping using Unmanned Underwater Vehicles for Aquaculture Operations
IMT-9-2020	Kun Xu	Design and Analysis of Mooring System for Semi-submersible Floating Wind Turbine in Shallow Water
IMT-10-2020	Jianxun Zhu	Cavity Flows and Wake Behind an Elliptic Cylinder Translating Above the Wall
IMT-11-2020	Sandra Hogenboom	Decision-making within Dynamic Positioning Operations in the Offshore Industry – A Human Factors based Approach
IMT-12-2020	Woongshik Nam	Structural Resistance of Ship and Offshore Structures Exposed to the Risk of Brittle Failure
IMT-13-2020	Svenn Are Tutturen Værnø	Transient Performance in Dynamic Positioning of Ships: Investigation of Residual Load Models and Control Methods for Effective Compensation
IMT-14-2020	Mohd Atif Siddiqui	Behaviour of a Damaged Ship in Waves: Experimental and Numerical Hydrodynamic Analysis of a Damaged Ship Section
IMT-15-2020	John Marius Hegseth	Efficient Modelling and Design Optimization of Large Floating Wind Turbines